Dipl.-Ing. Matthias Ehrhart

Applications of image-assisted total stations: Concepts, experiments, results and calibration

DOCTORAL THESIS

to achieve the university degree of

Doktor der technischen Wissenschaften

submitted to

Graz University of Technology

Supervisor

Univ.-Prof. Dr.techn. Werner Lienhart

Institute of Engineering Geodesy and Measurement Systems

Graz, October 2017

AFFIDAVIT

I declare that I have authored this thesis independently, that I have not used other than the declared sources/resources, and that I have explicitly indicated all material which has been quoted either literally or by content from the sources used. The text document uploaded to TUGRAZonline is identical to the present doctoral thesis.

Date

Signature

Abstract

Today, different manufacturers of total stations equip their instruments with additional cameras which results in image-assisted total stations (IATSs). In contrast to the fully operational hardware of these instruments, the number of available applications which use the additional cameras for image-based measurements is still very limited.

To exploit the potential of these new instruments, different applications of IATSs are presented in this thesis. Along with the preparation of the required theory and the description of the used image processing algorithms, the individual applications are evaluated by experimental measurements with commercially available state-of-the-art IATSs under realistic environmental conditions.

The presented applications include static and dynamic deformation monitoring of civil engineering structures in which an IATS serves as a contactless measurement system that does not require access to the monitored structure at any time. The image-based measurements of an IATS are also used to tackle the correction of the vertical refraction angle which biases the vertical angle measurement of every total station. By measurements in a small-scale geodetic network, it is demonstrated that an IATS allows the determination of the coordinates of passive targets, such as simple printouts of a circle, with an accuracy of a few 0.01 mm. Furthermore, the image data of an IATS is used for the improvement of the conventional prism tracking with total stations in terms of robustness and seamless operation.

Besides these applications, also concepts for relating the image-based measurements to theodolite angles and for a thorough but fast and simple calibration of an IATS are presented.

Zusammenfassung

Die Totalstationen verschiedener Hersteller sind heutzutage vielfach mit zusätzlichen Kameras ausgestattet und werden folglich als Video-Totalstationen (engl.: *image-assisted total station*, IATS) bezeichnet. Im Gegensatz zu den voll funktionsfähigen Kameras dieser Instrumente sind die verfügbaren Anwendungen für bildbasierte Messungen noch sehr limitiert.

Um das Potential dieser neuartigen Instrumente ausschöpfen zu können, werden in dieser Arbeit verschiedene Anwendungen von IATS vorgestellt. Neben der Aufbereitung der notwendigen theoretischen Grundlagen und der Beschreibung der verwendeten Algorithmen für die Bildverarbeitung, werden die Anwendungen durch experimentelle Messungen unter realistischen Bedingungen evaluiert. Dabei werden ausschließlich kommerziell erhältliche Standard-Instrumente verwendet.

Die vorgestellten Anwendungen beinhalten statische und dynamische Deformationsmessungen an Bauwerken wobei eine IATS als kontaktloses Messsystem dient. Daraus folgt, dass Zugang zum überwachten Bauwerk zu keiner Zeit notwendig ist. Mithilfe der Messdaten einer IATS wird der Versuch unternommen, den Einfluss des vertikalen Refraktionswinkels, welcher die Ableitung genauer Höhenunterschiede aus Vertikalwinkelmessungen von Totalstationen beeinträchtigt, zu korrigieren. Durch Messungen in einem kleinräumigen geodätischen Netz wird gezeigt, dass eine IATS die Bestimmung der Koordinaten von passiven Zielen, wie z.B. Ausdrucken von Kreisen, mit einer Genauigkeit von wenigen 0.01 mm ermöglicht. Weiteres werden die Bilddaten einer IATS zur Verbesserung von Robustheit und Unterbrechungsfreiheit der automatischen Zielverfolgung mit Totalstationen verwendet.

Neben den genannten Anwendungen werden zudem Konzepte für die Berechnung von bildbasierten Theodolit-Richtungen sowie für die vollständige aber zugleich auch einfache und schnelle Kalibrierung einer IATS vorgestellt.

Acknowledgments

I would like to thank Prof. Werner Lienhart for offering me the opportunity to write a doctoral thesis at his institute. I truly appreciate the trust he placed in me so that I could perform my research activities independently and focus on areas of my personal interest. Nevertheless, I also acknowledge the possibility to receive his input and feedback whenever needed.

I would further like to thank Prof. Thomas Wunderlich from TU Munich for the reviewing of this thesis as an external expert and also for his valuable comments.

Finally I express my gratitude to my colleagues at IGMS for the pleasant collaboration during the last years. Dr. Helmut Woschitz deserves special thanks for his input in different discussions and Prof. Fritz K. Brunner is mentioned for his indispensable help in the *Refraction* chapter of this thesis.

Contents

Symbols

α_{px}	angle per pixel
c	camera constant
δ	vertical refraction angle
Δ	correction, deviation or difference
ϵ_{coll}	collimation error
$\epsilon_{\mathrm{index}}$	vertical index error
ϵ_{long}	longitudinal zero point error of tilt compensator
ϵ_{tilt}	tilting axis error
$\epsilon_{\mathrm{trans}}$	transverse zero point error of tilt compensator
Hz	horizontal theodolite angle
i_{long}	longitudinal inclination measured by tilt compensator
i_{trans}	transverse inclination measured by tilt compensator

κ	rotation of image sensor about principal axis
K_1	first parameter of radial distortion polynomial
∂	partial derivative
$\mathbf{R}$	rotation matrix
s	slope distance or standard deviation
s_δ	standard deviation of angle-of-arrival fluctuations
u	image coordinate counted from left to right
u_0	principal point of image sensor in u-direction
v	image coordinate counted from top to bottom
v_0	principal point of image sensor in v-direction
V	vertical theodolite angle

Acronyms

2D	two-dimensional
3D	three-dimensional
AIT	Austrian Institute of Technology
ATR	automatic target recognition
AOV	angle of view
BRIEF	binary robust independent elementary features
CAMSHIFT	continuously adaptive mean shift
EDM	electronic distance measurement
FAST	features from accelerated segment test
FOV	field of view
HSV	hue saturation value
IATS	image-assisted total station

IGMS	Institute of Engineering Geodesy and Measurement Systems, Graz University of Technology, Austria
LSM	least-squares matching
ORB	oriented FAST and rotated BRIEF
PSD	position sensitive device
RAM	random-access memory
RANSAC	random sample consensus
ROI	region of interest
RTS	robotic total station
SDK	software development kit
SNR	signal-to-noise-ratio
TIN	triangulated irregular network
TLS	terrestrial laser scanner
TPSDK	Trimble Precision SDK

1

Introduction

1.1 MOTIVATION

Based on the optical theodolite, which can be dated back to the ancient times, Table 1.1 provides a brief overview on some milestones in the evolution of the modern robotic total station (RTS). A more detailed review including different prototypes can be found in the literature (Ingensand 1992; Deumlich and Staiger 2002; Wunderlich 2005; Wunderlich et al. 2014; Wagner et al. 2014b).

The new developments typically generated new fields of application or improved existing workflows. The electronic distance measurement (EDM) unit with a measurement axis coaxial to the sighting axis of the *Zeiss RegElta 14* (Leitz 1969) enabled polar measurements to selected points. The electronic registration of measurement data did not provide new measurement values but precluded human errors in the manual recording of the values (e.g. transposed digits). The automated angle measurements towards prisms of the

Table 1.1: Some milestones in the evolution of the modern RTS

Year	Instrument	New development
1968	*Zeiss RegElta 14*	coaxial EDM and electronic data storage
1990	*Geodimeter System 4000*	automated angle measurements to prisms
2007	*Topcon GPT-9000Ai*	RTS with telescope and wide-angle camera
2013	*Leica MS50*	laser scanning (also equipped with telescope and wide-angle camera)

Geodimeter System 4000 (Geotronics 1991) enabled the control of the instrument in one-person operation in which the operator carries the prism and manages the instrument via a remote controller. Furthermore, the instrument could be used for automated monitoring systems in which the measured angles did not depend on the skill of the operator. By integrating a laser scanning functionality with measurement rates of up to 1000 Hz in the *Leica MS50* (Leica 2013a), it was possible to generate dense, geo-referenced point clouds in reasonable time which led to many new fields of application.

The *Topcon GPT-9000Ai* was the first modern RTS equipped with a telescope and a wide-angle camera (GIM International 2007) which extends this instrument to a so-called *image-assisted total station* (IATS). Other designations used in the literature involve *imaging station*, *video-theodolite* or *video-tacheometer* (also cf. Wagner 2017, p. 5). The telescope camera is located in the optical path of the IATS' telescope and the content of its image data is comparable to the manual observation through the telescope's eyepiece. The wide-angle camera is mounted eccentrically to the telescope and its image data covers larger scenes but without the optical magnification of the telescope.

Table 1.1 omits the commercially available motorized video-theodolites *Kern E2-SE* (Gottwald 1987) and *Wild TM3000V* (Katowski 1989) which were primarily used in stereo configuration for industrial metrology. These instruments disappeared from the market shortly after the invention of the laser tracker (Wagner et al. 2014b) which also allowed the highly accurate determination of three-dimensional (3D) coordinates but by only using a single instrument.

However, compared to the new fields of application for RTSs arising from the developments listed in Table 1.1, the new possibilities for IATSs based on currently implemented camera applications are limited (cf. Section 1.3.2). Therefore, the goal of this thesis is to identify and evaluate possible fields of application for state-of-the-art IATSs.

1.2 OUTLINE OF THE THESIS

The present chapter includes the motivation of this thesis (Section 1.1), a review of currently available state-of-the-art IATSs including their system specifications and ready-made camera applications (Section 1.3), and a description of the IATSs evaluated in this thesis (Section 1.4).

In the following chapters, different applications of state-of-the-art IATSs are discussed and experimentally evaluated. In the introduction section of each chapter related publications, resulting from the research activities of this thesis, are listed. Publications of other authors concerning the respective research topic are mentioned in the text.

Chapter 2 covers the usage of an IATS for static and dynamic deformation monitoring. Compared to conventional measurements with RTSs and retroreflective prisms, the usage of an IATS allows the automated, high-frequent and accurate measurement of non-signalized points. These points can be visually prominent features of the observed structure so that access to the structure is not required for installing artificial targets such as retroreflective prisms.

In Chapter 3, the correction of variations in the vertical refraction angle is addressed. Hereby, no other sensor than the IATS itself is used for collecting the necessary measurement data.

Chapter 4 is dedicated to highly accurate measurements with an IATS in a geodetic network. At this, possible errors that can occur for IATS measurements are discussed and strategies for avoiding these errors are presented.

In Chapter 5, the improvement of the automated prism tracking with RTSs is addressed. Hereby, the wide-angle camera of an IATS is used to speed up the coarse prism search and to provide a method for target identification.

Chapter 6 summarizes the mapping relation between image coordinates and corresponding theodolite angles. Along with the necessary mapping parameters, simplifications for the telescope camera are discussed.

In Chapter 7, the calibration of an IATS is described. Hereby, special emphasis is dedicated to the automation and efficiency of the calibration process which does not require additional measurement equipment.

Chapters 6 and 7 (mapping and calibration) explain the preliminaries for evaluating the applications of the previous chapters. Experts for IATSs can skip these two chapters or can compare them to their own implementations for mapping and calibration. Inexperienced readers might want to start with these two chapters, especially with Chapter 6, before tackling the chapters covering actual applications.

Chapter 8 finally summarizes the findings of this thesis and provides an outlook on possible future research and developments.

1.3 STATE-OF-THE-ART

1.3.1 Hardware and system specifications

Compact reviews of the evolution of modern IATSs, including different prototypes, are provided by Wunderlich (2005), Wasmeier

(2009, pp. 3ff.), Wagner et al. (2014b), and Wagner (2017, pp. 5ff.). Concerning the different prototypes it can be distinguished between feasibility studies of different manufacturers (e.g. Walser 2004; Wasmeier 2009) and clip-on systems which replace the eyepiece of a commercially available RTS by a camera (e.g. Bürki et al. 2010; Hauth et al. 2012).

Original system specifications

Table 1.2 lists the camera specifications of commercially available IATSs which fulfill the hardware requirements of the applications presented in this thesis, i.e., instruments that are equipped with a telescope and a wide-angle camera. The list is limited to the most recent instrument of the different manufacturers and includes the original specifications taken from the respective user manuals or datasheets. Furthermore, the IATS *Nikon Nivo-i*, which was jointly developed by *Nikon Corporation* and *Trimble Inc.*, is omitted because its system specifications are only available in Japanese (Nikon-Trimble 2016). Further specifications of the listed instruments are summarized in Lachat et al. (2017) and can also be found in the respective user manuals or datasheets (Leica 2015a; Topcon 2011a; Topcon 2011b; Trimble 2016b).

The focusing range of the listed cameras ranges from about 2 m to infinity in which the telescope cameras provide functionality for automated focusing and the focus is fixed for the wide-angle cameras. The *Trimble SX10* is equipped with two fixed-focus cameras which are referred to as *overview* and *primary* camera (Trimble 2016b). The maximum frame rate of the video streams given in Table 1.2 refers to the displaying of the image data on the instrument screen or on a remote controller. It is noted that for the transmission of the video stream to an external computer via a wired connection higher frame rates can be possible (cf. Section 1.4).

The listed IATSs are available with a precision of 0.3 mgon for the angle measurements and provide the possibility of reflectorless

Table 1.2: Original camera specifications of state-of-the-art IATSs (Leica 2015a, pp. 70f; Topcon 2011a, p. 156; Topcon 2011b; Trimble 2016b)

Leica MS60	
resolution:	5 Mpx (2560 × 1920)
frame rate(1):	up to 20 fps
field of view:	1.5° diagonal (telescope camera)
	15.5° × 11.7° or 19.4° diagonal (overview camera)
focal length:	231 mm at infinity (telescope camera)
	21 mm (overview camera)
Topcon IS-3	
resolution:	1.3 Mpx (1280 × 1024)
image speed(1):	10 fps
angle of field:	1° diagonal (telescope camera)
	33° diagonal (wide-angle camera)
Trimble SX10	
resolution:	5 Mpx (2592 × 1944)
frame rate(1):	up to 15 fps
field of view max:	57.5° × 43.0°
field of view min:	0.65° × 0.5°
one pixel at 50 m:	0.88 mm (telescope camera)
	4.4 mm (primary camera)
	20 mm (overview camera)

(1) max. frame rate for displaying video stream on instrument screen or on remote controller

distance measurements. Furthermore, the instruments are so-called *scanning total stations* which comprise a laser scanning functionality with measurement rates of up to 1000 Hz (*Leica MS60*), 20 Hz (*Topcon IS-3*), and 26600 Hz (*Trimble SX10*).

However, the specifications of Table 1.2 are hard to compare because of different designations for presumably the same parameter (e.g. *field of view* and *angle of field*). Furthermore, different information content is provided.

Unified system specifications

Important specifications for the design of measurement concepts for different IATS applications involve

- the resolution (in pixel) of the image data in horizontal and vertical direction,
- the angle of view (AOV) in horizontal and vertical direction, i.e., the maximum angles which can be observed with the camera (also referred to as format angle or field angle, cf. Luhmann et al. 2014, p. 189),
- the angle per pixel α_{px}, i.e., the angular value to which one pixel corresponds to, and
- the maximum frame rate which is important for dynamic measurements.

These parameters can be computed or at least approximated by converting the original specifications of Table 1.2. It is hereby assumed that the specified *field of view* or *angle of field* designates the AOV. Based on the AOV, the angle per pixel α_{px} can be approximated by

$$\alpha_{\mathrm{px}} \approx \frac{\mathrm{AOV}}{\text{number of pixels}} \tag{1.1}$$

which can then be used to compute the AOV in horizontal and vertical direction in cases in which only a diagonal AOV is specified.

For example the specifications of the telescope camera of the *Leica MS60* (Table 1.2) list a diagonal AOV of 1.67 gon (= 1.5°) and an image diagonal of 3200 px ($= \sqrt{2560^2 + 1920^2}$) which results in $\alpha_{\mathrm{px}} = 0.52\,\mathrm{mgon/px}$. By rearranging Eq. (1.1), the AOV in horizontal and vertical direction can be computed by inserting the respective number of pixels for each direction.

It is noted that α_{px} is not constant for the entire image. For pixels in the boundary area of the image, the value is slightly smaller than for pixels in the central region of the image. Therefore, the camera constant, which is inversely proportional to α_{px}, is used for an accurate relation between the image coordinates and the corresponding theodolite angles (Chapter 6). Furthermore, for the telescope camera of an IATS the camera constant and consequently α_{px} vary with the focus position of the telescope and a precise calibration (Chapter 7) is required for measurement purposes. However, for comparing different IATSs and for coarse approximations of achievable accuracies, α_{px} is an intuitive value and its variations can be neglected for these purposes.

The specified values for the minimum AOV of the *Trimble SX10* (denoted as *field of view* in Table 1.2) result in $\alpha_{\text{px}} = 0.28\,\text{mgon/px}$ which translates to 0.22 mm at a distance of 50 m. For this distance, it is specified that one pixel of the telescope camera corresponds to 0.88 mm (Table 1.2) which is 4-times larger than the computed value. It is therefore assumed that the actual AOV of the telescope camera is 4-times larger than the specified minimum values and that these specified values result from using only a central region of the full image.

Table 1.3 lists the unified camera specifications of the state-of-the-art IATSs based on the original specifications provided by the manufacturers (Table 1.2). Concerning the accuracy of the image-based measurements, α_{px} can be regarded as the key specification in which it is again noted the values of Table 1.3 result from the original specifications of Table 1.2. A camera calibration (Chapter 7) can result in a different value which is demonstrated by α_{px} of the telescope camera of the *Leica MS60* (compare Table 1.3 and 1.6). For example in monitoring applications (Chapter 2), α_{px} and the coarse distance between the IATS and the observed structure provide a coarse approximation for the quantification of the image-based measurements. Consequently, small values for α_{px} are preferable. For the sake of completeness it is already mentioned that the image-based measurements are not limited to α_{px} but can be conducted with sub-pixel accuracy (cf. Section 2.4.2).

Table 1.3: Unified camera specifications of state-of-the-art IATSs computed from Table 1.2

	Leica MS60	**Topcon IS-3**	**Trimble SX10**
		Telescope camera	
AOV [gon × gon]:	1.3 × 1.0	0.9 × 0.7	2.9 × 2.2
α_{px} [mgon/px]:	0.5	0.7	1.1
		Wide-angle camera(s)$^{(1)}$	
AOV [gon × gon]:	17.2 × 13.0	28.6 × 22.9	14.4 × 11.1 63.9 × 47.8
α_{px} [mgon/px]:	6.7	22.4	5.6 24.6
		Common properties	
resolution [px × px]:	2560 × 1920	1280 × 1024	2592 × 1944
frame rate$^{(2)}$ [fps]:	20	10	15

(1) the *Trimble SX10* is equipped with two wide-angle cameras

(2) max. frame rate for displaying video stream on instrument screen or on remote controller

The AOV characterizes the extent of the scene that can be observed with the camera for a single telescope position, i.e., without rotating the telescope of the IATS. Accordingly, large values are preferable for the AOV. However, as illustrated in Table 1.3 a large AOV is typically accompanied by the compromise of a large α_{px}.

A high frame rate of the video stream is important for the monitoring of oscillating structures. For higher frame rates, higher frequencies can be resolved in the amplitude spectrum of the measured oscillation (cf. Section 2.6). It is again noted that the frame rates of Table 1.3 refer to the displaying of the video stream on the instrument screen or on a remote controller and higher frame rates can be possible for the transmission of the video stream to an external computer via a wired connection (compare Table 1.3 and 1.6).

Another important issue is the quality of the image data (e.g. noise level) for unfavorable illumination conditions which is a function of the camera system including lenses and image sensor. The quality of the image data is hard to quantify in a generally applicable way and none of the manuals or datasheets of the listed IATSs (Table 1.2) includes information on this issue. However, it is noted that instruments without an eyepiece, such as the *Trimble SX10*, tend to produce telescope camera images with less noise than instruments comprising an eyepiece. For the latter, the incoming light must be split onto the image sensor and towards the eyepiece (Leica 2013b). Consequently, less light is received by the image sensor which degrades the quality of the image data especially for unfavorable illumination conditions.

Outlook on possible future developments

The total station manufacturers filed numerous patents concerning the integration of different non-visual cameras (e.g. range imaging or thermal cameras) in a RTS. Apart from these patents, reports on the realization of such instruments are not publicly available elsewhere and the practical feasibility of constructing such instruments is unclear. Nevertheless, patents sometimes provide an outlook on possible future developments and the integration of a range imaging camera in a RTS is exemplarily mentioned here. Such an instrument could be used for the positioning of a 3D object in space (Walser et al. 2014; Pettersson et al. 2016) in which Schestauer et al. (2017) showed that this is also possible with the wide-angle camera of an IATS. Other applications using the range imaging camera are the steering of the RTS based on movements of the operator (Pettersson et al. 2015) or generally the measurement of a plurality of 3D points (Ohtomo and Kumagai 2016). In another embodiment, the RTS is equipped with a thermal camera which provides a method for the accurate geo-referencing of surface temperatures of different objects (Zimmermann et al. 2013).

1.3.2 Applications

As discussed in Section 1.3.1, different total station manufacturers include IATSs in their range of products. However, for practical measurement applications the usage of the camera is limited to the software which is either implemented in the IATS itself (onboard software) or is available for the postprocessing of the captured image data.

Onboard applications

The onboard software provided by different total station manufacturers (Topcon 2011a; Joyce et al. 2012; Leica 2013b; Leica 2014; Grimm 2014; Trimble 2016a) allows the steering of the IATS by tapping to a respective position in the video stream which is displayed on the instrument screen or on the remote controller. This is especially helpful for measurements in one-person operation in which the operator manages the instrument with the remote controller. It is also possible to store images of measured points for documentation purposes. Hereby, sketches can be drawn on the images instead of taking notes on a sheet of paper. Furthermore, measured points can be displayed in the video stream which allows an in-field verification whether a point has already been measured or not. In staking out, points to be marked in the field can also be displayed in the video stream which allows a fast positioning of the reflector pole on the respective points. Another application is the automated capturing of panorama images. For scanning total stations, the image data can be used to overlay the scanned points with color information to create a photorealistic 3D point cloud of the measured object. The area to be scanned can be selected by drawing a polygon in the displayed video stream.

However, the applications mentioned above utilize the camera sensor primarily for visualization purposes. An onboard application which uses the camera for actual measurements is the “edge abstraction mode” of the *Topcon IS-3* (Topcon 2011a, pp. 109f.). Hereby, points that do not permit a direct distance measurement (e.g. corners) are detected by image processing. The detailed operating principle cannot be found in the respective manual (Topcon 2011a, pp. 109f.) but it is assumed that the 3D coordinates result from a reflectorless distance measurement in the vicinity of the corner and from the image-based direction directly towards the corner. Another onboard measurement application of the *Topcon IS-3* is the “feature scan” which is described in Topcon (2007, pp. 15ff.). Hereby, the image data is used to automatically select features to be measured in a later scanning of the defined area of interest. The IATS *Nikon Nivo-i* also includes an onboard application for image-based measurements. After translation (https://translate.google.com) of the Japanese datasheet (Nikon-Trimble 2016), it can be concluded that the application allows the automated monitoring of cracks in civil engineering structures by means of image-based measurements.

Postprocessing applications

Image-based measurement applications for postprocessing (Joyce et al. 2012; Grimm 2014) involve the computation of 3D coordinates based on spatial forward intersection by using the image data from at least two instrument positions. Another method for the computation of 3D coordinates is the intersection of image rays with a target plane. For both methods, it is taken advantage of the total station capabilities which provide knowledge of the camera position and rotation for each captured image. Another application is the rectification of images which can then be used for image-based measurements on e.g. facades of buildings or for the detection of surface deficiencies of infrastructure objects like concrete dams (Kalenjuk and Lienhart 2017).

Patents

Compared to the limited number of ready-made measurement applications, the total station manufacturers filed myriads of patents describing different image-based measurement applications for IATSs and only a few ideas are mentioned here. Compared to research results published in scientific literature, the ideas proposed in patents are typically kept very general to protect the claims for a wide range of applications.

For example Metzler (2014) describes a method for automatically verifying a “surveying instrument’s” external orientation in which the description of the surveying instrument corresponds to an IATS. However, the proposed idea of image-based measurements towards a faraway reference point for checking the IATS’s external orientation could also be applied to e.g. laser trackers on a smaller scale.

Svanholm et al. (2011) propose a method for the automated aiming towards a target based on the IATS’s wide-angle camera which is eccentric to the theodolite center. The procedure involves a selection of the target in the video stream by the user. Afterwards, the telescope is iteratively positioned towards that target in which a distance measurement is conducted at each telescope position to account for the eccentricity of the wide-angle camera.

Ohtomo et al. (2010) describe a method for the automated selection of points to be measured. Hereby, an area of interest is defined by the user and a set of images covering the whole scene is automatically captured with the wide-angle camera of the IATS. After stitching the image set to a single panorama image, prominent features (e.g. lines or corners) are automatically detected. Afterwards, the telescope is successively positioned towards the detected image features in which an image with the telescope camera is captured at each position. In the image of the telescope camera, prominent image features are again detected. The positions of these features are used to set up a measurement program, i.e., in the vicinity of these features more points are measured than in areas with a homogeneous visual structure.

Kludas et al. (2013) also use the image data of an IATS with scanning functionality to define scan areas whereat areas with varying grid densities can be defined. It is also proposed to use the image data for an automated definition of the grid densities. The measurement of a crack in a building's facade is provided as an example. Hereby, the image data is used to define the whole facade as the area to be scanned. The crack is automatically identified as an object of special interest and the scanning is done with a higher density in the vicinity of the crack.

Hertzman et al. (2011) describe a method for measuring the instrument height and for evaluating the centering of the instrument above a ground mark. This is done by pointing the telescope of the IATS towards the nadir and taking an image with the wide-angle camera. After altering the horizontal angle of the IATS by 200 gon, a second image is captured. With knowledge of the eccentricity of the wide-angle camera w.r.t. the theodolite center, the baseline of the two camera positions can be computed and the 3D coordinates of the ground mark result from stereo photogrammetry. The difference between the 3D coordinates of the ground mark and the theodolite center yields the instrument height and provides a possibility for verifying the correct centering of the instrument above the ground mark.

The last-mentioned idea again points out the difference between scientific literature and patents. Scientific articles typically include the formulation of a problem, theoretic background for solving this problem, and an evaluation of the theory by appropriate experiments. Patents typically also address a certain problem and provide ideas for overcoming the present limitations. However, a verification of the proposed ideas by experimental measurements is no prerequisite for filing a patent. For example the image-based measurement of the instrument height mentioned above is not possible with currently available state-of-the-art IATSs (Section 1.3.1) because the line-of-sight between the wide-angle camera and the ground mark is obstructed by the IATS itself.

Table 1.4: Used IATSs with serial numbers and firmware versions

Name	**Serial**	**Firmware**
Leica MS50 I R2000	367005	5.00$^{(1)}$
Leica MS60 I R2000	882001	1.30$^{(2)}$, 2.00$^{(3)}$, 2.04$^{(4)}$, 2.13$^{(5)}$

(1) used in Section 2.6.1

(2) used in Section 2.5 and Chapter 4

(3) used in Chapter 5

(4) used in Chapter 3

(5) used in Section 2.6.2

1.4 USED INSTRUMENTS

The experimental measurements presented in this thesis were conducted by using the commercially available, state-of-the-art IATSs *Leica MS50* (Leica 2013a) and *Leica MS60* (Leica 2015a) from *Leica Geosystems AG*. It is emphasized that the instruments' hardware was not modified and that only regular firmware versions (no specialized development firmwares) were used. The instruments' serial numbers and the firmware versions, which were updated several times during the course of this thesis, are given in Table 1.4. Concerning the camera-related functionality, no differences could be observed for the different firmware versions of the *Leica MS60*.

Table 1.5 lists important measurement specifications of the used instruments in which it is noted that the given values are the same for both IATSs. Table 1.5 focuses on specifications which are important for image-based measurements to natural targets, i.e., measurements without retroreflective prisms. Accordingly, the properties of the EDM in reflectorless mode are displayed.

The accuracy of continuous reflectorless distance measurements is not published by the manufacturer. However, both instruments comprise a laser scanning functionality with measurement rates of up to 1000 Hz. The range noise in scanning mode is specified with 0.8 mm (1σ, measurement rate of 62 Hz) for measurements towards

Table 1.5: General measurement specifications of the used IATSs (Leica 2013a, pp. 51ff; Leica 2015a, pp. 64ff.)

Accuracies	
angle measurement:	0.3 mgon
automated angle to prism:	0.3 mgon but at least ±1 mm(1)
tilt compensator:	0.15 mgon
single distance:	2 mm + 2 ppm(2)
continuous distance:	3 mm + 1.5 ppm(3)
	0.5 mm at 25 m(4)
	0.8 mm at 100 m(4)
Average measurement rates(5)	
angle measurement:	about 20 Hz
automated angle to prism:	about 20 Hz
tilt compensator:	about 4 Hz
continuous distance:	about 20 Hz(6)

(1) for measurements to *Leica* circular (mini) prisms
(2) without reflector and for distances up to 500 m
(3) for measurements to reflective tape
(4) range noise (1σ) in scanning mode with 62 Hz towards *Kodak Grey Card* (albedo 90%)
(5) experimentally evaluated; non-constant measurement rates
(6) without reflector; evaluated for an absolute distance of 31 m

a *Kodak Grey Card* oriented perpendicular to the instrument at a distance of 100 m (Leica 2013a, p. 56; Leica 2015a, p. 69).

The measurement rates of Table 1.5 were experimentally evaluated and, similar to Lienhart et al. (2017), were found to be non-constant. Accordingly, the average measurement rates are listed in Table 1.5. It is hereby mentioned that the relatively high distance measurement rate of 20 Hz is achieved because of the specialized EDM sensor of the evaluated scanning total stations. For conventional RTSs, distance measurement rates of less than 10 Hz are reported in the literature (Psimoulis and Stiros 2007; Lienhart et al. 2017).

Table 1.6: Camera specifications of the used IATSs (Leica 2013a, p. 57; Leica 2015a, pp. 70f.)

Telescope camera	
image sensor:	2560 px × 1920 px CMOS sensor
AOV:	1.6 gon × 1.2 gon(1)
α_{px}:	0.6 mgon/px(1)
focal length:	231 mm at focus position infinity
optical magnification:	30x
focus range:	1.7 to infinity (automated focusing)
Wide-angle camera	
image sensor:	2560 px × 1920 px CMOS sensor
AOV:	17.2 gon × 13.0 gon
α_{px}:	6.7 mgon/px(2)
focal length:	21 mm
focus range:	2.0 m to infinity (fixed-focus)
Video transmission to external computer(3)	
resolution:	320 px × 240 px (*Leica MS50*)
	640 px × 480 px (*Leica MS60*)
frame rate(4):	up to 10 fps (*Leica MS50*)
	up to 30 fps (*Leica MS60*)

(1) computed from calibrated camera constant (Section 7.4)

(2) from Table 1.3

(3) experimentally evaluated

(4) can also be set to a lower value

Table 1.6 lists the camera-specific properties of the used instruments. Both IATSs are equipped with a telescope camera and a wide-angle camera in which the characteristics of the image sensor are the same for both instruments.

The angle per pixel α_{px} of the wide-angle camera is about 10-times larger than the corresponding value of the telescope camera. At a distance of e.g. 100 m, one pixel corresponds to about 10 mm for the wide-angle camera and to about 1 mm for the telescope camera.

Concerning the video transmission to an external computer, the interface of the *Leica MS60* was updated compared to its predecessor *Leica MS50* so that a higher resolution and a higher frame rate are possible. It is hereby noted that the video data can be transmitted for a reduced AOV so that the full image resolution, i.e., one pixel in the transmitted image data corresponds to one pixel of the image sensor, is preserved for both instruments (Ehrhart and Lienhart 2015b). Considering the resolution of the image sensor (2560 px × 1920 px), the transmission of the image data at full image resolution causes a reduction of the AOV by a factor 4 for the *Leica MS60* and by a factor 8 for the *Leica MS50*.

The experimental measurements presented in this thesis were conducted by steering the IATSs from an external computer with the *Leica GeoCOM* interface (Leica 2015b). Concerning the required computing power for evaluating the image processing algorithms of the different applications, the hardware of the used IATSs should be sufficient for an onboard implementation of these algorithms. Especially the *Leica MS60* is equipped with a computer (1 GHz *TI Cortex-A9* processor, 640 MB RAM) that outperforms the hardware which was used in the first implementations of most of the evaluated image processing algorithms. However, the firmware versions of the used IATSs (Table 1.4) are not designed to access the video streams of the cameras (telescope and wide-angle) in real-time.

Along with the evaluated *Leica* IATSs, other total station manufacturers offer comparable instruments (cf. Section 1.3.1). The applications presented in this thesis could also be used with these instruments – albeit with different accuracies and measurement rates (cf. Table 1.3). Hereby, the only prerequisites are the possibility to steer the IATS from an external computer and the transmission of the IATS's video stream. For e.g. *Trimble* IATSs, these prerequisites are fulfilled and were also tested by using the *Trimble Precision SDK* (TPSDK) interface.

2

Static and dynamic deformation monitoring

2.1 INTRODUCTION

"Engineering geodesy is the production of geodetic information necessary for the planning of technical projects, setting out of the project design, control of the correct construction, and monitoring of deformations." (Brunner 2007, p. 58)

"Engineering geodesy is the discipline of reality capture, setting-out and monitoring of local and regional geometry-related phenomena, paying particular attention to quality assessment, sensor systems and reference frames." (Kuhlmann et al. 2014, p. 333)

The above quotations on the definition of *engineering geodesy* agree that deformation monitoring of natural and artificial structures is one of its core competencies. The data acquisition, i.e., the measurement of the structure's changes, is an integral part of the monitoring process which also includes the analysis of the measurement data and the reporting of the results (DIN 18710-4).

In this thesis, it is distinguished between static (Section 2.5) and dynamic (Section 2.6) deformation monitoring in which the periods between the deformations are used for classification. High-frequent deformations, such as the vibrations of a structure, are observed by dynamic deformation monitoring. Along with the accuracy, which is important for static and dynamic deformation monitoring, the measurement frequency is a key feature of measurement systems for dynamic deformation monitoring. Long-term deformations, such as diurnal variations of a structure, are the subject of static deformation monitoring. Here, it is important that the measurements, which are taken over several days, weeks or months, refer to a common coordinate system. Accordingly, the verification of the measurement system's stability is an important issue for static deformation monitoring.

In this chapter, the usage of an IATS for both static and dynamic deformation monitoring is discussed. Different (known) measurement concepts are presented (Section 2.2) and an improved concept for deformation monitoring with a single IATS is described in detail (Section 2.3). A major advantage of the IATS over conventional total stations is that automated measurements can be conducted without retroreflective prisms but by using prominent features of the structure itself. Consequently, access to the monitored structure is not required which is especially beneficial for the monitoring of inaccessible points at civil engineering structures or for geo-monitoring applications. The automated image-based measurements towards the natural targets, which are based on well-known image processing techniques, are described in Section 2.4. The suitability of state-of-the-art IATSs for static (Section 2.5) and dynamic

(Section 2.6) deformation monitoring is experimentally evaluated at different bridges. Of course, the IATS measurements are not limited to bridges but can be used to monitor other civil engineering or natural structures as well.

Related publications

This chapter is based on the following articles: Ehrhart and Lienhart (2015a), Ehrhart and Lienhart (2015b), Ehrhart and Lienhart (2015c, with color illustrations), Lienhart and Ehrhart (2015), Lienhart et al. (2017, with color illustrations), and Ehrhart et al. (2017).

2.2 MEASUREMENT CONCEPTS

2.2.1 Polar measurements

Deformation monitoring with total stations comprises polar measurements, i.e., the observation of the horizontal and vertical angles *Hz* and *V* and the slope distance *s*, to selected points in different epochs. With knowledge of the station coordinates $\mathbf{x_0}$, the Cartesian coordinates of these points can be computed in a horizontal coordinate system after

$$\mathbf{x} = \mathbf{x_0} + s \begin{bmatrix} \cos Hz \sin V \\ \sin Hz \sin V \\ \cos V \end{bmatrix} \tag{2.1}$$

by using the measured polar coordinates Hz, V and s.

The measurement system for conventional total station measurements consists of the total station and retroreflective prisms to whose center the angles can be measured automatically. Inaccessible points at which no prism can be placed are typically measured by manual sighting in which the distance is measured by using the reflectorless EDM mode. For automated measurements with an IATS, artificial targets are not required because the angles to selected, visually definite points can be measured repeatably by using the image data of the IATS's camera (Wagner and Wasmeier 2014). The mapping relations between the image coordinates of a target and its corresponding theodolite angles are worked out in Chapter 6.

The image-based angle measurements can be used in Eq. (2.1) to compute the coordinates of selected points. As demonstrated in Chapter 4, the image-based angle measurements of a state-of-the-art IATS can be achieved with an *accuracy* of about 0.1 mgon which corresponds to 0.05 mm at a distance of 30 m. Concerning the accuracy of the 3D point, the accuracy of the distance in reflectorless EDM mode (e.g. 2 mm + 2 ppm, cf. Table 1.5) is typically the limiting factor. Along with the lower accuracy, also the measurement rate (e.g. 20 Hz, cf. Table 1.5) of the distance measurement is typically inferior to the update rate of the image data (e.g. 30 fps, cf. Table 1.6). Furthermore, the measurement rate of the EDM is not constant but shows irregular jump discontinuities (Lienhart et al. 2017) which is unfavorable for dynamic deformation monitoring.

A fundamental issue for image-based polar measurements is the calibration of the IATS (Chapter 7). Hereby, the relation between the principal axis of the image sensor and the EDM collimation axis (cf. Section 7.3.4) is especially important. To ensure that the involved measurements, i.e., the image-based angles and the EDM, refer to the same point, the telescope needs to be positioned so that the EDM axis points towards the point to be measured. This can involve an iterative positioning of the telescope which is a time consuming procedure. Furthermore, the pointing accuracy is limited to the positioning accuracy of the telescope.

An advantage of the polar measurements is that errors in most calibration parameters have negligible effects on the image-based angle measurements due to the iterative positioning of the telescope. An exception is the relation between the principal axis of the image sensor and the EDM collimation axis which is expressed by two rotation angles (cf. Section 7.3.4).

2.2.2 Stereo photogrammetry

An IATS utilizes an additional camera for automated, image-based angle measurements. Accordingly, an obvious method for the determination of 3D coordinates is the application of stereo photogrammetry which involves the intersection of oriented image rays towards the monitoring points from at least two instrument positions.

This principle was already used with the first commercially available video-theodolites (Gottwald 1987; Katowski 1989; Roic 1996; Mischke 2000) and was also successfully applied with different IATS prototypes (Huang 1992; Kahmen and Reiterer 2004; Reiterer et al. 2010; Zhang et al. 2012; Wagner et al. 2014a; Charalampous et al. 2015; Guillaume et al. 2016a). The principle of stereo photogrammetry can of course also be used with today's commercially available IATSs (Bretscher et al. 2017).

Furthermore, different patents exist in which the principle of stereo photogrammetry is either applied by using two instrument positions (Kludas and Vogel 2010) or one position and an instrument with two eccentric cameras (Svanholm et al. 2015). In another embodiment, one instrument with one camera, which is eccentric to the center of the total station, captures images in both telescope faces (Mein et al. 2016).

A drawback of the application of stereo photogrammetry for monitoring purposes is that at least two instruments are required to provide a continuous measurement system. Exceptions are the aforementioned single-instrument approaches. However, considering the maximum baseline of these approaches, a reasonable accuracy for the depth component can only be achieved for short distances (cf. Luhmann et al. 2014, pp. 317ff.).

The critical aspects for the application of stereo photogrammetry with IATSs are the automated and accurate detection and matching of homologous image points (Reiterer et al. 2010) and the system calibration which relates the matched image points to theodolite angles (Wagner et al. 2014a). A thorough calibration (cf. Chapter 7) is especially important when measuring points in the boundary areas of the image sensor. For dynamic deformation monitoring, the precise synchronization of the involved IATSs is another important issue (Guillaume et al. 2016a).

2.2.3 Surface texturing

Along with point-wise deformation measurements (e.g. after Section 2.2.1), an IATS also provides data for 3D surface deformation monitoring. Hereby, the surface model of an object is texturized with the image data of an IATS to generate a photo-realistic 3D model which can be analyzed for different epochs (Kalenjuk and Lienhart 2017). The surface of the object can be represented by a triangulated irregular network (TIN, Gong et al. 1999) or approximated by geometrical primitives (Scherer 2007). The necessary 3D points for generating the surface model result from reflectorless polar measurements towards the object. Hereby, only a few points are sufficient for the approximation of geometrical primitives in which a point cloud is necessary for the generation of a TIN. To measure a large number of 3D points in reasonable time, an IATS with scanning capability is essential.

A similar approach is reported by Wagner (2016) and Wagner et al. (2016) where an IATS with scanning capability is also used to measure the object's surface. The measured distances are then interpolated to each pixel of the captured images to generate a depth component for the image data. Accordingly, each pixel of the depth image can be regarded as an individual polar measurement (cf. Section 2.2.1) with Hz, V and s. For monitoring purposes, displacements transverse to the line-of-sight (or parallel to the image plane) of the IATS are detected by image-based measurements and displacements along the line-of-sight are obtained from comparing the corresponding pixels of the depth image.

Both approaches can only be used for static deformation monitoring because the scanning of the object's surface by reflectorless distance measurements is a sequential procedure and cannot be done simultaneously for all points in the region of interest (ROI). Furthermore, the heterogeneous quality of the measurement data along the line-of-sight, resulting from reflectorless distance measurements, and transverse to it, resulting from image-based measurements, is not ideal for 3D monitoring applications. Along with the higher accuracy (cf. Section 2.2.1), the image-based measurements also show a higher spatial resolution than the distance measurements. One pixel of the telescope camera of the evaluated IATSs (Section 1.4) corresponds to 1 mm at a distance of 100 m. The spatial resolution of the scanned 3D points cannot achieve this value even when setting the grid size for the scan to 1 mm. This is due to the size of the laser spot (e.g. more than 15 mm at 100 m, cf. Leica 2015a, p. 67) which causes a smoothing of the observed structures.

However, especially for geo-monitoring applications (Wagner 2016; Wagner et al. 2016) where the monitored object is hard to access, e.g. a rock face, 3D surface deformation monitoring by means of an IATS is a promising approach because it is a fully remote measurement technique. The relatively long time which is required for performing the distance measurements over the ROI is not an issue here because high-frequent measurements are typically not required for geo-monitoring applications. It is rather required to perform epoch-wise measurements in which the epochs can be separated by several hours, days, weeks or months. Hereby, a stable reference frame can be used to set up the IATS in each epoch so that the measurement results refer to a common coordinate system.

Similar to the application of stereo photogrammetry with IATSs (Section 2.2.2), an important issue for the application of surface texturing is the thorough calibration of the used instrument (cf. Chapter 7), especially when measuring points in the boundary areas of the image sensor. Furthermore, the relation between the principal axis of the image sensor and the EDM collimation axis requires a precise calibration (cf. Section 7.3.4) to ensure a congruency of the scanned surface and the image texture.

2.3 IN-PLANE AND OUT-OF-PLANE MEASUREMENTS

As discussed in Sections 2.2.1 and 2.2.3, the quality, including accuracy and temporal and spatial resolution, of the image-based measurements transverse to the sighting axis (or parallel to the image plane) is much higher than the quality of the distance measurements along the sighting axis. For monitoring applications it is therefore favorable to select the measurement geometry so that the relevant movements of the observed structure occur as *in-plane* movements, i.e., parallel to the image plane of the IATS. Compared to a conventional RTS, the usage of an IATS is hereby advantageous because its ability to automatically measure inaccessible points allows a more flexible selection of the instrument position and the monitoring points.

The concept of in-plane measurements accompanied by an analysis of possible *movement axes* is especially useful for the deformation monitoring of civil engineering structures. Here, the directions of the main movements of the observed structure along the movement axes are often known prior to the measurements and the instrument position can be chosen so that the relevant displacements occur as in-plane movements.

However, it is not always possible to adhere to the favorable measurement geometry, in which only in-plane movements occur, rigorously and *out-of-plane* movements of the structure can reduce the quality of the results if not handled adequately. Examples for different measurement geometries are illustrated in Section 2.3.1. In Section 2.3.2, strategies to reduce the errors caused by out-of-plane movements and to perform automated, high-frequent 3D measurements with an IATS are proposed. The effect of uncertainties in the involved measurements on the results is discussed in Section 2.3.3.

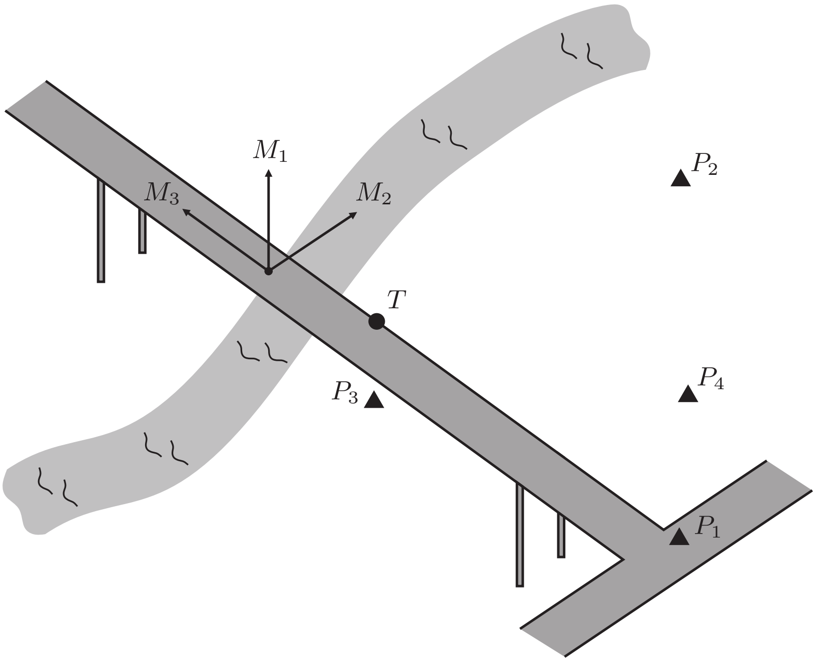

Figure 2.1: Different instrument positions P for bridge monitoring by observing the movement of a target T along the movement axes M_1, M_2 and M_3.

2.3.1 Measurement geometries

An example for different measurement geometries and the definition of the movement axes is depicted in Figure 2.1 which illustrates the monitoring of a target T on a bridge. A natural choice for the movement axes of a bridge would be in vertical direction (M_1), across (M_2) and along (M_3) the bridge. Hereby, it can be expected that the dynamic movements M_3 along the bridge are very small compared to M_1 and M_2.

For instrument position P_1, the movements along M_1 and M_2 appear as in-plane movements and out-of-plane movements occur along M_3. Since the movements along the bridge are assumed to be very small, the out-of-plane movements have a negligible effect on the observed movements along M_1 and M_2 (cf. Section 2.3.3). By using instrument position P_2 in the riverbed, the movements along M_1 and M_3 can be observed as approximate in-plane movements. Dependent on the vertical angle under which T is observed, the movements along M_1 cannot be regarded as rigorous in-plane movements. For instrument position P_3 directly underneath the bridge, the movements along M_2 and M_3 appear as in-plane movements. This measurement geometry has the disadvantage that the vertical movements M_1, which are probably the largest, occur as out-of-plane movements which are mapped to M_2 and M_3 if the telescope does not point along the vertical axis (cf. Section 2.3.3).

Instrument position P_4 in the riverbed illustrates an unfavorable measurement geometry since none of the movements is observed as an in-plane movement. The target is sighted under a small vertical angle because of the small distance and the movements along M_1 occur as out-of-plane movements. The oblique horizontal incident angle has the effect that the movements along M_2 and M_3 also occur as out-of-plane movements.

2.3.2 Proposed measurement concept

The surfaces of civil engineering structures can often be represented by geometrical primitives. This property is used by Scherer (2007) to measure individual 3D points by intersecting the corresponding image rays with the model of the structure. Alternatively, the image rays can also be intersected with the triangles of a TIN model (Gong et al. 1999) if the structure cannot be represented by geometrical primitives (cf. also Section 2.2.3).

The approach of Gong et al. (1999) and Scherer (2007) for computing 3D points by intersecting oriented image rays with a model of the structure is also proposed for highly accurate static and especially dynamic deformation monitoring with special emphasis on civil engineering structures. The basic idea is illustrated in Figure 2.2 where an element of the observed structure (e.g. the bridge of Section 2.3.1) with known movement axes and a visual target on

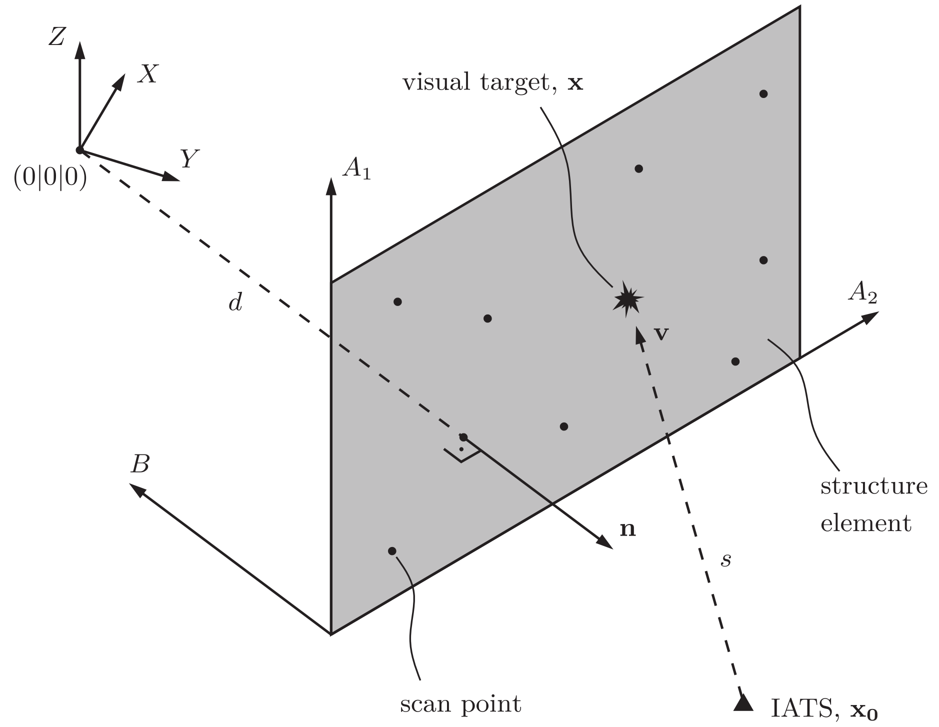

Figure 2.2: Element of a structure with primary (A_1 and A_2) and secondary (B) movement axes in a coordinate system XYZ (after Ehrhart et al. 2017).

it is represented by a plane.

This plane can be described by the Hesse normal form

$$\mathbf{n} \cdot \mathbf{x} - d = 0 \tag{2.2}$$

in which the parameters $\mathbf{n}$ and d can be determined by a plane fit of scanned points on the structure's surface. These points can result from distributed polar measurements towards the structure as proposed by Scherer (2007) or from a scan of the ROI as proposed by Gong et al. (1999) in which an IATS with scanning capability is required.

The framework of Chapter 6 for relating image coordinates to theodolite angles results in horizontal Hz and vertical V angles towards the visual target. These angles are used in combination with the slope distance s to compute 3D Cartesian coordinates in the local horizon system by

$$\mathbf{x} = \mathbf{x_0} + s \begin{bmatrix} \cos Hz \sin V \\ \sin Hz \sin V \\ \cos V \end{bmatrix} = \mathbf{x_0} + s\,\mathbf{v} \tag{2.3}$$

As discussed in Section 2.2.1, the quality, including accuracy and measurement rate, of the image-based angle measurements Hz and V is much higher than the quality of the distance measurement s. Consequently, the distance is not measured but computed by inserting Eq. (2.3) in Eq. (2.2) which, after slight rearrangement, results in

$$s = \frac{d - \mathbf{n} \cdot \mathbf{x_0}}{\mathbf{n} \cdot \mathbf{v}} \tag{2.4}$$

for the slope distance to the visual target point. For the computation of s it is of major importance that the scan points, from which the plane parameters $\mathbf{n}$ and d are computed, and the image-based angle measurements included in $\mathbf{v}$ refer to the same coordinate system XYZ (cf. Figure 2.2).

In deformation monitoring, the coordinate differences $\mathbf{\Delta x}$ between two epochs are the measurement results which are subject to further analysis. Assuming that the element of the observed structure exclusively moves along the primary movement axes A_1 and A_2 and that the element is not rotated, i.e., the plane parameters $\mathbf{n}$ and d are the same for both epochs, the coordinate differences are computed by

$$\begin{aligned} \mathbf{\Delta x} = \mathbf{x_2} - \mathbf{x_1} = s_2\,\mathbf{v_2} - s_1\,\mathbf{v_1} &= \frac{d - \mathbf{n} \cdot \mathbf{x_0}}{\mathbf{n} \cdot \mathbf{v_2}}\,\mathbf{v_2} - \frac{d - \mathbf{n} \cdot \mathbf{x_0}}{\mathbf{n} \cdot \mathbf{v_1}}\,\mathbf{v_1} \\ &= (d - \mathbf{n} \cdot \mathbf{x_0}) \left(\frac{\mathbf{v_2}}{\mathbf{n} \cdot \mathbf{v_2}} - \frac{\mathbf{v_1}}{\mathbf{n} \cdot \mathbf{v_1}} \right) \end{aligned} \tag{2.5}$$

in which the distances towards the target in the individual epochs are not measured but calculated after Eq. (2.4).

For $\mathbf{x_0} = [0, 0, 0]^T$, i.e., the origin of the coordinate system is located in the center of the IATS, Eq. (2.5) simplifies to

$$\mathbf{\Delta x} = d\left(\frac{\mathbf{v_2}}{\mathbf{n} \cdot \mathbf{v_2}} - \frac{\mathbf{v_1}}{\mathbf{n} \cdot \mathbf{v_1}}\right) \tag{2.6}$$

in which it is again noted that the plane parameters $\mathbf{n}$ and d must refer to the same coordinate system as the image-based angle measurements included in $\mathbf{v_1}$ and $\mathbf{v_2}$.

Uncertainties in the plane parameters $\mathbf{n} = [n_x, n_y, n_z]^T$ and d propagate on the displacements $\mathbf{\Delta x}$ after

$$\mathbf{\Sigma_{\Delta x}} = \mathbf{F}\,\mathbf{\Sigma_{plane}}\,\mathbf{F^T} \tag{2.7}$$

in which the Jacobian matrix

$$\begin{aligned} \mathbf{F} &= \begin{bmatrix} \frac{\partial \Delta x}{\partial n_x} & \frac{\partial \Delta x}{\partial n_y} & \frac{\partial \Delta x}{\partial n_z} & \frac{\partial \Delta x}{\partial d} \\ \frac{\partial \Delta y}{\partial n_x} & \frac{\partial \Delta y}{\partial n_y} & \frac{\partial \Delta y}{\partial n_z} & \frac{\partial \Delta y}{\partial d} \\ \frac{\partial \Delta z}{\partial n_x} & \frac{\partial \Delta z}{\partial n_y} & \frac{\partial \Delta z}{\partial n_z} & \frac{\partial \Delta z}{\partial d} \end{bmatrix} \\ &= \left[d\left(\frac{\mathbf{v_1}\,\mathbf{v_1^T}}{(\mathbf{n}\cdot\mathbf{v_1})^2} - \frac{\mathbf{v_2}\,\mathbf{v_2^T}}{(\mathbf{n}\cdot\mathbf{v_2})^2}\right), \quad \frac{\mathbf{v_2}}{\mathbf{n}\cdot\mathbf{v_2}} - \frac{\mathbf{v_1}}{\mathbf{n}\cdot\mathbf{v_1}} \right] \end{aligned} \tag{2.8}$$

of the relation of Eq. (2.6) is used.

In a typical monitoring situation, small displacements of a few millimeters are observed from distances of several tens of meters. Accordingly, the direction vectors $\mathbf{v_1}$ and $\mathbf{v_2}$ observed in different epochs are very similar. In Eq. (2.8) these similar values are subtracted from each other which results in small values for the entries of $\mathbf{F}$. Consequently, errors in the plane parameters, expressed by the covariance matrix $\mathbf{\Sigma_{plane}}$, have a small impact on the displacements. More detailed accuracy considerations are given in Section 2.3.3.

The normal vector of the plane can also be used to rotate the coordinate system XYZ so that the coordinate axes correspond to the movement axes of the observed structure. This has the advantage that the computed displacements Δz and Δy directly correspond to the displacements along the primary movement axes A_1 and A_2 (cf. Figure 2.2).

Especially for favorable measurement geometries in which the out-of-plane movements are small (cf. Section 2.3.1), the intersection of oriented image rays with a model of the observed structure results in a high accuracy for the measured displacements. It is therefore a good alternative to polar measurements (Section 2.2.1) in static deformation monitoring. In dynamic deformation monitoring, the high accuracy and sampling rate of the image-based measurements can be fully exploited if the resulting directions are intersected with a model of the structure.

In Figure 2.2, displacements along B or $\mathbf{n}$ cause a change of the plane parameter d, which is used in Eq. (2.4) to compute the slope distance towards the visual target, and thus influence the coordinate differences gained from Eq. (2.5) or (2.6).

To detect the displacements along B, a 3D point on the object's surface is computed by

$$\mathbf{x}_{\text{surf}} = \mathbf{x_0} + s_{\text{meas}} \begin{bmatrix} \cos Hz_{\text{tele}} \sin V_{\text{tele}} \\ \sin Hz_{\text{tele}} \sin V_{\text{tele}} \\ \cos V_{\text{tele}} \end{bmatrix} \tag{2.9}$$

in which s_{meas} results from a reflectorless distance measurement and Hz_{tele} and V_{tele} are the tilt-corrected theodolite angles of the current telescope position *without* image-based aiming towards the visual target point. The updated parameter d^* of the target plane results from

$$d^* = \mathbf{n} \cdot \mathbf{x}_{\text{surf}} \tag{2.10}$$

which can then be used in Eq. (2.5) or (2.6) to compute displacements for further image-based angle measurements.

By using the same approach it is also possible to compute displacements b along the secondary movement axis B by inserting $\mathbf{x}_{\text{surf}}$ in Eq. (2.2) so that

$$b = \mathbf{n} \cdot \mathbf{x}_{\text{surf}} - d \tag{2.11}$$

in which it is emphasized that the parameter d of the original plane fit has to be used.

Eqs. (2.10) and (2.11) are based on a single, reflectorless distance measurement which is included in $\mathbf{x}_{\text{surf}}$, cf. Eq. (2.9). Consequently, the results for d^* and b show a lower accuracy and sampling rate than the image-based angle measurements (cf. Sections 2.2.1 and 2.2.3).

For static deformation monitoring with slow movements of the observed structure, the time series of d^* can be filtered before applying Eq. (2.4) for the computation of the slope distance towards the visual target. This reduces the measurement noise of the reflectorless distance measurement.

In dynamic deformation monitoring rapid movements of the observed structure occur. Due to the lower, non-equidistant sampling rate of the EDM sensor, it is not possible to assign the updated plane parameter d^* to each image-based measurement. Interpolating d^* to the time of the angle measurements requires a precise synchronization of the image and the EDM sensor. Although the accuracy of relative distance measurements towards the same point is much higher than the accuracy of an absolute, reflectorless distance measurement (e.g. 2 mm + 2 ppm, cf. Table 1.5), the EDM sensor is still the limiting factor.

Summarizing, for highly accurate dynamic deformation monitoring, a favorable measurement geometry (cf. Section 2.3.1) should be established to reduce the effect of out-of-plane movements on the image-based measurements (cf. Section 2.3.3).

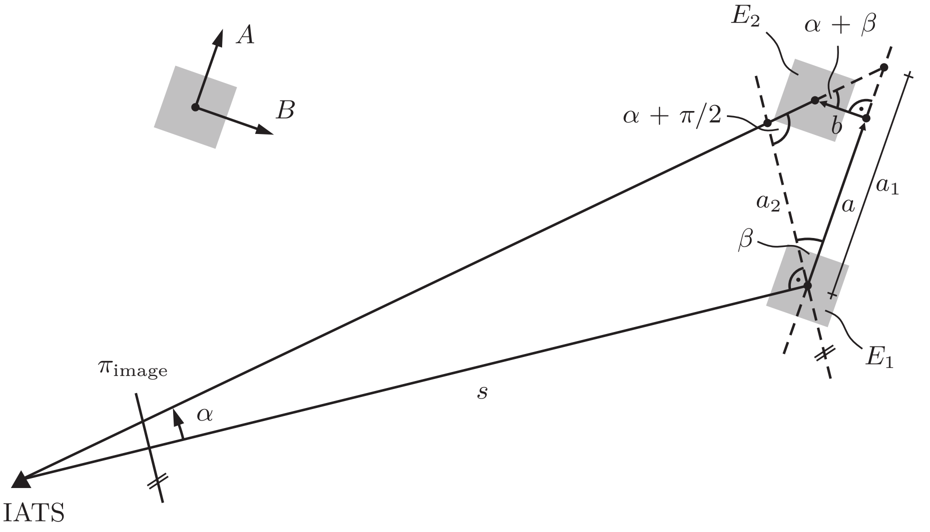

Figure 2.3: Element E of structure with movement axes A and B observed in epochs 1 and 2.

2.3.3 Accuracy considerations

Figure 2.3 depicts a side view on the measurement configuration of Figure 2.2 for an element E observed in epochs 1 and 2. In this example, the observed structure and consequently its element E has two movement axes A and B in which the displacement a along the primary movement axis A is of interest. Dependent on the viewpoint (side view or from above), this axis can either be A_1 or A_2 of Figure 2.2. In Figure 2.3, the primary movement axis A is not parallel to the image plane π_{image} of the IATS, as it would be for a favorable measurement geometry, but tilted by the angle β.

In epoch 1, the angles and the slope distance s to the element E_1 are measured which allows a computation of the 3D coordinates. If the same measurements are possible for epoch 2, the differences of the 3D coordinates can be computed directly. However, for an oscillating structure, the distance towards the same element cannot be measured in epoch 2 because it is not possible to steer the total station towards E_2 fast enough. Nevertheless, the angles can still be measured because a movement of the telescope is not required as long as E is visible in the AOV of the camera.

Summarizing, the slope distance s of epoch 1 and the angle difference α to epoch 2 are available as measurement data. The computation of the displacement a can be derived from Figure 2.3 with

$$a_2 = s \tan\alpha \tag{2.12}$$

$$a_1 = a_2 \frac{\cos\alpha}{\cos(\alpha+\beta)} \tag{2.13}$$

$$a = a_1 + b \tan(\alpha+\beta) \tag{2.14}$$

which can be summarized to

$$a = s \frac{\sin\alpha}{\cos(\alpha+\beta)} + b \tan(\alpha+\beta) \tag{2.15}$$

in which it is noted that the displacement a occurs along the positive A axis and b along the negative B axis in Figure 2.3.

For an ideal measurement geometry in which the primary movement axis A is parallel to the image plane ($\beta = 0$) and no displacements along the secondary movement axis B occur ($b = 0$), Eq. (2.15) simplifies to Eq. (2.12). However, this ideal geometry is hard to achieve in real monitoring situations and a secondary displacement b maps into the primary displacement a.

Effect of b and its uncertainties

In typical monitoring situations, small movements of a few millimeters are observed from a distance of several tens of meters which leads to small angles α in Eq. (2.15). Consequently, the influence of the displacement b on a primarily depends on the angle β between the image plane and the primary movement axis which is depicted in Figure 2.4.

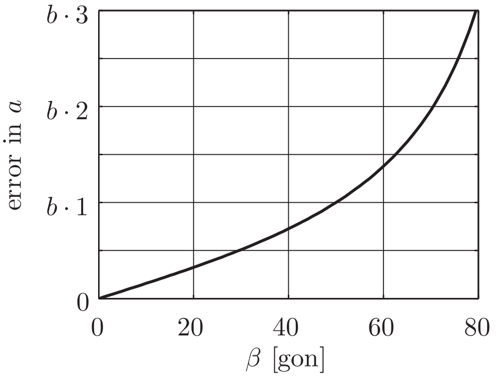

Figure 2.4: Effect of secondary displacement for different angles β between the image plane and the primary movement axis.

Dependent on the angle β, the effect of a secondary displacement b on a can be larger than b itself. Consequently, β must be kept small for accurate measurements which is achieved if the primary movement axis of the structure is parallel to the image plane of the IATS. Another possibility is to keep b itself small by choosing an appropriate measurement geometry which requires prior knowledge of the behavior of the monitored object (cf. Section 2.3.1).

For large angles β and unknown displacements along the secondary movement axis, the strategy of Section 2.3.2 is applied which involves a measurement of b, cf. Eq. (2.11). Hereby, the error in the measured b demonstrates its effect on a after

$$\epsilon_a = \tan(\alpha + \beta)\, \epsilon_b \tag{2.16}$$

which is also depicted in Figure 2.4 (replace b by ϵ_b). For example an absolute value of $\beta = 20\,\text{gon}$ causes $\epsilon_a = \epsilon_b/3$ and $\beta = 50\,\text{gon}$ results in $\epsilon_a = \epsilon_b$.

As the value of b results from a distance measurement (cf. Section 2.3.2), ϵ_b is primarily caused by uncertainties in the distance measurement. Although the accuracy of measured distance changes b is better than the accuracy of an absolute distance measurement (e.g. 2 mm + 2 ppm, cf. Table 1.5), a measurement geometry (cf. Section 2.3.1) with a small angle β is preferable to reduce a mapping of ϵ_b into a.

Effect of uncertainties in β

The angle β is a function of the viewing direction of the IATS relative to the primary movement axis of the observed structure. It is implicitly computed in Section 2.3.2 where it is included in the normal vector **n** of the target plane, cf. Eq. (2.2). An error in β propagates to an error in a after

$$\epsilon_a = (a \tan(\alpha + \beta) + b)\, \epsilon_\beta \tag{2.17}$$

As ϵ_β can be assumed to be a small quantity, e.g. $\epsilon_\beta < 1\,\text{gon}$, which is introduced in radians in Eq. (2.17), its effect on a is small for moderate values of the angle β itself. In typical monitoring situations the displacements a and b are small quantities of a few millimeters. For example $\beta = 50\,\text{gon}$ and $\epsilon_\beta = 1\,\text{gon}$, ϵ_a is less than 2% of $(a + b)$.

Effect of uncertainties in s

As already pointed out, the angle α is a small quantity because in typical monitoring situations small movements are observed from relatively large distances. Consequently, Eq. (2.15) can be approximated to

$$a \approx s\, \frac{\alpha}{\cos(\alpha + \beta)} \tag{2.18}$$

by using small-angle approximations and by neglecting the displacement b along the secondary movement axis. Accordingly, an error in s propagates to an error in a after

$$\epsilon_a = \frac{\alpha}{\cos(\alpha + \beta)}\, \epsilon_s \tag{2.19}$$

For a displacement of e.g. $a = 5\,\mathrm{mm}$ between two epochs, which is observed from a distance of e.g. $s = 30\,\mathrm{m}$, the measured angle difference corresponds to $\alpha = 10.6\,\mathrm{mgon}$. Even for a large angle between the image plane and the primary movement axis of e.g. $\beta = 80\,\mathrm{gon}$, the term $\alpha / \cos(\alpha + \beta)$ will be a small quantity ($5.4\mathrm{e}^{-4}$ in this example).

Consequently, an error in the measurement of the absolute distance s will have a small impact on the measured displacement a. An error of e.g. 10 mm, which is much larger than the accuracy of the reflectorless distance measurement of total stations (e.g. 2 mm + 2 ppm, cf. Table 1.5), results in an error of less than 0.006 mm for the displacement a of the present example.

Conclusions

In case of a negligibly small secondary displacement b or a small angle β, the accuracy of the measured displacement a, cf. Eq. (2.15), is primarily influenced by the accuracy of the image-based angle measurement α. It is shown in Section 4.3.2, that it is possible to achieve an accuracy of 0.1 mgon with a state-of-the-art IATS which leads to the expectation of highly accurate monitoring results.

2.4 MEASURING NATURAL TARGETS BY FEATURE MATCHING

In a typical monitoring situation, the structure of interest is observed from one instrument position in different epochs. The telescope of the IATS can be positioned to the same direction in each epoch and the distance towards the structure does only change marginally. Consequently, the captured image data is very similar for each epoch and a possible approach for image-based movement detection is template matching which is based on cross-correlation or least-squares matching (Szeliski 2010, pp. 235f.).

However, as shown in Section 2.6.1, template matching does not work well in situations in which the image content varies, e.g. because of snowfall or growing vegetation. To overcome this limitation, visually prominent features on the structure are detected and matched for the different epochs. The feature matching approach is a well-studied topic and numerous algorithms have been proposed (Tuytelaars and Mikolajczyk 2008; Krig 2014, pp. 217ff.).

2.4.1 Feature matching

Summarizing, the feature matching approach can be separated into the steps feature detection, feature description and feature matching (Szeliski 2010, pp. 207ff.).

The feature detection involves the localization of visually prominent features, so-called keypoints, in the image. Common detectors either search for corners, blobs or regions (Tuytelaars and Mikolajczyk 2008, p. 188). The results of the feature detection are the image coordinates of the keypoints. Based on these image coordinates, the surrounding image regions are used to describe the keypoints in the feature description step (Krig 2014, pp. 227ff.). The results of the feature description are compact and stable representations, so-called descriptors, of the detected keypoints (Szeliski 2010, p. 208). In the feature matching step, corresponding keypoints of different images are found based on their descriptors (Szeliski 2010, pp. 225ff.).

In this thesis, the ORB (oriented FAST and rotated BRIEF, cf. Rublee et al. 2011) framework for feature detection and description is used. It is based on the FAST (features from accelerated segment test, cf. Rosten and Drummond 2006) keypoint detector, which is classified as a corner detector, and uses a variant of the BRIEF (binary robust independent elementary features, cf. Calonder et al. 2010) descriptor. The ORB descriptor is a binary descriptor with 256 elements which are generated by comparing randomly selected pixel pairs around the detected keypoint. One element is either set to 1 or 0 (true or false) dependent on whether the intensity of the first or second pixel is larger (Rublee et al. 2011).

In the general case, in which the viewpoint and the orientation of the camera changes between capturing the image data, rotation- and scale-invariance are critical aspects of the feature matching procedure. Furthermore, invariance w.r.t. illumination changes is an important issue (Krig 2014, p. 219). The ORB framework achieves scale-invariance by computing multi-scale features in a scale pyramid of the original image (Rublee et al. 2011). As already mentioned, the distance between the IATS and the observed structure will only change marginally in typical monitoring situations of civil engineering structures. Accordingly, it is not necessary to compute these multi-scale features which would account for scale variations.

Binary descriptors are matched by using the Hamming distance which is the sum of the XOR operation on the tested descriptors (Krig 2014, p. 144). Hereby, a low number of the Hamming distance indicates a good match because only a few elements of the tested descriptors are different. A large number, the maximum is 256 which corresponds to the number of descriptor elements, indicates a bad match. Dependent on the threshold for the Hamming distance, which is used to classify a valid match, a large number of false matches is common.

Therefore, the random sample consensus (RANSAC, cf. e.g. Hartley and Zisserman 2004, p. 118) can be used as a robust estimator for removing these false matches in which the pixel movements of the matched keypoints are tested. Hereby, a rigid-body movement of the ROI is assumed. The selection of the ROI is done by the operator and marks the only manual interaction in the feature matching procedure. For non-planar objects in the AOV of the telescope camera of the IATS, the ROI can also be used to limit the processed image content to a planar object.

2.4.2 Sub-pixel refinement

The keypoints detected by the ORB framework show a one-pixel discretization. Consequently, also the calculated movements, which result from comparing the image coordinates of the matched keypoints, show this discretization which is unfavorable for accurate measurements. To overcome this limitation, the approach of Shi and Tomasi (1994), in which the pixel movements of the matched keypoints are refined by a local least-squares matching (LSM), is adopted. The LSM is described in e.g. Luhmann et al. (2014, pp. 454ff.) where the relation between two images is described by an affine transformation (6 parameters).

Due to the mentioned similarity of the different images in monitoring applications, employing a pure translation model

$$\begin{aligned} I(u,v) &= J(u+\Delta u, v+\Delta v) + J_0 \\ &\approx J(u,v) + J_u(u,v)\,\Delta u + J_v(u,v)\,\Delta v + J_0 \end{aligned} \tag{2.20}$$

is sufficient. Hereby, the image patches I and J of a first and a second image are selected in which the patches are centered around the matched, pixel-discrete keypoints of the ORB framework. The size of the patches must be sufficiently large to generate enough data for the LSM but should be limited to avoid errors in case of a varying image content (cf. Section 2.6.1). Patches of 11×11 or 21×21 pixels were empirically found to deliver good results for monitoring applications with the used IATSs.

In Eq. (2.20), the intensity of the first image $I(u,v)$, with values between 0 and 255 for an 8-bit grayscale image, at a certain pixel position (u,v) is modeled by using the intensity $J(u,v)$ of a second image. J_u and J_v denote the gradients and Δu and Δv denote the movements in u- and v-direction. The parameter J_0, which is assumed to be constant for the image patch, accounts for overall intensity changes between the first and the second image.

The parameter vector $\boldsymbol{\xi}$, the observations $\mathbf{l}$ and the design matrix $\mathbf{A}$ of the adjustment are given by

$$\boldsymbol{\xi} = \begin{bmatrix} \Delta u & \Delta v & J_0 \end{bmatrix}^T \tag{2.21}$$

$$\mathbf{l} = \begin{bmatrix} I(u,v) - J(u,v) \\ \vdots \end{bmatrix}_W \tag{2.22}$$

$$\mathbf{A} = \begin{bmatrix} J_u(u,v) & J_v(u,v) & 1 \\ \vdots & \vdots & \vdots \end{bmatrix}_W \tag{2.23}$$

in which $\mathbf{l}$ and $\mathbf{A}$ contain data from all pixel positions (u, v) in the region W of the image patches.

The parameter vector is computed by solving

$$\mathbf{A^T}\,\mathbf{A}\,\boldsymbol{\xi} = \mathbf{A^T}\,\mathbf{l} \tag{2.24}$$

for $\boldsymbol{\xi}$ in which

$$\mathbf{A^T}\,\mathbf{A} = \begin{bmatrix} \sum J_u^2 & \sum J_u\,J_v & \sum J_u \\ \sum J_u\,J_v & \sum J_v^2 & \sum J_v \\ \sum J_u & \sum J_v & \sum 1 \end{bmatrix} \tag{2.25}$$

and

$$\mathbf{A^T}\,\mathbf{l} = \begin{bmatrix} \sum (I - J)\,J_u \\ \sum (I - J)\,J_v \\ \sum (I - J) \end{bmatrix} \tag{2.26}$$

The sub-pixel movements Δu and Δv are finally added to the pixel-discrete movements resulting from the ORB framework.

2.4.3 Summary and relation to theodolite angles

The computation of theodolite angles based on natural features can be summarized as follows:

1. In a first step, the definition of the reference epoch and the selection of the ROI for each target is done by the operator.
2. In each image, keypoints are detected and described by using the ORB framework. These keypoints are matched between the reference frame and the actual frame based on their descriptors. The results are numerous, one for each matched keypoint, pixel-discrete movements. Since the image data of the individual epochs is very similar, the matched keypoints occur in similar regions of the image sensor. Accordingly, correcting their location due to radial distortion or a rotation of the image sensor (cf. Sections 6.3 and 7.3.2) is not necessary.
3. These matches are filtered by using the RANSAC algorithm to remove gross errors in the feature matching step.
4. The remaining matches are refined by a local LSM to compute sub-pixel movements for each match.
5. Assuming a rigid-body movement in the selected ROI, a representative movement is computed by averaging the individual sub-pixel movements.
6. For the reference epoch, the tilt-corrected theodolite angles of the current telescope position, *without* image-based measurements, are used to define the direction towards the monitoring area of each target.
7. For all other epochs, the theodolite angles to the monitoring area of each target are computed after Section 6.3 in which the averaged pixel movements of Step 5 are treated as corrected image coordinates.

2.5 STATIC DEFORMATION MONITORING

Conventional static deformation measurements with a RTS comprise the observation of selected survey points, marked by retroreflective prisms, from one instrument position. In each epoch, the 3D coordinates of the targets are determined by a polar measurement and the stability of the instrument is verified by measurements to stable reference points. Although the usage of a single IATS for conventional static deformation measurements is frequently mentioned in the literature (e.g. Wasmeier 2009; Hauth and Schlüter 2010; Knoblach 2011; Wagner and Wasmeier 2014), detailed experiment descriptions and reporting of results are pending yet – especially for practical measurements under outdoor conditions. An exception is the report of Kopacik et al. (1993) who used the video-theodolite *Wild TM3000V* for the monitoring of height variations of a bridge during load testing. However, the employed image processing algorithm requires the usage of specialized light sources as targets (Fabiankowitsch 1990). Accordingly, access to the bridge is required for installing these light sources and the necessary power supply which should be overcome by using natural features of the monitored structure as targets (Section 2.5.1).

2.5.1 Experiment description

The suitability of a state-of-the-art IATS (*Leica MS60*, cf. Section 1.4) for static deformation monitoring was evaluated at a road bridge with a length of about 62 m and a width of 10 m over the river Schwechat near Mannswörth, Austria. The prestressed concrete bridge was subject to be replaced by a new construction. Prior to the replacement, the bridge was used as test bed for experimental measurements carried out by the Austrian Institute of Technology (AIT, cf. Alten et al. 2017). The goal of these measurements was the experimental evaluation of possible safety assessments of structures based on metrology. Therefore, the old bridge was selectively damaged at different locations to simulate aging effects and a damage of the structure. Simultaneously, the bridge was monitored with different measurement sensors, such as inclinometers, accelerometers and strain sensors, to evaluate their suitability for damage detection. Parallel to the measurements by AIT, the Institute of Engineering Geodesy and Measurement Systems (IGMS) was permitted to carry out IATS measurements which is greatly acknowledged.

The IATS measurements were conducted on May 2nd and May 3rd, 2016 during the damage scenario in which a shear failure of a bridge pillar should be induced (Alten et al. 2017). The experimental setup is depicted in Figure 2.5. To induce the shear failure, holes were drilled into the pillar (Figure 2.5c) and filled with a non-explosive demolition agent on May 2nd, 2016 at 12:00.

A shearing of the bridge pillar would cause displacements of the bridge deck and of the pillar itself in vertical direction and along the bridge axis. To capture these displacements, the monitoring areas A to D on the pillar and the areas E to I on the bridge deck were defined (cf. Figure 2.5b). For the instrument position depicted in Figure 2.5a, the displacements in vertical direction and along the bridge axis approximately appear as in-plane movements which corresponds to a favorable measurement geometry (cf. Section 2.3.1).

Figure 2.5a also illustrates that the instrument is located in a safe distance (over 20 m) from the bridge which is potentially in danger of collapsing because of the demolition of the bridge pillar. It is further emphasized that for the IATS measurements, which use natural features of the observed structure as targets, access to the bridge is not required at any time. This is not the case for other measurement sensors, such as inclinometers, accelerometers and strain sensors. Along with safety issues involved in the installation of sensors on a structure in danger of collapsing, the mounting of the sensors e.g. underneath the bridge deck is a cumbersome procedure and requires special machinery.

In addition to the monitoring areas on the observed structure (Figure 2.5b), also reference areas at stable locations were defined

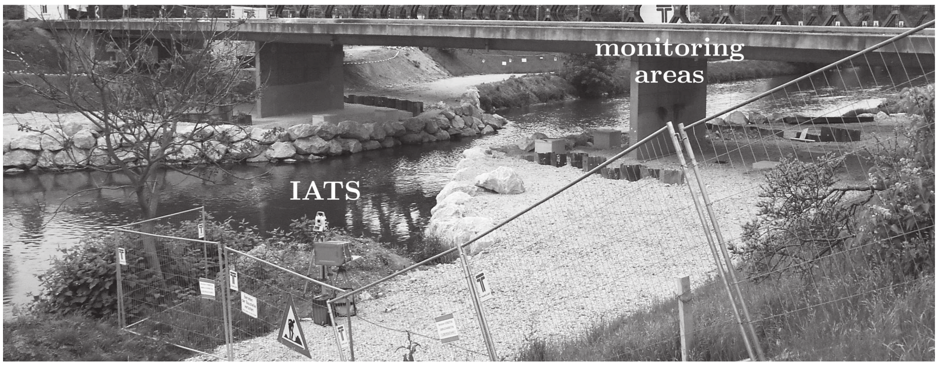

(a) overview with safe location of instrument (reference targets outside of image)

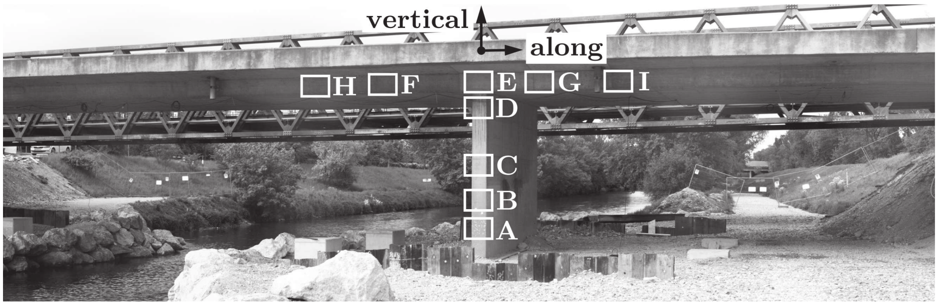

(b) definition of monitored areas A to I

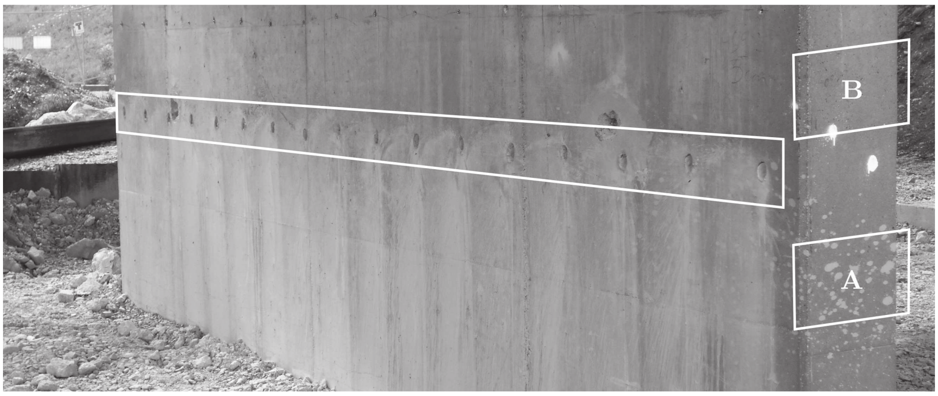

(c) introduced damage of pillar between monitoring areas A and B

Figure 2.5: Experimental setup for static deformation monitoring.

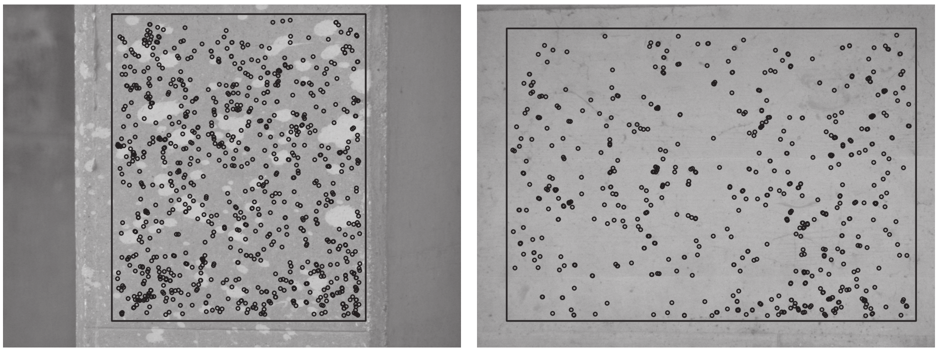

(a) monitoring area A **(b)** monitoring area E

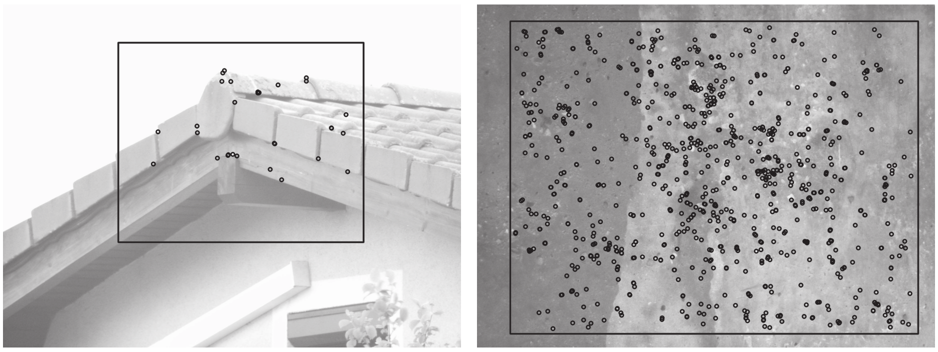

(c) reference area R1 on rooftop **(d)** reference area R6 on abutment

Figure 2.6: Exemplary representation of different monitoring and reference areas with selected ROIs and automatically detected keypoints.

to control the stability of the IATS during the measurements. Figure 2.6 exemplarily depicts measurement data, i.e., images of the IATS's telescope camera, of selected monitoring and reference areas. Furthermore, automatically detected feature points on the respective structures are shown.

It is evident that the feature points are only detected in a specified ROI, e.g. in Figure 2.6a only on the narrow side of the pillar or in Figure 2.6c only in a certain area on the roof. The definition of these ROIs is carried out by the operator and marks the only manual interaction in the image processing.

To determine the relative position of the individual monitoring areas and to allow further investigations on the measurement results, reflectorless distance measurements were conducted along with the image-based angle measurements. The measurements were taken in both telescope faces to eliminate the theodolite axes errors and the variation of the zero point errors of the electronic tilt compensator (cf. Section 6.3.3) which both depend on the temperature. The measurements in Face II were taken immediately after Face I so that it can be assumed that no movements of the object took place during the two-face measurement. The framework of Section 2.4 was used to relate the matched features to theodolite angles.

As already mentioned, the measurements were carried out at two consecutive days in which the instrument was removed from the tripod overnight. The tripod and the tribrach remained at their position. By using the angle measurements to the stable reference points, the stability of the setup (Section 2.5.2) can be controlled so that the measurements of both days can be carried out in a common coordinate system. It is hereby taken advantage of the constant position of the tripod and the tribrach. It would also be possible to set up the instrument at a different position and to compute its station coordinates by means of a resection.

The time differences of the following figures refer to the injection of the non-explosive demolition agent (Figure 2.5c) which was done on May 2nd, 2016 at 12:00.

2.5.2 Stability control

As shown in Figure 2.5a, the instrument was (intentionally) not shaded from environmental influences such as direct sunlight or rain. This causes strong variations in the instrument's internal temperature (Figure 2.7 top) which is measured on the mainboard of the IATS. On average, the reported internal temperature was 8°C above the ambient temperature during the measurements.

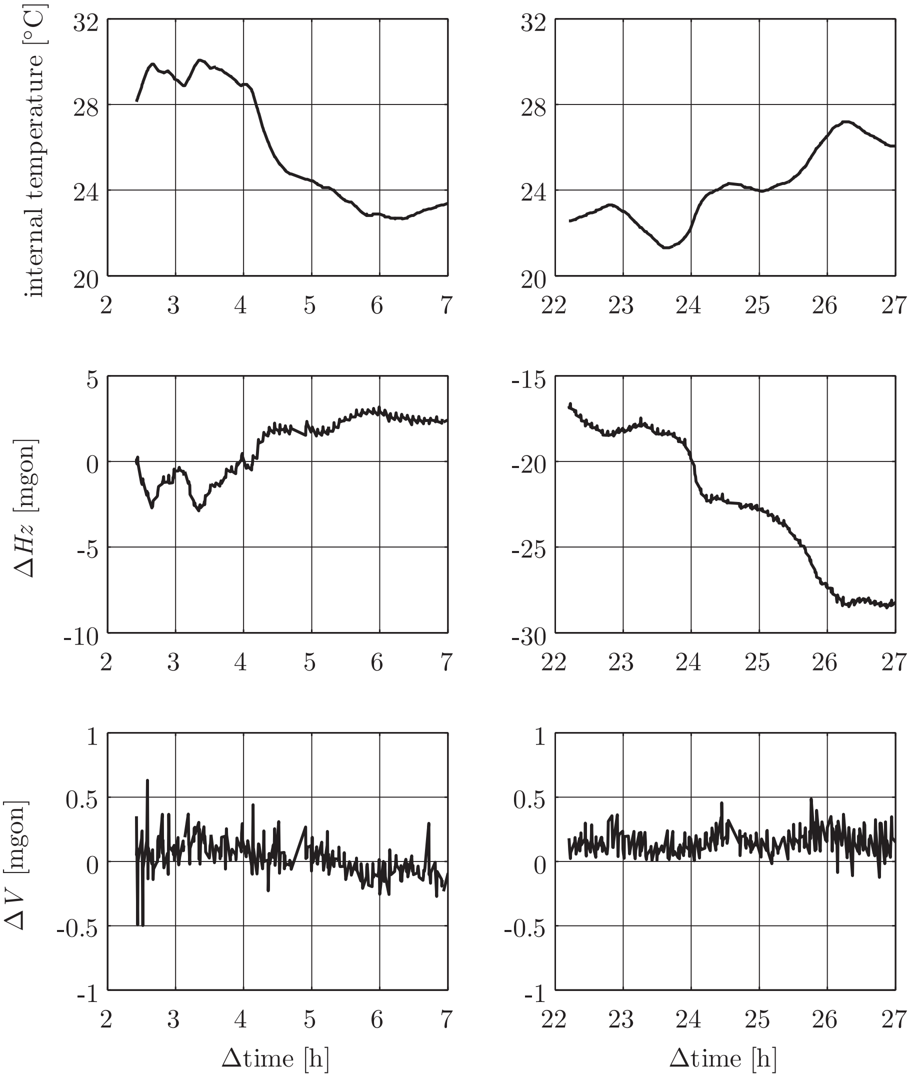

Figure 2.7: Change of instrument temperature and variations of the face averages of the image-based angle measurements towards stable reference points (note the different scales for ΔHz and ΔV).

The direct sunlight, which causes the variations in the instrument's internal temperature, also causes a torsion of the tripod and consequently heavy variations ΔHz in the horizontal angles towards the stable reference targets (Figure 2.7 middle). This is confirmed by the strong correlation between ΔHz and the changes of the internal temperature.

It is emphasized that the variations of the angles in Figure 2.7 are computed from the face averages of the measurements (Section 2.5.1) and are thus not biased by changes of the theodolite axes errors or zero point variations of the tilt compensator (cf. Section 6.3.3). The vertical angles towards the reference targets, and thus the instrument height, does only change marginally (Figure 2.7 bottom) – even when removing the IATS over night and reattaching it on the next day.

The variations ΔHz in Figure 2.7 are a good reminder that an IATS extends a total station with one or more cameras. Compared to a pure imaging system, it therefore benefits from the total station capabilities. However, an IATS of course also shares some weaknesses of conventional total stations and basic rules, such as a sufficient acclimatization to the ambient temperature or a shading from direct sunlight, must be followed to achieve highest accuracies.

The variations ΔHz and ΔV of Figure 2.7 are used to correct the measurements towards the monitoring areas depicted in Figure 2.5b.

2.5.3 Results

Figure 2.8 depicts the movements of the monitoring areas A to D located on the narrow side of the damaged pillar (Figure 2.5b). On the first day, no noticeable movements of the monitoring areas occurred which is because of the latency of the non-explosive demolition agent to fully expand after insertion into the holes (Figure 2.5c). However, on the second day a displacement between the monitoring area A and the areas B to D is visible in vertical direc-

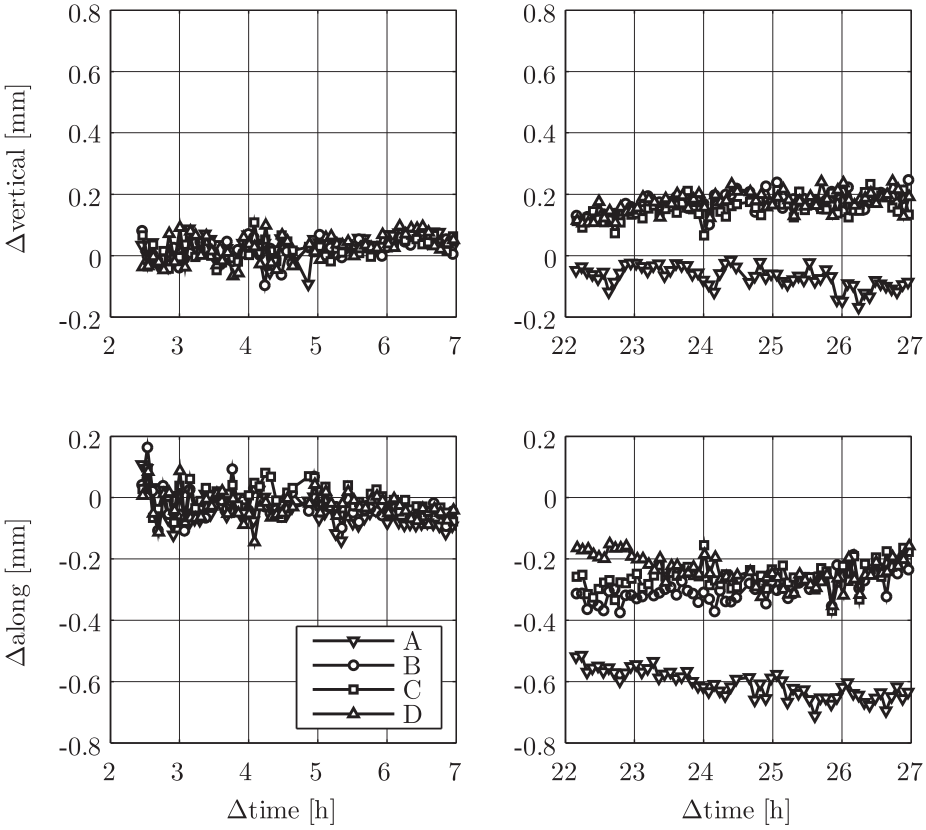

Figure 2.8: Movements of monitoring areas A to D in vertical direction and along the bridge axis.

tion and along the bridge. Regarding the distribution of the monitoring areas A to D (Figure 2.5b) and the demolition of the pillar between the areas A and B (Figure 2.5c), it can be concluded that the movements in Figure 2.8 are caused by the damaging of the pillar.

The displacements caused by the non-explosive demolition agent are about 0.3 mm in vertical direction and about 0.4 mm along the bridge axis (measured 27 hours after the insertion of the demolition agent, cf. Figure 2.8 right column). These values are in the same

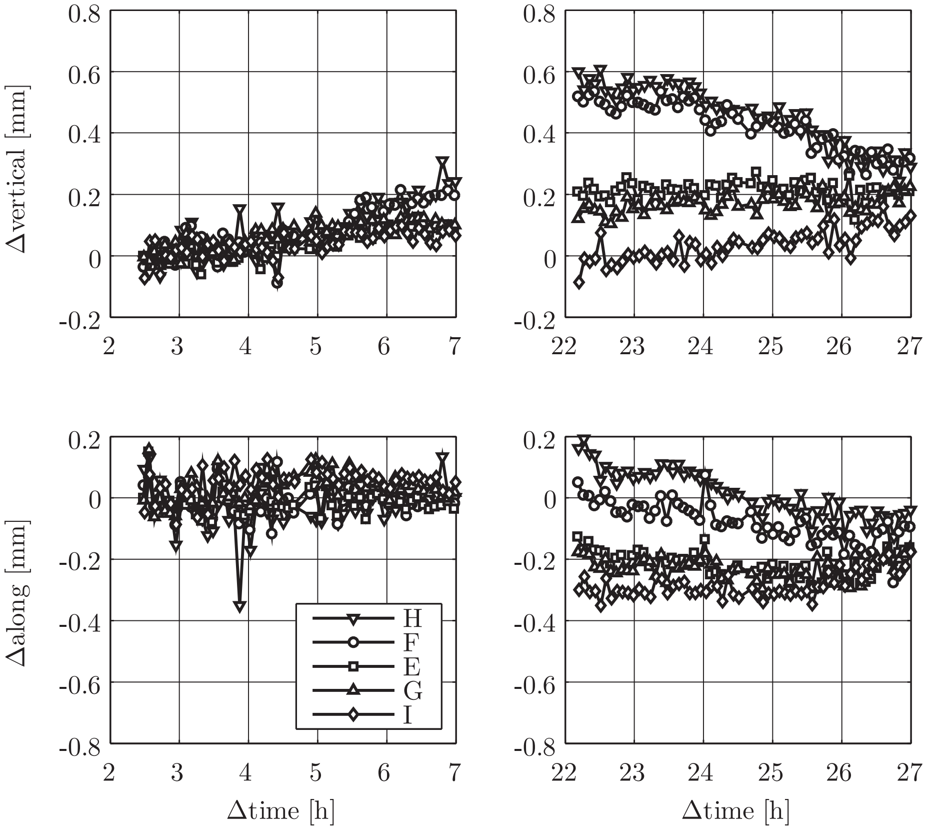

Figure 2.9: Movements of monitoring areas E to I in vertical direction and along the bridge axis.

order of magnitude as the width of the crack along the pillar which is also induced by the demolition agent. A visual inspection after 48 hours showed a crack width of 0.25 to 0.5 mm (measured by AIT, cf. Alten et al. 2017). Admittedly, the displacements (0.3 mm and 0.4 mm) are very small. However, they can be measured by using an IATS without entering the danger zone of the potentially collapsing bridge at any time.

Figure 2.9 depicts the movements of the monitoring areas E to I in vertical direction and along the bridge axis. The movements

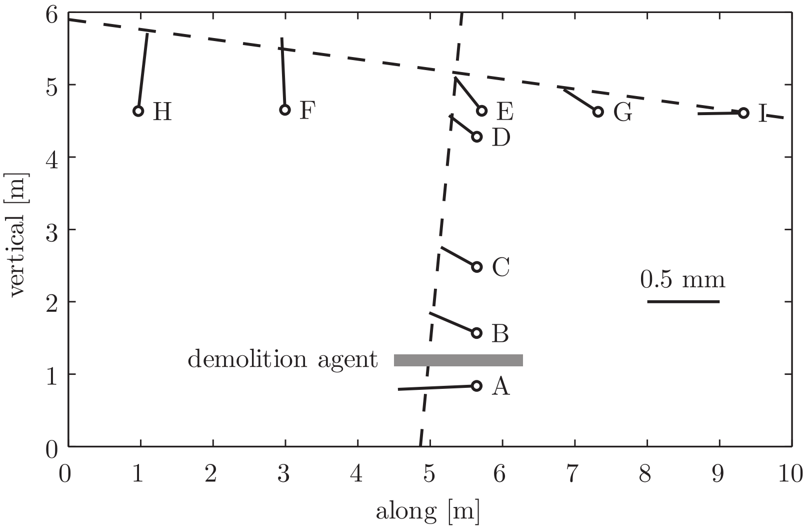

Figure 2.10: Movement vectors of the monitoring areas for Δtime = 23 h (cf. Figure 2.8 and 2.9) and computed inclinations of the bridge deck and the pillar (dashed lines).

show systematic effects w.r.t. their location along the bridge deck (cf. Figure 2.5b).

For Δtime = 23 h (cf. Figure 2.8 and 2.9), the movement vectors of the monitoring areas A to I are depicted in Figure 2.10. With knowledge of the relative positions of the monitoring areas, the inclinations along the bridge axis can be computed for the bridge deck and the pillar. Hereby, the inclination of the bridge deck is computed from the movements of the monitoring areas E to I which can be regarded as rigid body movements (cf. Figure 2.10). The inclination of the pillar is computed from the movements of the monitoring areas B to D because area A is not located on the same rigid body due to the demolition of the pillar (cf. Figure 2.5c and 2.8).

The variation of the bridge deck's inclination over time (computed as in Figure 2.10) is depicted in Figure 2.11 where also inclinometer measurements, carried out by AIT, are shown. The incli-

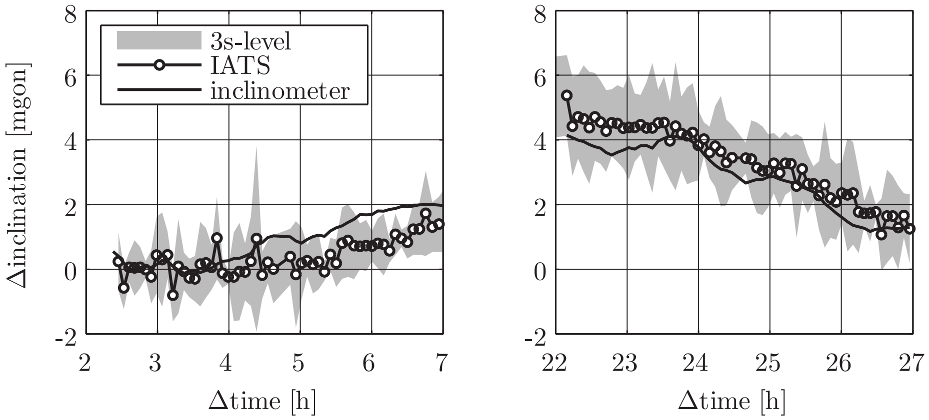

Figure 2.11: Inclination of bridge deck computed from monitoring areas E to I and temperature-corrected inclinometer measurements.

nometer was mounted between the monitoring areas E and F on the other side of the bridge deck (Figure 2.5b). The measurements of the used inclinometer (*Althen AIT230* with a measurement range of ±3°) have a strong dependence on the ambient temperature, which is also depicted in the specifications with a maximum zero point deviation of 2 mgon/°C (Althen 2015), and require correction. The inclinations deduced from the IATS measurements are in good correspondence to the temperature-corrected inclinometer measurements. It is again emphasized that the installation of the inclinometer underneath the bridge deck is a cumbersome procedure requiring special machinery whereat for the IATS measurements access to the structure is not required at any time.

The movements in Figure 2.9 and the deduced inclinations (Figure 2.11) are probably regular diurnal variations of the bridge and are not necessarily linked to the damaging of the pillar. To obtain assurance on this issue, it would have been necessary to start the monitoring measurements prior to the damaging of the pillar. For example at the Gotthard-Basetunnel whose construction took over two decades, the deformation monitoring at nearby retaining walls was started several years before drilling the tunnel (Studer and Ryf

2014). For the bridge measurements presented in this section, the regular diurnal variations of the structure could have been assessed by starting the monitoring measurements a few days before the damaging of the pillar.

However, the goal of the experiments was the evaluation of the IATS's suitability for static deformation monitoring which can be confirmed by comparison to the inclinometer measurements (Figure 2.11).

2.6 DYNAMIC DEFORMATION MONITORING

By using different IATS prototypes, Bürki et al. (2010) and Wagner et al. (2013) also performed dynamic deformation monitoring at bridges. However, in both cases light emitting targets, which can easily be found in the image by blob detection, had to be mounted onto the bridge. This limitation should be overcome by using natural features of the structure itself. Under controlled indoor conditions and by using light emitting (Charalampous et al. 2015) as well as natural (Wasmeier 2009, pp. 125f; Hauth et al. 2013) targets, dynamic deformation measurements were also performed with IATS prototypes. The prototype of Hauth et al. (2013) records videos with several kHz and was used for the measurement of the oscillation of a violin string with a frequency of 190 Hz. This demonstrates that the cameras of IATS prototypes can be superior to the cameras of commercially available instruments.

However, the goal of this section is to evaluate the suitability of state-of-the-art instruments and natural features of the observed structure as targets for dynamic deformation monitoring under outdoor conditions. Therefore, the *Augartensteg* and the *Pongratz-Moore-Steg*, which are both footbridges over the river Mur in Graz, Austria were used as test beds for dynamic deformation monitoring. In both experiments, the IATS measurements were conducted towards natural features of the observed structure.

The RTS *Leica TS15 I 1″ R1000* (Leica 2010c), in combination with a *Leica GPR1* circular prism, was used to compare the IATS measurements in time domain. By using the correct steering commands (Lienhart et al. 2017), the used RTS provides angle measurements with a frequency of 20 Hz. The instrument is specified with a standard deviation of 0.3 mgon for static angle measurements (Leica 2010c, p. 146) in which Lienhart et al. (2017) showed that this value also corresponds to the discretization of the measured angles in continuous measurement mode. The accelerometer *HBM B12/200* (HBM 2000) was used as a reference in the frequency domain. Its measurement frequency was set to 200 Hz.

The image data of the IATS is processed as described in Section 2.4. Hereby, two strategies for computing the pixel movements are applied (Ehrhart and Lienhart 2015c). The pixel movements are computed relative to the first frame of the measurements for evaluation in time domain and for comparison with the RTS measurements. To evaluate the measured signal in the frequency domain and to compare the frequency response to the accelerometer measurements, the pixel movements are computed between consecutive frames. The computation of the pixel movements between consecutive frames is hereby advantageous because it implicitly removes long-periodic effects in the time series.

The frequency response of the observed structure due to different stimuli is computed by the Fourier transform (e.g. Pollock 1999, pp. 365ff.). Prior to the frequency analysis, a high-pass Butterworth filter (Pollock 1999, pp. 499ff.) of order 2 with a cutoff frequency of 0.5 Hz is applied to the time series to remove long-periodic effects. While the accelerometer and the IATS measurements (based on consecutive frames) are implicitly high-pass filtered, the application of an additional filter is especially necessary for the RTS measurements to remove long-periodic effects before applying the Fourier transform for deriving vibration information.

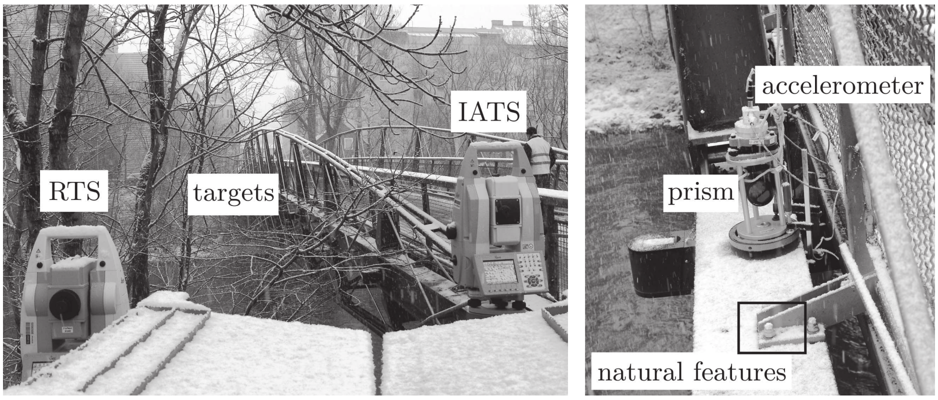

(a) location of RTS and IATS relative to targets **(b)** measurement positions

Figure 2.12: Setup for the *Augarten* experiment.

2.6.1 Dynamic deformation monitoring with favorable measurement geometry

Experiment description

The measurements at the *Augartensteg* (steel construction, 74 m span width) were started on January 29, 2015 at 10:30 with the state-of-the-art IATS *Leica MS50* (cf. Section 1.4). The experimental setup is illustrated in Figure 2.12 in which the distances to the respective targets were 32.6 m for the IATS and 33.4 m for the RTS.

The positions of both instruments result in the measurement geometry P_1 of Figure 2.1 which makes displacements in vertical direction and across the bridge appear as approximate in-plane movements (cf. Section 2.3.1). In this thesis, the investigations for the *Augarten* experiment are limited to the vertical movements of the bridge deck whereas other movement axes are investigated for the experiment described in Section 2.6.2.

Figure 2.13 depicts the measurement data of the IATS, i.e., frames of the video recorded by the instrument's telescope camera. For the *Leica MS50*, the video is recorded at 10 fps with a resolution

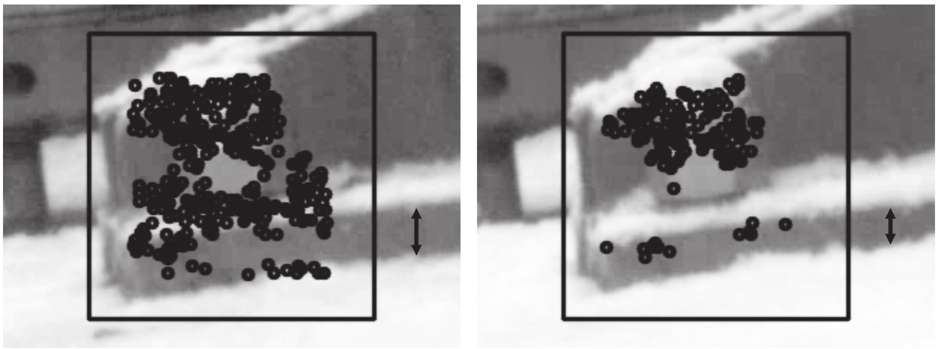

(a) start of measurements **(b)** end of measurements

Figure 2.13: IATS monitoring area with detected keypoints and selected ROI for the *Augarten* experiment with snowfall.

of 320 px × 240 px (cf. Section 1.4) in which one pixel corresponds to about 0.6 mgon (cf. Section 7.4). The ROI, in which keypoints are automatically detected and matched (cf. Section 2.4), was hereby selected so that similar distances between the IATS and the points in the ROI occur. The time span between Figure 2.13a and 2.13b is about 9 minutes which illustrates the snowfall during the experiment.

Time series overview with drift of template matching

Figure 2.14 shows the vertical movements of the bridge deck measured by the RTS and the IATS. For the IATS measurements, the individual frames are processed relative to the first frame. The filtered time series (Figure 2.14 bottom) result from applying a low-pass Butterworth filter of order 2 and a cutoff-frequency of 0.2 Hz on the raw data.

Obviously, the RTS was not fully acclimatized to the ambient temperature before starting the measurements which causes the drift of the corresponding time series until a time of 100 s (Figure 2.14 bottom). Besides that, the IATS measurements are in good

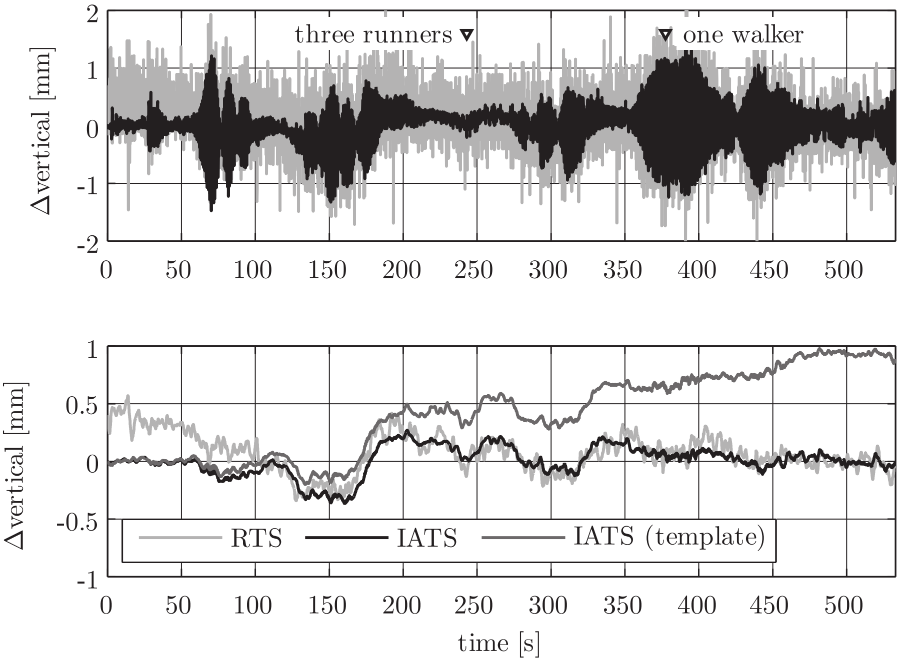

Figure 2.14: Vertical movements of the bridge deck measured by RTS and IATS with different image processing techniques applied. Top: raw measurements. Bottom: filtered measurements.

correspondence to the RTS measurements when using the feature matching approach described in Section 2.4.

The application of template matching on the selected ROI according to Eq. (2.20) causes a drift of the time series which accumulates to an error of about 1 mm after 9 minutes (Figure 2.14 bottom). This is due to the snowfall (Figure 2.13) causing a change of the image content which is not handled by template matching.

The effect of the snowfall is also depicted in Figure 2.15 which illustrates the decreasing correlation coefficient resulting from the template matching approach. The feature matching approach accounts for this issue and the keypoints at the snow cover, which are detected at the beginning of the measurements (Figure 2.13a), cannot be matched in later frames (Figure 2.13b) and thus do not

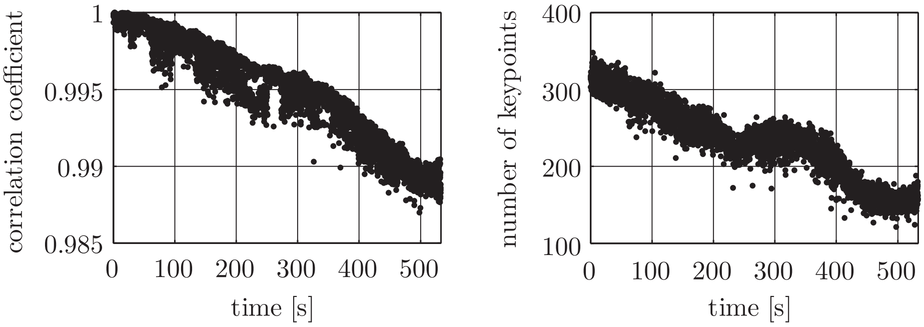

Figure 2.15: Correlation coefficients (template matching) and number of detected keypoints (feature matching) for the *Augarten* experiment with snowfall.

falsify the results. Figure 2.15 also illustrates the decreasing number of matched keypoints because of the snowfall. However, about 150 successfully matched keypoints at the end of the experiment are still sufficient for reliable image-based measurements.

Bridge response

Figure 2.14 also shows the response of the bridge deck to different stimuli. For example one walker on the bridge causes an increasing amplitude of the oscillation in which this effect does not occur for three runners crossing the bridge. The response due to three runners is depicted in Figure 2.16 in greater detail. The IATS measurements in time domain are computed relative to the first frame of the measurement series. The frequency analysis is based on the movements between consecutive frames of the captured video data.

For dynamic angle measurements, the used RTS shows a discretization of 0.3 mgon (Lienhart et al. 2017) which corresponds to 0.16 mm at a distance of 33.4 m. This discretization, and the higher measurement noise, is also visible in Figure 2.16. As the amplitude of the oscillation caused by three runners is just about these 0.16 mm, it is not possible to recover the frequency response of the bridge deck by using RTS measurements. On the contrary, the fre-

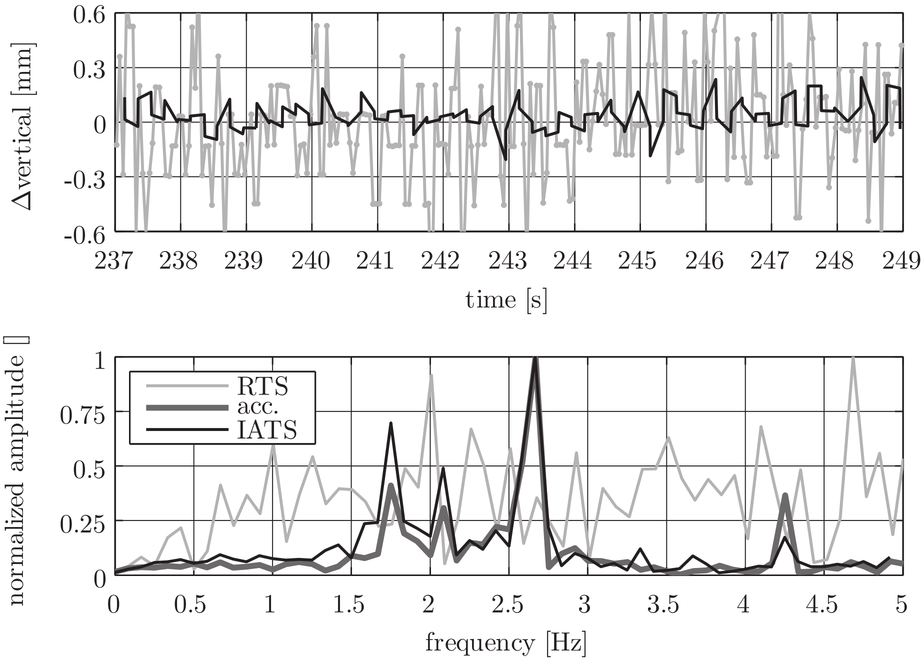

Figure 2.16: Response of the bridge deck due to three runners.

quency response measured by the IATS is in good correspondence to the accelerometer measurements and the frequencies of 1.7, 2.1, 2.7 and 4.3 Hz can be detected. The dominant signal component with a frequency of 2.7 Hz corresponds to the step frequency of the synchronously moving runners.

The response of the bridge deck due to the impulse of one walker is depicted in Figure 2.17. The comparison of the IATS and RTS measurements in time domain confirms the correct conversion of the image-based measurements of the IATS to units of length. Compared to the impulse of three runners, the amplitude of the oscillation of about 0.8 mm is much larger here (note the different scales of the ordinate axes in Figures 2.16 top and 2.17 top). Consequently, it is possible to recover the dominant signal component with a frequency of 1.7 Hz not only with the IATS but also with the RTS.

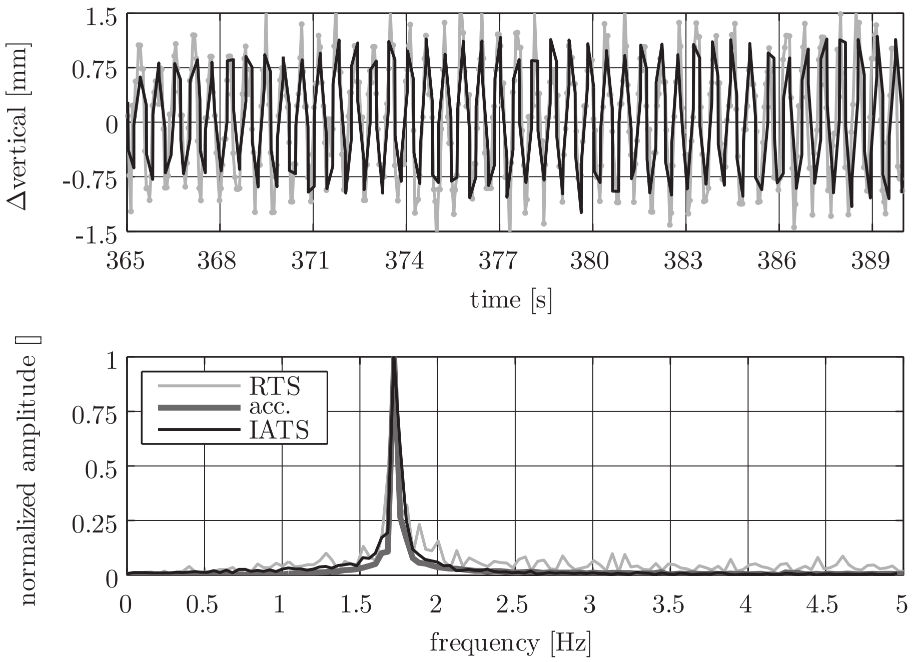

Figure 2.17: Response of the bridge deck due to one walker.

2.6.2 Dynamic deformation monitoring with unfavorable measurement geometry

Experiment description

The measurements at the *Pongratz-Moore-Steg* (steel construction, 72 m span width) were started on January 25, 2017 at 10:30 with the state-of-the-art IATS *Leica MS60* (Section 1.4). The experimental setup is illustrated in Figure 2.18 in which the IGMS beachflag accentuated in Figure 2.18b was used as a visual indicator for wind direction and wind intensity. The instrument position of the RTS with a distance of 31.5 m to the prism corresponds to the measurement geometry P_1 of Figure 2.1 which allows the accurate and high-frequent measurement of the movements in vertical direction and across the bridge (cf. Section 2.3.1 and Lienhart et al. 2017).

(a) location of RTS and IATS relative to targets

(b) measurement positions

Figure 2.18: Setup for the *Pongratz-Moore* experiment.

The position of the IATS with a distance of 30.6 m towards the natural features corresponds to the unfavorable measurement geometry P_4 of Figure 2.1. Compared to the experiment described in Section 2.6.1, none of the bridge's movement axes (vertical, across

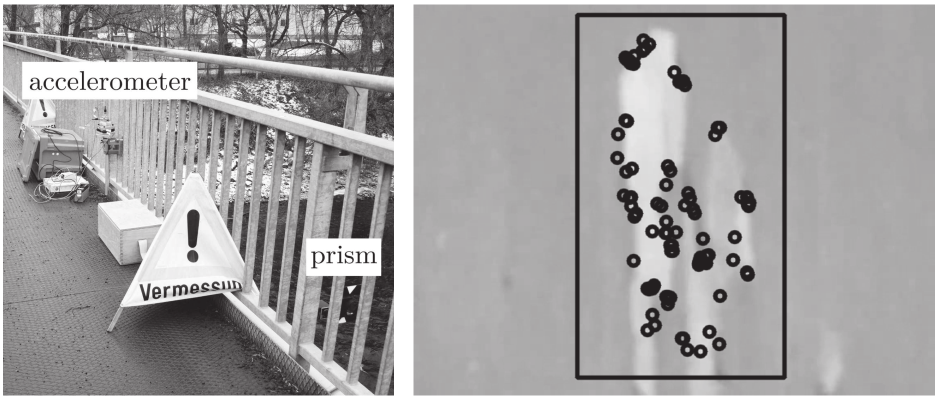

(a) accelerometer and prism **(b)** IATS monitoring area with detected keypoints and ROI

Figure 2.19: Measurement positions for the *Pongratz-Moore* experiment.

and along the bridge) appears as an in-plane movement (cf. Section 2.3.1) for the *Pongratz-Moore* experiment. Consequently, the approach described in Section 2.3.2 is used to extract these movement axes from the IATS measurements. Therefore, the monitoring area of the IATS, which can be approximated by a plane (cf. Figure 2.18b), was scanned at the beginning of the experiment.

Figure 2.19 depicts the measurement positions of the accelerometer, the RTS and the IATS. The measurement data of the IATS is again represented by frames of the video recorded by the instrument's telescope camera. For the *Leica MS60*, the video is recorded at 30 fps with a resolution of 640 px × 480 px (cf. Section 1.4) in which one pixel corresponds to about 0.6 mgon (cf. Section 7.4). Along with the automatically detected keypoints, Figure 2.19b also shows a ROI which can be specified by the operator.

As mentioned in Section 2.5.1, the ROI can be used to exclude inappropriate areas in the image data which is not necessary for the present monitoring area. However, specifying a ROI also decreases the computation time of the feature matching since less pixels need

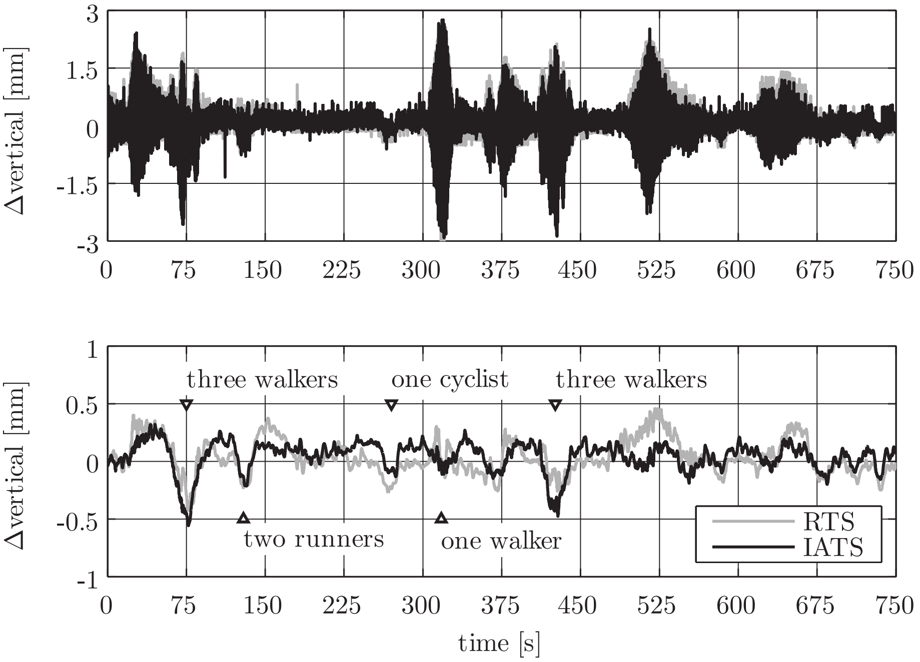

Figure 2.20: Vertical movements of the bridge deck measured by RTS and IATS. Top: raw measurements. Bottom: filtered measurements.

to be analyzed. Investigating Figure 2.19b shows that not much information is lost by applying the feature matching exclusively to the specified ROI because only a small number of keypoints would be detected outside this area due to lack of visually prominent features.

Vertical bridge response

Figure 2.20 shows the vertical movements of the bridge deck measured by the RTS and the IATS. The filtered time series result from applying a low-pass Butterworth filter of order 2 and a cutoff-frequency of 0.2 Hz on the raw data. Although different measurement geometries are used for the IATS and the RTS measurements (cf. Figure 2.18), the results are in good correspondence which con-

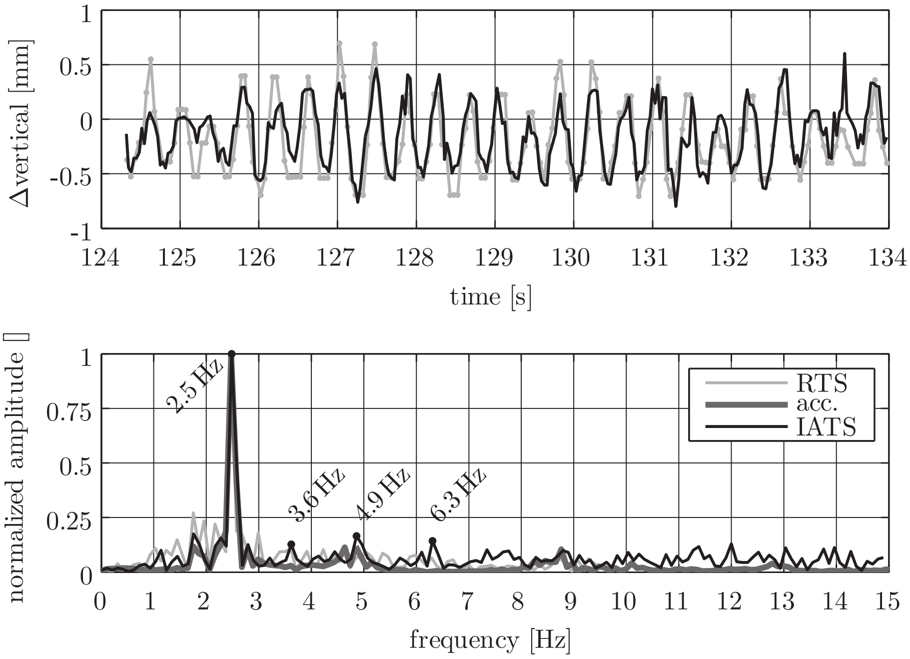

Figure 2.21: Response of the bridge deck due to two runners.

firms the approach of Section 2.3.2.

Investigating the raw and the filtered time series (Figure 2.20) shows the bridge responses due to different stimuli. As for the *Augarten* experiment (Section 2.6.1), the amplitude of the oscillation caused by one walker crossing the bridge is much higher than the amplitude of the oscillation caused by two runners (Figure 2.20 top). For the *Pongratz-Moore-Steg* it can also be observed that the bridge deck is lowered dependent on the applied load (Figure 2.20 bottom). For example three runners lower the bridge deck by about 0.5 mm whereas e.g. two runners or one walker lower the bridge deck by a smaller amount.

The response of the bridge deck due to the impulse of the two runners is depicted in Figure 2.21 in greater detail. The IATS measurements in time domain are hereby computed relative to the first

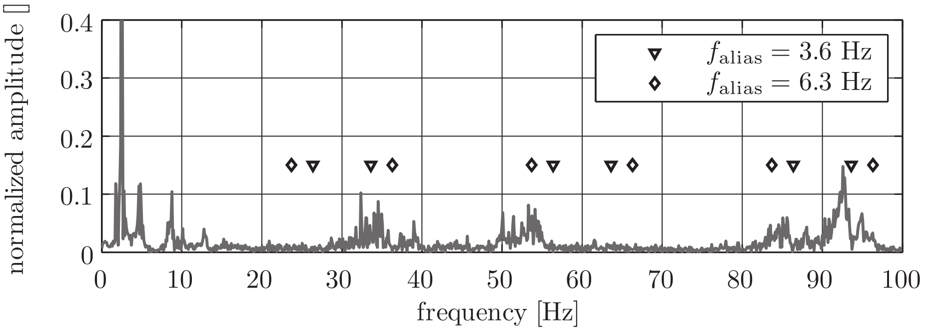

Figure 2.22: Amplitude spectrum computed from accelerometer measurements for two runners crossing the bridge.

frame in which the frequency analysis is based on consecutive frames of the captured video data. For this structure, the amplitude of the oscillation caused by two runners of about 0.5 mm is large enough so that the RTS with its discretization of the dynamic angle measurements (cf. Lienhart et al. 2017), corresponding to 0.15 mm for the distance of 31.5 m, can detect the runners' step frequency of 2.5 Hz. With the IATS, it is also possible to detect this frequency in which the signal component with 4.9 Hz can also be resolved.

However, the IATS measurements also report frequencies of 3.6 and 6.3 Hz which are not detected by the accelerometer (cf. Figure 2.21 bottom). This is probably caused by an aliasing of signal components with higher frequencies (larger than 15 Hz). For further investigations, the full amplitude spectrum of the accelerometer measurements is shown in Figure 2.22 where possible frequencies, which cause alias frequencies f_{alias} of 3.6 and 6.3 Hz for a measurement rate of 30 Hz, are accentuated. The alias frequencies of 3.6 and 6.3 Hz are potentially caused by the true signal components with 33.6 and 53.7 Hz, respectively.

The response of the bridge deck due to the impulse of one walker is depicted in Figure 2.23. The amplitude of the resulting oscillation of over 1.5 mm is equally measured by the IATS and the RTS in which it is again emphasized that the measurement geometries of

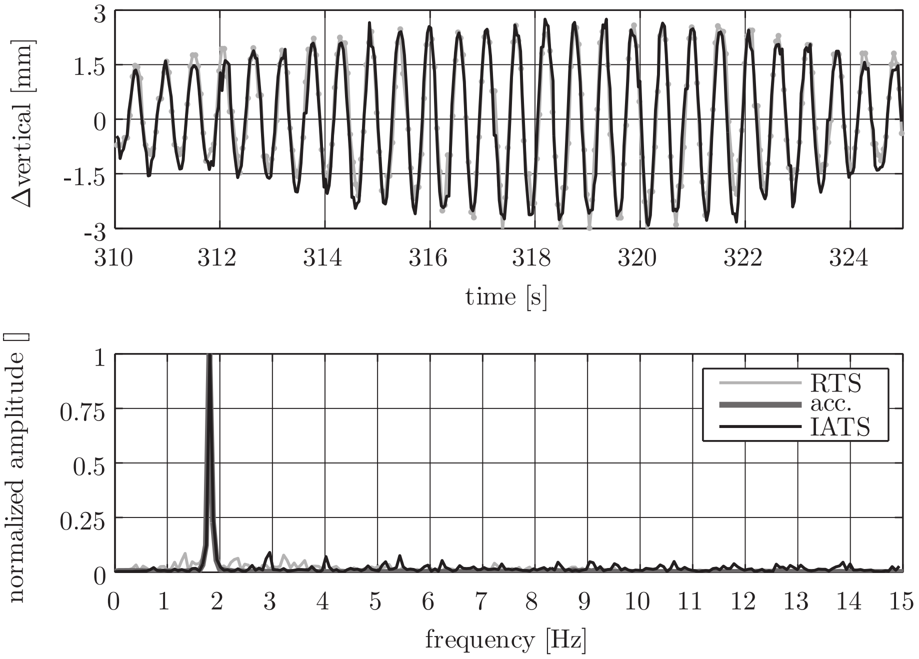

Figure 2.23: Response of the bridge deck due to one walker.

the two instruments are completely different (cf. Figure 2.18). The frequency of the dominant signal component of 1.8 Hz is clearly detected by all evaluated sensors (RTS, accelerometer and IATS) in which also aliasing frequencies with very small amplitudes occur for the IATS and the RTS.

Movements across the bridge observed with distance measurements

Figure 2.24 shows the movement of the bridge deck across the bridge axis. For the RTS measurements, these movements occur orthogonal to the line-of-sight and thus can be detected from angle-only measurements. The results of the IATS are computed according to Eq. (2.11) which involves a continuous, reflectorless distance measurement towards the target. For the evaluated instrument (*Leica*

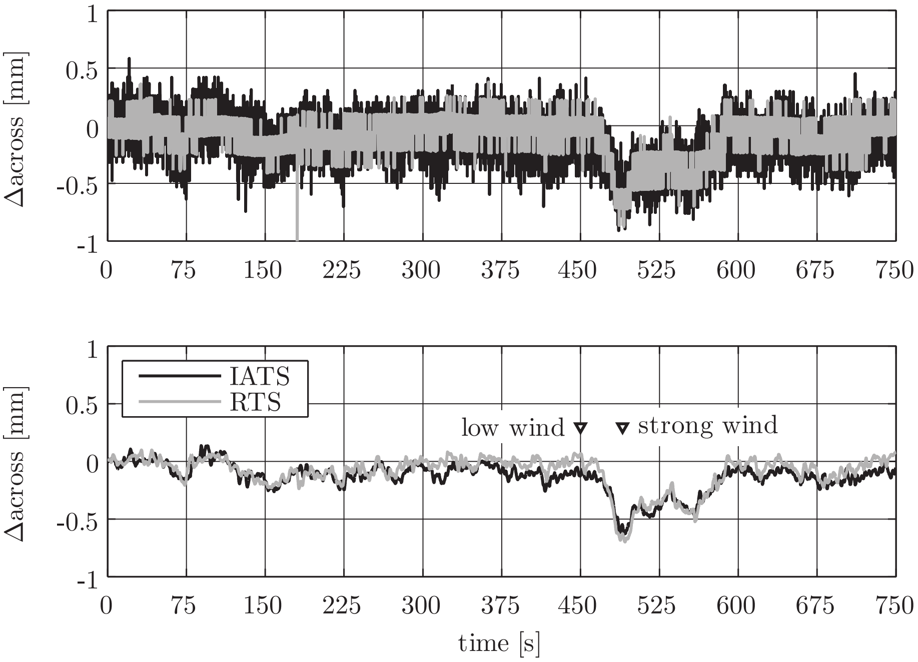

Figure 2.24: Movements of the bridge deck across the bridge axis measured by RTS and IATS. Top: raw measurements. Bottom: filtered measurements.

MS60, cf. Section 1.4), these measurements can be performed with a non-constant measurement frequency of about 20 Hz (Lienhart et al. 2017). The accuracy for continuous distance measurement with the used instrument is specified with 3 mm + 1.5 ppm (to reflective tape) whereas the range noise in scanning mode is specified with 0.5 mm (1σ) at a distance of 25 m (cf. Table 1.5).

A comparison to the RTS measurements shows that these values are outperformed for relative distance measurements and that movements of a few 0.1 mm can be resolved. The eye-catching event in the filtered time series (Figure 2.24 bottom) between 450 and 600 s can be linked to a wind load on the bridge. The wind force is indicated by the beachflag (Figure 2.18b) which was recorded by a standard video camera. Figure 2.25 shows the beachflag for the

Figure 2.25: Wind load measured in Figure 2.24 indicated by IGMS beachflag.

epochs accented in Figure 2.24 whereat its movements are emphasized by the optical flow (Zach et al. 2007) between the two images.

A frequency analysis of the across bridge movements based on the IATS and the RTS measurements is of limited use here because the accelerometer measurements showed that the dominant components of the signal consist of frequencies above 30 Hz.

Movements along the bridge with correction of secondary displacement

Figure 2.26 shows the movements along the bridge axis. At this, no RTS measurements are available because this direction approximately corresponds to the line-of-sight of the instrument (cf. Figure 2.18). With the used RTS (*Leica TS15 I 1″ R1000*), continuous distance measurements can only be conducted with a measurement rate of a few Hz (Lienhart et al. 2017). Consequently, angle-only measurements with a measurement rate of about 20 Hz were executed.

However, for the observed bridge (steel construction) it can be assumed that the dynamic movements along the bridge axis are too small to be resolved anyhow and the resulting time series is expected to consist of measurement noise only. Contrary to this assumption, the IATS measurements, which result from the intersection of the image rays towards the natural targets with the target plane (Section 2.3.2), show systematic effects (cf. the uncorrected time series in Figure 2.26). Comparing these movements to Figure 2.24 reveals

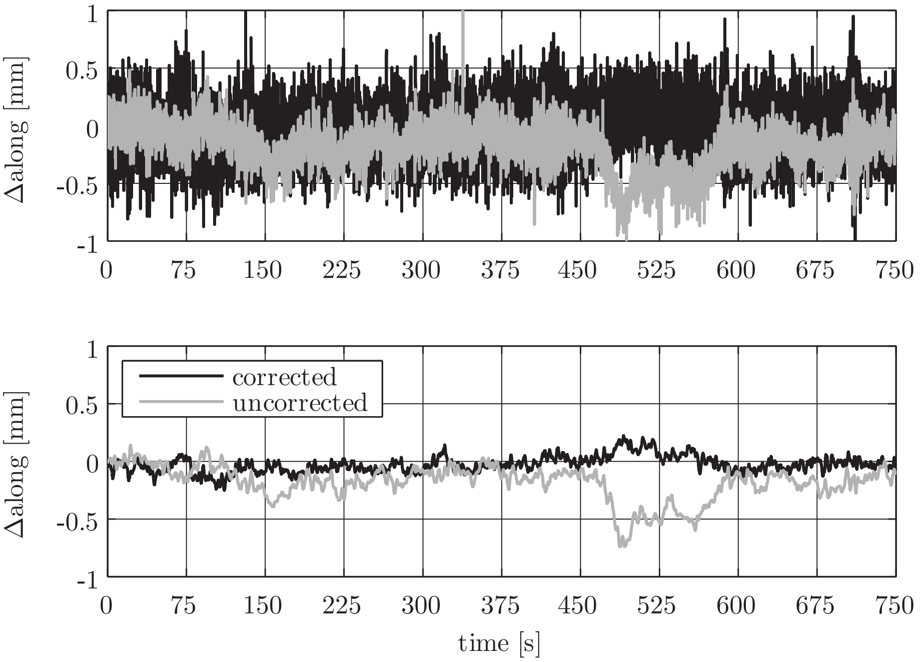

Figure 2.26: Movements of the bridge deck along the bridge axis gained from uncorrected and corrected IATS measurements. Top: raw measurements. Bottom: filtered measurements.

a mapping of the across- to the along-movements. This mapping effect is theoretically discussed in Section 2.3.3.

A correction of the bridge movements orthogonal to the target plane, i.e., across the bridge axis in this case, according to Eq. (2.10) reduces the mapping effect to a large extent (cf. the corrected time series in Figure 2.26). The higher noise of the corrected time series is hereby incorporated from the distance measurements which are included in the correction (Section 2.3.2). If necessary, this effect can be reduced by filtering the time series of the distance measurements prior to the correction.

2.7 CONCLUSIONS

The previous sections showed that a state-of-the-art IATS is a powerful sensor for static and dynamic deformation monitoring. While retaining the same or even a better accuracy as achievable with conventional RTSs and prisms, an IATS has the advantage that access to the monitored structure is not required at any time.

The IATS measurements can be separated to in-plane measurements based on image processing and out-of-plane measurements based on the EDM sensor of the instrument. The image-based measurements hereby outperform the distance measurements concerning accuracy and measurement rate. However, in combination with the analysis of the possible movement axes of the observed structure, it is possible to design the measurement geometry so that primarily in-plane movements occur. In practice, the analysis of possible movement axes is not regarded as a disadvantage since the expected movements of the observed structure must be included in the task description of any monitoring application (DIN 18710-4).

The proposed measurement concept, which is based on the intersection of image rays to natural targets with the target plane, allows a reliable detection of 3D movements even for unfavorable measurement geometries. It is hereby noted that small planes can be found on almost every civil engineering structure. Alternatively, the surface of the structure can also be modeled by a TIN.

The proposed measurement concept performs very well for static deformation monitoring applications in which the observed structure shows long-periodic movements. Consequently, the synchronization of the image-based and the distance measurements is not important. Furthermore, the stability of the IATS can be verified regularly by using the internal tilt sensor (Ehrhart and Lienhart 2015a) or with measurements to stable reference points. The latter also provides a possibility to check the IATS's external orientation.

For dynamic deformation monitoring, the IATS does not deliver full 3D measurements in a homogeneous quality. This is due to the lower, non-constant sampling rate of the EDM sensor compared to the image sensor. However, selected IATSs offer a laser scanning capability with measurement rates of up to 1 kHz (Leica 2015a, p. 69) or even 26.6 kHz (Trimble 2016b). Accordingly, the necessary hardware for fast distance measurements is already available for state-of-the-art IATSs. To access this sensor for monitoring applications with high dynamics, modifications in the instrument firmware are required. For full 3D measurements in dynamic measurement mode, the precise synchronization of the image-based angle measurements and the EDM sensor is an important issue which is subject to further investigations.

Another issue for dynamic deformation monitoring is the stability control of the instrument. The tilt compensator, which is integrated in every total station, is not able to measure high-frequent tilt changes. Furthermore, high-frequent oscillations of the IATS, e.g. caused by construction machinery in the vicinity of the instrument position, are observed as apparent oscillations of the monitored structure. To overcome this limitation, the telescope of the IATS could be equipped with accelerometers which capture its oscillations. Another possibility could be the parallel capturing of image data with an additional camera with a larger AOV. If the measurement geometry can be designed so that stable reference points are available in the AOV of the additional camera, the apparent oscillation of these stable points can be considered as an oscillation of the IATS itself. This additional camera, referred to as overview or wide-angle camera, is already implemented in many IATSs (cf. Section 1.3.1). With some modifications in the instrument firmware it may be possible to access both cameras (wide-angle and telescope) in parallel.

3

Refraction

3.1 ACKNOWLEDGMENTS

This chapter would not exist without the help of Em.Univ.-Prof. Dipl.-Ing. Dr.techn. Fritz K. Brunner: my teacher as an undergraduate student and well-known expert in the field of geodetic refraction. His valuable input in numerous discussions made me understand at least the basic parts of the theory presented in this chapter and helped in the design of the conducted experiments.

Graz, August 2017
Matthias Ehrhart

3.2 INTRODUCTION

In trigonometric leveling, the height difference between the tilting axis of a RTS or an IATS and a target results from

$$\Delta h = s \cos V + (1 - k)\, \frac{s^2 \sin^2 V}{2R} \tag{3.1}$$

in which k denotes the refraction coefficient and R is the radius of the Earth (about 6378 km). The measured quantities are the slope distance s and the vertical angle V from the RTS or IATS to the target. The second term in Eq. (3.1) accounts for the curvature of the Earth and for vertical refraction. For the refraction coefficient k, which is defined as the ratio between the radius of the Earth and the radius of the curved line-of-sight, the constant $k = 0.13$ is frequently used in practice (Möser et al. 2012, pp. 317f.).

However, for typical instrument heights of around 1.5 m, already Brocks (1950) showed that k varies in the range of ± 2 dependent on the hour of day and on the season. For a distance of e.g. 300 m between the instrument and the target, this corresponds to about ±14 mm in the measured height difference. For instrument heights below 1.5 m, the magnitude of k can be much larger (cf. also Brunner and Kukuvec 2011). Accordingly, the value of k must be known for accurate trigonometric height measurements with a RTS or an IATS.

Another approach to encounter the problem of vertical refraction is to compare the true vertical angle V_0 towards the target to the observed vertical angle V in which the difference

$$\delta = V_0 - V \tag{3.2}$$

is known as the vertical refraction angle δ. This relation is also illustrated in Figure 3.1 in which V_0 refers to the geometric connection (straight line) between the IATS and the target. The vertical angle V, which must be set at the IATS to observe the target along the

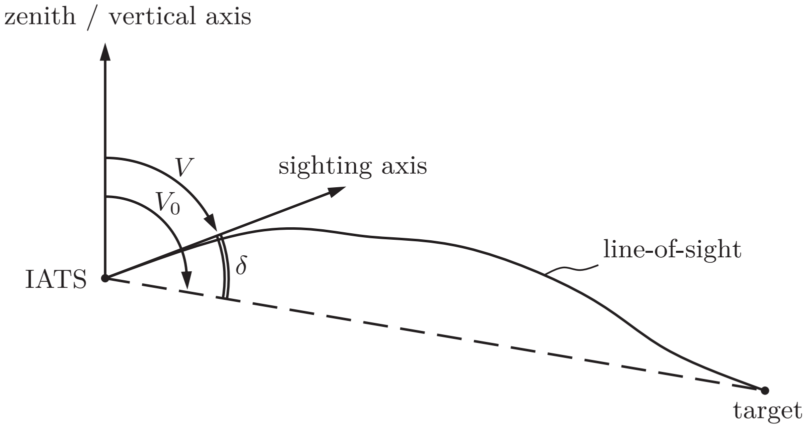

Figure 3.1: True (V_0) and observed (V) vertical angle towards a target differing by the vertical refraction angle δ.

curved line-of-sight, differs from V_0 by the refraction angle δ. By using V_0 instead of V, Eq. (3.1) can be written as

$$\Delta h = s \cos V_0 + \frac{s^2 \sin^2 V_0}{2R} \tag{3.3}$$

in which the second term only accounts for the curvature of the Earth because V_0 is not biased by the effect of vertical refraction (cf. Figure 3.1).

A common approach to determine δ in monitoring applications using a RTS and prisms is based on vertical angle measurements to a stable reference prism in the vicinity of the monitoring targets. From these measurements, the refraction angle δ results from Eq. (3.2) in which V is the actual measurement and V_0 is calculated from known coordinates or is taken from the measurements of the reference epoch (Leica 2010b, p. 236; Lienhart 2017). With knowledge of δ, the true vertical angles towards the monitoring targets are obtained from

$$V_0 = V + \delta \tag{3.4}$$

which allows the computation of the height differences between the

RTS and the targets according to Eq. (3.3). However, the drawback of this approach is that the measurement towards the stable reference target does not pass through the same atmosphere as the measurements towards the monitoring targets. Therefore, the correction will be incomplete and differential errors remain.

The goal of this chapter is to determine δ, or at least its variation $\Delta\delta$ over time, so that the true vertical angle V_0 can be computed from the measured vertical angle V after Eq. (3.4). For the measurement of δ, no other sensor than the IATS itself is used. Accordingly, the measured vertical angle V, which requires a correction for δ, and δ itself are obtained from measurements through exactly the same atmosphere.

Compared to the other chapters of this thesis, in which different applications of IATSs were successfully evaluated by experimental measurements, it is already mentioned here that the problem of vertical refraction could not be fully overcome by the experiments described in this chapter. Nevertheless, the results of the conducted experimental measurements demonstrate that it should be possible to estimate the vertical refraction angle δ based on observations with an IATS.

3.2.1 Related research

The theory for estimating the vertical refraction angle δ which is used in this chapter was first proposed by Brunner (1979) and later refined by Brunner (2014) and Brunner (2015). As mentioned in Section 3.1, the input of Prof. Brunner was also essential for setting up the theoretical framework of Section 3.3.2. The basic principle of the proposed theory is to estimate the vertical refraction angle δ from the standard deviation of the angle-of-arrival fluctuations s_δ under the assumption of a turbulent atmosphere. Further assumptions are a homogeneous terrain underneath the line-of-sight and measurements through the atmospheric surface layer, i.e., within a few tens of meters above ground level (Brunner 1979).

It is emphasized that investigations on the theory of vertical refraction as such, which require expert knowledge of micrometeorology, are beyond the author's expertise and beyond the scope of this thesis. Fundamental works on refraction in general, i.e., not only vertical refraction, include Andreas (1990) and Brunner (1984) in which the latter focuses on the effects of refraction on geodetic measurements (total station and satellite-based measurements).

Following the basic principle proposed by Brunner (1979), the angle-of-arrival fluctuations, which form the basis for estimating δ, were deduced from image-based measurements with different IATS prototypes. For a distance of 256 m between the IATS (RTS and external camera) and the target, Casott and Deußen (2000) report variations of δ by up to 2.5 mgon for experimental measurements between 8:00 and 19:00. After applying a correction deduced from the angle-of-arrival fluctuations, which were obtained from image-based measurements towards the target, the effect of δ on the vertical angle measurements could be reduced to less than 1.5 mgon.

Flach (2000) and Reiterer (2012) compare the angle-of-arrival fluctuations obtained from image-based measurements to reference fluctuations observed by *scintillometer* (cf. Flach 2000, pp. 81f.) measurements. The underlying theoretical models of both publications additionally require the measurement of the intensity fluctuations of the observed target. However, after a satisfactory comparison between the measured and the reference fluctuations, Flach (2000) and Reiterer (2012) do not compute the vertical refraction angle δ itself (cf. also Hoben 2013).

Eschelbach (2009) uses a scintillometer to determine vertical temperature gradients for different environmental conditions (temperature, wind speed and cloudiness). These vertical temperature gradients are compared to reference values obtained from temperature measurements in different heights. From the results of the conducted experiments, Eschelbach (2009) concludes that the effect of δ, which can be computed from the measured vertical temperature gradients, can be reduced by at least 75%. However, similar to

Flach (2000) and Reiterer (2012), values or reference measurements for δ itself are not presented by Eschelbach (2009).

Another method to determine δ is to employ simultaneous, reciprocal observations of the vertical angle with a RTS or an IATS (Kabashi 2004; Hirt et al. 2010; Brunner and Kukuvec 2011). Along with the apparent drawback of utilizing two instruments, this approach is also not feasible in many practical measurement situations. For example when observing targets located on a rock face or on parts of civil engineering structures that are difficult to access (cf. Section 2.5.1), the installation of a second instrument at the target location is not possible. Furthermore, reciprocal observations of the vertical angle only yield accurate results for the measured height difference if the influence of δ is the same for both instrument positions (cf. Wunderlich 1985, p. 63) which cannot be assumed as the general case (cf. Figure 3.1).

As proposed by Böckem (2001), a thorough metrological solution to determine the vertical refraction angle δ (and also refraction effects in horizontal direction) would be a so-called *dispersometer*. This instrument comprises a dual-wavelength laser emitter and a corresponding detection unit. Because of atmospheric dispersion, laser beams with different wavelengths are differently bent in the atmosphere. The angle difference between the two laser beams, which is observed at the detection unit, is proportional to the value of δ (Böckem 2001, p. 8, pp. 25ff.) and can be used for a correction. For measurements under laboratory conditions, Böckem (2001, p. 121) reports that δ can be determined with an accuracy of 0.01 mgon. Considering the size of the necessary hardware, a dispersometer could be implemented into a RTS or an IATS (Böckem 2001, pp. 128f.). However, because of the complexity of such an instrument and the accompanied development costs, it can be assumed that its construction will not be commercially attractive in the near future.

This gives the motivation to estimate the vertical refraction angle δ, or at least its variation $\Delta\delta$ over time, by using a single state-of-the-art IATS without any additional measurement equipment.

3.3 MEASUREMENT CONCEPT AND THEORY

3.3.1 Basic considerations

For transferring heights between different points, as done in trigonometric leveling (for which the image-based measurements of an IATS can be used, cf. Wiedemann et al. 2017), the absolute value of the refraction angle δ is required for evaluating Eq. (3.3) by using Eq. (3.4). For monitoring applications with an IATS (cf. Chapter 2), the absolute height difference Δh between the IATS's tilting axis and the target is of minor importance whereat the variations of Δh over time are used for an assessment of the behavior of the observed object.

For a stable setup of the IATS, which can be verified by measurements to stable reference points (cf. Section 2.5.2), the measured height variations of different epochs can either be caused by movements of the observed object or by changes of the vertical refraction angle $\Delta\delta$.

In monitoring applications, the movements of the observed object in different epochs result from comparing the individual epochs to a reference epoch. For the measurements of this reference epoch, the "true" vertical angle can be computed from

$$V_{0,1} = V_1 + \delta_1 \tag{3.5}$$

in which an arbitrary (but reasonably small) value is chosen for δ_1, e.g. $\delta_1 = 0$. For the measurements in later epochs i, the "true" vertical angle results from

$$V_{0,i} = V_i + (\delta_1 + \Delta\delta_i) \tag{3.6}$$

in which only the refraction angle's variation $\Delta\delta_i$ w.r.t. the reference epoch is required to separate the movements of the object from changes in the refraction angle. Evaluating Eq. (3.3) does not produce accurate results for the absolute values of Δh when using an arbitrary value δ_1 in Eqs. (3.5) and (3.6). However, this is not required for most monitoring purposes and knowledge of the variation $\Delta\delta$ w.r.t. the reference epoch is sufficient for measuring accurate height variations of the observed object.

3.3.2 Estimation of the vertical refraction angle

The basic principle for estimating the vertical refraction angle δ is to use the standard deviation of the angle-of-arrival fluctuations s_δ which was first proposed by Brunner (1979). Both quantities, i.e., the mean value δ and the standard deviation of its fluctuations s_δ, result from the same micrometeorological processes (Brunner 1979) so that δ can be expressed by

$$\delta = \delta(s_\delta) \tag{3.7}$$

The proposed method of using an IATS to determine s_δ is advantageous because s_δ can be measured along the same line-of-sight along which the refraction angle δ occurs. Furthermore, the measurements of s_δ are performed simultaneously with the measurements of the vertical angle V, which requires a correction for δ after Eq. (3.4), and can be conducted with a single commercially available measurement system.

Following Brunner (2015, pp. 13f.) and taking the input of Prof. Brunner (cf. Section 3.1) into account, Eq. (3.7) can be written as

$$\delta = -\sin V^* \, \frac{\mu}{T} \, \frac{s}{2} \left(A - \frac{W}{z\,k} \, \frac{\varphi_h}{f^{1/2}} \right) \tag{3.8}$$

in which the sign of δ corresponds to the definition in Eq. (3.2),

$$\mu = 79\mathrm{e}^{-6} \, p/T \tag{3.9}$$

$$W = 0.97 \ \operatorname{sign}\Theta_* \, s_\delta \, (z\,k)^{1/3} \, D^{1/6} \, T \, \mu^{-1} \, (3.2\,s)^{-1/2} \tag{3.10}$$

and the remaining quantities are described in Table 3.1.

Table 3.1: Used constants, measured and derived quantities with symbols and values after Brunner (2015); the values of the measured and derived quantities result for the experiment described in Section 3.4

Symbol	Value	Description
A [K/m] ✤	$-24.33\mathrm{e}^{-3}$	auxiliary quantity (Brunner 2015, p. 6)
D [m] ✪	0.04	diameter of IATS's objective
f [] ★	1	combined profile function (Brunner 2015, p. 32)(1)
k [] ✤	0.40	Kármán's constant
μ [] ★	$265\mathrm{e}^{-6}$ to $276\mathrm{e}^{-6}$	atmospheric part of the air's refractive index, cf. Eq. (3.9)
p [hPa] ✪	973 to 976	atmospheric pressure
s [m] ✪	102.940	slope distance from IATS to target
s_δ [rad] ★	0 to $4.2\mathrm{e}^{-6}$	standard deviation of angle-of-arrival fluctuations, cf. Eq. (3.11)
s_V^* [rad] ★	$0.4\mathrm{e}^{-6}$ to $4.2\mathrm{e}^{-6}$	segment-wise standard deviation of measured vertical angle
T [K] ✪	279 to 291	air temperature
$\operatorname{sign}\Theta_*$ [] ★	-1 or +1	sign of temperature scale, cf. Eq. (3.12)
φ_h [] ★	1	flux-profile function (Brunner 2015, pp. 23ff.)(1)
V [rad] ✪	$\approx \pi/2$	measured vertical angle to target
V^* [rad] ★	$\approx \pi/2$	segment-wise average of measured vertical angle
W [K] ★	0 to 0.10	auxiliary quantity, cf. Eq. (3.10)
z [m] ✪	0.89	average height of line-of-sight over ground

✤ constant, ✪ measured, ★ derived

(1) depends on horizontal wind speed; set to unity in the absence of this observation

The key observation for evaluating Eq. (3.8) is the image-based vertical angle V from the IATS to the target which is recorded at a relatively high measurement rate (e.g. 10 Hz or higher) and which is used to compute the segment-wise average V^* (cf. Section 3.4.4).

Further measured values are the air temperature T, the atmospheric pressure p, the slope distance s from the IATS to the target, the average height of the line-of-sight over ground z, and the diameter of the IATS's objective D. Hereby, the sensor for measuring T and p is not regarded as additional equipment because these meteorological values are also required to correct the electronic distance measurements from the IATS to the target (cf. e.g. Möser et al. 2012, pp. 264f.).

The standard deviation of the angle-of-arrival fluctuations s_δ, which is used in Eq. (3.10), is computed from

$$s_\delta = \sqrt{{s_V^*}^2 - \min {s_V^*}^2} \tag{3.11}$$

in which s_V^* denotes the standard deviation of the measured vertical angle's fluctuations. To obtain s_V^*, the vertical angle measurements are subdivided into segments from which the standard deviations s_V^* and the segment averages V^* can be computed (cf. Section 3.4.4). In Eq. (3.11), s_V^* is reduced by the minimum value of all segments to separate the contribution of the IATS's measurement noise from the standard deviation of the angle-of-arrival fluctuations.

The flux-profile function φ_h and the combined profile function f are both set to unity because they depend on the horizontal wind speed which was not measured in the experiment described in Section 3.4.

For measurements starting in the early morning, the time t_0 where $s_\delta = 0$, i.e., where $s_V^* = \min s_V^*$, marks the transition from stable (night) to unstable (day) atmospheric conditions. The time t_0 can be used to determine the sign of the temperature scale

$$\operatorname{sign} \Theta_* = \begin{cases} +1 & \text{for stable atmospheric conditions} \\ -1 & \text{for unstable atmospheric conditions} \end{cases} \tag{3.12}$$

which is used in Eq. (3.10).

3.4 EXPERIMENTAL MEASUREMENTS

3.4.1 Experimental setup

To evaluate the theory of Section 3.3, experimental measurements with the state-of-the-art IATS *Leica MS60* (cf. Section 1.4) were performed over a horizontal field of short grass (average grass length of 3 cm) between the street Sandgasse and the buildings Inffeldgasse 16a and 16c in Graz, Austria. The measurements were conducted on November 21st, 2016 with an almost cloudless sky. The IATS observed a circular target (diameter of 40 mm) located at a distance of about 103 m under an almost horizontal sighting ($V \approx 100\,\mathrm{gon}$). The heights of the IATS's tilting axis and the target's center over ground were about 0.89 m. The IATS and the target were both shaded from the sun by umbrellas. The experimental setup is depicted in Figure 3.2 and the meteorological conditions for the duration of the experiment are shown in Figure 3.3. The wind speed was not measured but it is noted that there was hardly any sensible wind throughout the experimental measurements.

3.4.2 Stability control

Although the tripods of the IATS and the target were mounted on wooden pegs for establishing a stable setup (cf. Figure 3.2a and 3.2b), the height difference between the IATS and the target was controlled at the beginning, during and after the experimental measurements. Therefore, the analogue level *Wild NA2* with a plane parallel micrometer *Wild GPM1* (Figure 3.2c), which allows direct staff readings to 0.1 mm (readings were estimated to 0.01 mm), was used in combination with the analogue leveling staff *Wild GWL 92*.

The height transfer from the center of the target to the IATS's tilting axis was performed by means of a double leveling using equal sight lengths of about 17 m. At the last position of the leveling staff (distance to IATS of about 3.6 m, cf. Figure 3.2a), the height of the IATS's tilting axis was deduced from image-based staff readings as

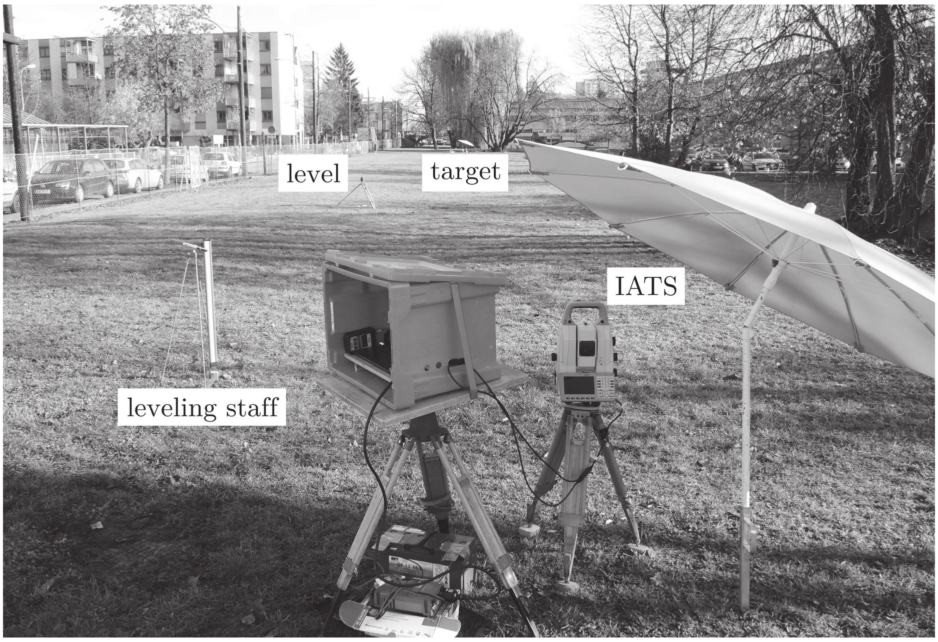

(a) overview

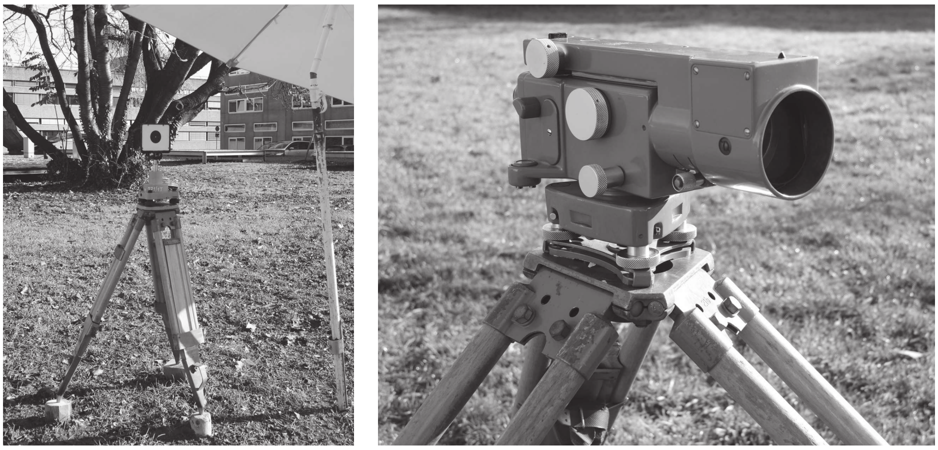

(b) target **(c)** level with plane parallel micrometer

Figure 3.2: Experimental setup.

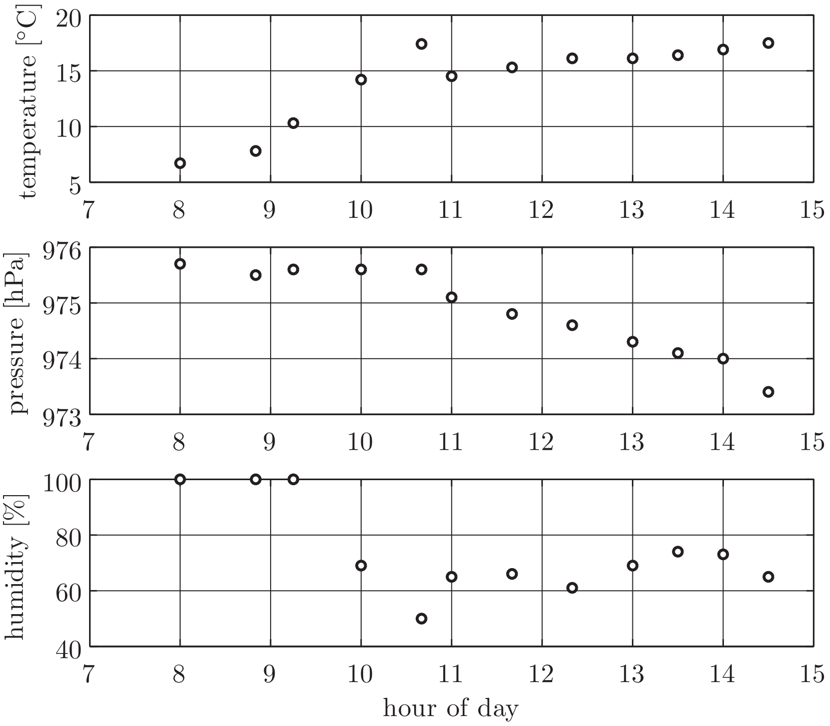

Figure 3.3: Meteorological conditions.

proposed by Wiedemann et al. (2017).

As already mentioned, the height difference was controlled at the beginning, during and after the experimental measurements whereat the individual height differences showed a range of 0.1 mm. For the distance of about 103 m between the IATS and the target, this corresponds to an angle of 0.06 mgon which is withing the measurement noise of the IATS's image-based angle measurements (cf. Section 4.3.2). Accordingly, the height difference between the IATS and the target can be regarded to be stable and the variations in the observed vertical angle can be regarded to be caused by changes in the vertical refraction angle or by changes in the instrument errors.

3.4.3 Measurement program

To measure the variations of the vertical refraction angle $\Delta\delta$, image-based measurements were conducted towards the circular target. Hereby, the IATS (*Leica MS60*, cf. Section 1.4) recorded a video of the target with a resolution of 640 px × 480 px in which one pixel of the used telescope camera corresponds to about 0.6 mgon (cf. Section 7.4). For the used IATS, a frame rate of 30 fps would be possible in which a value of 10 fps was regarded to be sufficient. A smaller frame rate has the advantage that larger shutter times are possible which increases the quality of the image data at low ambient light conditions, e.g. for measurements in the morning. Simultaneously to the capturing of the video data, the readings of the angular encoders, the values of the tilt compensator, and the internal temperature were recorded. The image-based angles towards the center of the circular target were computed according to Section 6.3 in which only the vertical angle is of interest for further computations.

It is shown in Section 4.2.2 that the instrument errors of an IATS change in dependence of temperature variations. For the experimental measurements described in this section, in which only the vertical angle is used, the IATS's vertical index error and the zero point error of the tilt compensator in longitudinal direction are of interest. To determine these values, the following measurement program was defined:

1. Record data (telescope camera video, readings of angular encoders and tilt compensator, internal temperature) for 10 s in Face I.
2. Record data for 10 s in Face II.
3. Record data for 15 min in Face I.
4. Go to Step 1.

From the averages of the image-based vertical angle measurements computed in Step 1 and 2 (measured in telescope Face I and

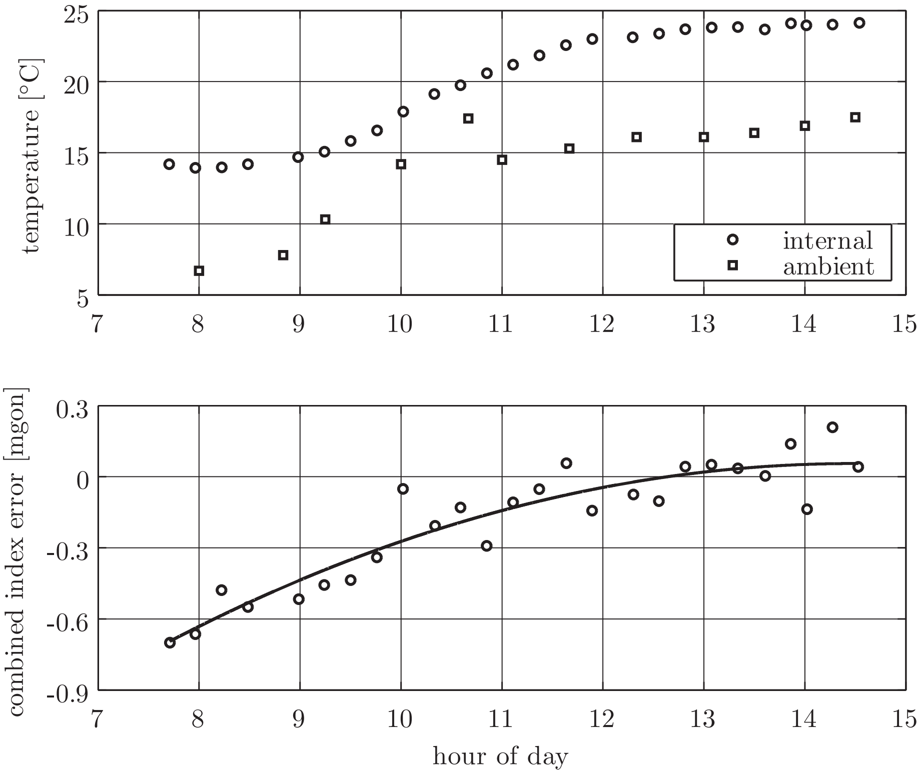

Figure 3.4: Internal and ambient temperature (top) and variations of the combined index error modeled by a quadratic polynomial of time (bottom).

II), a combined vertical index error can be computed. This value includes the telescope's vertical index error, the zero point error of the tilt compensator in longitudinal direction, and potential variations of the image sensor's principal point (cf. Section 6.3.3).

Figure 3.4 shows the combined index error, the ambient temperature, and the IATS's internal temperature for the duration of the experimental measurements. On average, the internal temperature is about 6°C above the ambient temperature. In Section 2.5.2, an average temperature difference of 8°C could be observed. This is probably caused by the fact that the instrument was not shaded from the sun in the experimental measurements

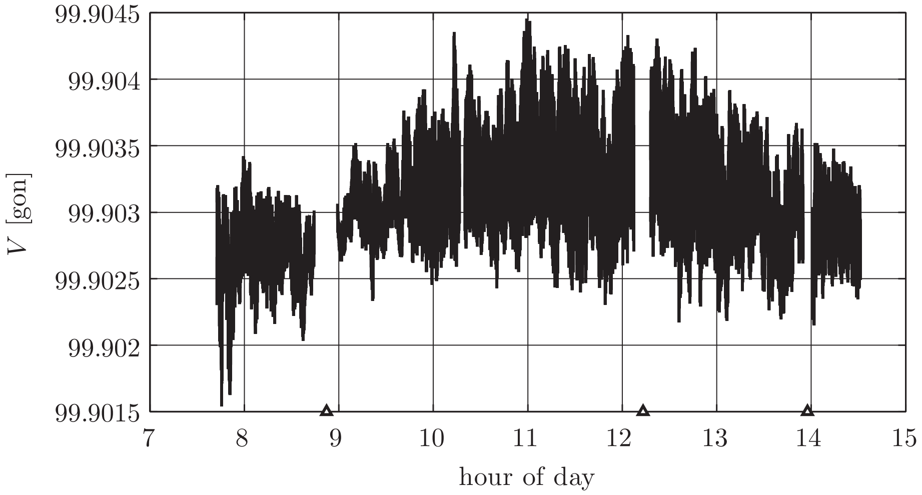

Figure 3.5: Image-based vertical angle measurements towards target with data gaps (triangles) caused by measurements for stability control.

of Section 2.5 whereas an umbrella was used for the experiments described in this section (cf. Figure 3.2a).

The 15 min-measurements in Face I (Step 3), which are used to investigate the variations of the vertical refraction angle $\Delta\delta$, were corrected with the model of the combined index error (quadratic polynomial of time, cf. Figure 3.4 bottom). Without correction of the varying index error, its variations would be mistakenly interpreted as variations of the vertical refraction angle.

Figure 3.5 depicts the image-based vertical angle measurements towards the target which are computed from the consecutive 15 min-measurements and corrected for the combined index error (Figure 3.4 bottom). Furthermore, outliers caused by pedestrians crossing the line-of-sight are removed. Along with the changes of the absolute value of the vertical angle V, also variations in the magnitude of its fluctuations can be observed for different hours of day.

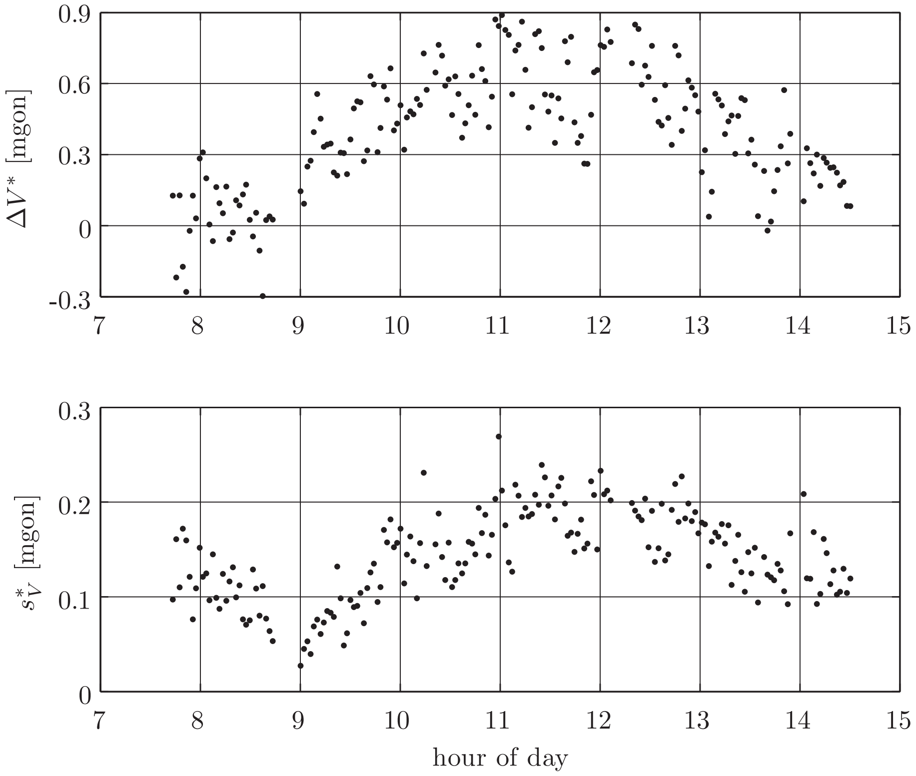

Figure 3.6: Variation of mean values and standard deviations of the measured vertical angle computed from 2 min-segments.

3.4.4 Preparation of measurement data

To illustrate the changes of the vertical angle's fluctuations, the data from Figure 3.5 is divided into segments of two minutes. From these segments, the mean value V^* and the standard deviation s_V^* of the observed vertical angle V are computed. For the set video rate of 10 fps, the 2 min-segments consist of about 1200 measured vertical angles which provides a sufficient sample for computing s_V^*.

Figure 3.5 shows that the measured vertical angle V does not only change in the magnitude of its fluctuations but also includes a trend. Consequently, the standard deviations computed from longer

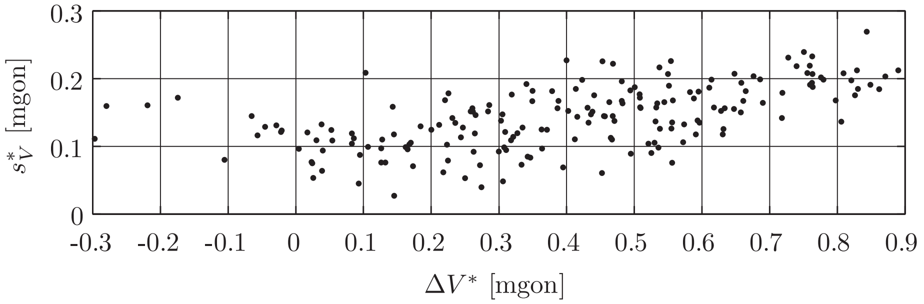

Figure 3.7: Correlation between variation of vertical angle ΔV^* and its standard deviation s_V^*.

segments can take improperly high values. This can be avoided by removing the trend of the segments (e.g. by a polynomial of order one or two) before computing s_V^*. However, a measurement time of over two minutes is also considered as inconvenient for practical measurements.

The variations of the segment averages ΔV^* and the segment-wise standard deviations s_V^* are depicted in Figure 3.6. As the height difference between the IATS's tilting axis and the target can be regarded to be constant (cf. Section 3.4.2) and as V is free of the instrument errors (cf. Section 3.4.3), the changes in ΔV^* and s_V^* can be assumed to be caused by refraction effects.

Figure 3.7 shows that there exists a correlation between $\Delta\delta$, which is measured by ΔV^*, and the standard deviation of the angle-of-arrival fluctuations s_δ which is measured by s_V^*.

3.4.5 Experimental results

By using the prepared measurement data of Section 3.4.4, i.e., the segment-wise averages V^* and standard deviations s_V^* of the measured vertical angle, the framework of Section 3.3.2 was used to estimate the vertical refraction angle δ and its variations $\Delta\delta$.

From solving Eq. (3.3) for V_0 and by using the height difference

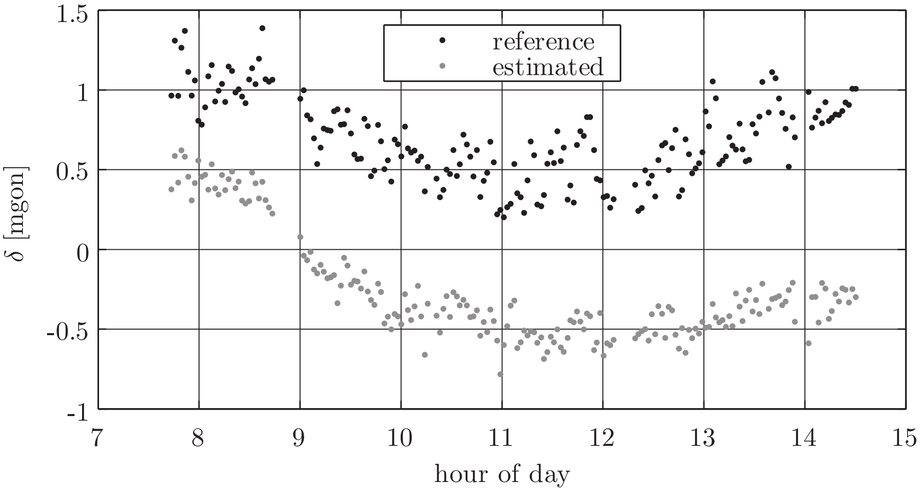

Figure 3.8: Experimentally determined refraction angle δ.

Δh between the IATS's tilting axis and the target gained from leveling (Section 3.4.2), a reference value for the refraction angle can be computed from Eq. (3.2). This reference value and the estimated refraction angle (after Section 3.3.2) are depicted in Figure 3.8.

Apart from an offset between the reference and the estimated values of δ, which is uncritical for monitoring applications (cf. Section 3.3.1), both data sets of Figure 3.8 show a similar behavior.

To illustrate the quality of the estimated vertical refraction angle, the variations $\Delta\delta$ and the errors $\epsilon_{\Delta\delta}$ to the reference are depicted in Figure 3.9. The variations $\Delta\delta$ result from subtracting the averages of the data sets of Figure 3.8 between 11:00 and 13:00. This corresponds to choosing an arbitrary value for δ_1 in Eqs. (3.5) and (3.6) of Section 3.3.1.

For the conducted experiment, 93% of the errors $\epsilon_{\Delta\delta}$ between 9:00 and 15:00 (Figure 3.9 bottom) are within the specified standard deviation of 0.3 mgon for conventional automated angle measurements to prisms of a typical RTS (e.g. Leica 2015a, p. 68). Accordingly, the estimated variations of the refraction angle $\Delta\delta$

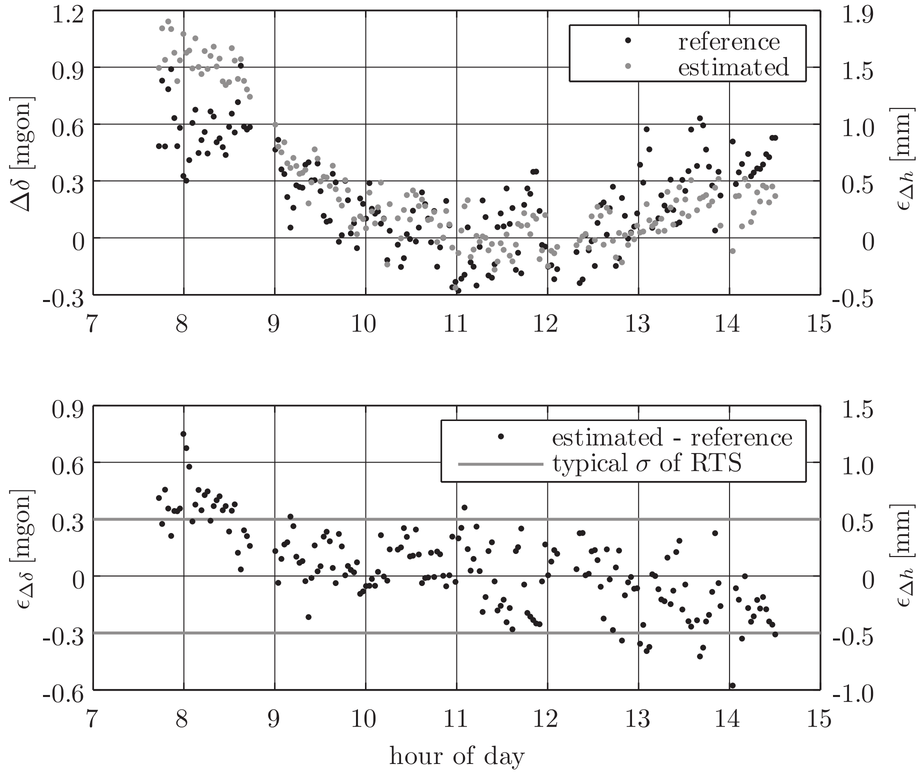

Figure 3.9: Experimentally determined variations of the refraction angle $\Delta\delta$ (top) and errors $\epsilon_{\Delta\delta}$ to reference measurements (bottom). Right ordinate: corresponding errors in the measured height difference $\epsilon_{\Delta h}$ for the present distance (103 m).

could be used to correct monitoring measurements (according to Section 3.3.1) between 9:00 and 15:00 for the given measurement configuration (cf. Section 3.4.1).

Admittedly, the above constraints, especially the homogeneous terrain underneath the line-of-sight, are unrealistic for practical measurements. Furthermore, the errors $\epsilon_{\Delta\delta}$ to the reference show large values before 9:00 and still include a slight trend from 9:00 to 15:00 (cf. Figure 3.9 bottom).

The reason for this behavior is unclear to the present day. A possible explanation could be the lack of the horizontal wind speed measurements which would change the values of the profile functions φ_h and f of Section 3.3.2.

The relatively small variation of the refraction angle with a range of about 1 mgon (cf. the reference values of Figure 3.9 top) complicates a further analysis of the results. This small variation is primarily due to the time of the experimental measurements in November (cf. Section 3.4.1) when the low solar radiation causes relatively small refraction effects. Accordingly, experiments in summer, when the refraction effects are expected to be much larger (cf. the extensive tables of Brocks 1950), are proposed for further investigations. Another possibility to increase the refraction effects is to increase the relatively short distance between the IATS and the target (103 m, cf. Section 3.4.1).

3.5 CONCLUSIONS AND OUTLOOK

In this chapter, the correction of the influence of refraction on the vertical angle measurements with an IATS was tackled. It was pointed out that the absolute value of the vertical refraction angle δ is not required to correct the relative measurements of monitoring applications and that the variation of the refraction angle $\Delta\delta$ over time is sufficient for this purpose.

The evaluated estimation of $\Delta\delta$ is based on the standard deviation of the angle-of-arrival fluctuations s_δ which can be derived from high-frequent image-based measurements with an IATS. Besides a sensor for the measurement of the ambient temperature and the atmospheric pressure, which are both required to correct the electronic distance measurements anyhow, no other sensor than the IATS itself was used for collecting the necessary measurement data.

For selected hours of day, the estimates for $\Delta\delta$ showed a good correspondence to the reference values obtained from a leveling between the IATS's tilting axis and the center of the target. However, especially for measurements in the morning, the estimates for $\Delta\delta$

showed deviations to the reference values with the same order of magnitude as $\Delta\delta$ itself. The reason for this behavior is unclear to the present day. Furthermore, the used formulas for the estimation of $\Delta\delta$ assume a homogeneous terrain underneath the line-of-sight. For the performed experimental measurements, this constraint was fulfilled by measurements over a horizontal field of short grass. Measurements in practice, which are typically conducted over an inhomogeneous terrain, do not comply with this restriction.

However, the noticeable correlation between $\Delta\delta$ and s_δ encourages the presumption that is possible to estimate variations of the vertical refraction angle based on its fluctuations – albeit with slight adjustments of the used formulas and by capturing additional measurement data such as the wind speed. For monitoring applications, in which the measurements towards a target are always conducted over the same (inhomogeneous) terrain, it could be possible to eliminate the constraint of a homogeneous terrain in the used formulas.

Furthermore, it could also be possible to apply the proposed measurements to correct for horizontal refraction effects. For example in tunneling, the difference between the rock and the air temperature causes a horizontal temperature gradient which in turn biases the horizontal angle measurements. These angle measurements are used to steer the tunnel driving and typically require a high accuracy (e.g. 0.3 mgon) in which Hennes et al. (1999) report temperature-induced biases of up to 6 mgon (up to 50 mm for a distance of 500 m). However, it is noted that in this case the absolute value of the refraction effect and not only its variation has to be determined for a correction.

It is further noted that the video-theodolite *Wild TM3000V* was used in tunneling to steer the tunnel boring machine (Grübl and Schütz 1994, pp. 190ff.) before it was transitionally replaced by a more cost-efficient pure imaging system with light emitting targets (Grübl and Schütz 1994, pp. 193ff.). Nevertheless, this confirms the ability of an IATS to operate under the harsh environmental conditions that are present during the tunnel driving.

For the conducted experiment with a distance of 103 m between the IATS and the target, the variation of the vertical refraction angle $\Delta\delta$ showed a maximum value of about 1 mgon. For further investigations, experiments that produce larger values for $\Delta\delta$ would be useful.

Concluding this chapter, the following recommendations for future refraction experiments are made:

- Retain the homogeneous terrain underneath the line-of-sight from the IATS towards the target. Once the estimation of $\Delta\delta$ succeeds, an inhomogeneous situation can be tackled.
- Allow the IATS to acclimatize to the ambient temperature and eliminate warm-up effects (cf. Section 4.2.2) by switching on the IATS at least one hour before capturing the first measurements.
- Verify the stability of the setup. This can be achieved by a leveling of the height difference between the IATS's tilting axis and the center of the target (cf. Section 3.4.2) which also allows the computation of reference values for δ (cf. Section 3.4.5).
- Choose an experimental setup for which large values for $\Delta\delta$ can be observed. This can be achieved by measurements in summer (cf. Brocks 1950) and by a larger distance between the IATS and the target (e.g. 200 m).
- For image-based measurements at night, the target requires artificial illumination. The vertical angles could also be measured by using a RTS and its automated angle measurements to prisms (cf. Section 5.1.1) which can be conducted with up to 20 Hz. Hereby, it is noted that some instruments show a discretization of the measured angles in continuous measurement mode (e.g. 0.3 mgon, cf. Lienhart et al. 2017).
- Measure the horizontal wind speed which is required to compute the profile functions φ_h and f of Section 3.3.2.

- For a thorough verification of the underlying theory, experiments in different seasons and with different heights of the line-of-sight above ground are required.

4

High-precision measurements

4.1 INTRODUCTION

Concerning the accuracy of 3D points measured with an IATS, it is pointed out in Section 2.2.1 that the distance measurement with an accuracy of a few millimeters is the limiting factor. Accordingly, for establishing highly accurate reference frames or for measuring accurate 3D points, which is required in many industrial applications, the EDM sensor of the IATS cannot be used. Instead, the coordinates of the 3D points can be determined by a geodetic network measurement which purely relies on angle measurements, i.e., a triangulation. Hereby, the scale of the network can be determined by angle measurements towards the markings of a reference scale with an accurately known length.

In the late 1980s, a similar principle was already used in two commercial systems: the *System for Positioning and Automated Coordinate Evaluation* (SPACE, cf. Gottwald 1987) and the *Automated Theodolite Measurement System* (ATMS, cf. Katowski 1989) which were based on the video-theodolites *Kern E2-SE* and *Wild TM3000V*, respectively. The basic principle was to determine the 3D coordinates of selected, signalized points (such as circular targets) by a spatial forward intersection which involved at least two video-theodolites. The scale was introduced by measurements towards the markings of a known reference scale. In another embodiment, one theodolite projected a laser beam towards the observed structure which was then automatically detected by another video-theodolite (Katowski 1989; Kahmen and Seixas 1999; Webern and Kahmen 2004).

In this chapter, the achievable 3D accuracy of point coordinates determined from a triangulation with a state-of-the-art IATS is evaluated. The empirical standard deviations of the angle measurements, which are estimated after the geodetic network adjustment, are used to qualify the accuracy of the image-based angle measurements. Furthermore, different error sources, such as an insufficient calibration, warm-up effects or target specific errors, are discussed and their impact on the measurements is evaluated.

Related publications

This chapter follows the article of Ehrhart and Lienhart (2017a).

4.2 ERROR SOURCES

An IATS extends a conventional RTS by one or more cameras. Consequently, it shares some error sources such as the theodolite axes errors or the zero point errors of the two-axis tilt compensator (Section 6.3.3). These errors cancel out when performing two-face measurements (Deumlich and Staiger 2002, pp. 205ff.) and a detailed discussion is omitted here.

Furthermore, errors due to an insufficient mapping relation between image coordinates and theodolite angles are not reviewed in this thesis and it is referred to Ehrhart and Lienhart (2017a) for a detailed discussion on this issue. It is however noted that using the intuitive relation

$$\begin{aligned}\cancel{Hz_\mathrm{T} = Hz + (u - u_0)/c}\\ \cancel{V_\mathrm{T} = V + (v - v_0)/c}\end{aligned}$$

instead of the relations given in Chapter 6 can, dependent on the position of the target on the image sensor and the vertical angle of the telescope, result in errors of several 100 mgon.

The investigated error sources involve errors in the calibration parameters due to an insufficient calibration (Section 4.2.1), warm-up effects of the instrument (Section 4.2.2) and target specific errors (Section 4.2.3).

4.2.1 Insufficient calibration

The calibration of the mapping parameters which relate image coordinates to theodolite angles (cf. Chapter 6) is discussed in Chapter 7. For the IATSs used in this thesis (cf. Section 1.4), the relation was found to be sufficiently parameterized by the principal point u_0 and v_0, the camera constant c, the rotation of the image sensor about the principal axis κ and one radial distortion coefficient K_1 (cf. Table 6.2). Hereby, u_0, v_0, c and K_1 depend on the focus position of the telescope which is a function of the distance to the target (cf. Section 7.3.3).

The calibration parameters of a state-of-the-art IATS and their standard deviations can be found in Table 7.2 of Section 7.4. For an exemplary focus position of 103, which corresponds to a distance of 30 m, the standard deviations of the calibration parameters are given in Table 4.1.

Based on these values, it is computationally evaluated how er-

Table 4.1: Standard deviations of calibration parameters at focus position 103 corresponding to a distance of 30 m (computed from the results of Table 7.2)

c [px]	κ [mgon]	K_1 [px^{-2}]	u_0 [px]	v_0 [px]
2.3	0.7	0.34e^{-10}	0.1	0.1

rors in the calibration parameters demonstrate their effect on the measurements for different positions of the target on the image sensor and for different vertical angles of the telescope. Hereby, the fivefold values of the standard deviations given in Table 4.1 are introduced as errors of the respective parameters.

The patterns of the deviations caused by errors in the calibration parameters are exemplarily shown in Figure 4.1 for a vertical telescope angle of $V = 100$ gon. Errors in the principal point (u_0, v_0), which are not shown in Figure 4.1, hereby result in deviations of 0.3 mgon in horizontal (for an error in u_0) and vertical (for an error in v_0) direction for all positions of the target on the image sensor.

It can be observed that errors in c and K_1 result in radial-symmetric deviations to the principle point which approximately corresponds to the center of the image sensor. Hereby, the deviations caused by an error in c increase with an increasing radial distance to the principal point. The deviations caused by an error in K_1 are small at a radial distance of 1067 px which corresponds to the second zero crossing of the distortion polynomial at r_0 (cf. Section 6.2.2). An error in κ causes a rotation-symmetric pattern of the deviations in which the magnitude also increases with an increasing radial distance to the principal point.

Figure 4.2 depicts the maximum deviations of the measured angles caused by errors in the calibration parameters for different vertical angles and positions of the target on the image sensor. Figure 4.1 shows that these maximum deviations occur for targets observed in the boundary areas of the image sensor.

For a sighting with $V = 100$ gon, the maximum deviations of the horizontal angle ϵ_{Hz} approximately correspond to the maximum

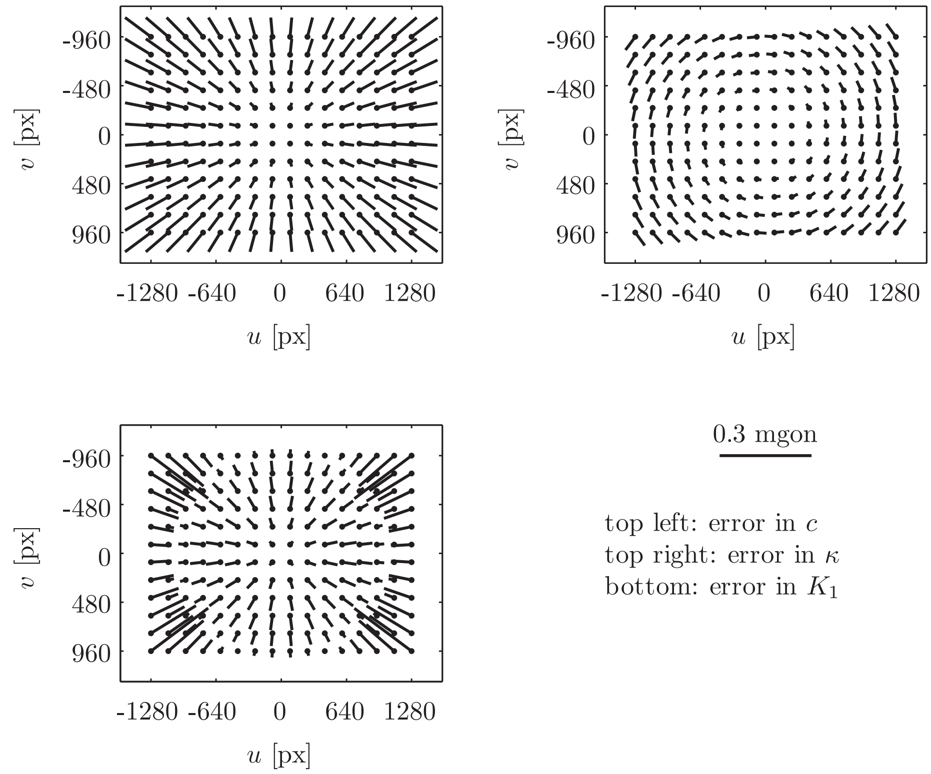

Figure 4.1: Deviations of the measured angles caused by errors in the calibration parameters for $V = 100\,\mathrm{gon}$ and different positions of the target on the image sensor.

deviations of the vertical angle ϵ_{V}. Except for the deviations caused by errors in u_0 and v_0, the ratio between ϵ_{Hz} and ϵ_{V} is $4/3$ for $V = 100\,\mathrm{gon}$ which corresponds to the ratio of the image sensor size of 2560/1920.

Figure 4.2 further shows that the deviations ϵ_{V} of the measured vertical angle caused by errors in the calibration parameters are roughly constant for different values of the vertical angle V itself. On the contrary, the deviations ϵ_{Hz} of the measured horizontal angle depend on the vertical angle of the telescope.

This can be explained by investigating the relation between im-

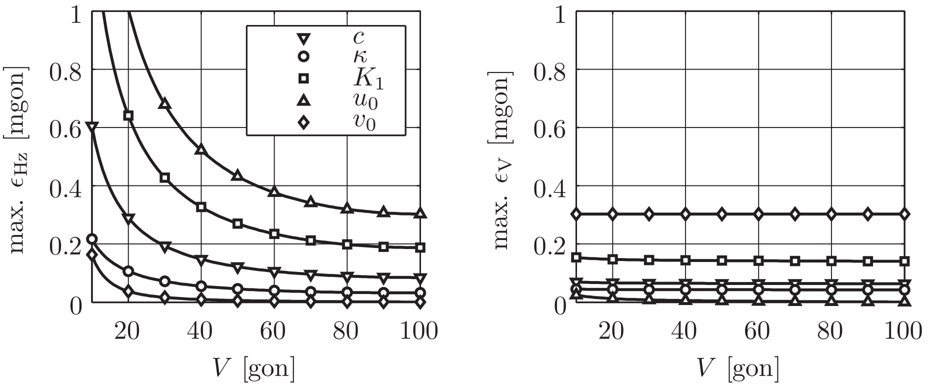

Figure 4.2: Maximum deviations ϵ_{Hz} (left) and ϵ_{V} (right) of the measured theodolite angles caused by errors in the calibration parameters for different vertical angles V and positions of the target on the image sensor.

age coordinates and theodolite angles (cf. Chapter 6). For simplicity, the approximation

$$Hz_{\mathrm{T}} = Hz + \arctan\frac{u}{c\sin V} \tag{4.1}$$

$$V_{\mathrm{T}} = V + \frac{v}{c} \tag{4.2}$$

of Bürki et al. (2010) is used. Hereby, u and v are the corrected image coordinates which include the calibration parameters κ, K_1, u_0 and v_0 after Eq. (6.27).

The effects of errors in the calibration parameters can be evaluated with the partial derivatives of Eqs. (4.1) and (4.2) w.r.t. the corresponding parameter. For c, this is exemplarily done by

$$\frac{\partial Hz_{\mathrm{T}}}{\partial c} = -\frac{u\sin V}{c^2\sin^2 V + u^2} \overset{c\gg u}{\approx} -\frac{u}{c^2\sin V} \tag{4.3}$$

$$\frac{\partial V_{\mathrm{T}}}{\partial c} = -\frac{v}{c^2} \tag{4.4}$$

in which it is again noted that the other calibration parameters are included in u and v.

It results from Eq. (4.4) that an error in c demonstrates its effect on the measured vertical angle independently of the vertical angle itself which is confirmed by Figure 4.2 (right). It is hereby noted that Eqs. (4.1) and (4.2) are approximations which only yield accurate results for moderate vertical angles (Ehrhart and Lienhart 2017a). Accordingly, slight changes of ϵ_{V} are visible in Figure 4.2 (right) which was generated by using the thorough mapping relations (cf. Chapter 6).

Eq. (4.3) demonstrates that the deviations in the measured horizontal angle due to an error in c (and also due to errors in the other parameters) depend on the telescope's vertical angle V. This is also illustrated in Figure 4.2 (left).

Conclusions

It is again noted that the deviations in the measured angles shown in Figure 4.1 and 4.2 result from using the fivefold value of the standard deviation of the respective parameters as errors. Furthermore, Figure 4.2 shows the maximum deviations which occur for targets observed in the boundary area of the image sensor.

When using the single standard deviation of the calibration parameters as errors, the maximum deviations of Figure 4.2 are smaller than 0.1 mgon for vertical angles V between 30 and 170 gon. An exception is ϵ_{Hz} caused by an error in u_0. However, when using two-face measurements the principal point (u_0, v_0) cancels out (Section 6.3.3) and errors in its calibrated values do not affect the measured angles.

4.2.2 Warm-up effects

The change of the measurement values due to a change of the instrument temperature are a well-studied topic for IATSs (Walser 2004, pp. 25ff; Wasmeier 2009, pp. 73ff; Knoblach 2011, pp. 117ff; Zhou et al. 2016). The changes of the measurement values caused by a self-heating of the instrument after switching on are known as warm-up effects and are investigated in this section.

The image-based angle measurements of an IATS result from the measurements of three individual sensors, namely the angle encoders, the tilt compensator and the image sensor (cf. Sections 6.1 and 7.1). Each of these sensors is potentially affected by warm-up effects and a separation of the individual effects is hard to establish in practice (Wasmeier 2009, p. 78). However, for practical use, the warm-up effects of the system IATS, i.e., the change of the image-based angle measurements due to a self-heating of the instrument, are of interest.

For a *Leica MS60* (Section 1.4), the warm-up effects were evaluated in the temperature-controlled laboratory of IGMS. The constant temperature (20°C) of the laboratory ensures that only variations of the measurements caused by a self-heating of the instrument are observed. In preparation for the experiment, the switched-off IATS was acclimatized to the ambient temperature of the laboratory for over 12 hours. For a stable setup of the IATS and the target which were both mounted on measurement pillars decoupled from the building, consecutive measurements were executed immediately after switching on the IATS. Hereby, the target was observed under a horizontal sighting ($V = 100\,\text{gon}$). The measurements were taken for over 3 hours in which the telescope face was changed after each measurement.

The variation of the angle measurements and the increase of the internal temperature, which is measured on the mainboard of the instrument, due to a self-heating of the IATS after switching on are shown in Figure 4.3. The depicted variations refer to a distance of 6.1 m between the IATS and the target.

The single-face measurements show strong variations of up to 0.8 mgon in which a similar behavior was observed by Zhou et al. (2016) for the *Leica MS50*, i.e., the predecessor of the *Leica MS60* which was used in Figure 4.3. It is noted that the depicted warm-up effects are no IATS-specific errors but also occur for con-

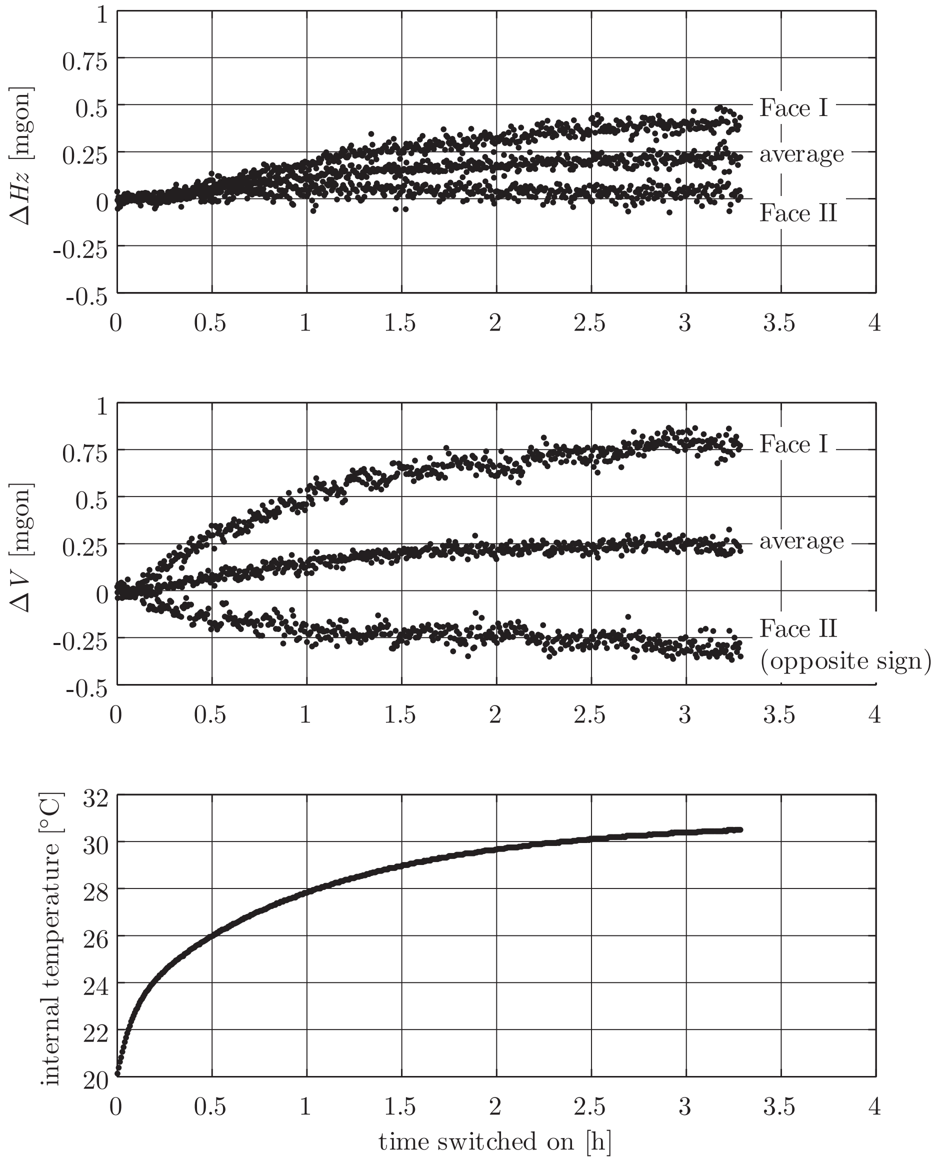

Figure 4.3: Variations of the image-based angle measurements to a target at 6.1 m caused by a self-heating of the IATS after switching on (data from Ehrhart and Lienhart 2017a).

ventional automated angle measurements towards retroreflective prisms (Flach and Naterop 1999) and also for other theodolite-based measurement systems such as surveying gyros (cf. Grillmayer 2003, pp. 86ff.). It is emphasized that the depicted variations are exclusively caused by a self-heating of the instrument and that for changes of the ambient temperature much larger variations can occur (Brunner and Grillmayer 2002; Grillmayer 2003, p. 127).

Wasmeier (2009, pp. 73ff.) discusses the warm-up effects of the *individual* sensors of an IATS that lead to the *combined* variations of the image-based angle measurements depicted in Figure 4.3. Hereby, temperature-induced changes of the theodolite axes errors are mentioned. Furthermore, temperature-induced zero point changes of the tilt compensator are reported by Hennes (2003). However, these effects cancel out for the face-averages of the measurements which is not the case in Figure 4.3.

Therefore, the height change of the IATS is computed from the face-averages of the vertical angles and the measured slope distance. Hereby, the target height is assumed to be constant for the stable setup in the temperature-controlled laboratory. In Figure 4.4 the height changes are displayed w.r.t. the instrument temperature (Figure 4.4 left) and w.r.t. the time since switching the instrument on (Figure 4.4 right). Additionally to the data from Figure 4.3 which results from measurements to a target at a distance of 6.1 m, the results from a second experiment with a distance of 1.5 m towards the target are displayed. Furthermore, the results from a third experiment (distance of 6.1 m towards the target), in which three two-face measurements were conducted immediately after switching on the instrument and after about three hours, are depicted. In between, the instrument was switched on but no measurements were performed and the IATS's motor was not used.

What can be observed is that the height change of the IATS due to a self-heating after switching on is a repeatable effect in which the height increases by less than 0.03 mm. At this, the instrument temperature increases by about 10°C from 20°C, which corresponds

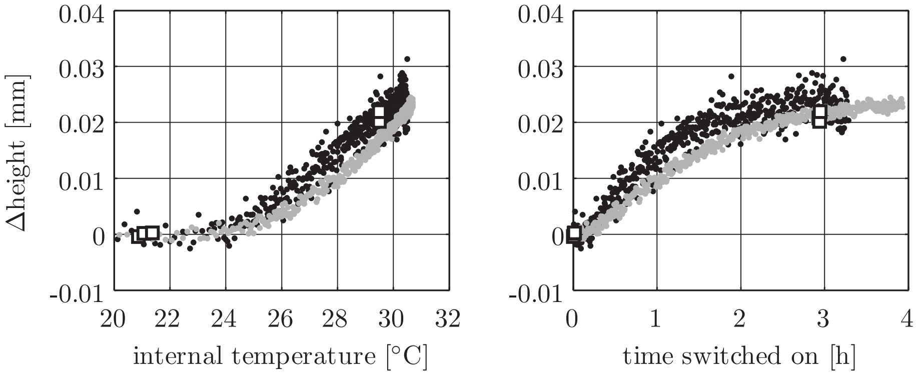

Figure 4.4: Height change of the IATS caused by a self-heating after switching on for different setups with distances of 6.1 m (black dots and white squares) and 1.5 m (gray dots) towards the target.

to the ambient temperature of the laboratory, to 30°C. Hereby, no noticeable difference can be observed for different measurement programs, e.g. consecutive measurements or measurements only in selected epochs (compare the white squares to the dots in Figure 4.4). Accordingly, it can be concluded that the major part of the self-heating is caused by the IATS's internal computer. However, it is emphasized that these values are valid for the conducted experiments with an ambient temperature of 20°C and that the response of the IATS may differ for other ambient temperatures.

Figure 4.4 further shows that, after a dead time of about 20 minutes, the height of the IATS increases almost linearly with the instrument temperature. The sensor for measuring the instrument temperature is located on the mainboard of the IATS and reacts to temperature changes more quickly than the other components of the IATS's alidade which react to temperature changes with a certain latency.

Compared to the height change of the IATS (Figure 4.4), the lateral displacements of the IATS caused by a self-heating of the instrument cannot be evaluated repeatably for different distances. This is because a warming of the instrument also causes a slight torsion of the IATS's alidade which demonstrates its effect in dependence of the distance. However, it is mentioned that the warm-up effects on the face-averaged horizontal angle are in the same order of magnitude as the temperature-induced variations of the vertical angle (cf. Figure 4.3). The displacements of the IATS's alidade caused by a self-heating of the instrument were also found by Wasmeier (2009, p. 77) for an IATS prototype.

Conclusions

As for conventional total stations or other measurement systems based on theodolites such as surveying gyros, the image-based angle measurements of an IATS vary with temperature changes caused by a self-heating of the instrument. Hereby, the single-face measurements show strong variations of almost 1 mgon.

For two-face measurements, which are employed for applications with high accuracy demands, the warm-up effects are much smaller. However, for highest accuracy demands, the displacements of the IATS's alidade of a few 0.01 mm caused by the self-heating of the instrument after switching on must be considered by accounting for a warm-up time of at least one hour.

It is emphasized that the temperature-induced variations of the angle measurements discussed in this section are exclusively caused by a self-heating of the instrument. For temperature differences between the storage and the working environment, an additional warm-up time must be considered (e.g. 2 min/°C but at least 15 min, cf. Leica 2015a, p. 55). Furthermore, changes in the ambient temperature of the working environment must be taken into account. For e.g. monitoring applications, this can be achieved by observing stable reference points (cf. Section 2.5.2).

4.2.3 Target specific errors

The image-based angle measurements of an IATS result from the image coordinates of the target which are measured on the IATS's image sensor. Hereby, the observed 3D real-world object is projected to the 2D image sensor (cf. Section 6.2.3). Target specific errors result from a mismatch between the computed direction to the target on the image sensor and the actual direction to the corresponding real-world target.

For circular or blob-shaped targets, the direction refers to the circle center and the centroid of the blob, respectively. Corners, which are also frequently used as visual targets, can be interpreted as the intersection of two lines in which the direction refers to the intersection point.

Edge detector offset

Figure 4.5 depicts a target marking of the Invar tooling bar used in Section 4.3. Its center is defined as the intersection point of the lines l_1 to l_8. For detecting these lines or edges, different strategies exist in which the most frequently used methods are based on the first or second derivative of the image (Gonzalez and Woods 2002, pp. 572ff.). For targets with strong intensity variations between the target and the background, such as the white target on a black background in Figure 4.5, a threshold image (Gonzalez and Woods 2002, pp. 595ff.) can be used for edge detection.

Edge detectors based on the first derivative of the image compute the magnitude of the image gradient (Gonzalez and Woods 2002, p. 577) by

$$\triangledown f = \left(\left(\frac{\partial I}{\partial u} \right)^2 + \left(\frac{\partial I}{\partial v} \right)^2 \right)^{1/2} \tag{4.5}$$

in which $\partial I / \partial u$ and $\partial I / \partial v$ denote the partial derivatives of the image I in u- and v-direction. Edge detectors based on the second derivative compute the Laplacian (Gonzalez and Woods 2002, p. 581)

$$\triangledown^2 f = \frac{\partial^2 I}{\partial u^2} + \frac{\partial^2 I}{\partial v^2} \tag{4.6}$$

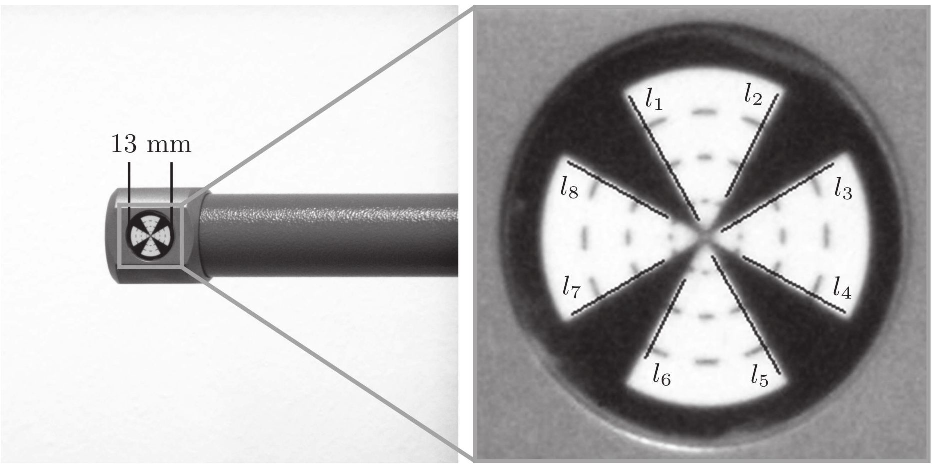

Figure 4.5: Telescope camera image of Invar tooling bar with center defined as intersection of lines (image data after Ehrhart and Lienhart 2017a).

of the image. Hereby, the second-order partial derivatives $\partial^2 f/\partial u^2$ and $\partial^2 f/\partial v^2$ of the image I are used. The first- and second-order partial derivatives can be efficiently computed by a convolution of the image with dedicated kernel masks (Krig 2014, p. 66).

The thresholding of an image (Gonzalez and Woods 2002, pp. 595ff.) comprises an analysis of the intensity values of the image. For an 8-bit grayscale image, each pixel can take an intensity value between 0 and 255. For a given threshold t, the threshold image J of the original image I is computed from (Gonzalez and Woods 2002, p. 596)

$$J(u,v) = \begin{cases} 1 & \text{if } I(u,v) > t \\ 0 & \text{if } I(u,v) \le t \end{cases} \tag{4.7}$$

which results in a binary image with values 1 (white) and 0 (black).

Figure 4.6 depicts the results of the mentioned image processing techniques on the original image (detail of Figure 4.5). The magnitude of the gradients clearly points out the edges (black regions in Figure 4.6a) but does not provide a sharp representation of these edges. The zero values of the Laplacian (white regions in Fig-

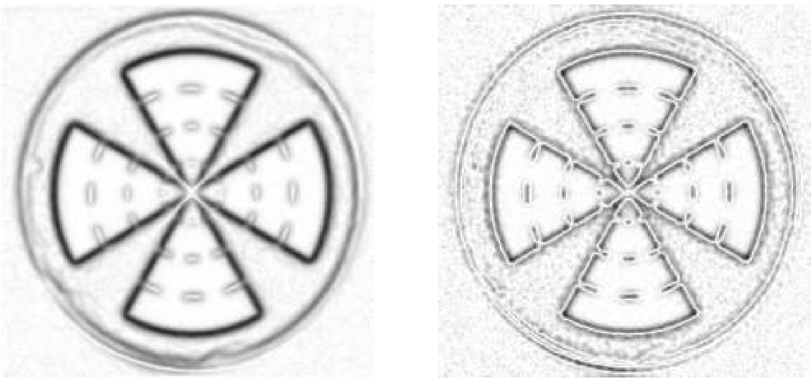

(a) magnitude of image gradients with large values shown in black

(b) absolute values of Laplacian with large values shown in black

(c) threshold of $t = 170$

(d) threshold of $t = 200$

Figure 4.6: Different image processing strategies for edge detection.

ure 4.6b) provide a sharp representation of the edges but the result is more sensitive to image noise because of the double-differentiation in Eq. (4.6). The theory of these effects is described by e.g. Gonzalez and Woods (2002, pp. 572ff.).

The threshold images shown in Figure 4.6c and 4.6d vary dependent on the set threshold t, cf. Eq. (4.7). Accordingly, also the detected lines, which are used to compute the center of the target, can be shifted from the true edge of the real-world target (cf.

Figure 4.5 right).

If e.g. only the lines l_1 and l_3 of Figure 4.5 were intersected to compute the target center, the detected center would differ from the center of the real-world target. Consequently, this would result in a mismatch between the computed direction to the target on the image sensor and the actual direction to the corresponding real-world target.

When using all lines l_1 to l_8 of the target shown in Figure 4.5 for computing the intersection point by a least-squares adjustment, the depicted edge detector offset does not influence the result because of the symmetric target design. However, for asymmetric targets or targets which are based on two edges only, the edge detector offset must be taken into account by appropriate image processing such as the computation of the Laplacian, cf. Eq. (4.6).

Ellipse center offset

Real-world circular targets, which are frequently used for image-based measurements, are represented by their circle center. Due to the perspective projection, the circles are observed as ellipses on the image sensor (Davies 2012, p. 460).

The ellipse center can be computed by an iterative solving of the corresponding Gauss-Helmert-Model (Lösler and Nitschke 2010) or by a computationally efficient direct solving of an eigensystem (Fitzgibbon et al. 1996). Hereby, the contour of the observed ellipse, which can be found by one of the image processing techniques illustrated in Figure 4.6, forms the basis of the computations.

For a non-parallelism of the target plane and the image sensor plane, which must be assumed as the general case, the center of the detected ellipse does not correspond to the center of the real-world circular target (Dold 1996; Ahn et al. 1999; Luhmann 2014). This effect is illustrated in Figure 4.7 for a circular target used in Section 4.3.

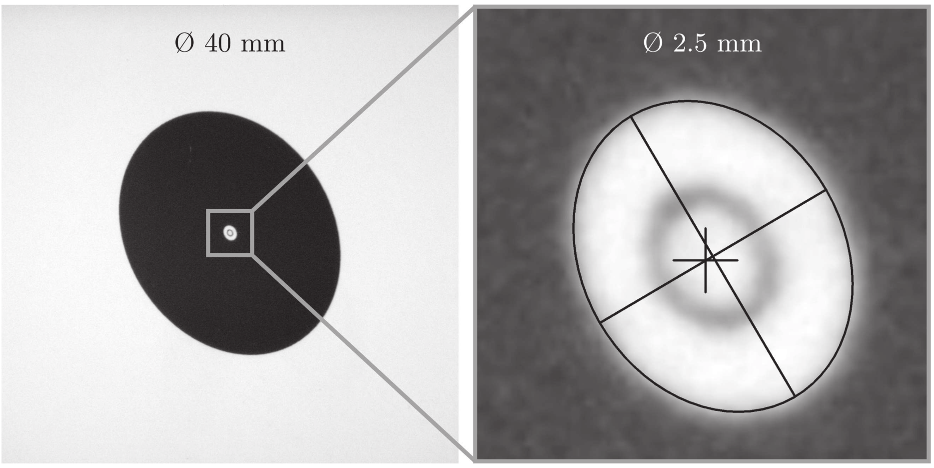

Figure 4.7: Ellipse center offset for a circular target observed under a skew angle. The ellipse center estimated from the large black circle (cross) deviates from the ellipse fit to the small white circle (image data after Ehrhart and Lienhart 2017a).

The estimated center of the large black ellipse (indicated by a cross in Figure 4.7 right) is shifted from the circle center by

$$\epsilon = \frac{b^2}{d_{\mathrm{vl}}} \tag{4.8}$$

(Davies 2012, p. 460). Hereby, b denotes the semiminor axis of the ellipse and d_{vl} corresponds to the distance of the ellipse center to the vanishing line of the target plane. For the exemplarily depicted case of Figure 4.7, the ellipse center offset amounts to 1.3 px which corresponds to a deviation of 0.8 mgon between the directions to the observed and to the real-world target.

The vanishing line results from intersecting the image plane π_{image} with the target plane π_{target} shifted towards the camera center (cf. Figure 4.8 or Hartley and Zisserman 2004, p. 217). These two planes, expressed in the 3D camera system (cf. Sections 6.2.3 and 6.2.4), are represented by

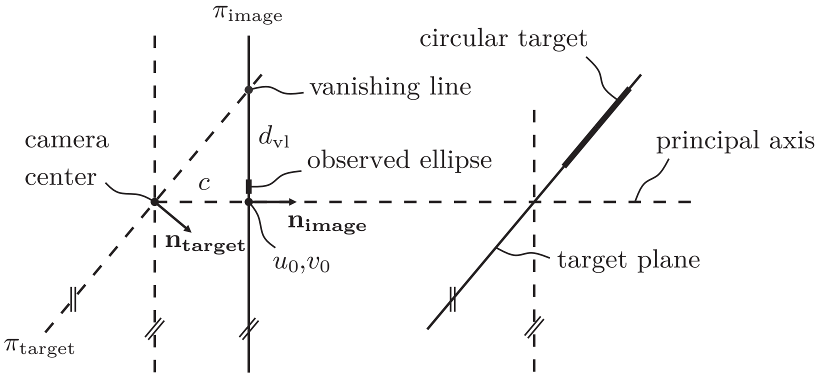

Figure 4.8: Vanishing line of a target plane on the image sensor (after Ehrhart and Lienhart 2017a).

$$\pi_{\text{image}}: \quad \mathbf{n_{image}} \cdot \mathbf{x} - c = 0 \tag{4.9}$$

$$\pi_{\text{target}}: \quad \mathbf{n_{target}} \cdot \mathbf{x} = 0 \tag{4.10}$$

in which

$$\mathbf{n_{image}} = \begin{bmatrix} 1 & 0 & 0 \end{bmatrix}^T \tag{4.11}$$

and c denotes the camera constant (cf. Section 6.2.3)

Analogously to Section 2.3.2, the normal vector of the target plane can be obtained by a plane fit to a plurality of 3D points which are measured on the surface of the target plane. However, the resulting normal vector refers to the theodolite system (Section 6.2.5) and needs to be transformed to the camera system by

$$\mathbf{n_{target}} \approx \mathbf{R^T}\, \mathbf{n_{target}^{(theodolite)}} \tag{4.12}$$

in which $\mathbf{R}$ results from Eq. (6.16) and the small differences between the camera and the telescope system can be neglected for the telescope cameras of the evaluated IATSs (cf. Sections 6.2.4 and 6.3).

The direction vector of the vanishing line in the 3D camera system is obtained from

$$\mathbf{v} = \mathbf{n_{target}} \times \mathbf{n_{image}} = \begin{bmatrix} 0 & n_{\text{target},z} & -n_{\text{target},y} \end{bmatrix}^T \tag{4.13}$$

and a point on the 3D vanishing line can be computed from

$$\mathbf{p} = \begin{cases} \begin{bmatrix} c & 0 & -c\, n_{\text{target},x}/n_{\text{target},z} \end{bmatrix}^T & \text{if } |n_{\text{target},z}| > |n_{\text{target},y}| \\ \begin{bmatrix} c & -c\, n_{\text{target},x}/n_{\text{target},y} & 0 \end{bmatrix}^T & \text{otherwise} \end{cases} \tag{4.14}$$

The image-based measurements refer to the 2D image sensor with image coordinates u and v (Section 6.2.3). Accordingly, the vanishing line l also needs to be expressed in the 2D image system by

$$l: \quad \mathbf{n} \cdot \begin{bmatrix} u & v \end{bmatrix}^T - d = 0 \tag{4.15}$$

with

$$\mathbf{n} = \begin{bmatrix} -n_{\text{target},y} & n_{\text{target},z} \end{bmatrix}^T / \sqrt{n^2_{\text{target},y} + n^2_{\text{target},z}} \tag{4.16}$$

$$d = \mathbf{n} \cdot \mathbf{q} \tag{4.17}$$

$$\mathbf{q} = \begin{bmatrix} p_y & -p_z \end{bmatrix}^T \tag{4.18}$$

in which **n** and **q** result from **v** and **p** given by Eqs. (4.13) and (4.14) considering the opposite sign of the v- and z-direction of the image and the camera system, respectively (cf. Section 6.2.3).

The distance of the detected ellipse center to the vanishing line of the target plane results from

$$d_{\text{vl}} = \mathbf{n} \cdot \begin{bmatrix} u_{\text{ellipse}} & v_{\text{ellipse}} \end{bmatrix}^T - d \tag{4.19}$$

which can be used to evaluate Eq. (4.8). Hereby, the semiminor axis b of the ellipse also results from the ellipse fit.

Finally, the corrected image coordinates of the ellipse center are obtained from

$$\begin{bmatrix} u_{\text{ellipse,corr}} \\ v_{\text{ellipse,corr}} \end{bmatrix} = \begin{bmatrix} u_{\text{ellipse}} \\ v_{\text{ellipse}} \end{bmatrix} - \epsilon\,\mathbf{n} \qquad (4.20)$$

Considering the large value of d, which is caused by the large value of c (about 105000, cf. Section 7.4) in Eq. (4.14) and consequently in Eq. (4.18), it is uncritical whether the corrections of Section 6.2.2 are applied to u_{ellipse} and v_{ellipse} before or after evaluating Eqs. (4.19) and (4.20).

Conclusions

Target specific errors, i.e., a mismatch between the computed direction to the target on the image sensor and the actual direction to the corresponding real-world target, occur for circular targets and corners which are both frequently used for image-based measurements. The edge detector offset, which causes errors in the image-based measurements to corners, can be avoided by a symmetric target design or by choosing appropriate image processing methods. The ellipse center offset, which affects the image-based measurements to circular targets, can be corrected with knowledge of the relative orientation of the target plane to the image plane. It is noted that the described errors also occur for least-squares matching where the direction to the target is found based on a template, e.g. a corner or a disc, of the corresponding target (Walser 2004, pp. 76ff.).

For monitoring applications (Chapter 2), in which the targets are observed from similar viewing directions in each epoch, target specific errors have negligible effects because their systematic behavior cancels out when computing the differences between the individual epochs. However, for applications in which the targets are observed from different viewing directions, such as measurements in a geodetic network (cf. Section 4.3), the target specific errors must be taken into account for achieving highly accurate results.

4.3 EXPERIMENTAL MEASUREMENTS

The suitability of a state-of-the-art IATS (*Leica MS60*, cf. Section 1.4) for high-precision measurements was evaluated by establishing a small-scale 3D geodetic network in the laboratory of IGMS. As mentioned in Section 2.2.1, the accuracy of the distance measurement is much lower than the accuracy of the image-based angle measurements. Accordingly, the geodetic network was established by a pure triangulation.

By using an IATS prototype, Guillaume et al. (2012) performed similar measurements for the determination of highly accurate 3D coordinates under controlled indoor conditions. The IATS prototype was a clip-on system (cf. Section 1.3.1) in which the eyepiece of a *Leica TDA 5005* industrial total station was replaced by a camera. The used total station is specified with a precision of 0.15 mgon for the angle measurements which was empirically confirmed for the image-based angle measurements of the IATS (Guillaume et al. 2012). Based on IATS measurements in a micro-triangulation network with three instrument positions, the 3D coordinates of selected targets in a volume of $1\,\mathrm{m} \times 4\,\mathrm{m} \times 1\,\mathrm{m}$ could be determined with standard deviations of better than 0.01 mm (1σ) in all coordinate directions. The scale of the geodetic network was fixed by using a known reference length (measured by a coordinate measurement machine) and the targets were embodied as illuminated ceramic spheres.

In this section, the usage of a commercially available state-of-the-art IATS for high-precision measurements is evaluated. Hereby, simple printouts of circles are used as targets and the measurements are carried out by only using standard measurement equipment (e.g. no coordinate measurement machine). Another goal of this section is to evaluate the accuracy of the image-based angle measurements of the *system* IATS which comprises different measurement sensors and data processing steps (cf. Section 4.3.2).

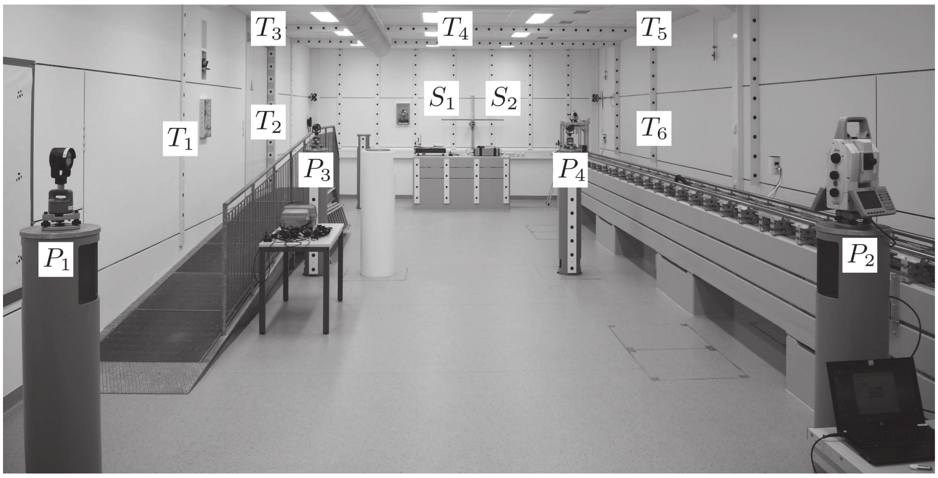

Figure 4.9: Measurement site with instrument positions P, targets T and markings of the reference scale S.

4.3.1 Experimental setup

The experimental 3D geodetic network measurements were carried out in the laboratory of IGMS. Hereby, the 3D coordinates of selected targets of the calibration field for photogrammetric cameras (Figure 4.9) should be determined with a high accuracy. The targets are represented by circles with a diameter of 40 mm (cf. Figure 4.7) and the selected targets are distributed over a volume of 6.3 m × 4.9 m × 1.5 m. The scale of the geodetic network was determined by measurements towards the markings of an Invar tooling bar (cf. Figure 4.5) with an accurately known length (1.308129 m ± 2 µm).

The used IATS *Leica MS60* is specified with a precision of 0.3 mgon for the angle measurements and with 0.15 mgon for the readings of the tilt compensator (cf. Section 1.4). After a sufficient warm-up time of 1.5 hours (cf. Section 4.2.2), four sets of angles towards the targets T and the markings of the reference scale S were measured at each instrument position P. It is noted that the retroreflective prisms at the positions P_1, P_3 and P_4 in Figure 4.9

Table 4.2: Parameters of the geodetic network adjustment

instrument positions:	**4**	
targets:	**8**	6 circular targets
		2 markings of Invar tooling bar
observations:	**65**	$4 \cdot 8 = 32$ horizontal angles
		$4 \cdot 8 = 32$ vertical angles
		1 distance (Invar tooling bar)
unknowns:	**40**	$4 \cdot 3 = 12$ coordinates of instrument positions
		$8 \cdot 3 = 24$ coordinates of targets
		4 orientations (at instrument positions)
datum deficiency:	**4**	3 translations of network
		1 horizontal rotation of network
degree of freedom:	**29**	$= 65 - 40 + 4$

are not used for the present experiment. It is further noted that the measurement data is the same as in Ehrhart and Lienhart (2017a). However, an additional instrument position located in the center of P_1 to P_4 is omitted here.

The image-based angle measurements towards the circular targets of the calibration field were corrected by the ellipse center offset (cf. Section 4.2.3). The measured image coordinates of the circular targets and the markings of the reference scale were related to theodolite angles by using the focus-dependent calibration parameters of Section 7.4. In the network adjustment, only the target points T_1 to T_6 were used to define the datum. This is because the instrument positions P and the markings of the scale S have no physical representation after the IATS or the temporarily installed Invar tooling bar are removed from their positions. Further parameters of the geodetic network adjustment are given in Table 4.2.

Table 4.3: Empirical standard deviations (1σ) for horizontal ($\tilde{s}_{\mathrm{Hz}}$) and vertical ($\tilde{s}_{\mathrm{V}}$) image-based angle measurements resulting from four measured sets of angles at each instrument position

Instrument position	$\tilde{s}_{\mathbf{Hz}}$ **[mgon]**	$\tilde{s}_{\mathbf{V}}$ **[mgon]**
P_1	0.06	0.04
P_2	0.05	0.05
P_3	0.02	0.03
P_4	0.03	0.02
average	0.04	0.04

4.3.2 Results

Set of angles and variance component estimation

The results of the adjustment of the four sets of angles measured at each instrument position are given in Table 4.3. On average, the empirical standard deviations of the horizontal and vertical image-based angle measurements both result in 0.04 mgon. Regarding the specified standard deviation of the IATS's angle measurements of 0.3 mgon (Leica 2015a, p. 64), this is a remarkable result.

However, as discussed by Ehrhart and Lienhart (2017a), the empirical standard deviations resulting from the adjustment of sets of angles provide values for the measurement *precision*. The *accuracy* of the measurements cannot be qualified by sets of angles because systematic errors, such as target specific errors (Section 4.2.3) or errors in the calibration parameters (Section 4.2.1), cannot be detected by repeated measurements. To obtain an estimate for the measurement accuracy, redundant measurements, such as the measurements in a geodetic network, are required.

Therefore, the geodetic network was initially adjusted to determine the standard deviations of the image-based angle measurements by a variance component estimation (Niemeier 2008, pp. 318ff.). The results are given in Table 4.4 whereat it is mentioned

Table 4.4: Empirical standard deviations (1σ) and degrees of freedom for horizontal (s_{Hz} and f_{Hz}) and vertical (s_{V} and f_{V}) image-based angle measurements resulting from variance component estimation

s_{Hz} [mgon]	s_{V} [mgon]	f_{Hz} [ ]	f_{V} [ ]
0.04	0.07	8.586	20.414

that similar values for s_{Hz} and s_{V} also result from the measurements presented in Section 7.5 (about 0.06 mgon, cf. Table 7.3).

The degrees of freedom f_{Hz} and f_{V} are computed during the variance component estimation by (Niemeier 2008, p. 324)

$$f_{\mathrm{Hz}} = \sum r_{\mathrm{Hz},i} \tag{4.21}$$

$$f_{\mathrm{V}} = \sum r_{\mathrm{V},i} \tag{4.22}$$

in which $r_{\mathrm{Hz},i}$ and $r_{\mathrm{V},i}$ are the redundancies of the individual observations. It is pointed out that the degrees of freedom are no integer values (cf. Table 4.4). This is because *Hz* and *V* are jointly used to determine the 3D coordinates of the markings of the Invar tooling bar in the adjustment which introduces the scale of the geodetic network. However, $f_{\mathrm{Hz}} + f_{\mathrm{V}} = 29$ which corresponds to the degree of freedom of the network adjustment (cf. Table 4.2). It is noted that the redundancy of the length of the Invar tooling bar is zero because this observation is not controlled for the configuration of the geodetic network (cf. Section 4.3.1).

Numerically, s_{Hz} and s_{V} are obviously different (cf. Table 4.4). A statistical test according to (cf. Niemeier 2008, pp. 110f.)

$$\begin{array}{ll}
\mathrm{H}_0 \ : \ s_{\mathrm{Hz}} = s_{\mathrm{V}} & \\
\mathrm{H}_{\mathrm{A}} \ : \ s_{\mathrm{Hz}} \neq s_{\mathrm{V}} & \\
F = s_{\mathrm{V}}^2 / s_{\mathrm{Hz}}^2 & \\
F_{f_{\mathrm{V}},f_{\mathrm{Hz}},\alpha/2} \leq F \leq F_{f_{\mathrm{V}},f_{\mathrm{Hz}},1-\alpha/2} & \Rightarrow \text{do not reject } \mathrm{H}_0 \\
\text{otherwise} & \Rightarrow \text{reject } \mathrm{H}_0
\end{array}$$

shows that s_{Hz} and s_{V} cannot be regarded as significantly different on a 95% confidence level ($\alpha = 0.05$) because $F = 2.634$ is between the values $F_{f_{\mathrm{V}},f_{\mathrm{Hz}},\alpha/2} = 0.351$ and $F_{f_{\mathrm{V}},f_{\mathrm{Hz}},1-\alpha/2} = 3.786$ of the F-distribution. It is noted that the involved computations were performed with double precision whereas rounded values are given in the text.

The standard deviations $\tilde{s}_{\mathrm{Hz}}$ and $\tilde{s}_{\mathrm{V}}$ resulting from the adjustment of the sets of angles (Table 4.3) refer to a single two-face measurement. The standard deviations s_{Hz} and s_{V} resulting from the variance component estimation in the geodetic network (Table 4.4) refer to the average of four two-face measurements because four sets of angles were measured at each instrument position (Section 4.3.1). Accordingly, s_{Hz} and s_{V} are expected to be smaller than $\tilde{s}_{\mathrm{Hz}}$ and $\tilde{s}_{\mathrm{V}}$ by a factor $\sqrt{4}$ which is not the case.

The $\sqrt{n}$-law (cf. Niemeier 2008, pp. 53f.) is only valid for normally distributed measurements. Considering the specified standard deviation of the IATS's angle measurements (0.3 mgon, cf. Leica 2015a, p. 64) and the setting accuracy of the tilt compensator (0.15 mgon, cf. Leica 2015a, p. 80), measurements of less than 0.1 mgon probably include quantification artifacts and cannot be regarded as normally distributed. This is confirmed by the fact that using only one set of angles (instead of all four sets of angles) at each instrument position in the geodetic network adjustment results in estimates for s_{Hz} and s_{V} which are similar to the values given in Table 4.4.

Accordingly, it is concluded that three sets of angles are a reasonable choice for geodetic network measurements with an IATS under controlled environmental conditions. This provides the possibility to detect and identify gross errors in the observations while retaining a reasonable effort for conducting the measurements. Under controlled environmental conditions and for a stable setup of the IATS and the targets, more than three sets of angles do not noticeably improve the precision of the averaged angles.

However, the estimated standard deviations for horizontal and vertical image-based angle measurements of less than 0.1 mgon (1σ, cf. Tables 4.3 and 4.4) provide an estimate for the quality of the measurements with the *system* IATS which include

- the readings of the angle encoders,
- the readings of the tilt compensator,
- the mapping of the real world to the image sensor,
- the digital image processing for target detection which is potentially affected by target specific errors, and
- the relation of image coordinates to theodolite angles which is potentially affected by errors in the calibration parameters.

Effectively, the estimated standard deviations for horizontal and vertical image-based angle measurements with an IATS of less than 0.1 mgon (1σ) can be regarded as the final results of this chapter. These image-based angle measurements potentially show a better precision than conventional automated angle measurements to retroreflective prisms. For the evaluated instrument (*Leica MS60*, cf. Section 1.4), the automated angle measurements to prisms can also be regarded as image-based measurements and it is referred to Section 5.1.1 for a description of the operating principle. Although the image coordinates of the target are computed with a resolution of 0.01 px (Grimm and Hornung 2015), the involved image sensor has an angle per pixel of $\alpha_{\text{px}} = 3\,\text{mgon}$ (Lienhart et al. 2017) which is five times larger than α_{px} of the evaluated IATS's telescope camera ($\alpha_{\text{px}} = 0.6\,\text{mgon}$, cf. Section 1.4). Furthermore, systematic errors of several millimeters in the measured prism center can occur dependent on the orientation of the prism relative to the instrument (Lackner and Lienhart 2016; Lienhart 2017). Accordingly, especially the accuracy of the image-based measurements excels the accuracy of conventional automated angle measurements to retroreflective prisms.

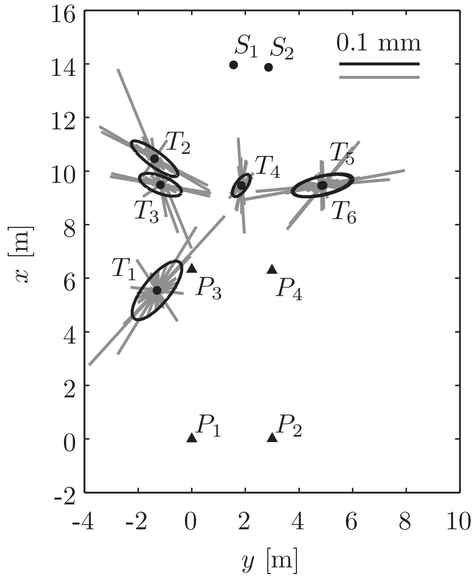

Figure 4.10: Network sketch with 95% confidence ellipses and external reliabilities ($\alpha_0 = 0.1\%$, $\beta_0 = 20\%$) of target points.

Adjustment of real measurements

To demonstrate the accuracy of the 3D coordinates gained from IATS measurements, the geodetic network was readjusted by using the standard deviations resulting from the variance component estimation (Table 4.4). Figure 4.10 and Table 4.5 provide data for an accuracy assessment of the target points T_1 to T_6.

The standard deviations with values around 0.01 mm in all coordinate directions are comparable to the results of Guillaume et al. (2012). However, an assessment of the accuracy is typically achieved by observing the semiaxes of the confidence ellipses (2D representation) or confidence ellipsoids (3D representation) and the external reliabilities (Niemeier 2008, pp. 304ff.) which are around 0.05 mm and 0.1 mm, respectively (cf. Table 4.5).

It is noted that the distance between the markings of the tooling bar, which is introduced with a standard deviation of 2 µm,

Table 4.5: Standard deviations s_x, s_y, s_z (1σ), semiaxes a, b, c of 95% confidence ellipsoids and maximum external reliability $\nabla\xi$ ($\alpha_0 = 0.1\%$, $\beta_0 = 20\%$) of target points

Target	[µm]						
Point	s_x	s_y	s_z	a	b	c	$\nabla\xi$
T_1	15	13	4	52	19	6	127
T_2	9	12	4	41	12	8	121
T_3	6	11	5	33	12	8	67
T_4	6	5	4	21	9	8	63
T_5	6	15	5	44	14	9	104
T_6	6	15	4	44	14	8	105

produces an external reliability of infinity because this distance cannot be controlled for the given measurement configuration (cf. Section 4.3.1). To overcome this limitation, at least one additional distance measurement needs to be introduced.

Geodetic network simulation

The accuracy of the estimated coordinates in a geodetic network depends on the precision of the measurements and on the geometry of the geodetic network. Once the precision of the measurement is known, the accuracy of the coordinates can be predicted from the confidence ellipses (2D network) or confidence ellipsoids (3D network) and the external reliabilities. Both quantities result from a geodetic network simulation which does not require real observations (Niemeier 2008, pp. 340f.).

This is exemplarily depicted in Figure 4.11 where an additional instrument position P_5 is introduced. Furthermore, the Invar tooling bar is replaced by two vertically aligned scales with the markings S_1, S_2 and S_3, S_4, respectively. The scales could be represented by Invar leveling staffs (also referred to as leveling rods) which are common measurement equipment in every surveyor's office. These staffs are available in different lengths, e.g. 3 m, and are marked

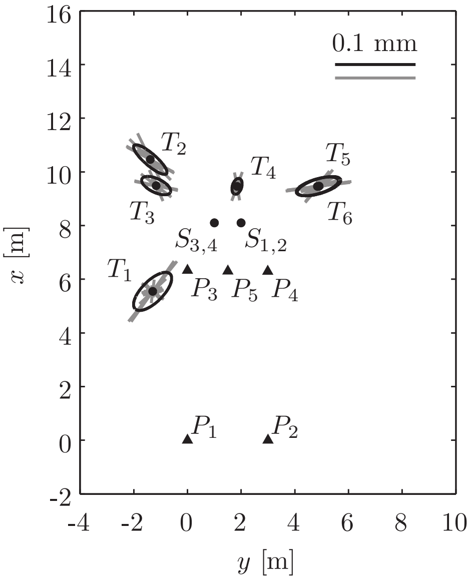

Figure 4.11: Network sketch with 95% confidence ellipses and external reliabilities ($\alpha_0 = 0.1\%$, $\beta_0 = 20\%$) of target points resulting from network simulation.

with visually prominent code elements over the entire length of the staff. For high-precision leveling staffs, the random errors of these code elements are less than 7 µm and the error in the scale factor is less than 1.2 ppm (Fischer and Fischer 1999). For further information on digital leveling systems cf. Woschitz (2003). Coded leveling staffs were also used by Wiedemann et al. (2017) for trigonometric leveling with an IATS.

The precisely known separations of the code elements of an Invar leveling staff can be used analogously to the markings of the Invar tooling bar (cf. Section 4.3.1). For the geodetic network simulation, the distances from S_1 to S_2 and from S_3 to S_4 were set to 2.8 m assuming the usage of a 3 m Invar leveling staff. The standard deviation of the distances was set to 0.01 mm which results from the maximum errors of the code elements (7 µm and 1.2 ppm, cf. Fischer and Fischer 1999) and the fact that two code elements are required to generate a reference length. The standard deviations

Table 4.6: Standard deviations s_x, s_y, s_z (1σ), semiaxes a, b, c of 95% confidence ellipsoids and maximum external reliability $\nabla\xi$ ($\alpha_0 = 0.1\%$, $\beta_0 = 20\%$) of target points resulting from network simulation

Target				[µm]			
Point	$\boldsymbol{s_x}$	$\boldsymbol{s_y}$	$\boldsymbol{s_z}$	$\boldsymbol{a}$	$\boldsymbol{b}$	$\boldsymbol{c}$	$\boldsymbol{\nabla\xi}$
T_1	10	10	3	36	15	5	49
T_2	8	8	3	31	10	7	36
T_3	5	7	4	24	10	7	29
T_4	4	3	3	13	7	6	20
T_5	5	11	4	32	11	7	41
T_6	5	11	3	32	11	7	42

of the horizontal and vertical angle measurements were set as in the adjustment of the real measurements (cf. Table 4.4).

Figure 4.11 and Table 4.6 depict the results of the geodetic network simulation. The semiminor axes of the 95% confidence ellipsoids and the maximum external reliabilities are smaller than 0.05 mm. Compared to the adjustment of the real measurements (Figure 4.10 and Table 4.5), especially the external reliabilities are smaller in the network simulation (Figure 4.11 and Table 4.6) which is due to the additional instrument position P_5. Furthermore, the introduction of a second reference scale in the network simulation allows the assessment of the external reliability which can be impacted by uncertainties in the scales.

4.4 CONCLUSIONS

Especially for small-scale geodetic networks under controlled environmental conditions, the highly accurate image-based angle measurements of an IATS can be used to establish reference frames with an accuracy of a few 0.01 mm for the 3D points. A thorough calibration of the used instrument and a sufficient warm-up time after switching on the IATS are prerequisites for a high accuracy of the 3D points. Furthermore, a deviation between the direction towards the center of the real-world target and the direction towards the target center resulting from image processing must be considered. This deviation occurs for circular targets and corner points in which correction strategies are available for both target types.

When accounting for all mentioned error sources, standard deviations of less than 0.1 mgon (1σ) are possible for horizontal and vertical image-based angle measurements with a state-of-the-art IATS. It is emphasized that this value results from a variance component estimation in a geodetic network. This provides a more reliably estimate for the quality of measurements than the standard deviations resulting from the adjustment of sets of angles. For the latter, systematic effects, such as an erroneous calibration or target specific errors, cannot be detected by the involved repeated measurements.

With pure angle measurements (triangulation) it is not possible to determine the scale of the geodetic network and measurements towards the end points of a reference scale, such as an Invar tooling bar with an accurately known length, are necessary. Another possibility to determine the scale of the network in practice is to use Invar leveling staffs which are common measurement equipment in every surveyor's office. These staffs are marked with visually prominent code elements with precisely known separations (Fischer and Fischer 1999). Measuring different code elements on the staff from different instrument positions allows the computation of their 3D coordinates. By using the known length between the code elements, the scale of the network can be determined. A state-of-the-art IATS and digital leveling staffs were experimentally used by Wiedemann et al. (2017) to perform trigonometric leveling. For two staffs separated by 22 m, the height difference of about 3.8 m was measured by a digital level and the IATS. The resulting height differences showed a deviation of about 0.25 mm. Under controlled environmental conditions, as for high-precision measurements in a small-scale geodetic network indoors, it can be assumed that this value can be outperformed.

Compared to the conventional automated angle measurements of a RTS to retroreflective prisms, an IATS offers several advantages. The repeatable accuracy of angle measurements with a RTS towards prisms, such as the standard deviation obtained from adjusting a set of angles, is probably better than the specified value (e.g. 0.3 mgon but at least 1 mm, cf. Leica 2015a, p. 68) and can be compared to the image-based angle measurements of an IATS. However, it was shown by Lackner and Lienhart (2016) and also by Lienhart (2017) that, dependent on the orientation of the prism relative to the RTS, errors of several millimeters in the measured prism center can occur – even when using special prisms dedicated to high-precision measurements. Although the center deviation is a systematic effect, a correction is hard to achieve in practice because it requires knowledge of the prism's orientation relative to the RTS. Aligning all prisms of a geodetic network with the sighting axis of the RTS for each instrument position is a cumbersome and time-consuming procedure. Furthermore, this introduces additional errors because of possible deviations between the prism center and the rotation center of the prism housing.

For image-based measurements towards visual targets, an offset between the real and the imaged target can be avoided by an appropriate target design or can be corrected automatically by measuring the orientation of the target plane relative to the sighting axis of the IATS. Another advantage of visual targets is that they can also be measured by other, e.g. tactile, measurement sensors which is not possible for retroreflective prisms because their coordinates refer to the inaccessible prism center.

5

Object tracking

5.1 INTRODUCTION

Most of today's RTSs offer the possibility of automated target tracking. Hereby, a retroreflective prism is locked by the RTS and is continuously followed so that the telescope is aligned with the prism center. This enables continuous measurements and the control of the instrument in one-person operation. Continuous measurements can be used for the steering of e.g. construction machinery where the 3D coordinates are continuously measured to enable a comparison between the actual and the planed position of the machine. For measurements in one-person operation, the RTS follows the moving prism which is carried by the operator so that measurements at selected points can be conducted immediately once the operator has positioned the reflector pole at the desired point. For both working modes, i.e., continuous measurements and one-person operation, the tracking of the prism involves the steps coarse search, fine aiming, and target identification (Ingensand and Böckem 1997; Ehrhart and Lienhart 2017b).

In this chapter, it is described and experimentally evaluated how the wide-angle camera of a state-of-the-art IATS (*Leica MS60*, cf. Section 1.4) can be used to speed up the coarse prism search and to provide a method for target identification. The basic idea is to use the image data of the wide-angle camera for visual object tracking while the prism tracking based on the fine aiming module is in operation. The maximum observable angle of the fine aiming module is typically referred to as field of view (FOV) whereas the designation angle of view (AOV) is used for the wide-angle and the telescope camera (cf. Section 1.3.1). Compared to the narrow FOV of the fine aiming module (1.6 mgon for the evaluated IATS, cf. Leica 2015a, p. 69), the AOV of the wide-angle camera is about 10-times larger (17.2 gon × 13.0 gon, cf. Table 1.6). Based on the results of the visual tracker, the telescope can be repositioned towards the prism once the tracker of the fine aiming module fails. This enables a fast continuation of the prism-based tracking with the fine aiming module. Furthermore, the color image data of the wide-angle camera also provides possibilities for target identification.

Related publications

This chapter is based on the article of Ehrhart and Lienhart (2017b) which includes color instead of grayscale images.

5.1.1 State-of-the-art tracking techniques

For the automated tracking of a prism, the state-of-the art IATS (*Leica MS60*, cf. Section 1.4) evaluated in this chapter includes a fine aiming module based on an image sensor. The technology is denoted as *automatic target recognition* (ATR) for total stations produced by *Leica Geosystems AG* (Leica 2015a). In contrast to the telescope camera, the image sensor of the fine aiming module is positioned in front of the focusing lens. Accordingly, it does not produce sharp images for targets observed at short distances. The operating principle of the fine aiming module involves the emission of an infrared laser beam from the instrument which is then reflected by a prism. The reflected beam is received by the image sensor of the fine aiming module where the center coordinates of the light spot are computed. Consequently, a sharp image of the reflected beam is not required for an accurate detection of the spot's center on the image sensor. The center coordinates of the imaged light spot are then used to steer the telescope more precisely towards the prism center or to computationally correct the current telescope angles so that the measured angles refer to the center of the prism. It is hereby noted that Wasmeier (2003) used the image sensor of the fine aiming module also for static image-based measurements towards natural objects. Due to the small FOV of the fine aiming module (e.g. 1.6 gon for the evaluated IATS, cf. Leica 2015a, p. 69), a motion model of the tracked prism is used to steer the telescope during occlusions of the prism, e.g. when moving the prism behind a tree. However, in practical surveying situations a fail of the fine aiming module, i.e., a loss of the prism, occurs frequently at locations with many obstructions (e.g. trees, cars, etc.).

Once the prism is lost by the fine aiming module, a fan search, which is denoted as *PowerSearch* for the evaluated IATS, can be used for an automated and quick retrieval of the prism. Hereby, the fan search module emits an infrared beam with a large aperture in vertical direction while simultaneously rotating the instrument about its vertical axis. The detector of the fan search unit also has a large aperture in vertical direction (40 gon for the evaluated instrument, cf. Grimm et al. 2015) and reports the detection of the prism if the coarse horizontal direction towards the prism is found. Afterwards, the telescope's vertical angle is altered until the prism is visible in the FOV of the fine aiming module. Obviously, the coarse search is much faster when the fan search is executed directly towards the prism which, as seen from the instrument, is either left or right. Otherwise, a full turn about the vertical axis is required. Another method for the reacquisition of the prism is to move the telescope in a spiral pattern (spiral search) until the fine aiming module with its small FOV detects the prism.

The evaluated IATS also provides strategies for target identification which should ensure that only the desired prism is tracked by the fine aiming module. Therefore, the reflected infrared spot, which is received by the image sensor of the fine aiming module, is analyzed and non-prism reflections are rejected (Grimm et al. 2015). These distracting reflections can be caused by reflections of the emitted infrared beam by e.g. traffic signs. The tracking of an invalid prism should be prevented by storing the position and the brightness of the received infrared spots on the image sensor (Grimm and Hornung 2015). Once the desired prism is occluded for a short time, e.g. when moving the prism behind a tree, and only a distracting prism is visible, the fine aiming module can be prevented from locking onto the distracting prism by analyzing the stored information of the different light spots.

More details on these state-of-the-art tracking techniques can be found in Ehrhart and Lienhart (2017b) where the used hardware and the operating principles utilized by other total station manufacturers are also described.

5.1.2 Patents for visual tracking with total stations

The basic principle of using two tracking systems with different FOVs, i.e., narrow and large, was also proposed in patents of different total station manufacturers (Dold et al. 2012; Otani and Kumagai 2012). Both patents propose a tracking system which is based on the automated fine aiming described in Section 5.1.1. Instead of emitting an infrared beam which is then reflected by the prism, the use of active targets which emit light themselves (cf. Ehrhart and Lienhart 2017b) is mentioned. The tracking system is improved by a second tracking unit with a larger FOV, such as the wide-angle camera, which detects the target or the support of the target and allows a fast reacquisition of the prism in cases in which the fine aiming module fails. Hereby, the direction towards the prism gained from the second tracking unit is not used for actual measurements which are solely carried out by the fine aiming module.

The differences between the two patents are rather subtle. Dold et al. (2012) propose to use the second tracking unit only when the fine aiming module fails. Hereby, the instrument is controlled by the second tracking unit until the fine aiming module redetects the prism. This second tracking unit is embellished as a wide-angle camera in combination with a position sensitive device (PSD) which can determine the direction towards a target that emits light at a certain wavelength. In another embodiment, the instrument can be equipped with an additional emitter unit with an aperture matching the aperture of the detection unit based on the PSD. Hereby, the emitted light is reflected by the target which allows the usage of retroreflective prisms that do not emit light by themselves. The shape and color of the target or the light emitted or reflected by the target can be used to follow the prism and to identify whether the correct prism is tracked.

Otani and Kumagai (2012) propose to use the second tracking unit, which is also based on a wide-angle camera, in parallel to the fine aiming module. The second tracking unit detects the target or the support of the target, such as a construction machine, based on template matching or by finding “characteristic points” (presumably keypoints, cf. Section 2.4.1). The measured distance towards the target can be used to update the size of the target template. The cameras of the second tracking unit take images at low or high magnification dependent on the distance towards the target (presumably by using a telescope and a wide-angle camera).

Kludas (2012) also describes a tracking system with a narrow and a large FOV. Both tracking units work similar to the fine aiming module described in Section 5.1.1 in which light emitting, active targets are also possible. Hereby, the tracking unit with the narrow FOV is used for measurements to prisms at large distances and the tracking unit with the large FOV performs measurements to prisms at short distances. In another embodiment, the tracking system switches to the tracking unit with the narrow FOV before executing a measurement and the tracking unit with the large FOV is only used to follow a rapidly moving prism at short distances. Both tracking units try to constantly align the telescope with the prism center so that distance measurements are possible at all times.

The idea proposed by Dold et al. (2012) of implementing a second tracking unit with a larger FOV for the fast reacquisition of a prism or an active target is implemented in laser trackers, which work similar to total stations, of *Leica Geosystems AG* (Leica 2010a). The patent of Kludas (2012) for tracking prisms and active targets is implemented in different *Trimble* total stations in which a double-quadrant detector with a narrow and a larger FOV is used (Trimble 2009; Ehrhart and Lienhart 2017b). However, no reports of implementing the proposed solutions for the fast reacquisition of a prism and the target identification based on a second tracking unit (wide-angle camera) and passive targets (e.g. the support of the prism) are available in the literature.

5.2 COARSE SEARCH AND TARGET IDENTIFICATION

The coarse prism search and the target identification based on the visual tracking of an object in the video data of the wide-angle camera both involve similar processing steps. In a first step the object is automatically identified in the video data of the wide-angle camera (Section 5.2.1). Afterwards, the resulting image coordinates of the object are related to theodolite angles so that they refer to the same coordinate system as the angle measurements of the fine aiming module which are conducted towards the prism center (Section 5.2.2). The theodolite angles towards the visual object and towards the prism center then provide possibilities for a coarse prism search (Section 5.2.3) and for target identification (Section 5.2.4).

5.2.1 Visual tracking

The visual tracking of an object in a series of images or frames, such as the video stream of the IATS, is an important issue in many industries. The basic principle of most visual trackers is to initially select the object to be tracked in which the tracker automatically detects this object in the following frames. Numerous algorithms for visual tracking have been proposed and it is referred to Wu et al. (2015) for an overview and comparison. For an automated detection of the object, the reported tracking algorithms use different representations of the object such as the color, a template image, image features (cf. Section 2.4.1) or combinations of several representations.

Challenging aspects in visual object tracking involve illumination changes, occlusions and fast movements of the object, and changes in the object's size or attitude (Wu et al. 2015). A further aspect for visual tracking with the wide-angle camera of an IATS is the movement of the telescope. For e.g. a static surveillance camera, an object can be easily separated from the background by subtracting a background image from the actual image containing the object (Davies 2012, pp. 585ff.). This is not possible for the image data of an IATS as the background constantly changes because of the movement of the telescope.

For the studies in this chapter, the CAMSHIFT (continuously adaptive mean shift, cf. Bradski 1998) algorithm is used for the visual object tracking with the wide-angle camera of the IATS. Hereby, the object to be tracked is represented by a color histogram of the hue (or color) channel of the HSV (hue saturation value, cf. Szeliski 2010, pp. 91f.) color space. The HSV color space has three channels which contain information on the color (hue), the colorfulness (saturation), and the brightness (value). The operating principle of the implemented visual tracker is illustrated in Figure 5.1 (cf. Ehrhart and Lienhart 2017b for colored illustrations) and is summarized as follows:

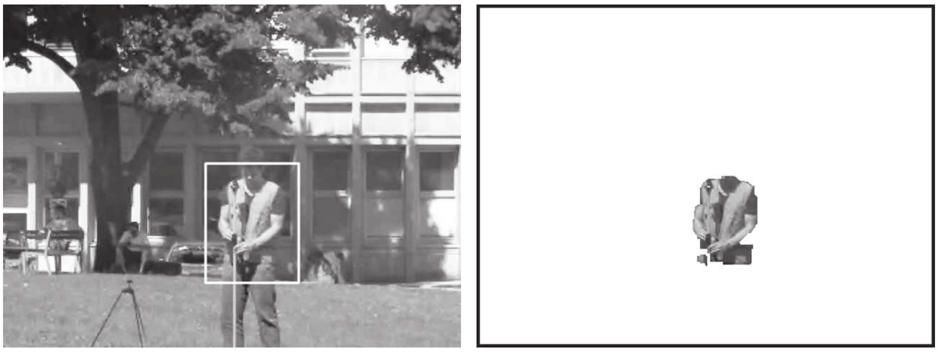

(a) coarse object selection **(b)** foreground segmentation

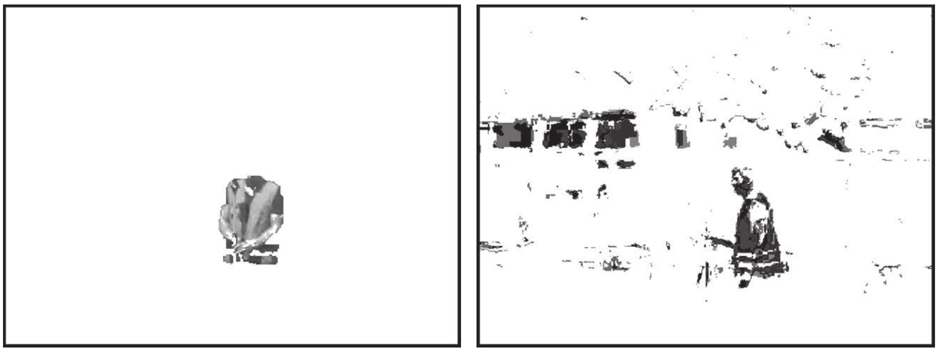

(c) filtered foreground **(d)** filtered backprojection

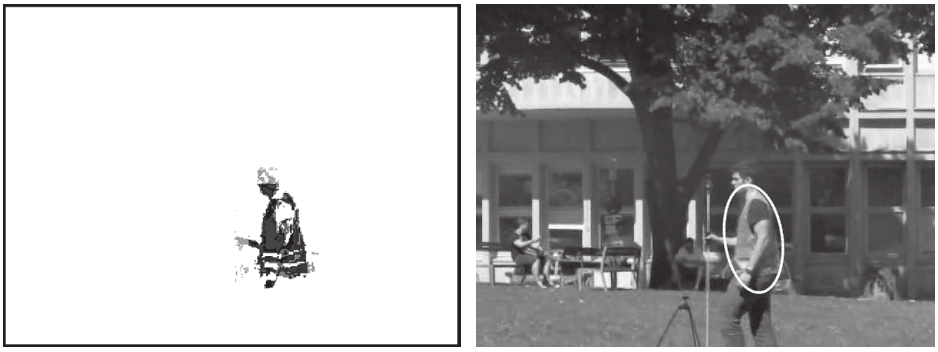

(e) windowed backprojection **(f)** update of track window

Figure 5.1: Operating principle of the visual object tracker.

(a) The object to be tracked is selected by the operator. In Figure 5.1a, the object is the body of the operator who wears an orange safety vest, a wine red shirt, and black trousers.

(b) The selected object is automatically segmented from the background by using the GrabCut algorithm (cf. Rother et al. 2004). After the segmentation (Figure 5.1b), the operator has the possibility to confirm whether the object was segmented correctly. The subsequent steps are carried out fully automatically.

(c) As already mentioned, the CAMSHIFT algorithm operates on the hue channel of the HSV colorspace. Hereby, very dark pixels, i.e., close to black, are represented by a low number in the value (brightness) channel. Very bright pixels, i.e., close to white, are represented by a low number in the saturation (colorfulness) channel. In both cases, the corresponding hue component is not well defined (Bradski 1998) and these pixels are filtered. Following Bradski (1998), 10% of the maximum pixel value, i.e., 26 for an 8-bit image with values from 0 to 255 in the V- and S-channel, are used as a threshold to filter very dark and bright pixels. Figure 5.1c depicts the filtered foreground.

(-) Afterwards, a histogram is computed from the hue channel of the pixels of the filtered foreground. There is no point in depicting this histogram on grayscale in Figure 5.1 but it is again referred to Ehrhart and Lienhart (2017b) for colored illustrations.

(d) In subsequent frames of the video stream, the hue channel is analyzed in which the value of the corresponding histogram bin is assigned to each pixel. This results in the so-called backprojection in which very dark and very bright pixels are also filtered by using the same threshold as in Step (c). Furthermore, backprojections with a low value (e.g. pixels containing the green grass, cf. Figure 5.1a) are also rejected from further computations. However, due to the large AOV of the wide-angle camera, the filtered backprojection still contains distracting objects such as parts of the building in the background (Figure 5.1d).

(e) Therefore, the backprojection is windowed based on the track window of the previous frame (Bradski 1998) which is depicted in Figure 5.1e. The update of the track window in Step (f) then only uses this windowed backprojection. Obviously, windowing the image data before the computations of Step (d) is advantageous in terms of computation time. For illustration purposes, this is not done in Figure 5.1.

(f) In a final step, the window of the visual tracker is updated. To update the location of the track window, the mean shift algorithm (Fukunaga and Hostetler 1975; Cheng 1995), which is also compactly described by Bradski (1998), is applied on the windowed backprojection. The CAMSHIFT algorithm enhances the mean shift algorithm by also updating the size and the orientation of the track window (Figure 5.1f). This is necessary to account for variations in the object's size and attitude.

As the CAMSHIFT algorithm represents the tracked object by its color, the visual tracker evaluated in this chapter only works for colored objects. It is hereby noted that black and white cannot be regarded as colors in this sense. However, in many practical surveying situations, an object in the vicinity of the prism fulfills the requirements of the CAMSHIFT algorithm. For example it is obligatory at many construction sites to wear colored safety vests which also applies to the surveyor carrying a prism. Also construction machinery is painted in eye-catching colors for safety reasons.

The center of the visually tracked object does not necessarily correspond to the prism center which is measured by the fine aiming module of the total station. This is depicted in Figure 5.1f where the body of the operator is clearly separated from the prism on the reflector pole. A strategy for correcting this mismatch between the two tracking units, i.e., fine aiming module and wide-angle camera, is presented in Section 5.2.2.

5.2.2 Theodolite angles to prism

The visual object tracker (Section 5.2.1) provides the image sensor coordinates of the visual object. The prism-based tracking of the total station with the fine aiming module refers to the theodolite angles towards the prism center. Accordingly, the results of the visual object tracker, i.e., pixel coordinates, need to be transformed to theodolite angles.

The relation between the image sensor coordinates of the eccentric (w.r.t. the theodolite center) wide-angle camera and the corresponding theodolite angles is discussed in Chapter 6. It involves

- the computation of the image coordinates from the sensor coordinates after Eq. (6.6) which requires the camera calibration parameters,
- the transformation of the image to the camera system after Eq. (6.9) which requires the slope distance towards the target,
- the transformation of the camera to the telescope system after Eq. (6.11) which requires the offset between the camera center and the center of the theodolite,
- the transformation of the telescope to the theodolite system after Eq. (6.15), and finally
- the computation of the horizontal and vertical theodolite angles towards the target after Eqs. (6.17) and (6.18).

Along with the camera calibration parameters, including the offset between the camera and the telescope system (cf. Table 6.1), the thorough relation between the image coordinates of the wide-angle camera and the theodolite angles requires the slope distance towards the target. Loosely speaking, the distance is used to determine the position of the theodolite's sighting axis in the image of the eccentric wide-angle camera. For the telescope camera, whose center approximately corresponds to the center of the theodolite, the knowledge of the slope distance is not the required (cf. Section 6.3).

For continuous measurements, in which the distance is constantly measured for the continuous computation of 3D coordinates (cf. Section 5.1), the rigorous relation between image coordinates and theodolite angles can be applied. For measurements in one-person operation, in which the distance is only measured at selected points (cf. Section 5.1), the slope distance is not available between those measurements.

However, even for a known distance towards the target, the theodolite angles towards the visual object do not necessarily correspond to the angles towards the prism center (cf. Figure 5.1f). This must be assumed as the general case for situations in which the visual object is eccentric to the prism center. Furthermore, even for a constant separation between the visual object and the prism, the deviations between the image-based angles gained from the visual object tracker and the theodolite angles towards the prism center vary with the distance.

Based on the results of the visual object tracker, the theodolite angles towards the prism center can be approximated with the strategy proposed by Ehrhart and Lienhart (2017b) which is depicted in Figure 5.2. During a successful tracking of the prism by the fine aiming module, the corresponding theodolite angles $Hz_{\text{prism},0}$ and $V_{\text{prism},0}$ towards the prism center are recorded. Simultaneously, the coarse theodolite angles $Hz^{*}_{\text{object},0}$ and $V^{*}_{\text{object},0}$ towards the visual object, which are gained from the visual tracker, are computed. The angular corrections of the coarse direction towards the visual object to the direction towards the prism center can be computed by

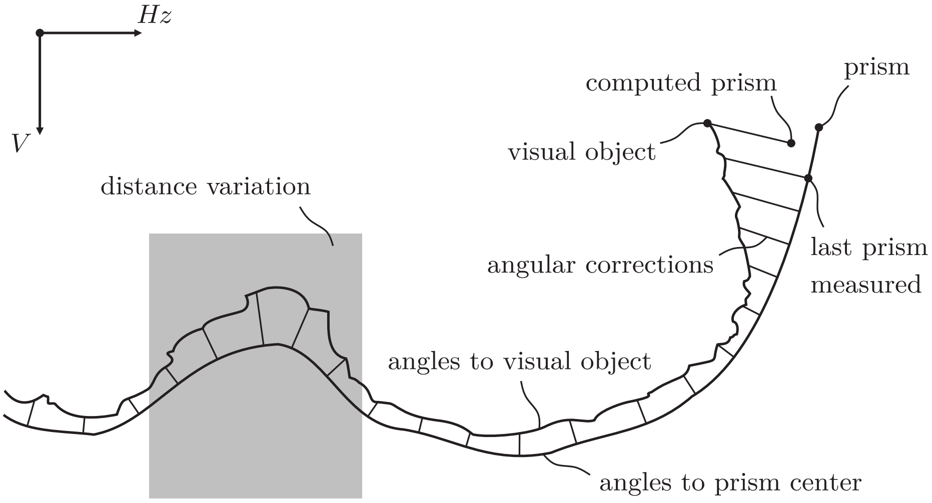

Figure 5.2: Theodolite angles towards visual object and prism center.

$$\Delta Hz = Hz_{\text{prism},0} - Hz^*_{\text{object},0} \tag{5.1}$$

$$\Delta V = V_{\text{prism},0} - V^*_{\text{object},0} \tag{5.2}$$

In a later epoch i, the theodolite angles towards the prism can be approximated by

$$Hz_{\text{prism},i} \approx Hz^*_{\text{object},i} + \Delta Hz_{i-1} \tag{5.3}$$

$$V_{\text{prism},i} \approx V^*_{\text{object},i} + \Delta V_{i-1} \tag{5.4}$$

in which ΔHz_{i-1} and ΔV_{i-1} of the last successful prism tracking and the current coarse theodolite angles $Hz^*_{\text{object},i}$ and $V^*_{\text{object},i}$ towards the visual object are used. The angular corrections ΔHz and ΔV of Eqs. (5.1) and (5.2) hereby absorb

- an angular deviation between the visual object and the prism center for the actual distance,
- errors in the mapping relation between the image coordinates

and the theodolite angles because of an unknown distance,

- errors in the calibration parameters of the wide-angle camera, and
- a delay of the video data w.r.t. the angle measurements (about 1 s for the evaluated IATS).

The effect of changes in the distance on the angular corrections ΔHz and ΔV is also depicted in Figure 5.2 where the values change with distance variations. Consequently, Eqs. (5.3) and (5.4) only provide accurate results as long as the distance towards the target did not change since the last successful tracking of the prism by the fine aiming module. However, the image-assisted coarse search and target identification do not influence the accuracy of the angle measurements which is solely defined by the measurements of the fine aiming module. Therefore, a change of the distance is acceptable because Eqs. (5.3) and (5.4) must only provide approximations for the theodolite angles towards the prism (cf. Sections 5.2.3 and 5.2.4).

5.2.3 Coarse search

In situations in which the prism tracking of the fine aiming module fails, i.e., the prism is lost, the visual object might still be found by the visual tracker because of the larger AOV of the wide-angle camera. The theodolite angles towards the prism can then be approximated after Eqs. (5.3) and (5.4) so that the telescope can be repositioned and the prism tracking based on the fine aiming module can be resumed.

As mentioned in Section 5.2.2, Eqs. (5.3) and (5.4) only provide coarse approximations of the theodolite angles. However, this is not a critical issue because it is only necessary to reposition the telescope so that the prism is visible in the FOV of the fine aiming module. For the evaluated IATS (*Leica MS60*, cf. Section 1.4) the FOV is specified with 1.6 gon (Leica 2015a, p. 69). Accordingly, the deviations between the repositioned telescope and the actual location of the prism must be within 0.8 mgon which corresponds to the half FOV of the fine aiming module.

Consequently, the camera calibration parameters, such as the polynomial for a correction of radial distortion or rotations between the camera and the theodolite system (cf. Table 6.1), can be neglected. Furthermore, the principal point of the image sensor can be approximated as the center of the image and the camera constant is approximated by using the angle per pixel α_{px} of the wide-angle camera ($\alpha_{\mathrm{px}} = 6.7\,\mathrm{mgon/px}$, cf. Table 1.6).

As discussed in Section 1.4, the video stream of the $2560\,\mathrm{px} \times 1920\,\mathrm{px}$ image sensor is transmitted at a resolution of $640\,\mathrm{px} \times 480\,\mathrm{px}$ and it must be decided whether a reduced AOV with full image resolution or the full AOV with a larger value for α_{px} is used. For the coarse prism search, a large AOV of the second tracking unit, i.e., the wide-angle camera, is preferable. Therefore, the video stream is transmitted for the full AOV ($17.2\,\mathrm{gon} \times 13.0\,\mathrm{gon}$, cf. Table 1.6) which increases α_{px} by a factor 4 to $\alpha_{\mathrm{px}} = 26.8\,\mathrm{mgon/px}$. From this value, a camera constant of $c \approx 2375\,\mathrm{px}$ can be approximated. For the computations (Section 5.2.2), the principal point also refers to the transmitted image data ($u_0 \approx 320\,\mathrm{px}$, $v_0 \approx 240\,\mathrm{px}$).

As seen from the instrument, the wide-angle camera is located about 16 mm right and 61 mm above the theodolite center of the evaluated IATS (*Leica MS60*, cf. Section 1.4). Accordingly, the sighting axis of the telescope is eccentric to the center of the image in which the eccentricity varies with the distance to the target. These variations of the telescope's reticule in the transmitted video data ($640\,\mathrm{px} \times 480\,\mathrm{px}$, full AOV) are depicted in Figure 5.3. For a comparison with the FOV of the fine aiming module (1.6 gon), these pixel variations are also translated to angles.

Without knowledge of the distance towards the target, the deviations between the image-based and the true direction towards the same target, i.e. the prism, are within the FOV of the fine aiming module for distances larger than 5 m. This distance corresponds

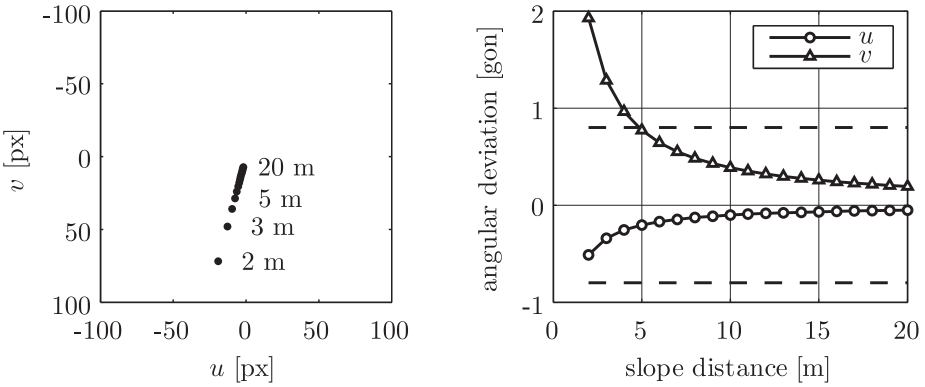

Figure 5.3: Position of the telescope's reticule in the wide-angle camera image (left) and corresponding angular deviations between image-based and true direction towards the same target (right) for different distances. Dashed line: FOV of the fine aiming module.

to the minimum specified distance for tracking 360° prisms (Leica 2015a, p. 68) which are frequently used in one-person operation and machine guidance.

It is noted that the corrections of Eqs. (5.1) and (5.2) absorb errors induced by the eccentricity of the wide-angle camera (cf. Section 5.2.2). Hence, for a failing of the fine aiming module at a distance of e.g. 7 m, the apparent direction towards the prism center gained from the visual tracker is sufficient even if the target has moved to a distance of 3 m since the last evaluation of Eqs. (5.1) and (5.2). This is because the deviation between the apparent direction and the actual position of the prism is within the FOV of the fine aiming module.

However, in Figure 5.3 it is assumed that the visual tracker and the fine aiming module refer to the same target which cannot be regarded as the general case (cf. Figure 5.1f). For two selected separations between the center of the visual object and the prism, Figure 5.4 depicts the angular deviations between the image-based theodolite angles towards the prism and the actual prism position for different distances.

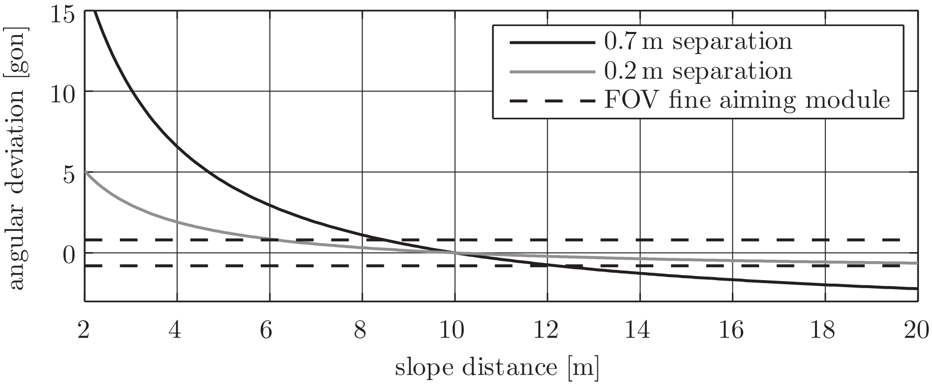

Figure 5.4: Angular deviations between image-based and true direction towards prism for different distances and separations between visual target and prism. Last measurement of prism by fine aiming module at a distance of 10 m.

Hereby, it is assumed that the last evaluation of Eqs. (5.1) and (5.2) could be performed at a distance of 10 m so that the angular deviations are zero at this distance. Figure 5.3 shows that large separations between the visual object and the prism limit the distance changes of the target that still allow a successful reacquisition of the prism by the fine aiming module. These distance changes occur between the last successful prism tracking with the fine aiming module and the coarse prism search based on the results of the visual tracker.

For corrections evaluated at a distance of 10 m and for a separation of 0.7 m between the visual object and the prism, the target must be located within a distance range of 8.5 to 12 m for a successful reacquisition of the prism. The value of 0.7 m roughly corresponds to the separation between the body of a person, which can be visually tracked, and the prism carried by hand (cf. Sections 5.2.4 and 5.3.2). Assuming a walking speed of 1 m/s and a movement directly towards the instrument, the duration for a successful coarse search of the prism must not exceed 1.5 s in this example. For a separation of only 0.2 m, the range which allows a successful reacquisition of the prism is extended to about 6 to 27 m.

In situations in which the visual object also disappears from the wide-angle camera's AOV after the prism is lost by the fine aiming module, a direct repositioning of the telescope is not possible. However, the information of the visual tracker can still be used to execute a fan search in the correct horizontal direction (cf. Section 5.1.1).

5.2.4 Robust target tracking

The angular corrections of Eqs. (5.1) and (5.2) can also be used to evaluate whether the correct prism is tracked by the fine aiming module. For a known separation between the visual object and the prism, the angular corrections can be compared to this value if the distance towards the target is known. This information is provided when measuring the 3D coordinates of the prism which also yields the angle measurements of the fine aiming module towards the prism. Consequently, Eqs. (5.1) and (5.2) can be evaluated and the results can be compared to the expected separation between the visual object and the prism. This provides a method for evaluating whether the measurements were conducted to the correct prism.

In situations in which the separation between the visual object and the prism varies, at least a maximum separation can be specified. This is the case for e.g. a person carrying a prism by hand in which the body of the person is visually tracked (cf. Figure 5.1). Here, the maximum separation can be set to the arm length which allows a convenient carrying of the prism by hand (e.g. 0.7 m).

Following one of the ideas of Otani and Kumagai (2012), cf. Section 5.1.2, it would also be possible to use the image data of the telescope camera for the identification of targets observed at large distances.

5.3 EXPERIMENTAL MEASUREMENTS

The image-based coarse prism search and the target identification were evaluated with the state-of-the-art IATS *Leica MS60* (cf. Section 1.4). The 640 px × 480 px video stream was transmitted to an external computer with the maximum video rate of 30 fps. Hereby, the full AOV of the wide-angle camera (17.2 gon × 13.0 gon, cf. Table 1.6) was preserved which causes an increase of the angle per pixel by a factor 4 (cf. Sections 1.4 and 5.2.3).

For computing the image-based theodolite angles towards the visual object, the camera constant was approximated with 2375 px based on the angle per pixel (26.8 mgon/px, cf. Section 5.2.3) of the transmitted video stream. The principal point was set to the center of the image ($u_0 = 320\,\text{px}$, $v_0 = 240\,\text{px}$) and further calibration parameters (cf. Table 6.1) were omitted. Accordingly, a calibration of the mapping parameters of the wide-angle camera is not necessary for the experiments described in this section.

5.3.1 Coarse search

Figure 5.5 depicts a situation in which a 360° mini prism attached to a toy car is tracked by the total station. Hereby, the red chassis of the car is the target of the visual tracker. The tracking results are accented with a white ellipse in Figure 5.5. On a larger scale, the toy car could be replaced by a construction machine carrying a larger prism.

Figure 5.5 also depicts the position of the telescope's reticule (black cross) and the FOV of the fine aiming module (black circle). The image data results from the video stream of the wide-angle camera which, compared to the fine aiming module (black circle), illustrates the larger AOV of the wide-angle camera.

In Figure 5.5a and 5.5b the prism is successfully tracked by the fine aiming module. After the prism was moved behind an obstacle (Figure 5.5c), the fine aiming module loses the prism and the telescope is moved based on the predicted movements of the prism.

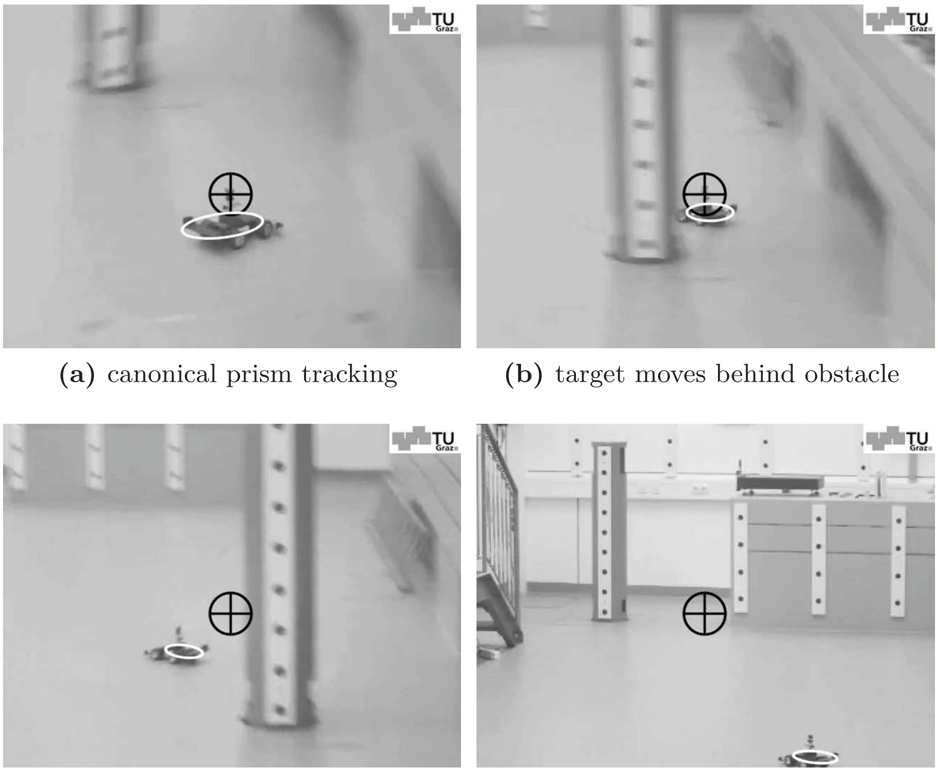

(a) canonical prism tracking **(b)** target moves behind obstacle

(c) fine aiming in prediction mode **(d)** fine aiming fails

Figure 5.5: Image-assisted prism search with position of the telescope (black cross), FOV of the fine aiming module (black circle) and object (white ellipse) detected by the visual tracker (after Ehrhart and Lienhart 2017b).

The visual tracker with its larger AOV is still locked to the visual target, i.e., the chassis of the car. After the fine aiming module fails to reacquire the prism, the movements of the telescope are stopped. Based on the situation depicted in Figure 5.5d, in which the visual object is visible in the AOV of the wide-angle camera, different search methods for a fast reacquisition of the prism were evaluated.

The results are given in Table 5.1 in which the standard search methods are briefly described in Section 5.1.1. The durations refer

Table 5.1: Durations for target reacquisition with different search methods resulting from five test runs (data from Ehrhart and Lienhart 2017b)

Search method	**Search time**
spiral search with 20 gon window	17.7 to 18.0 s
spiral search with 10 gon window	11.8 to 12.7 s
fan search leftwards	12.5 to 13.1 s
fan search rightwards	4.8 to 5.5 s
image-assisted search	1.2 to 1.5 s

to the period between the start of the search operation and the successful reacquisition of the prism by the fine aiming module.

The image-assisted search described in Section 5.2.3 is about 4-times faster than the fan search rightwards and about 10-times faster than the fan search leftwards and the spiral search. It is hereby noted that the correct direction of the fan search (rightwards in the case of Figure 5.5d), which heavily reduces the search time, can also be deduced from the results of the visual tracker.

5.3.2 Robust target tracking

Figure 5.6 depicts a typical situation for the prism tracking in one-person operation. The 360° prism attached to a reflector pole is carried by hand and the orange safety vest worn by the operator is tracked by the visual tracker. Similar to Figure 5.5, the results of the visual tracker (white ellipse) and the telescope position (black cross) with the FOV of the fine aiming module (black circle) are accented in Figure 5.6.

In Figure 5.6a, the fine aiming module successfully tracks the rover prism carried by the operator. After the rover prism is moved behind a distracting prism (Figure 5.6b), the fine aiming module stays locked onto this prism (Figure 5.6c and 5.6d). Such distracting prisms are frequently present at construction sites. There, these prisms are located at known reference points and are used to determine the coordinates of the instrument position and to check the

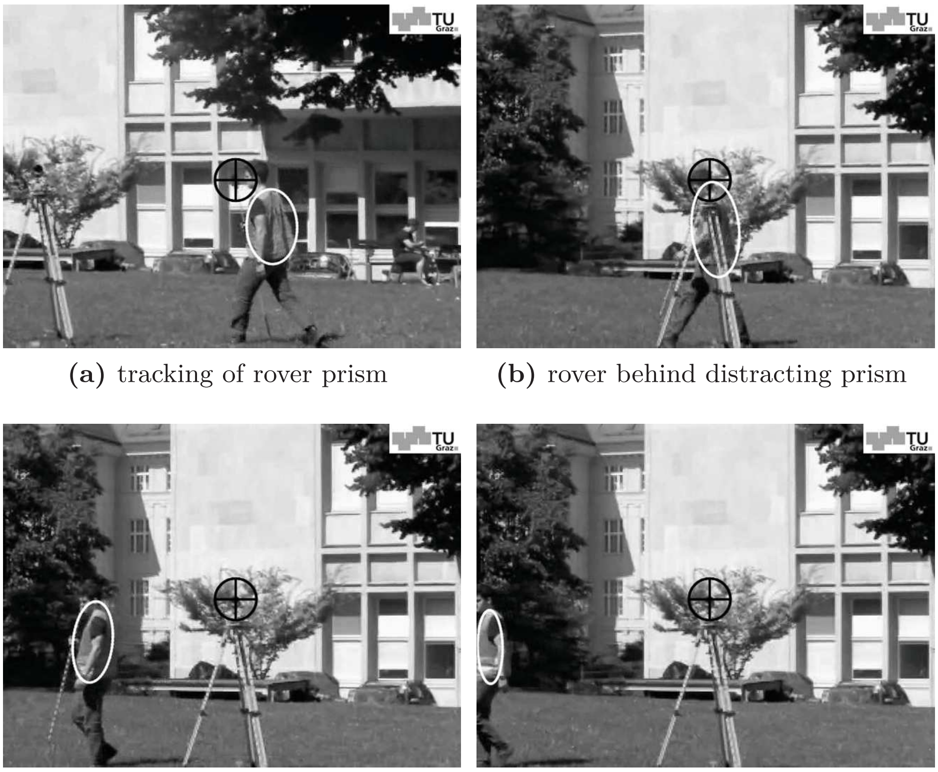

(a) tracking of rover prism **(b)** rover behind distracting prism

(c) fine aiming to distracting prism **(d)** rover disappears from AOV

Figure 5.6: Image-assisted robust target tracking with position of the telescope (black cross), FOV of the fine aiming module (black circle) and object (white ellipse) detected by the visual tracker (after Ehrhart and Lienhart 2017b).

instrument stability from time to time.

If the operator measured a supposed point at the location depicted in Figure 5.6c, the total station would yield 3D coordinates because it is locked to a prism. However, the visual tracker reports the measurement of a distracting prism because the deviation between the prism and the visual object is larger than the set maximum value (e.g. larger than the arm length of the operator, cf. Section 5.2.4). Even if no point is measured and the distance towards the target is unknown, the visual tracker reports the tracking of an invalid prism once the visual object disappears from the AOV of the wide-angle camera (Figure 5.6d).

5.4 CONCLUSIONS

The automated and robust tracking of a prism with total stations is an important issue in many applications, especially in machine guidance and in one-person operation. In this chapter, it was discussed and experimentally evaluated how the wide-angle camera of a state-of-the-art IATS can be used for improving the automated tracking of a prism. Hereby, it is taken advantage of the AOV of the wide-angle camera ($17.2\,\mathrm{gon} \times 13.0\,\mathrm{gon}$) which is about 10-times larger than the FOV of the fine aiming module which is used for conventional prism tracking.

By using the image data of the wide-angle camera, it was demonstrated that the reacquisition of a prism is 4 to 10-times faster than currently implemented methods. This reduces interruptions in the measurements and consequently speeds up the measurement process. The additional image data can also be used for identifying whether the correct prism is measured by the total station. This reduces the possibility of mistakenly tracking a wrong prism which results in gross errors in the measurement data. Accordingly, the time spent on removing these errors in postprocessing can be heavily reduced.

The proposed system is intended as an assistance system which improves the robustness of the conventional prism tracking based on the fine aiming module of the total station. Therefore, the image data of the wide-angle camera does not produce measurement results, i.e., coordinates of selected points. Accordingly, the accuracy of the image-based tracking is of minor importance and only a few calibration parameters, which can be taken from the datasheet of the used IATS, are sufficient. However, it is mentioned that the image data of an IATS can also be used for the determination of

3D coordinates of moving objects. For example Guillaume et al. (2016b) use the image data of the telescope cameras of two IATSs to determine the trajectories of aircrafts based on spatial forward intersection. For achieving the reported precision of about 10 mgon for the image-based angle measurements, a calibration of the cameras is of course required.

The system proposed in this chapter is based on the well-known CAMSHIFT algorithm for the visual tracking of the target. After an initial coarse selection of the target by the operator, the visual tracking is a fully automated procedure that does not require any user interaction. For the visual tracking, the CAMSHIFT algorithm represents the object by its color in which numerous tracking algorithms using other object representations are also available (Wu et al. 2015). As proposed by Kalal et al. (2012), the update of the object's representation in a learning step is regarded as a promising approach for improving the robustness of the implemented visual tracker. For the visual tracking with an IATS, the learning steps can be limited to periods in which the fine aiming module reports a successful tracking of the prism.

The wide-angle cameras of IATSs are eccentric w.r.t. the theodolite center in which the constant values of this eccentricity are provided by the manufacturer or can be calibrated. However, for a thorough relation between the image coordinates of the visually tracked object and the corresponding theodolite angles, the distance towards the target is also required. It is therefore proposed to compute angular corrections for the coarse image-based theodolite angles towards the visual object in periods in which the tracking of the prism based on the fine aiming module operates successfully. Accordingly, the proposed method does neither require knowledge of the wide-angle camera's eccentricity nor the distance towards the target.

In cases in which the fine aiming module loses the prism, the image-based theodolite angles towards the prism result from the visual tracker and the angular corrections of the last successful tracking step. Thus, the corrections are inaccurate if the distance towards the target has changed since the last successful tracking with the fine aiming module. This is especially an issue for rapid distance changes of a target observed at a short absolute distance (e.g. less than 10 m). To improve the robustness of the visual tracker, i.e., to increase the success rate of the coarse prism search, a motion model of the computed angular corrections could be employed. Hereby, size variations of the visually tracked object could be incorporated in the motion model as an indicator for distance changes.

Of course, a larger AOV of the wide-angle camera also increases the probability for detecting the visual target in the image data in cases in which the fine aiming module fails. Hereby, the wide-angle camera of the *Trimble SX10* with a 63.9 gon × 47.8 gon AOV (Trimble 2016b) is mentioned.

The current implementation of the proposed system for visual object tracking is based on transmitting the video stream of the IATS to an external computer for further processing. Regarding the hardware used in the first implementation of the CAMSHIFT algorithm (300 MHz *Pentium II* processor, cf. Bradski 1998), the hardware of state-of-the-art IATSs (e.g. 1 GHz *TI Cortex-A9* processor and 640 MB RAM for the evaluated *Leica MS60*) should be sufficient for an onboard implementation of the proposed tracking system. Furthermore, the computational effort of the tracking system can be reduced by downsizing the video frames prior to the processing or by reducing the frame rate of the video stream. An onboard implementation requires real-time access to the video stream which is not possible for the firmware of the evaluated IATS (cf. Section 1.4). However, the video stream can be transmitted to an external computer in almost real-time (delay of about 1 s) and it can be assumed that this will also be possible for customized onboard applications in the future.

6

Mapping relations

6.1 INTRODUCTION

The image-based angle measurement of an IATS towards a target result from the measurements of three individual sensors, namely

- angle encoders,
- tilt compensator, and
- image sensor.

The angle encoders measure the position of the telescope, the tilt compensator observes the inclination of the instrument and the image sensor provides the image coordinates towards the target.

The goal of this chapter is to derive the mapping relations between the image coordinates of a target and its corresponding theodolite angles. In Section 6.2 the mapping relations of the generic case, in which the camera center is eccentric to the center of the total station (wide-angle camera), are described. In Section 6.3 simplifications for cameras with a center corresponding to the total station center (telescope camera) are discussed.

Related publications

This chapter is based on but heavily extends the article of Ehrhart and Lienhart (2017a).

6.2 GENERIC MAPPING RELATION

The generic mapping relation between the image coordinates of a camera, which is rigidly mounted to the telescope of a theodolite, and the corresponding theodolite angles was worked out by Huang and Harley (1989) and shall be explained in this section.

6.2.1 Involved coordinate systems

Following Walser (2004, p. 50), four orthogonal coordinate systems are defined to derive the mapping relation. An overview is depicted in Figure 6.1.

Theodolite system

The origin of the 3D theodolite system is the intersection of the theodolite's collimation, tilting and vertical axis (theodolite center). $z_{\text{theodolite}}$ corresponds to the local vertical which differs from the vertical axis of the instrument in case of a tilted setup. $x_{\text{theodolite}}$ points towards an arbitrary zero direction and $y_{\text{theodolite}}$ completes the left-handed coordinate system.

Telescope system

The origin of the 3D telescope system is the theodolite center. $x_{\text{telescope}}$ and $y_{\text{telescope}}$ correspond to the theodolite's collimation

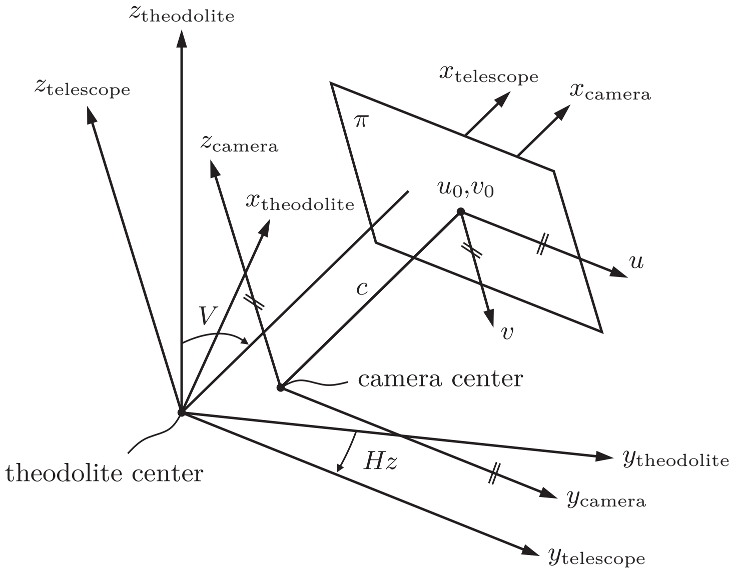

Figure 6.1: Coordinate systems for image-based measurements.

and tilting axis and $z_{\text{telescope}}$ completes the left-handed coordinate system. The telescope system results from the theodolite system by rotations with the horizontal Hz and the vertical V theodolite angle.

Camera system

The origin of the 3D camera system is the center of projection (camera center). The orthogonal distance between the camera center and the image plane π is referred to as camera constant c. x_{camera} corresponds to the principal axis of the camera which passes through the camera center and is orthogonal to π. The principal axis intersects π in the principal point u_0 and v_0. y_{camera} and z_{camera} are parallel to the axes of the image system (u and v) and form a left-handed coordinate system.

Image system

The origin of the 2D image system is the principal point u_0 and v_0. The ideal or corrected image coordinates u and v are measured in pixels. For telescope Face I, u is counted from left to right and v from top to bottom. For telescope Face II, u is counted from right to left and v from bottom to top. The corrected image coordinates are computed from the measured image sensor coordinates u_{sensor} and v_{sensor} which are stored as digital pixel coordinates u_{pixel} and v_{pixel}.

Disambiguation

The *principal axis* of the camera is sometimes referred to as *optical axis*. The lens system in the telescope of an IATS (cf. Walser 2004, pp. 34ff.) differs from the simplified pinhole camera geometry used in Section 6.2.3. In a more complex lens system, the *optical axis* should pass through the centers of all involved lenses (Kraus 2007, p. 49) which is impossible to assemble in practice. The reference axis of the camera is therefore defined as the line through the camera center and orthogonal to the image plane and is referred to as *principal ray* or *principal axis* (Hartley and Zisserman 2004, p. 154).

The orthogonal distance from the camera center to the image plane is sometimes referred to as *focal length* (Hartley and Zisserman 2004, p. 154 and p. 157). The rigorous designation is *camera constant* or *principal distance* (Kraus 2007, p. 21) because for cameras with a variable focus, the camera constant only corresponds to the focal length when the focus is set to infinity (Luhmann et al. 2014, p. 149).

6.2.2 Relation between image sensor and image system

The image-based measurements are conducted by the physical image sensor and result in image sensor coordinates u_{sensor} and v_{sensor}.

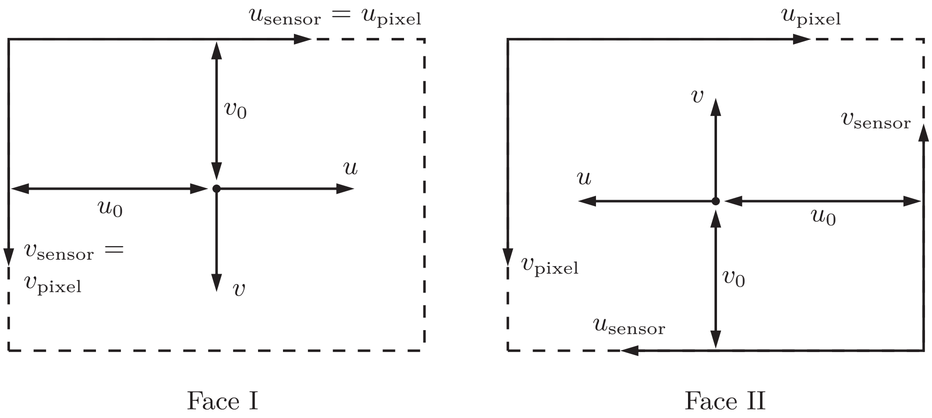

Figure 6.2: Different image systems for telescope Face I and II.

For further processing, these measurements are stored as digital image data (image or video) with pixel coordinates u_{pixel} and v_{pixel}.

Figure 6.2 shows that the physical image sensor, and consequently the image sensor system, changes its orientation with a change of the telescope face. Independent of the telescope face, the coordinate system of the digital image has its origin in the top left corner, u_{pixel} is counted from left to right and v_{pixel} from top to bottom.

Consequently, the image sensor coordinates result from the pixel coordinates of the digital image by

$$u_{\text{sensor}}^{(\text{I})} = u_{\text{pixel}}^{(\text{I})} \tag{6.1}$$

$$v_{\text{sensor}}^{(\text{I})} = v_{\text{pixel}}^{(\text{I})} \tag{6.2}$$

$$u_{\text{sensor}}^{(\text{II})} = w - u_{\text{pixel}}^{(\text{II})} \tag{6.3}$$

$$v_{\text{sensor}}^{(\text{II})} = h - v_{\text{pixel}}^{(\text{II})} \tag{6.4}$$

for measurements in telescope Face I and II in which w and h denote the width and the height of the image sensor in pixels.

For further processing (Section 6.2.3), the image sensor coordinate system is shifted to the principal point (u_0, v_0) so that

$$\begin{bmatrix} u' \\ v' \end{bmatrix} = \begin{bmatrix} u_{\text{sensor}} - u_0 \\ v_{\text{sensor}} - v_0 \end{bmatrix} \tag{6.5}$$

However, using the raw image coordinates u' and v' in Section 6.2.3 is only valid for an ideal camera with the following properties:

- The u- and v-axis have the same scale.
- The u- and v-axis are orthogonal.
- There is no lens distortion.

Deviations from the previous properties can be corrected by

$$\begin{bmatrix} u \\ v \end{bmatrix} = \begin{bmatrix} m & o \\ 0 & 1 \end{bmatrix} \begin{bmatrix} u' \\ v' \end{bmatrix} + \begin{bmatrix} \Delta u_{\text{rad}} \\ \Delta v_{\text{rad}} \end{bmatrix} + \begin{bmatrix} \Delta u_{\text{tan}} \\ \Delta v_{\text{tan}} \end{bmatrix} \tag{6.6}$$

in which m accounts for different scales of the u- and v-axis and o describes a non-orthogonality of u and v. The image coordinates u and v are corrected for radial (Δu_{rad} and Δv_{rad}) and tangential (Δu_{tan} and Δv_{tan}) lens distortion.

Lens distortion can be described by radial and tangential distortion in which the effect of radial distortion is typically an order of magnitude larger than the effect of tangential distortion (Kraus 2007, p. 53). Both distortion types are functions of the location on the image sensor and can be modeled by polynomials of different order.

The correction for radial distortion is obtained from (Luhmann et al. 2014, p. 153)

$$\begin{bmatrix} \Delta u_{\text{rad}} \\ \Delta v_{\text{rad}} \end{bmatrix} = \begin{bmatrix} u' \\ v' \end{bmatrix} \Big((r^2 - r_0^2)\, K_1 + (r^4 - r_0^4)\, K_2 + (r^6 - r_0^6)\, K_3 \Big) \tag{6.7}$$

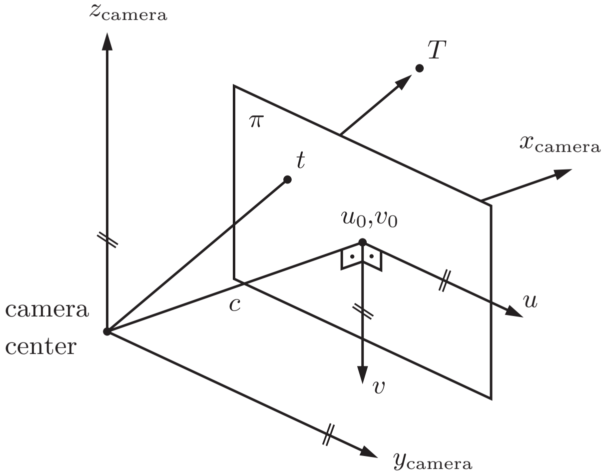

Figure 6.3: Relationship between image and camera system described by pinhole camera geometry.

in which $r^2 = u'^2 + v'^2$ and r_0 is introduced to de-correlate the coefficients K_i and the camera constant c. The fixed value of r_0 is typically chosen with 1/3 of the image diagonal (Luhmann et al. 2014, p. 154). The correction for tangential distortion can be computed by (Luhmann et al. 2014, p. 157)

$$\begin{bmatrix} \Delta u_{\text{tan}} \\ \Delta v_{\text{tan}} \end{bmatrix} = \begin{bmatrix} (r^2 + 2\,u'^2)\,P_1 + 2\,P_2\,u'\,v' \\ (r^2 + 2\,v'^2)\,P_2 + 2\,P_1\,u'\,v' \end{bmatrix} \tag{6.8}$$

6.2.3 Relation between image and camera system

Figure 6.3 depicts a pinhole camera model which relates the 3D camera coordinates of a target T to the 2D image coordinates u and v of the imaged target t by

$$\begin{bmatrix} x_{\text{camera}} \\ y_{\text{camera}} \\ z_{\text{camera}} \end{bmatrix} = \frac{d}{\sqrt{u^2 + v^2 + c^2}} \begin{bmatrix} c \\ u \\ -v \end{bmatrix} = \alpha \begin{bmatrix} c \\ u \\ -v \end{bmatrix} \tag{6.9}$$

in which c is the camera constant, i.e., the orthogonal distance between the camera center and the image plane π, and d is the distance between the camera center and the target T. The corrected image coordinates u and v are computed from the measured sensor coordinates by Eq. (6.6).

When computing the theodolite angles to T by using the IATS' telescope camera, the scale factor α in Eq. (6.9), and consequently the distance d, can be omitted (cf. Section 6.3). For measurements with the wide-angle camera, whose center has an offset to the theodolite center (x_0, y_0, z_0; cf. Section 6.2.4), d can be computed from

$$d = \sqrt{(s - x_0)^2 + y_0^2 + z_0^2} \tag{6.10}$$

in which s is the slope distance between the theodolite center and T. In case of a measured point, s results from the distance measurement of the total station. For the visualization of stakeout points in the image of the wide-angle camera (cf. Section 1.3.2), s can also be calculated by using the known coordinates of the total station and the stakeout point.

6.2.4 Relation between camera and telescope system

Figure 6.4 depicts the relationship between the camera system and the telescope system which can be described by the 6-parameter transformation

$$\begin{bmatrix} x_{\text{telescope}} \\ y_{\text{telescope}} \\ z_{\text{telescope}} \end{bmatrix} = \mathbf{R}_\omega \, \mathbf{R}_\varphi \, \mathbf{R}_\kappa \begin{bmatrix} x_{\text{camera}} \\ y_{\text{camera}} \\ z_{\text{camera}} \end{bmatrix} + \begin{bmatrix} x_0 \\ y_0 \\ z_0 \end{bmatrix} \tag{6.11}$$

in which κ, φ and ω are the three rotation angles and $[x_0, y_0, z_0]^T$ represents the coordinates of the camera center in the telescope system.

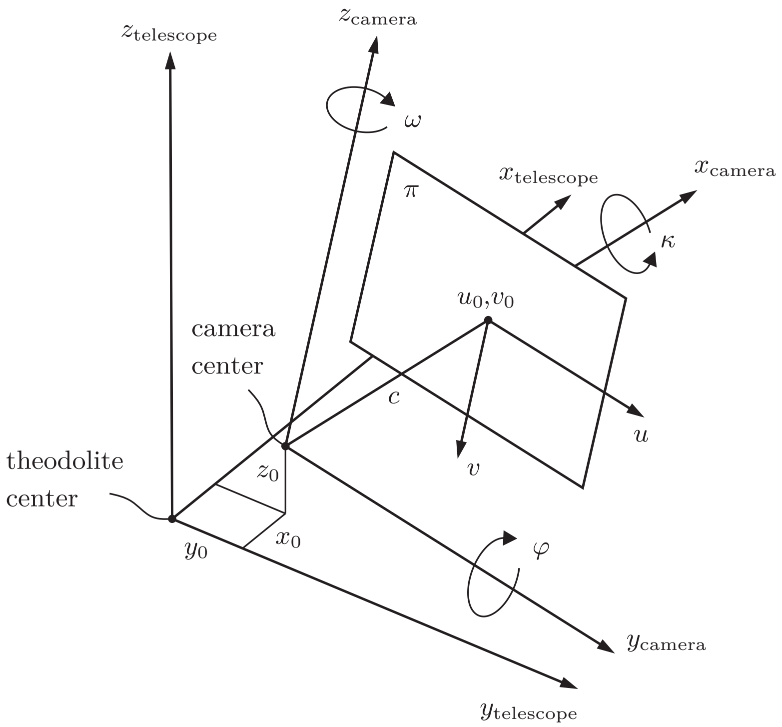

Figure 6.4: Relationship between camera and telescope system.

The rotation matrices are given by

$$\mathbf{R}_\kappa = \begin{bmatrix} 1 & 0 & 0 \\ 0 & \cos\kappa & -\sin\kappa \\ 0 & \sin\kappa & \cos\kappa \end{bmatrix} \tag{6.12}$$

$$\mathbf{R}_\varphi = \begin{bmatrix} \cos\varphi & 0 & \sin\varphi \\ 0 & 1 & 0 \\ -\sin\varphi & 0 & \cos\varphi \end{bmatrix} \tag{6.13}$$

$$\mathbf{R}_\omega = \begin{bmatrix} \cos\omega & -\sin\omega & 0 \\ \sin\omega & \cos\omega & 0 \\ 0 & 0 & 1 \end{bmatrix} \tag{6.14}$$

From Eq. (6.11) it is evident that in case of an offset (x_0, y_0, z_0), which is expressed in meters, the camera coordinates are also required in meters. This is achieved by introducing the distance d from the camera center to the target in Eq. (6.9).

6.2.5 Relation between telescope and theodolite system

The relationship between the telescope system and the theodolite system is given by

$$\begin{bmatrix} x_{\text{theodolite}} \\ y_{\text{theodolite}} \\ z_{\text{theodolite}} \end{bmatrix} = \mathbf{R} \begin{bmatrix} x_{\text{telescope}} \\ y_{\text{telescope}} \\ z_{\text{telescope}} \end{bmatrix} \tag{6.15}$$

where

$$\begin{aligned} \mathbf{R} &= \begin{bmatrix} \cos Hz & -\sin Hz & 0 \\ \sin Hz & \cos Hz & 0 \\ 0 & 0 & 1 \end{bmatrix} \begin{bmatrix} \sin V & 0 & -\cos V \\ 0 & 1 & 0 \\ \cos V & 0 & \sin V \end{bmatrix} \\ &= \begin{bmatrix} \cos Hz \sin V & -\sin Hz & -\cos Hz \cos V \\ \sin Hz \sin V & \cos Hz & -\sin Hz \cos V \\ \cos V & 0 & \sin V \end{bmatrix} \end{aligned} \tag{6.16}$$

in which Hz and V are the raw theodolite angles (no tilt correction) of the current telescope position which are measured by the angle encoders of the IATS. The theodolite angles to the target are computed by

$$Hz_{\text{T}} = \arctan\left(\frac{y_{\text{theodolite}}}{x_{\text{theodolite}}}\right) \tag{6.17}$$

$$V_{\text{T}} = \arctan\left(\frac{\sqrt{x^2_{\text{theodolite}} + y^2_{\text{theodolite}}}}{z_{\text{theodolite}}}\right) \tag{6.18}$$

For a vanishing offset ($x_0 = y_0 = z_0 = 0$) between the camera and the theodolite center, cf. Eq. (6.11), the scale factor α of Eq. (6.9) and consequently the distance to the target s, which is introduced by Eq. (6.10), cancels out.

Eqs. (6.17) and (6.18) yield the theodolite angles in Face I ($0 \leq V_{\mathrm{T}}^{(\mathrm{I})} < \pi$). For measurements in Face II ($\pi \leq V_{\mathrm{T}}^{(\mathrm{II})} < 2\pi$), the conversion

$$Hz_{\mathrm{T}}^{(\mathrm{II})} = \left(Hz_{\mathrm{T}}^{(\mathrm{I})} + \pi\right) \bmod 2\pi \tag{6.19}$$

$$V_{\mathrm{T}}^{(\mathrm{II})} = 2\pi - V_{\mathrm{T}}^{(\mathrm{I})} \tag{6.20}$$

has to be applied.

In case of a tilted setup of the instrument, the computed theodolite angles need to be corrected by (Walser 2004, p. 56)

$$V_{\mathrm{T,tilt}} = V_{\mathrm{T}} + i_{\mathrm{long,T}} \tag{6.21}$$

$$Hz_{\mathrm{T,tilt}} = Hz_{\mathrm{T}} + i_{\mathrm{trans,T}} \cot V_{\mathrm{T,tilt}} \tag{6.22}$$

in which $i_{\mathrm{long,T}}$ and $i_{\mathrm{trans,T}}$ are the longitudinal and transverse inclinations relative to Hz_{T}. These values can be computed from the inclinations i_{long} and i_{trans} relative to the horizontal pointing direction of the telescope Hz, which are measured by the IATS's two-axis tilt compensator, by (Walser 2004, p. 56)

$$i_{\mathrm{long,T}} = i_{\mathrm{abs}} \sin(i_{\mathrm{angle}} + Hz_{\mathrm{T}}) \tag{6.23}$$

$$i_{\mathrm{trans,T}} = i_{\mathrm{abs}} \cos(i_{\mathrm{angle}} + Hz_{\mathrm{T}}) \tag{6.24}$$

where

$$i_{\mathrm{abs}} = \sqrt{i_{\mathrm{long}}^2 + i_{\mathrm{trans}}^2} \tag{6.25}$$

$$i_{\mathrm{angle}} = \arctan\left(\frac{i_{\mathrm{long}}}{i_{\mathrm{trans}}}\right) - Hz \tag{6.26}$$

Table 6.1: Parameters for generic mapping relation between image coordinates and theodolite angles

Symbol	Description
x_0, y_0, z_0	offset between camera and the telescope system
κ, φ, ω	rotations between camera and the telescope system
c	camera constant
u_0, v_0	image sensor coordinates of principal point
m	scale difference of u- and v-axis
o	non-orthogonality of u- and v-axis
K_i, P_i	coefficients of polynomials describing radial and tangential lens distortion

6.2.6 Summary of required parameters

Summarizing Sections 6.2.2 to 6.2.5, the necessary parameters for a thorough computation of the theodolite angles towards a target based on its image coordinates are shown in Table 6.1. It is noted that the image sensor coordinates of the target $(u_{\text{sensor}}, v_{\text{sensor}})$, the theodolite angles of the telescope (Hz, V) and the readings of the tilt compensator $(i_{\text{long}}, i_{\text{trans}})$ are observations and not parameters.

6.3 MAPPING RELATION FOR TELESCOPE CAMERA

For the telescope camera of an IATS, not all parameters listed in Table 6.1 are required. Furthermore, not all parameters can be determined with statistical significance.

For small rotation angles κ, φ and ω, which can be assumed for carefully assembled instruments (Vogel 2006, p. 96), the parameters c, u_0 and v_0 are highly correlated to x_0, y_0 and z_0 (cf. Figure 6.4 and Huang and Harley 1989, p. 52). Furthermore, by using an IATS prototype, Vogel (2006, p. 96) estimated the distance between the camera center and the telescope center with a precision of about 2 mm. Accordingly, x_0, y_0 and z_0 cannot be estimated significantly for a small offset between the centers of the camera and the telescope (Wasmeier 2009, p. 35) which is assumed for a carefully assembled state-of-the-art IATS.

It is further difficult to estimate the rotation angles φ and ω significantly because of the large focal length of the telescope camera and correlations to u_0 and v_0 (Vogel 2006, p. 96; Wasmeier 2009, p. 35). However, φ and ω are required when using image-based measurements in combination with other measurement sensors, such as EDM, automated fine aiming to prisms or manual angle measurements. The angles φ and ω then account for a non-parallelism of the image-based collimation axis, i.e., the principal axis of the camera, and the other collimation axes, such as the EDM axis.

A non-orthogonality and a scale difference of the u- and v-axis of the image sensor are unlikely (Schirmer 1994, p. 27; Hartley and Zisserman 2004, p. 164) and the corresponding parameters are omitted ($m = 1$ and $o = 0$). For the telescope cameras of IATS prototypes, Walser (2004, p. 48) and Vogel (2006, p. 95) conclude that lens distortion can be approximated by a linear function or can be neglected. For the instruments evaluated in this thesis (cf. Section 1.4), the first coefficient K_1 of the radial distortion polynomial is considered (following Wasmeier 2009, pp. 34f.) and tangential distortion, which is typically an order of magnitude smaller than radial distortion (Kraus 2007, p. 53), is neglected.

Summarizing, for the evaluated state-of-the-art IATSs (cf. Section 1.4), the mapping relation between image sensor coordinates and theodolite angles is sufficiently parameterized by the seven quantities shown in Table 6.2.

For $m = 1$ and $o = 0$ in Eq. (6.6), $K_2 = K_3 = 0$ in Eq. (6.7) and $P_1 = P_2 = 0$ in Eq. (6.8), Eq. (6.6) can be written as

$$\begin{bmatrix} u \\ v \end{bmatrix} = \Big(1 + (r^2 - r_0^2)\, K_1\Big) \begin{bmatrix} \cos\kappa & -\sin\kappa \\ \sin\kappa & \cos\kappa \end{bmatrix} \begin{bmatrix} u_{\text{sensor}} - u_0 \\ v_{\text{sensor}} - v_0 \end{bmatrix} \tag{6.27}$$

in which the rotation κ of Eq. (6.11) is mathematically incorporated

Table 6.2: Parameters for mapping relation between image coordinates of telescope camera and theodolite angles

Symbol	Description
c	camera constant
κ	rotation of image sensor about the principal axis
φ, ω	rotation angles describing non-parallelism of principal axis to other collimation axes (e.g. EDM axis)
K_1	first parameter of radial distortion polynomial
u_0, v_0	image sensor coordinates of principal point

in the correction of the image coordinates. For $x_0 = y_0 = z_0 = 0$ and by using Eq. (6.27), Eq. (6.11) can be written as

$$\begin{bmatrix} x_{\text{telescope}} \\ y_{\text{telescope}} \\ z_{\text{telescope}} \end{bmatrix} = \mathbf{R}_\omega \, \mathbf{R}_\varphi \begin{bmatrix} c \\ u \\ -v \end{bmatrix} \alpha \tag{6.28}$$

in which the factor α is also used in Eq. (6.9). For small rotations φ and ω, the matrix product

$$\mathbf{R}_\omega \, \mathbf{R}_\varphi = \begin{bmatrix} \cos\omega\cos\varphi & -\sin\omega & \cos\omega\sin\varphi \\ \sin\omega\cos\varphi & \cos\omega & \sin\omega\sin\varphi \\ -\sin\varphi & 0 & \cos\varphi \end{bmatrix} \tag{6.29}$$

cf. Eqs. (6.13) and (6.14), is approximated by

$$\mathbf{R}_\omega \, \mathbf{R}_\varphi \approx \begin{bmatrix} 1 & -\omega & \varphi \\ \omega & 1 & 0 \\ -\varphi & 0 & 1 \end{bmatrix} \tag{6.30}$$

in which φ and ω are expressed in radians.

Following Eq. (6.15) and summarizing the previous findings, the direction towards a target in the theodolite system can be computed based on the corrected image coordinates u and v by

$$\begin{bmatrix} x_{\text{theodolite}} \\ y_{\text{theodolite}} \\ z_{\text{theodolite}} \end{bmatrix} = \mathbf{R} \begin{bmatrix} 1 & -\omega & \varphi \\ \omega & 1 & 0 \\ -\varphi & 0 & 1 \end{bmatrix} \begin{bmatrix} c \\ u \\ -v \end{bmatrix} \alpha \tag{6.31}$$

in which **R** includes the theodolite angles of the current telescope position and is computed by Eq. (6.16). It is noted that the rotations φ and ω are only required when using image-based measurements in combination with other measurements sensors (e.g. EDM, cf. Section 7.3.4). The theodolite angles towards the target are finally computed by Eqs. (6.17) and (6.18) in which the factor α of Eq. (6.31) cancels out. In case of a tilted setup of the IATS, the theodolite angles can be corrected by Eqs. (6.21) and (6.22).

The distance to the target, which is included in α, cf. Eq. (6.9), is not required for computing the theodolite angles towards the target here. Compared to the wide-angle camera, this is a major advantage of the telescope camera with its camera center corresponding to the theodolite center. A disadvantage of the telescope camera is that the calibration parameters (Table 6.2) are not constant but depend on the focus position of the telescope. However, it is possible to model these dependencies (cf. Section 7.3.3).

6.3.1 Alternative mapping relation by gnomonic projection

By using the previous simplifications for the mapping relation with the telescope camera of an IATS, Schirmer (1994, p. 32) and Juretzko (2005, p. 62) interpret the image coordinates of a target as the gnomonic projection of the corresponding theodolite angles on the image plane (Figure 6.5).

Accordingly, the theodolite angles to the target can alternatively be computed by (rearranged from Snyder 1987, p. 167)

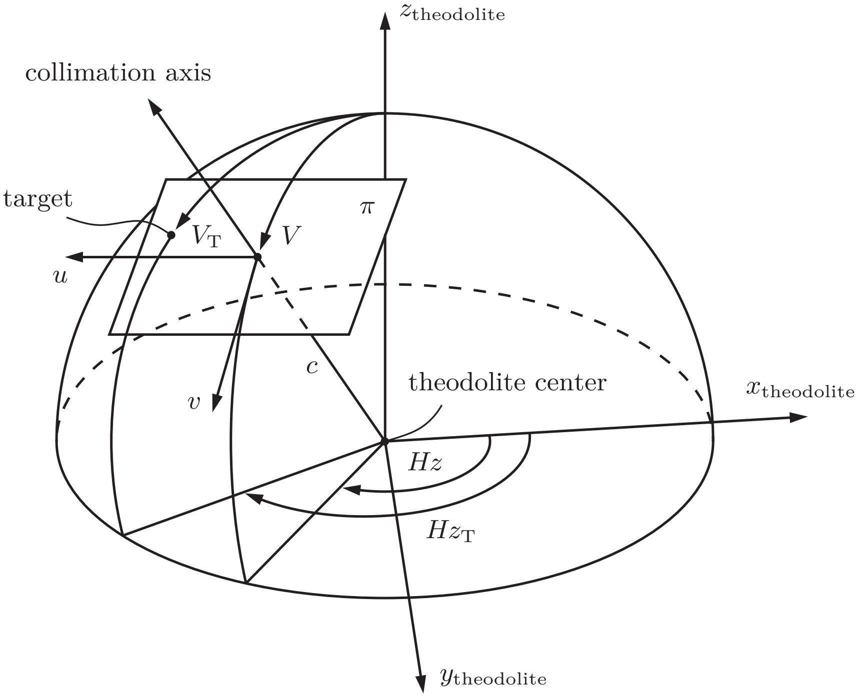

Figure 6.5: Image coordinates and theodolite angles related by gnomonic projection.

$$Hz_{\text{T}} = Hz + \arctan\left(\frac{u}{c\sin V + v\cos V}\right) \tag{6.32}$$

$$V_{\text{T}} = \arccos\left(\frac{c\cos V - v\sin V}{\sqrt{u^2 + v^2 + c^2}}\right) \tag{6.33}$$

where u and v are the corrected image coordinates of the target computed by Eq. (6.27), c is the camera constant and the rotations φ and ω are neglected. Hz and V denote the raw theodolite angles (no tilt correction) of the current telescope position and Hz_{T} and V_{T} are the theodolite angles towards the target.

Eqs. (6.32) and (6.33) yield the telescope angles in Face I. For measurements in Face II, the angles are converted by Eqs. (6.19) and (6.20). In case of a tilted instrument setup, the theodolite angles need to be corrected after Eqs. (6.21) and (6.22).

6.3.2 Notes for practical use

In a practical surveying situation the following observations are carried out for an image-based angle measurement with the IATS' telescope camera:

- Horizontal and vertical theodolite angles (Hz, V) of the current telescope position measured by the angle encoders.
- Longitudinal and transverse inclinations $(i_{\text{long}}, i_{\text{trans}})$ relative to the horizontal pointing direction of the current telescope position measured by the tilt compensator.
- Image coordinates $(u_{\text{sensor}}, v_{\text{sensor}})$ of the target measured on the image sensor.

When reading the theodolite angles from the total station, the resulting values are usually tilt-corrected $(Hz_{\text{tilt}}, V_{\text{tilt}})$ in which the values of the tilt compensator can also be read out. The raw theodolite angles Hz and V result from inverting Eqs. (6.21) and (6.22) so that

$$Hz = Hz_{\text{tilt}} - i_{\text{trans}} \cot V_{\text{tilt}} \tag{6.34}$$

$$V = V_{\text{tilt}} - i_{\text{long}} \tag{6.35}$$

Based on the conducted observations, the theodolite angles to the target can then be computed after the following procedure:

1. The raw theodolite angles of the current telescope position are obtained from reverting the tilt correction according to Eqs. (6.34) and (6.35).
2. The image coordinates are corrected according to Eq. (6.27) by using the calibration parameters for the actual focus position of the telescope (cf. Section 7.3).

3. The theodolite angles to the target are computed after Eqs. (6.17) and (6.18) by using Eq. (6.31) or alternatively by Eqs. (6.32) and (6.33).
4. The tilt-corrected theodolite angles to the target are gained from Eqs. (6.21) and (6.22).

The apparent cumbersome procedure of firstly removing the tilt from the theodolite angles (Step 1) and to re-apply it later (Step 4) is especially necessary for large inclinations, resulting from a careless setup of the IATS, and for targets observed in the boundary areas of the image sensor.

6.3.3 Measurements in different telescope faces

Measurements in Face II

The formulas of Sections 6.2 and 6.3 are valid for both telescope faces. However, for measurements in Face II the image sensor coordinates are computed from the pixel coordinates of the digital image by Eqs. (6.3) and (6.4). Furthermore, the theodolite angles resulting from Eqs. (6.17) and (6.18) or alternatively from Eqs. (6.32) and (6.33) always refer to Face I. Consequently, the resulting angles have to be converted back to Face II, cf. Eqs. (6.19) and (6.20), before applying Eqs. (6.21) and (6.22) for tilt correction.

Two-face measurements

The face averages of the image-based theodolite angles can be computed in two ways. Firstly, the image-based theodolite angles of Face I and II, which result from Steps 1 to 4 in Section 6.3.2, can be averaged.

Alternatively, the face averages of the measurements, i.e., the raw theodolite angles, the tilt readings and the image coordinates, can be computed and Steps 1 to 4 in Section 6.3.2 are applied using these face averages. The face averages of the theodolite angles and the tilt readings are computed by

$$Hz = \left(Hz^{(\mathrm{I})} + \left[(Hz^{(\mathrm{II})} - \pi) \bmod 2\,\pi\right]\right) / \, 2 \tag{6.36}$$

$$V = \left(V^{(\mathrm{I})} + 2\,\pi - V^{(\mathrm{II})}\right) / \, 2 \tag{6.37}$$

$$i_{\mathrm{long}} = \left(i^{(\mathrm{I})}_{\mathrm{long}} - i^{(\mathrm{II})}_{\mathrm{long}}\right) / \, 2 \tag{6.38}$$

$$i_{\mathrm{trans}} = \left(i^{(\mathrm{I})}_{\mathrm{trans}} - i^{(\mathrm{II})}_{\mathrm{trans}}\right) / \, 2 \tag{6.39}$$

By setting

$$\begin{aligned}\begin{bmatrix} u_{\mathrm{sensor}} - u_0 \\ v_{\mathrm{sensor}} - v_0 \end{bmatrix} &= \begin{bmatrix} (u^{(\mathrm{I})}_{\mathrm{sensor}} - u_0) - (u^{(\mathrm{II})}_{\mathrm{sensor}} - u_0) \\ (v^{(\mathrm{I})}_{\mathrm{sensor}} - v_0) - (v^{(\mathrm{II})}_{\mathrm{sensor}} - v_0) \end{bmatrix} / \, 2 \\ &= \begin{bmatrix} u^{(\mathrm{I})}_{\mathrm{sensor}} - u^{(\mathrm{II})}_{\mathrm{sensor}} \\ v^{(\mathrm{I})}_{\mathrm{sensor}} - v^{(\mathrm{II})}_{\mathrm{sensor}} \end{bmatrix} / \, 2 = \begin{bmatrix} u^{(\mathrm{I})}_{\mathrm{pixel}} + u^{(\mathrm{II})}_{\mathrm{pixel}} - w \\ v^{(\mathrm{I})}_{\mathrm{pixel}} + v^{(\mathrm{II})}_{\mathrm{pixel}} - h \end{bmatrix} / \, 2\end{aligned} \tag{6.40}$$

in Eq. (6.27), the face averages of the corrected image coordinates are computed. What can be observed is that the principal point (u_0, v_0) cancels out and that only the width w and the height h of the image sensor need to be known. The relationship between the image coordinates on the physical image sensor $(u_{\mathrm{sensor}}, v_{\mathrm{sensor}})$ and the pixel coordinates in the digital image $(u_{\mathrm{pixel}}, v_{\mathrm{pixel}})$ is discussed in Section 6.2.2.

Along with the canceling of the principal point, using the face averages of the measurements is further advantageous because the theodolite axes errors, i.e., the collimation error ϵ_{coll}, the tilting axis error ϵ_{tilt} and the vertical index error $\epsilon_{\mathrm{index}}$ (Deumlich and Staiger 2002, pp. 205ff.), cancel out. Furthermore, the inclinations of the IATS, which are measured longitudinal i_{long} and transverse i_{trans} to the pointing direction of the telescope by using the instrument's tilt compensator, are biased by index or zero point errors ϵ_{long} and $\epsilon_{\mathrm{trans}}$. These zero point errors also vanish when using the face averages of the tilt readings.

Summarizing, the angle measurements used in Eq. (6.36) and (6.37) result from the readings of the angle encoders Hz_{raw} and V_{raw} and the mentioned instrument errors and tilt readings by

$$V^{(\text{I})} = \underbrace{V^{(\text{I})}_{\text{raw}} - \epsilon_{\text{index}}}_{V^{(\text{I})}_{*}} + \left(i^{(\text{I})}_{\text{long}} - \epsilon_{\text{long}}\right) \tag{6.41}$$

$$V^{(\text{II})} = \underbrace{V^{(\text{II})}_{\text{raw}} - \epsilon_{\text{index}}}_{V^{(\text{II})}_{*}} + \left(i^{(\text{II})}_{\text{long}} - \epsilon_{\text{long}}\right) \tag{6.42}$$

and

$$Hz^{(\text{I})} = Hz^{(\text{I})}_{\text{raw}} - \epsilon_{\text{coll}}/\sin V^{(\text{I})}_{*} + \left(i^{(\text{I})}_{\text{trans}} - \epsilon_{\text{trans}} - \epsilon_{\text{tilt}}\right)\cot V^{(\text{I})} \tag{6.43}$$

$$Hz^{(\text{II})} = Hz^{(\text{II})}_{\text{raw}} - \epsilon_{\text{coll}}/\sin V^{(\text{II})}_{*} + \left(i^{(\text{II})}_{\text{trans}} - \epsilon_{\text{trans}} - \epsilon_{\text{tilt}}\right)\cot V^{(\text{II})} \tag{6.44}$$

for measurements in Face I and II. Concerning the signs of the individual errors, different conventions exist (e.g. Walser 2004, pp. 45f; Wasmeier 2009, p. 20). In Eqs. (6.41) to (6.44) negative signs are used because the corrected measurements result from the biased measurements by subtracting the errors.

It can be seen from Eq. (6.20) that

$$\sin V^{(\text{II})} = -\sin V^{(\text{I})} \tag{6.45}$$

$$\cot V^{(\text{II})} = -\cot V^{(\text{I})} \tag{6.46}$$

in which similar relations

$$i^{(\text{II})}_{\text{long}} = -i^{(\text{I})}_{\text{long}} \tag{6.47}$$

$$i^{(\text{II})}_{\text{trans}} = -i^{(\text{I})}_{\text{trans}} \tag{6.48}$$

are available for the measured inclinations of the IATS. Inserting Eqs. (6.45) to (6.48) in Eqs. (6.41) to (6.44) and computing the face averages after Eqs. (6.36) and (6.37) reveals that the theodolite axes errors ϵ_{coll}, ϵ_{tilt} and ϵ_{index} and the zero point errors of the tilt compensator ϵ_{long} and ϵ_{trans} cancel out. The inclinations i_{long} and i_{trans} themselves remain in the face averages. This is because a tilted setup cannot be corrected by two-face measurements (Deumlich and Staiger 2002, p. 209).

6.4 CONCLUSIONS

In this chapter the mapping relation between image coordinates and theodolite angles has been worked out. This is essential for image-based measurements with an IATS because the image coordinates of a target, which result from different image processing techniques, must be related to the corresponding theodolite angles for further computations. The general relation involves a camera whose center is eccentric to the theodolite center (such as the wide-angle camera of an IATS). For an eccentric camera, the slope distance towards the target is required for a thorough mapping. For the IATS's telescope camera, whose center approximately corresponds to the theodolite center, the slope distance is not required and the mapping relation is sufficiently parameterized by seven mapping parameters. The calibration of these parameters is discussed in Chapter 7.

7

Calibration

7.1 INTRODUCTION

An IATS combines one or more cameras with a total station. Accordingly, its calibration comprises

- the calibration of the total station and
- the calibration of the mapping parameters that relate the camera system to the system of the total station.

The calibration of the total station, which involves

- the theodolite axes errors,
- the zero point errors of the two-axis tilt compensator,
- the zero point offset of the fine aiming module, and
- different EDM errors (zero point, scale, cyclic phase)

is carried out by well-known calibration routines and it is referred to Deumlich and Staiger (2002) for a discussion.

In general, the calibration of the mapping parameters involves the quantities given by Table 6.1. For applications with high accuracy demands (e.g. Chapters 2 and 4), the telescope camera is used because its angle per pixel α_{px} is smaller than α_{px} of the wide-angle camera (cf. Section 1.3.1). For the telescope cameras of the evaluated instruments (cf. Section 1.4), the transformation from image coordinates to theodolite angles is sufficiently parameterized by the quantities of Table 6.2.

As discussed in Section 6.3, another advantage of the telescope camera over the wide-angle camera is that the distance to the target is not required for the image-based computation of the theodolite angles towards the target.

In this chapter, the calibration of the telescope camera's mapping parameters is explained and experimentally evaluated. The proposed calibration procedure does not require additional hardware and is fast and automated albeit providing a sufficient accuracy for the results.

Related publications

This chapter is based on but heavily extends the article of Ehrhart and Lienhart (2017a).

7.2 REPORTED CALIBRATION APPROACHES

The calibration of an IATS is a well-studied topic and reports date back to the late 1980s. Based on the original calibration approach of Huang and Harley (1989), where the total station's ability to automatically rotate its telescope by precisely known angles is used, numerous modifications were proposed (Walser 2004; Juretzko 2005; Vogel 2006; Wasmeier 2009; Schlüter et al. 2009; Bürki et al. 2010; Knoblach 2011; Zhou et al. 2016). The reported calibrations mainly differ in the number of estimated calibration parameters and the usage of additional equipment such as a collimator (Walser 2004, p. 110; Vogel 2006, pp. 42ff.).

The basic idea (Huang and Harley 1989) of the different approaches is the generation of a virtual calibration field by observing one or more targets under different telescope positions, i.e., viewing directions of the telescope. The observations at each telescope position are the readings of the angle encoders, the inclinations measured by the two-axis tilt compensator and the position of the target on the image sensor. These observations can be used to determine the mapping parameters.

For some mapping parameters, such as the camera constant, a dependency on the focus position of the telescope is reported (Vogel 2006, pp. 99f; Wasmeier 2009, p. 37; Knoblach 2011, pp. 106f.). Fortunately, these dependencies can be described by polynomials of the focus position. The camera constant c can be modeled by a quadratic polynomial and the distortion coefficient K_1 and the coordinates of the principal point (u_0, v_0) by linear functions (Wasmeier 2009, pp. 36f.). However, it is therefore required to calibrate the telescope camera at different focus positions to determine the coefficients of the respective polynomials.

The reported approaches either focus on a calibration of the camera only or introduce the theodolite axes errors (cf. Deumlich and Staiger 2002, pp. 205ff.) of the total station as additional parameters. The latter is necessary for instruments without a physical reticle such as the IATS prototypes investigated by Walser (2004), Vogel (2006) and Wasmeier (2009) and recent state-of-the-art IATSs (Trimble 2016b). When estimating the theodolite axes errors, several targets at different vertical angles are observed for one focus position. This reduces the correlation between the axes errors and the mapping parameters (Walser 2004, p. 107). However, especially the collimation error and the vertical index error are still difficult to separate from the image coordinates u_0 and v_0 of the principle point (Wasmeier 2009, p. 35).

Table 7.1: Number of targets, grid size of virtual calibration field and number of focus position of different calibration approaches

Calibration approach	**Number of targets**	**Grid size**	**Focus positions**
Walser (2004)	$6^{(1)}$	3×3	n.a.
Juretzko (2005)	1	n.a.	n.a.
Vogel (2006)	4	6×8	13
Wasmeier (2009)	$4^{(1)}$	6×8	$23^{(2)}$
Schlüter et al. (2009)	2	24 to $60^{(3)}$	$1^{(4)}$
Bürki et al. (2010)	1	6×6	8
Knoblach (2011)	n.a.	n.a.	8
Zhou et al. (2016)	1	4×4	8
proposed (Sections 7.3 and 7.4)	1	$16^{(5)}$	6

(1) observed under different vertical angles
(2) a reduction is considered (Wasmeier 2009, p. 36)
(3) circular arrangement of telescope positions
(4) calibration only at focus position infinity
(5) irregular distribution of virtual targets; different for each focus position

For the reported calibration approaches and the proposed approach (cf. Sections 7.3 and 7.4), Table 7.1 summarizes the number of targets and the grid size of the virtual calibration field, i.e., the number of telescope positions for each focus position. Furthermore, the number of evaluated focus positions, which are typically distributed equally over the focusing range, are given. Dependent on the number of the estimated calibration parameters, the number of used targets, which are partly measured under different vertical angles, and the grid size of the virtual calibration field vary.

7.3 PROPOSED CALIBRATION APPROACH

The calibration approach proposed in this thesis is based on the findings summarized in Section 7.2. The goal is a calibration procedure which is fast and automated albeit providing a sufficient accuracy of the results. Furthermore, no additional hardware, such as a collimator, should be used.

The basic idea is to separate time-variable parameters from temporally stable parameters. For the time-variable parameters a fast and simple field calibration routine is required in which a more time consuming calibration procedure is acceptable for temporally stable parameters.

Table 6.2 summarizes the seven required mapping parameters for the telescope cameras of the state-of-the-art IATSs evaluated in this thesis (cf. Section 1.4). The camera constant c, the rotation of the image sensor κ, the radial distortion coefficient K_1, and the principal point u_0, v_0 can be calibrated automatically for different focus positions by using the virtual calibration field mentioned in Section 7.2. The calibration procedure is described in Sections 7.3.1 to 7.3.3. The calibration of the rotations φ and ω between the image-based collimation axis, i.e., the principal axis of the camera, and other collimation axes (e.g. EDM axis) is described in Section 7.3.4.

7.3.1 Principal point

The image sensor coordinates of the principal point u_0 and v_0 can be computed from (Bürki et al. 2010; Knoblach 2011, p. 105)

$$u_0 = \frac{u_{\text{sensor}}^{(\text{I})} + u_{\text{sensor}}^{(\text{II})}}{2} \tag{7.1}$$

$$v_0 = \frac{v_{\text{sensor}}^{(\text{I})} + v_{\text{sensor}}^{(\text{II})}}{2} \tag{7.2}$$

in which the coordinates of the target on the image sensor are measured in Face I and II. It is hereby not necessary that the telescope is positioned towards the target center for the measurements. Accordingly, u_0 and v_0 can be determined automatically for a motorized IATS.

The correction of the image coordinates according to Eq. (6.27) is not necessary prior to the computation. This is because the corrections show an opposite sign for Face I and II and consequently cancel out due to the sum in the computation of u_0 and v_0. However, it is noted that u_0 and v_0 according to Eqs. (7.1) and (7.2) also include the collimation and the index error of the total station. Furthermore, v_0 includes the zero point error of the tilt compensator in longitudinal direction if this error was not calibrated in advance. To avoid an absorbing of the tilting axis error, the measurements should be carried out under a horizontal sighting ($V \approx 100\,\mathrm{gon}$).

Using u_0 and v_0 according to Eqs. (7.1) and (7.2) for image-based measurements has the effect that the theodolite angles to a target are the same for both telescope faces – which is a desirable achievement. For computing u_0 and v_0, Eqs. (7.1) and (7.2) are of course evaluated for different telescope positions and subsequently averaged (Bürki et al. 2010; Knoblach 2011, p. 105) to increase the precision of the results.

As mentioned in Section 7.2, the principal point varies with the focus position of the telescope. To model this dependency, u_0 and v_0 must be determined at different focus positions (Section 7.3.3).

7.3.2 Camera constant, rotation of image sensor and distortion

The parameters c, κ and K_1 can be determined by using the virtual calibration field mentioned in Section 7.2. The true, tilt-corrected theodolite angles to the target ($Hz_{\mathrm{T,tilt}}, V_{\mathrm{T,tilt}}$) are introduced as additional parameters. The observations are the theodolite angles (Hz, V), the readings of the tilt compensator ($i_{\mathrm{long}}, i_{\mathrm{trans}}$), and the image sensor coordinates of the target ($u_{\mathrm{sensor}}, v_{\mathrm{sensor}}$) at n different telescope positions.

To lower the correlation between c and K_1, a second zero crossing of the distortion polynomial at a radial distance r_0 from the principal point is specified (cf. Section 6.2.2). As discussed in Section 7.4, the selection of the targets in the virtual calibration field, i.e., the telescope positions, is also crucial for the correlation of c

and K_1. To obtain reliable estimates for κ and K_1, the telescope positions should be chosen so that the imaged targets also occur in the boundary areas of the image sensor.

The functional relationship between the unknown parameters and the observations is given by

$$\psi_1 = u - c\,\frac{y_{\text{telescope}}}{x_{\text{telescope}}} = 0 \tag{7.3}$$

$$\psi_2 = v + c\,\frac{z_{\text{telescope}}}{x_{\text{telescope}}} = 0 \tag{7.4}$$

where

$$\begin{bmatrix} x_{\text{telescope}} \\ y_{\text{telescope}} \\ z_{\text{telescope}} \end{bmatrix} = \begin{bmatrix} \cos Hz \sin V & \sin Hz \sin V & \cos V \\ -\sin Hz & \cos Hz & 0 \\ -\cos Hz \cos V & -\sin Hz \cos V & \sin V \end{bmatrix} \begin{bmatrix} \cos Hz_{\text{T}} \sin V_{\text{T}} \\ \sin Hz_{\text{T}} \sin V_{\text{T}} \\ \cos V_{\text{T}} \end{bmatrix} \tag{7.5}$$

in which Hz and V are the measured, raw theodolite angles (without tilt correction) of the current telescope position. As mentioned in Section 6.3.2, the theodolite angles read from the IATS are usually tilt-corrected in which the raw angles Hz and V can be obtained from Eqs. (6.34) and (6.35).

From Eqs. (6.21) to (6.24) it follows that the raw theodolite angles (no tilt correction) to the target can be computed by

$$Hz_{\text{T}} = Hz_{\text{T,tilt}} - i_{\text{abs}} \cos(i_{\text{angle}} + Hz_{\text{T}}) \cot V_{\text{T,tilt}} \tag{7.6}$$

$$V_{\text{T}} = V_{\text{T,tilt}} - i_{\text{abs}} \sin(i_{\text{angle}} + Hz_{\text{T}}) \tag{7.7}$$

in which i_{abs} and i_{angle} are computed from i_{long} and i_{trans} by using Eqs. (6.25) and (6.26). Removing the tilt is necessary because a transverse inclination relative to the target during the calibration procedure results in a biased estimation of κ. For a carefully set up IATS with a small inclination i_{abs}, an iterative computation of Eqs. (7.6) and (7.7) is typically not required.

The corrected image coordinates results from, cf. Eq. (6.27),

$$\begin{bmatrix} u \\ v \end{bmatrix} = \left(1 + (r^2 - r_0^2)\, K_1\right) \begin{bmatrix} \cos\kappa & -\sin\kappa \\ \sin\kappa & \cos\kappa \end{bmatrix} \begin{bmatrix} (u_{\text{sensor}} + \mathrm{v}_u) - u_0 \\ (v_{\text{sensor}} + \mathrm{v}_v) - v_0 \end{bmatrix} \tag{7.8}$$

in which v_u and v_v are the residuals of the observations u_{sensor} and v_{sensor}. The image sensor coordinates of the principal point u_0 and v_0 are known from Section 7.3.1. However, when using the face averages of the measurements (Section 6.3.3), the principal point is not required, cf. Eq. (6.40).

The adjustment of the unknown parameters is done according to the Gauss-Helmert-Model (e.g. Niemeier 2008, pp. 172ff.) accounting for the findings of Lenzmann and Lenzmann (2004). The functional relationship between the unknown parameters and the observations is hereby established by Eqs. (7.3) and (7.4). The Jacobian matrices **A** and **B** of the adjustment problem, which include the partial derivatives w.r.t. the m unknown parameters and the residuals of the n observations, respectively, can be set up by

$$\mathbf{A}_{[\mathbf{2n}\times\mathbf{m}]} = \begin{bmatrix} \frac{\partial\boldsymbol{\psi_1}}{\partial c} & \frac{\partial\boldsymbol{\psi_1}}{\partial\kappa} & \frac{\partial\boldsymbol{\psi_1}}{\partial K_1} & \frac{\partial\boldsymbol{\psi_1}}{\partial Hz_{\text{T,tilt}}} & \frac{\partial\boldsymbol{\psi_1}}{\partial V_{\text{T,tilt}}} \\ \frac{\partial\boldsymbol{\psi_2}}{\partial c} & \frac{\partial\boldsymbol{\psi_2}}{\partial\kappa} & \frac{\partial\boldsymbol{\psi_2}}{\partial K_1} & \frac{\partial\boldsymbol{\psi_2}}{\partial Hz_{\text{T,tilt}}} & \frac{\partial\boldsymbol{\psi_2}}{\partial V_{\text{T,tilt}}} \end{bmatrix} \tag{7.9}$$

and

$$\mathbf{B}_{[\mathbf{2n}\times\mathbf{2n}]} = \begin{bmatrix} \mathrm{diag}(\frac{\partial\boldsymbol{\psi_1}}{\partial\mathrm{v}_u}) & \mathrm{diag}(\frac{\partial\boldsymbol{\psi_1}}{\partial\mathrm{v}_v}) \\ \mathrm{diag}(\frac{\partial\boldsymbol{\psi_2}}{\partial\mathrm{v}_u}) & \mathrm{diag}(\frac{\partial\boldsymbol{\psi_2}}{\partial\mathrm{v}_v}) \end{bmatrix} \tag{7.10}$$

It can be seen from Eqs. (6.32) and (6.33) that changes of the theodolite angles are proportional to changes of the image coordinates. Accordingly, errors in the observations of u_{sensor} and v_{sensor} would cause residuals for the measurements of Hz and V and vice versa if both measurement types were introduced as observations in the adjustment. This leads to convergence problems in the iterative adjustment of the parameters. Accordingly, the partial derivatives w.r.t. the residuals of the theodolite angles are omitted in Eq. (7.10). However, errors in the measured theodolite angles will be absorbed by u_{sensor} and v_{sensor} so that Hz and V also contribute to the standard deviations of the estimated parameters which is a desirable effect for a system calibration.

The equation system

$$\begin{bmatrix} \mathbf{BQB^T} & \mathbf{A} \\ \mathbf{A^T} & \mathbf{0_{[u,u]}} \end{bmatrix} \begin{bmatrix} \mathbf{k} \\ \boldsymbol{\Delta\xi} \end{bmatrix} + \begin{bmatrix} \mathbf{w} \\ \mathbf{0} \end{bmatrix} = \mathbf{0} \tag{7.11}$$

in which the vector of inconsistency

$$\mathbf{w} = \begin{bmatrix} \boldsymbol{\psi_1} \\ \boldsymbol{\psi_2} \end{bmatrix} - \mathbf{B}\,\mathbf{v_0} \tag{7.12}$$

and the covariance matrix of the observations $\mathbf{Q}$ are used, can be solved for $\mathbf{k}$ and $\boldsymbol{\Delta\xi}$ which are used to update the parameter vector by

$$\boldsymbol{\xi} = \boldsymbol{\xi_0} + \boldsymbol{\Delta\xi} \tag{7.13}$$

and the vector of residuals by

$$\mathbf{v} = \begin{bmatrix} \mathbf{v_u} \\ \mathbf{v_v} \end{bmatrix} = \mathbf{Q}\,\mathbf{B^T}\,\mathbf{k} \tag{7.14}$$

Mathematically, the only observations of the adjustment problem are the image coordinates of the target at the different telescope positions. Accordingly, the covariance matrix of the observations can be set to

$$\mathbf{Q} = \mathbf{I} \tag{7.15}$$

assuming an equal precision of the measured image coordinates in u- and v-direction.

The adjustment is iteratively repeated until a sufficient accuracy is achieved, i.e., until $|\boldsymbol{\Delta\xi}|$ and $|\mathbf{v}-\mathbf{v_0}|$ are smaller than a certain threshold. For each new iteration, the updated parameter vector and the updated vector of residuals is used by setting

$$\boldsymbol{\xi}_\mathbf{0} = \boldsymbol{\xi} \tag{7.16}$$

and

$$\mathbf{v_0} = \mathbf{v} \tag{7.17}$$

in which it is emphasized that the residuals v_u and v_v in Eq. (7.8) are updated by Eq. (7.14), cf. Lenzmann and Lenzmann (2004).

The initial values of the iterative adjustment can be stated with

$$\boldsymbol{\xi}_\mathbf{0} = \begin{bmatrix} c \\ \kappa \\ K_1 \\ Hz_{\mathrm{T,tilt}} \\ V_{\mathrm{T,tilt}} \end{bmatrix}_0 = \begin{bmatrix} 1/k \\ 0 \\ 0 \\ d_1 \\ d_2 \end{bmatrix} \tag{7.18}$$

for the parameter vector in which k, d_1 and d_2 result from solving

$$\begin{bmatrix} Hz \\ \vdots \\ V \\ \vdots \end{bmatrix} = \begin{bmatrix} -(u_{\mathrm{sensor}} - u_0) & 1 & 0 \\ \vdots & \vdots & \vdots \\ -(v_{\mathrm{sensor}} - v_0) & 0 & 1 \\ \vdots & \vdots & \vdots \end{bmatrix} \begin{bmatrix} k \\ d_1 \\ d_2 \end{bmatrix} \tag{7.19}$$

and with

$$\mathbf{v_0} = \begin{bmatrix} \mathbf{v_u} \\ \mathbf{v_v} \end{bmatrix} = \mathbf{0} \tag{7.20}$$

for the vector of residuals.

The adjustment typically converges after a few iterations. For low correlations between the estimated parameters (cf. Section 7.4), the selection of the initial values does not influence the results.

The rotation κ of the image sensor about the principal axis of the camera is invariant w.r.t. the focus position of the telescope. However, c and K_1 are known to vary with the focus position (Section 7.2) and calibrations at different focus positions are required to model this dependency (Section 7.3.3).

7.3.3 Focus-dependent calibration

As mentioned in Section 7.2, the calibration parameters u_0 and v_0 (Section 7.3.1) and c and K_1 (Section 7.3.2) depend on the focus position of the telescope. These dependencies can be modeled by polynomials of different order of the focus position f by

$$c(f) = c^{(0)} + c^{(1)} f + c^{(2)} f^2 \tag{7.21}$$

$$K_1(f) = K_1^{(0)} + K_1^{(1)} f \tag{7.22}$$

$$u_0(f) = u_0^{(0)} + u_0^{(1)} f \tag{7.23}$$

$$v_0(f) = v_0^{(0)} + v_0^{(1)} f \tag{7.24}$$

in which the rotation κ of the image sensor about the principal axis of the camera is invariant w.r.t. the focus position of the telescope.

To determine the coefficients of the polynomials, calibrations according to Sections 7.3.1 and 7.3.2 are performed at n different focus positions f. The coefficients of the respective polynomials are gained from solving

$$\begin{bmatrix} c(f_1) \\ \vdots \\ c(f_n) \end{bmatrix} = \begin{bmatrix} 1 & f_1 & f_1^2 \\ \vdots & \vdots & \vdots \\ 1 & f_n & f_n^2 \end{bmatrix} \begin{bmatrix} c^{(0)} \\ c^{(1)} \\ c^{(2)} \end{bmatrix} \tag{7.25}$$

$$\begin{bmatrix} K_1(f_1) \\ \vdots \\ K_1(f_n) \end{bmatrix} = \begin{bmatrix} 1 & f_1 \\ \vdots & \vdots \\ 1 & f_n \end{bmatrix} \begin{bmatrix} K_1^{(0)} \\ K_1^{(1)} \end{bmatrix} \tag{7.26}$$

in which the coefficients of u_0 and v_0 are obtained analogously to Eq. (7.26) and κ results from averaging the individual $\kappa(f)$.

Alternatively, the coefficients of the polynomials can be introduced in the adjustment of Section 7.3.2 directly to obtain the correlations between the individual parameters (cf. Section 7.4).

When estimating the coefficients of the polynomials directly, 16 virtual targets measured at 6 different focus positions were found to produce reliable results for the calibration parameters (cf. Sections 7.4 and 7.5). Excluding the warm-up time of the instrument prior to the calibration, the full calibration takes less than 40 minutes. It is hereby noted that the calibration is a fully automated procedure after the targets at the different distances (resulting in different focus positions) have been set up and the virtual targets (i.e., the different telescope positions) have been defined.

7.3.4 Rotation between different collimation axes

A rotation between the image-based collimation axis, i.e., the principal axis of the camera, and other collimation axes (e.g. EDM axis) can be described by the rotation angles φ and ω (cf. Figure 6.4). For the image-based collimation axis being aligned with a target, i.e., the image coordinates u and v of the target are zero, the angles φ and ω describe the necessary rotation of the telescope for an alignment of e.g. the EDM axis with the target.

Following Eq. (6.31), the theodolite angles to the target can be expressed by

$$\begin{bmatrix} \cos Hz_{\mathrm{T}} \sin V_{\mathrm{T}} \\ \sin Hz_{\mathrm{T}} \sin V_{\mathrm{T}} \\ \cos V_{\mathrm{T}} \end{bmatrix} = \mathbf{R} \begin{bmatrix} 1 & -\omega & \varphi \\ \omega & 1 & 0 \\ -\varphi & 0 & 1 \end{bmatrix} \begin{bmatrix} \overline{c} \\ \overline{u} \\ -\overline{v} \end{bmatrix} \tag{7.27}$$

where **R** is computed from Eq. (6.16) and $\overline{c}$, $\overline{u}$ and $\overline{v}$ result from

$$\begin{bmatrix} \overline{c} \\ \overline{u} \\ -\overline{v} \end{bmatrix} = \begin{bmatrix} c \\ u \\ -v \end{bmatrix} / \sqrt{c^2 + u^2 + v^2} \tag{7.28}$$

in which u and v are computed from Eq. (6.27). It is hereby not necessary that the image-based collimation axis is aligned with the target which would result in $u = v = 0$.

Eq. (7.27) can be rearranged to

$$\mathbf{R}^T \begin{bmatrix} \cos Hz_\mathrm{T} \sin V_\mathrm{T} \\ \sin Hz_\mathrm{T} \sin V_\mathrm{T} \\ \cos V_\mathrm{T} \end{bmatrix} - \begin{bmatrix} \overline{c} \\ \overline{u} \\ -\overline{v} \end{bmatrix} = \begin{bmatrix} -\overline{v} & -\overline{u} \\ 0 & \overline{c} \\ -\overline{c} & 0 \end{bmatrix} \begin{bmatrix} \varphi \\ \omega \end{bmatrix} \tag{7.29}$$

which can be solved for φ and ω. The theodolite angles to the target Hz_T and V_T are hereby gained from the measurement sensor whose collimation axis should be rotated to the image-based collimation axis. The matrix **R** includes the raw theodolite angles (no tilt correction) of the telescope position at which the image is captured (cf. Section 6.2.5). Consequently, Hz_T and V_T also need to be introduced without tilt in which the corresponding values can be computed by Eqs. (7.6) and (7.7).

Dependent on the application, the rotations φ and ω of the image-based collimation axis to three other collimation axes are of interest. These axes are the collimation axis of manual angle measurements, the collimation axis of the automated fine aiming to prisms, and the collimation axis of the EDM sensor. To determine the rotation angles by solving Eq. (7.29) for φ and ω, the theodolite angles to the target Hz_T and V_T need to be computed by the respective measurement sensor. Additionally, the image coordinates of the target and the corresponding telescope angles, which are included in **R**, are measured.

For manual measurements this is a straightforward procedure in which the angles to a visual target are measured manually and also by image-based measurements. For automated measurements with the IATS's fine aiming module an analogous procedure is applied in which the angles towards the center of a prism are measured.

EDM axis

The rotation between the image-based collimation axis and the EDM collimation axis can be determined by using the findings of Omidalizarandi and Neumann (2015) where the reflectivity values of a terrestrial laser scanner (TLS) are used to determine the extrinsic calibration parameters between the TLS and a digital camera. Some IATS are available as scanning total stations which are able to measure 3D coordinates at a measurement rate comparable to a TLS, e.g. 1 kHz (Leica 2015a, p. 69) or 26.6 kHz (Trimble 2016b).

When scanning a target with different reflective properties, e.g. a black circle on a white background, the intensity or the signal-to-noise-ratio (SNR) of the reflected EDM signal typically varies dependent on the measurement point (black circle or white background). Accordingly, the center coordinates of the circle can be determined from the results of the scan, i.e., the coordinates and reflectivity values of points on the black circle and the white background. With knowledge of the station coordinates of the ITAS, the angles Hz_T and V_T to the circle center can be computed. The circle center can also be determined from image-based measurements which provides the necessary observations for computing φ and ω by Eq. (7.29).

For an IATS without scanning functionality, the approach of Ullrich and Möser (2016) for identifying target markings can be adopted. Here, the intensity values of the reflectorless EDM of a total station are recorded while moving the telescope over the target area at constant speed.

The image-based angle measurements are affected by an inexact movement of the focusing lens (Wasmeier 2009, p. 28) which demonstrates its effect in a change of u_0 and v_0 (computed after Section 7.3.1) with a change of the focus position. This is neither the case for the scanning results because the EDM signals do not pass the movable focusing lens nor for the face averages of the angle measurements (Deumlich and Staiger 2002, p. 83). Consequently, the face averages of the image-based angle measurements are used in Eq. (7.29). An alternative is to use single-face image-based measurements and up-to-date parameters for u_0 and v_0 for the respective focus position of the telescope.

However, the single-face image-based measurements with up-to-date parameters for the principal point are free of the instrument errors which are included in u_0 and v_0 (cf. Section 7.3.1). This is also the case for the face-averaged image-based angle measurements but not for the scanning results which are measured in Face I (scanning in Face II is not possible with the used firmware versions of the evaluated IATSs, cf. Section 1.4). Consequently, the rotation angles φ and ω absorb the deviations between the actual instrument errors and the values set in the onboard software of the IATS. Hereby, deviations of the collimation error are absorbed by ω whereas deviations of the vertical index error are absorbed by φ (cf. Figure 6.4). To avoid an absorbing of the frequently changing instrument errors by φ and ω, the up-to-date instrument errors should be set in the onboard software of the IATS before calibrating φ and ω. The zero point errors of the tilt compensator are no issue here because raw angles (no tilt correction) are used in Eq. (7.29).

7.3.5 Fast recalibration

As outlined in Section 7.3.3, most calibration parameters depend on the focus position of the telescope in which these dependencies are modeled by polynomials of different order by Eqs. (7.21) to (7.24). Consequently, the calibration must involve measurements at different focus positions which is time consuming (about 40 minutes for the setup of Section 7.4) and impractical for a fast in-field calibration.

However, it is shown in Section 7.6 that the effects of temporal changes of most parameters are negligible for many measurements applications. For example, by using 8-months-old calibration parameters and two-face measurements, the image-based theodolite angles towards a target vary by ± 0.3 mgon dependent on the position of the target on the image sensor in which ± 0.2 mgon can be achieved when using up-to-date parameters (cf. Section 7.5).

The principal point (u_0, v_0), which also includes the instrument's collimation and index error (cf. Section 7.3.1), varies noticeably and quite frequently over time. The principal point depends on the focus position and its calibration thus requires measurements at different focus positions. However, it is found in Section 7.6 that the focus-dependent coefficients of the linear functions in Eqs. (7.23) and (7.24) are temporally stable.

Consequently, measurements at one focus position are sufficient to update the focus-independent coefficients by

$$u_{0,\text{new}}^{(0)} = u_0(f) - u_{0,\text{old}}^{(1)}\, f \tag{7.30}$$

$$v_{0,\text{new}}^{(0)} = v_0(f) - v_{0,\text{old}}^{(1)}\, f \tag{7.31}$$

in which $u_0(f)$ and $v_0(f)$ result after Section 7.3.1. This is a very fast method for recalibrating the principal point, which also includes the instrument's collimation and index error (Section 7.3.1), and should be performed prior to each measurement task including measurements in one telescope face only.

7.3.6 Notes for practical use

For an accurate calibration of the IATS according to the previous sections, different aspects must be considered:

- The calibration should be performed under controlled environmental conditions and with a stable setup of the IATS and the target. Nevertheless, the stability of the setup should be verified by measuring a selected virtual target at the beginning, during and at the end of the calibration.

- A sufficient warm-up time after switching on the instrument, e.g. 1 hour, should be taken into account before starting the calibration. It is demonstrated in Section 4.2.2 that the alidade of the instrument changes its position during the warm-up time which can bias the calibration results. For temperature differences between the storage and the working environment, an additional warm-up time must be considered (e.g. 2 min/°C but at least 15 min, cf. Leica 2015a, p. 55).
- The measurements should be taken in both telescope faces. Compared to measurements in one face, the uncertainties in the calibration results caused by changes of the instrument errors during the calibration are much smaller.
- The target should be observed under a horizontal sighting. It is mentioned in Section 7.3.1 that u_0 and v_0 absorb the collimation and the vertical index error of the total station. For measurements under steep vertical angles, also the tilting axis error will be incorporated which is an undesired effect.
- The tilt of the IATS must be handled correctly, cf. Eqs. (7.6) and (7.7). Otherwise, the calibrated rotation of the image sensor κ will include the transverse inclination of the IATS.
- The focus positions for the focus-dependent calibration should be distributed equally over the specified focusing range. It is hereby noted that the relationship between the focus position and the distance is not linear (cf. Section 7.4).
- The selection of the targets in the virtual calibration field is crucial for the correlation between the estimated parameters (cf. Section 7.4). A simulation of the involved adjustment (cf. Sections 7.3.2 and 7.3.3), which does not require real measurement data (Niemeier 2008, pp. 340f.), can be used to identify appropriate virtual targets prior to the calibration procedure.

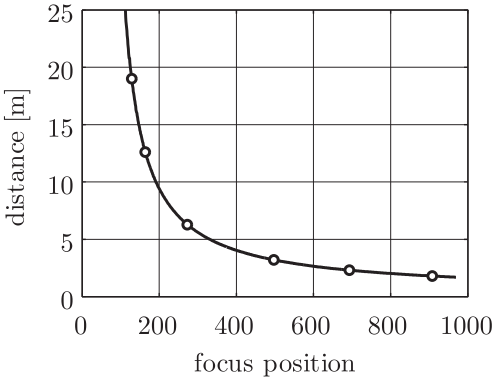

Figure 7.1: Relationship between focus position and distance for the investigated *Leica MS60* with positions used for calibration (a similar relation can be found for the *Leica MS50*, cf. Zhou et al. 2016).

7.4 CALIBRATION RESULTS

The calibration procedure proposed in Section 7.3 was evaluated by using a *Leica MS60* (cf. Section 1.4). For this instrument, the focus range is specified from 1.7 m to infinity (Leica 2015a, p. 71) which corresponds to the focus positions 969 and 62 (unknown unit). The current focus position of the telescope can be read out by using the *Leica GeoCOM* interface (Leica 2015b). The instrument was switched on several hours before the beginning of the calibration. To account for the variability of the calibration parameters with the focus position, six different distances and thus focus positions were used (Figure 7.1). The maximum distance of the calibration was less than 20 m. Consequently, the calibration can be, and also was, carried out indoors under controlled environmental conditions. This mitigates the reservations of Wasmeier (2009, p. 32) concerning the impracticability of this calibration approach due to the requirement of large distances. Accordingly, further instrumentation, such as an optical collimator (Walser 2004, p. 110; Vogel 2006, pp. 42ff.), is not required.

For each focus position or distance, the target was observed under an approximately horizontal sighting ($V \approx 100\,\mathrm{gon}$) and was measured in both telescope faces. For the generation of the virtual calibration field at each focus position, the stable target was observed under 16 different telescope positions. The stability of the setup was checked by measuring a selected virtual target at the beginning and the end of the measurements at each focus position. Excluding the acclimatization and the warm-up time of the instrument, the duration for this (automated) calibration is about 6 minutes for each focus position and less than 40 minutes in total.

As illustrated in Figure 7.2, the distribution of the targets on the image sensor is crucial for the correlations between the estimated parameters. For both calibrations, 16 virtual targets are observed at 6 different focus positions resulting in 96 targets in total. The coefficients for modeling the individual calibration parameters, e.g. $c^{(0)}$, $c^{(1)}$ and $c^{(2)}$ for the modeling of c by a quadratic polynomial after Eq. (7.21), are of course highly correlated. Apart from that, the coefficients for modeling c and K_1 are also correlated.

For a symmetric distribution of the targets on the image sensor (Figure 7.2a), which is an intuitive definition of the virtual calibration field, the model coefficients of c and K_1 show correlation coefficients of up to 0.4. When choosing different distributions of the virtual target for each focus positions (Figure 7.2b), the correlation coefficients can be reduced to less than 0.1. It is hereby noted that the relatively low correlations for both cases result from introducing the second zero crossing of the distortion polynomial at a radial distance r_0 from the principal point (cf. Section 6.2.2). If r_0 is omitted ($r_0 = 0$), the coefficients of c and K_1 are correlated by up to 0.8 for the present calibration.

The focus-dependent calibration parameters and their 99% confidence levels obtained from the proposed calibration procedure with the target distributions of Figure 7.2b are visualized in Figure 7.3. The camera constant c varies with the focus position by over 1700 px. It is therefore inevitable to use the focus-dependent value of this parameter for computing the theodolite angles towards a tar-

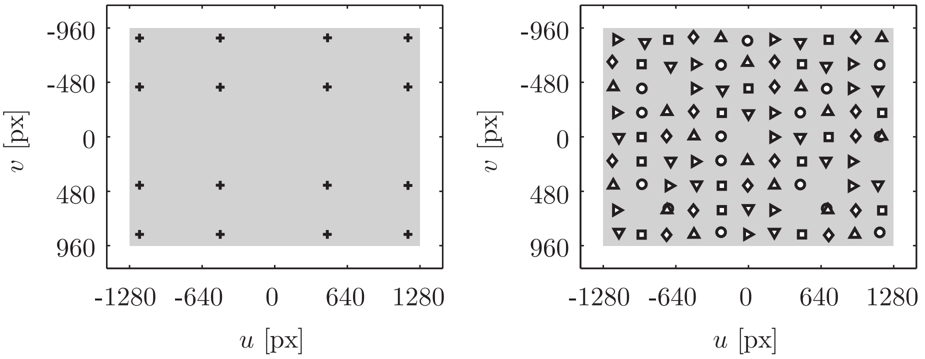

(a) symmetric and identical for all focus positions

(b) different for focus positions 908 ○, 693 △, 497 ◇, 273 □, 164 ▽ and 129 ▷

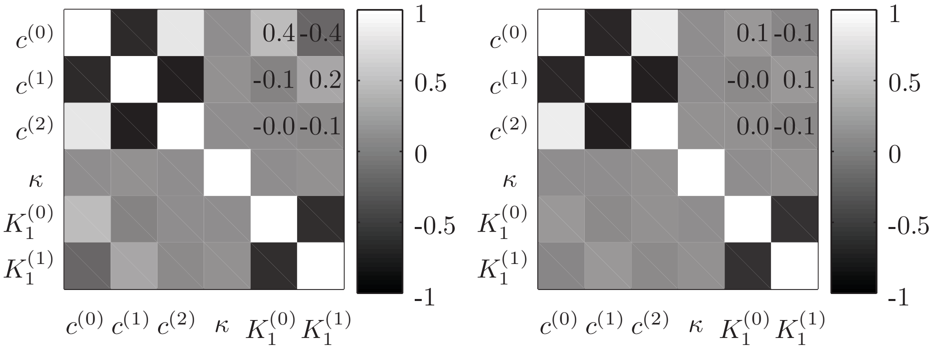

(c)

(d)

Figure 7.2: Positions of the target on the image sensor (top row) and resulting correlations coefficients of the estimated parameters (bottom row).

get after Section 6.3. For the specified focusing range of the instrument, the 99% confidence level of the calibrated camera constant is within ±9 px and cannot be displayed in Figure 7.3. The values for c correspond to an angle per pixel of about $\alpha_{\text{px}} = 0.6\,\text{mgon/px}$ $(= \arctan 1/c)$ which can be used for coarse approximations of achievable accuracies of the image-based measurements (cf. Section 1.3.1).

The radial distortion coefficient K_1 is modeled by a linear func-

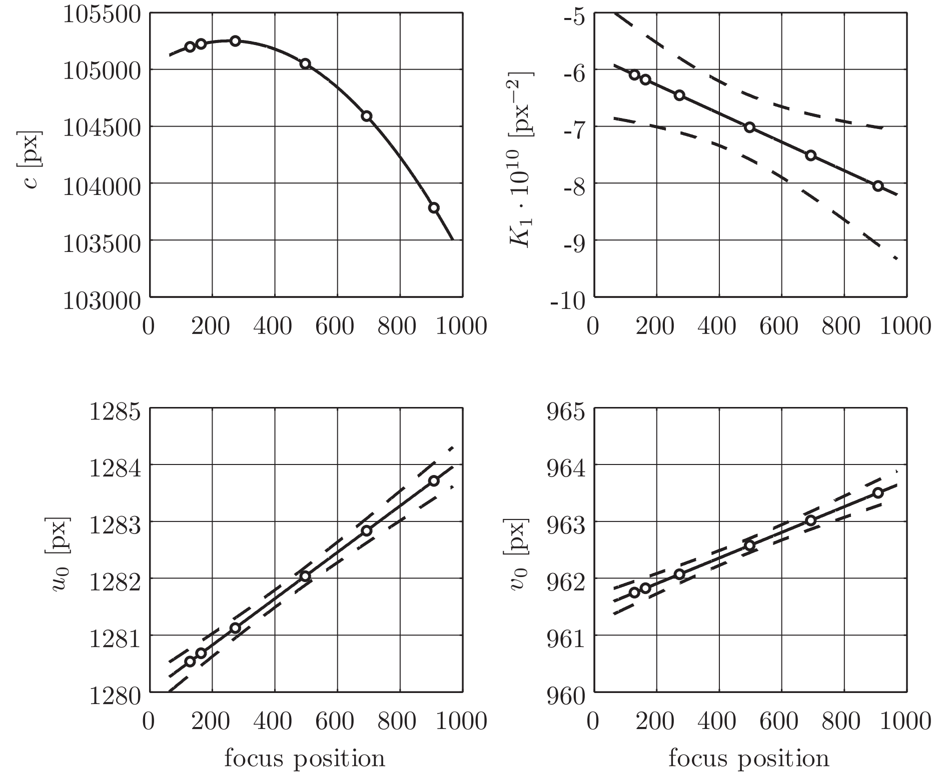

Figure 7.3: Focus-dependent calibration parameters with 99% confidence levels (dashed line) and focus positions used in the calibration (circles). Top left: Camera constant modeled by quadratic polynomial (confidence level of less than ±9 px too small to be visible). Top right: Radial distortion coefficient modeled by linear function. Bottom row: Principal point modeled by linear function.

tion of the focus position and also needs to be accounted for achieving accurate results. The coordinates u_0 and v_0 of the principal point vary with the focus position by up to 4 px which corresponds to over 2 mgon. Consequently, the focus-dependent values are required for measurements in one telescope face. For two-face measurements the principle point cancels out (cf. Section 6.3.3) and its coordinates are not required.

The focus-dependence of the mapping parameters (Figure 7.3)

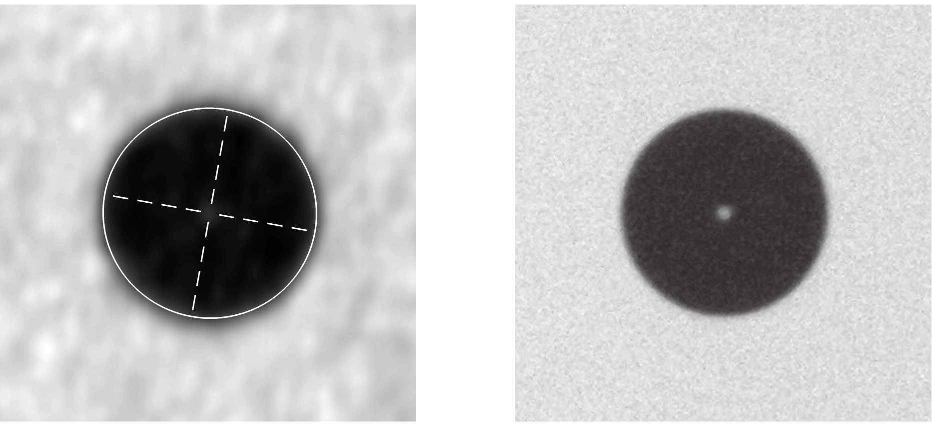

(a) reflectivity values from EDM with fitted ellipse

(b) image data from telescope camera

Figure 7.4: Circular target (diameter: 40 mm) scanned and imaged at a distance of 26.6 m.

of the evaluated state-of-the-art IATS is similar to different IATS prototypes (Vogel 2006; Wasmeier 2009; Bürki et al. 2010; Knoblach 2011). This is unsurprising since the variations are caused by the optics of the telescope which are similar for the different instruments.

To determine the rotation angles φ and ω (Section 7.3.4) between the principal axis of the camera and the collimation axis of the EDM sensor, a circular target (diameter: 40 mm) was scanned at a distance of 26.6 m. The target was oriented roughly orthogonal to the sighting axis of the IATS to avoid effects caused by a skew incident angle of the laser beam on the target (e.g. Kowalczyk and Rapinski 2014). Additionally, image-based measurements were conducted towards the target center. The reflectivity values are shown in Figure 7.4a and are used to compute the center of the circle with an ellipse fit. The 3D coordinates of the circle center resulting from the distance measurements are then converted to polar angles Hz_{T} and V_{T} and are used in Eq. (7.29) to compute the rotation angles φ

Table 7.2: Estimated calibration parameters with standard deviations (1σ) for the telescope camera of a *Leica MS60* from February 2016

c [px]:	$c^{(0)} = 105029 \pm 4$
	$c^{(1)} = 1.75 \pm 0.02$
	$c^{(2)} = -0.00343 \pm 0.00002$
κ [mgon]:	-21.0 ± 0.7
K_1 [px^{-2}]:	$K_1^{(0)} = -5.8\mathrm{e}^{-10} \pm 0.4\mathrm{e}^{-10}$
	$K_1^{(1)} = -2.5\mathrm{e}^{-13} \pm 0.7\mathrm{e}^{-13}$
u_0 [px]:	$u_0^{(0)} = 1280.0 \pm 0.1$
	$u_0^{(1)} = 0.0041 \pm 0.0002$
v_0 [px]:	$v_0^{(0)} = 961.5 \pm 0.1$
	$v_0^{(1)} = 0.0023 \pm 0.0002$
φ [mgon]:	$-4 \pm$ n.a.
ω [mgon]:	$-3 \pm$ n.a.

and ω. Instead of using the artificial target displayed in Figure 7.4, it should also be possible to apply this approach on natural features included in the observed structure which allows an on-the-fly calibration of φ and ω.

Table 7.2 shows the calibration parameters of the instrument's telescope camera in which the focus-dependent parameters are modeled by the polynomials of Eqs. (7.21) to (7.24). For the camera constant c the parameters of a quadratic polynomial are shown. The radial distortion coefficient K_1 and the principal point (u_0, v_0) are expressed by linear functions. For κ, which is invariant w.r.t. the focus position, only one value is used. The estimated parameters are significant on a 99% confidence level. It is emphasized that the full covariance matrix of the model coefficients needs to be considered for computing the standard deviation of the parameters itself at a certain focus position. For example at a focus position of 103 (corresponding to 30 m), $s_c = 2.3$ px which is smaller than the standard deviation of 4 px for $c^{(0)}$.

The rotation angles φ and ω between the principal axis of the

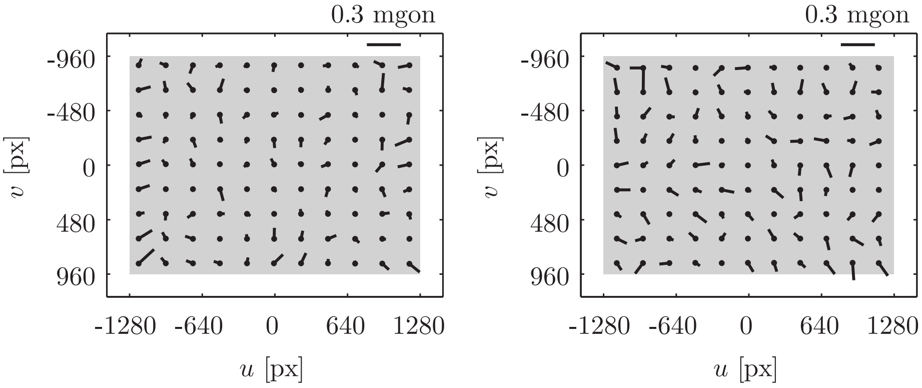

(a) focus position 497 at 3.2 m **(b)** focus position 129 at 18.9 m

Figure 7.5: Residuals of theodolite angles for different positions of the target on the image sensor.

camera and the collimation axis of the EDM sensor (Section 7.3.4) are given without a standard deviation. Although the ellipse fit (Figure 7.4a) would yield a standard deviation for the estimated circle center which could be propagated to φ and ω, this does not generate realistic values for the quality of the rotation angles. For the exemplarily illustrated calibration at a distance of 26.6 m (Figure 7.4), the standard deviation of the circle center is reported with 4 µm which corresponds to 0.01 mgon. Considering the size of the laser spot (7 mm × 10 mm at a distance of 30 m, cf. Leica 2015a, p. 67), 4 µm cannot be regarded as a meaningful value for the precision of the circle center. However, the quality of the parameters φ and ω can be evaluated visually as shown in Section 7.5.

7.5 VERIFICATION OF THE CALIBRATION

To check the calibrated mapping parameters, a virtual target field with an 11 × 9 target grid (99 virtual targets) is established at different focus positions. By using the calibration parameters of Table 7.2, which result from using only 16 virtual targets for each

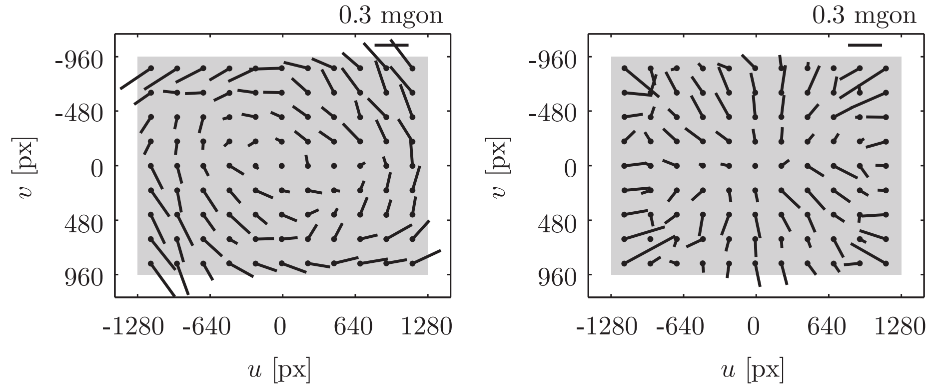

(a) K_1 used, without κ **(b)** κ used, without K_1

Figure 7.6: Residuals of theodolite angles for different positions of the target on the image sensor and different calibration parameters taken into account (for focus position 129 at 18.9 m, compare to Figure 7.5b).

focus position, the theodolite angles towards the target center can be computed for each telescope position. The residuals from the average direction are exemplarily depicted in Figure 7.5 for two different distances and thus focus positions.

For the same measurement data as used in Figure 7.5b, Figure 7.6 depicts the effects of neglecting the calibration parameters κ and K_1 in the mapping relation. The systematic of the residuals clearly points out that the parameters κ and K_1 must be considered for accurate image-based measurements.

Table 7.3 and Figure 7.7 numerically and graphically display the residuals for other focus positions in which an 11×9 target grid (as in Figure 7.5) was used at each position. Table 7.3 shows that the residuals, expressed in units of angles, do not change with the distance towards the target. Therefore, high-precision measurements towards targets at close distances are possible (cf. Chapter 4).

Plotting the residuals against the theoretic quantiles of the normal distribution $\mathcal{N}(0, 0.06^2)$ in Figure 7.7 (left) demonstrates their random character in which a standard deviation of 0.06 mgon can

Table 7.3: Residuals of theodolite angles with standard deviations and maximum values for different focus positions

focus	**dist.**	***Hz* [mgon]**		***V* [mgon]**	
[step]	**[m]**	**std.**	**max.**	**std.**	**max.**
129	18.875	0.05	0.13	0.06	0.20
164	12.569	0.06	0.14	0.06	0.21
273	6.283	0.07	0.18	0.06	0.22
497	3.213	0.05	0.13	0.05	0.15
693	2.308	0.07	0.21	0.06	0.21
908	1.801	0.05	0.16	0.06	0.16

be stated for horizontal and vertical angle measurements (compare to Section 4.3.2). It can be concluded from the normal distribution of the residuals that the mapping from image coordinates to theodolite angles is sufficiently parameterized by the quantities of Table 6.2 expressed by the calibration parameters of Table 7.2. The quality of the calibration parameters is further verified by plotting the residuals against the radial distance r towards the principal point (Figure 7.7 right). This demonstrates that the accuracy of the theodolite angles towards a target is scarcely influenced by the position of the target on the image sensor.

Regarding the specified accuracies of the used IATS for the angle measurements (0.3 mgon) and the readings of the tilt compensator (0.15 mgon, cf. Table 1.5), the residuals of Table 7.3 and Figure 7.7 are remarkable since they include the measurements of these sensors (cf. Section 6.2.5). This is confirmed by Walser (2004, p. 113) and Wasmeier (2009, p. 44) where image-based angle measurements with a standard deviation of a few 0.1 mgon also outperform the specified values of the used IATS prototypes.

It is carefully noted that the outstanding values of Table 7.3 and Figure 7.7 with maximum residuals of about 0.2 mgon and standard deviations of less than 0.1 mgon for the image-based angle measurements are obtained under controlled environmental conditions in-

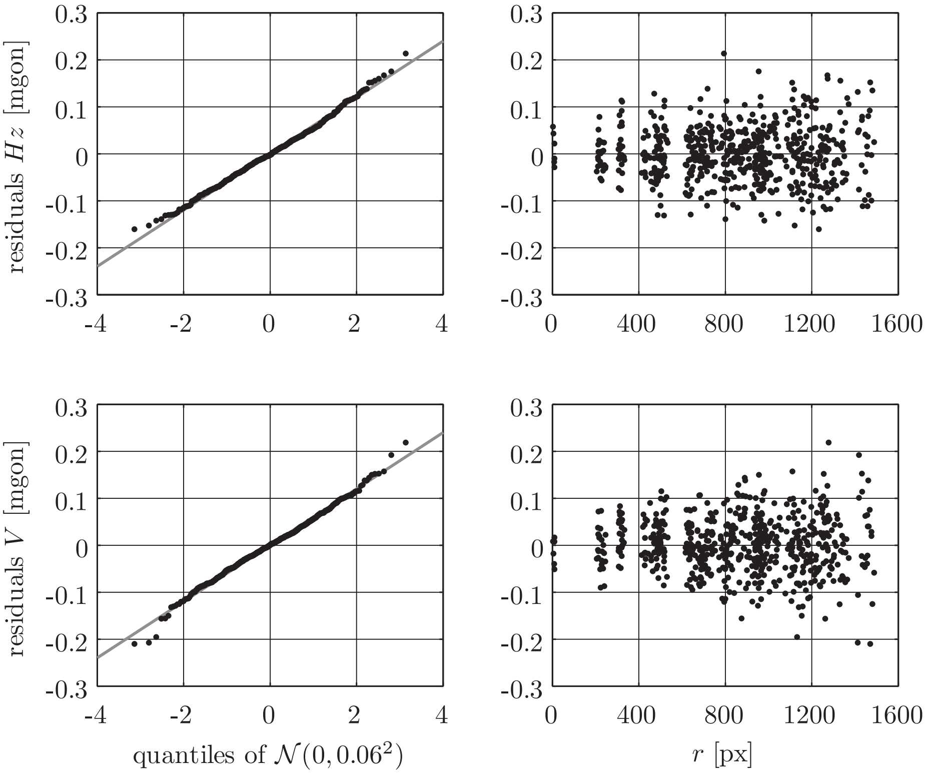

Figure 7.7: Residuals of horizontal and vertical theodolite angles plotted against quantiles of the normal distribution (left column) and against the radial distance of the imaged target towards the principal point (right column).

doors. For measurements outdoors, turbulences in the atmosphere (cf. Chapter 3) can heavily degrade these values. Furthermore, the values do not include target specific errors which are discussed in Section 4.2.3.

The quality of the determined rotation angles φ and ω between the image-based collimation axis, i.e., the principal axis of the image sensor, and the collimation axis of the EDM sensor is assessed by pointing the telescope towards a visual target while the laser of the EDM is switched on. An image of the EDM spot, which was taken with a standard digital camera, is shown in Figure 7.8.

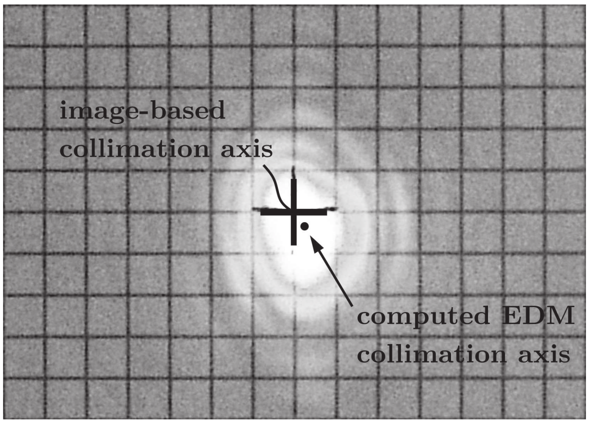

Figure 7.8: EDM spot at 26.6 m on a squared paper (spacing: 5 mm) for the telescope being aligned with the marked cross.

At a distance of 26.6 m, the calibrated values of $\varphi = -4$ mgon and $\omega = -3$ mgon (Table 7.3) correspond to 1.7 mm in vertical and 1.3 mm in horizontal direction (cf. Figure 6.4). The calibrated values for φ and ω can be validated by comparing the computed location of the EDM collimation axis (based on φ and ω) with the centroid of the EDM spot in Figure 7.8.

For a polar measurement, where the image-based angles and the distance must refer to the same point, the telescope must be rotated towards the angle computed from Eq. (6.31) so that the center of the EDM spot is aligned with the marked cross. At the new telescope position, the angles still refer to the target because the changed position of the target (the marked cross in Figure 7.8) on the image sensor is accounted in the image-based computation of the theodolite angles.

7.6 TEMPORAL STABILITY

The calibration parameters of Table 7.2 result from a calibration in February 2016. To assess the stability of these parameters, a similar calibration procedure was carried out in October 2016. Between the

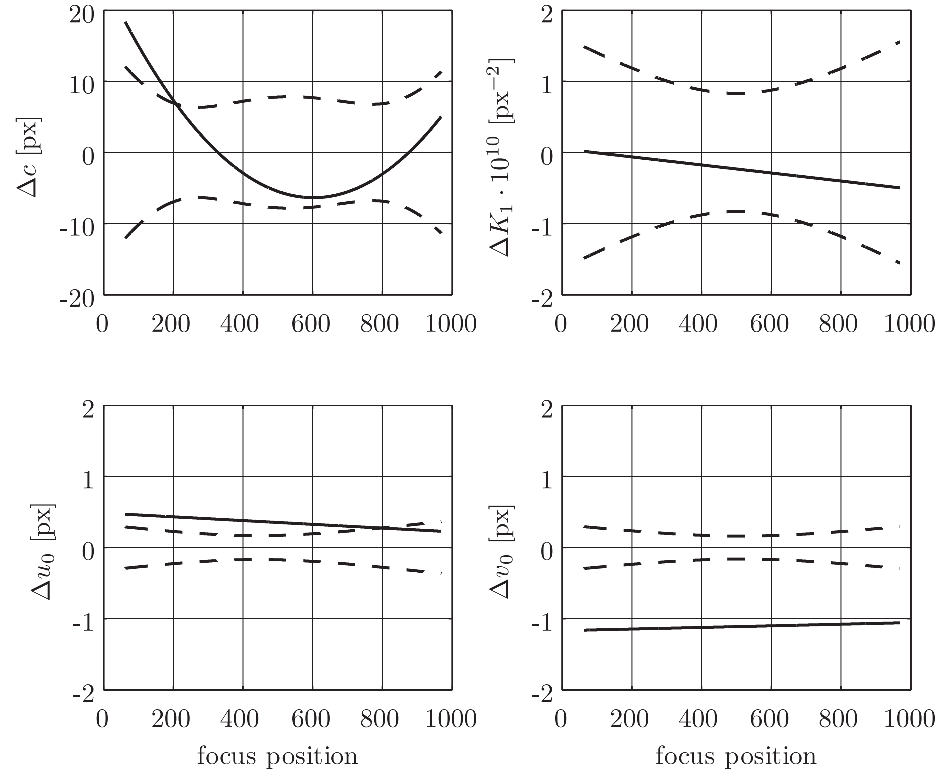

Figure 7.9: Changes of calibration parameters (solid line) between February and October 2016 with 99% significance levels (dashed line).

two calibrations, the instrument was used in different long-term experiments and field measurements with exposure to temperature changes, solar radiation, snowfall and rain. Furthermore, the IATS underwent two shipments by a parcel service.

The changes of the calibration parameters and their 99% significance levels are shown in Figure 7.9. For the specified focusing range (focus positions 62 to 969), the changes in the parameters of the camera constant, cf. Eq. (7.21), result in deviations of less than 20 px for the modeled camera constant. The absolute value of c is about 105 000 px (Section 7.4) or 231 mm (Leica 2015a, p. 71) and the maximum change in c corresponds to about 0.04 mm. Considering the movable optics inside the telescope of the IATS, this deviation is not regarded as extraordinary. It is further mentioned that a change in c of 20 px translates to less than 0.2 mgon for the measured theodolite angles to a target observed in the boundary area of the image sensor. For targets located closer to the center of the image sensor or relative measurements, as used for deformation monitoring (Chapter 2), the maximum change in c of 20 px is absolutely negligible.

The radial distortion is a function of the lens design (Luhmann et al. 2014, p. 121) which did not change between the two calibrations. This is also reflected in the non-significant changes in K_1. The rotation angle κ of the image sensor about the sighting axis significantly changed by 6 mgon (-21 mgon in February 2016, -27 mgon in October 2016). For the measured theodolite angles to a target observed in the boundary area of the image sensor, this corresponds to a change of less than 0.1 mgon in which smaller changes result for targets observed closer to the center of the image sensor. Thus, κ is regarded to be stable because its variation has a negligible effect on the measured image-based angles.

The principal point (u_0, v_0) is modeled as a linear function of the focus position, cf. Eqs. (7.23) and (7.24), in which only the offsets of these functions changed significantly between the two calibrations. This is also depicted in Figure 7.9 (bottom row) where the differences between the two calibrations are roughly constant. It is hereby noted that the principal point is computed according to Section 7.3.1 and includes the collimation and the vertical index error of the IATS. Consequently, the changes of about 0.5 and 1.1 px in Figure 7.9, which correspond to 0.3 and 0.7 mgon, are unsurprising. It is further noted that the mentioned instrument errors were adjusted several times between the two calibrations by using the onboard routines of the IATS (Leica 2015a, pp. 54ff.).

To demonstrate the effects of the changed parameters on the measurements, an 8×6 virtual target grid was established. Analogously to Figure 7.5, the residuals from the average direction are

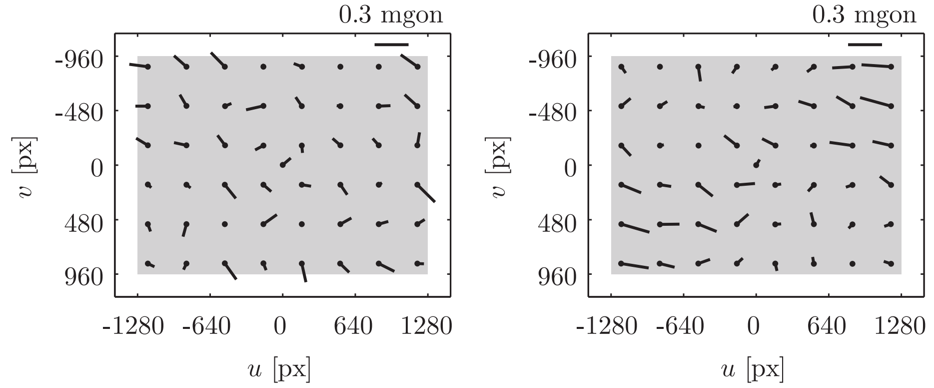

(a) focus position 460 at 3.5 m **(b)** focus position 102 at 31.4 m

Figure 7.10: Residuals of theodolite angles computed with 8-months-old calibration parameters for different positions of the target on the image sensor.

depicted in Figure 7.10 for two different distances and thus focus positions.

When using up-to-date calibration parameters, the image-based angle measurements show a standard deviation of 0.06 mgon and maximum residuals of 0.2 mgon (cf. Table 7.3). When using the 8-months-old calibration parameters, these values are slightly degraded to about 0.1 mgon for the standard deviations and 0.3 mgon for the maximum residuals. However, these values are still perfectly sufficient for many measurement applications. It is hereby noted that the changes in the principal point, which affect the measured angles by roughly 1 mgon, cancel out in Figure 7.10 because of the used two-face measurements. For measurements in one telescope face only, the principal point must be recalibrated regularly which can be done very efficiently as discussed in Section 7.3.5.

The rotation between the principal axis of the image sensor and the collimation axis of the EDM sensor was also recalibrated in which the values $\varphi = -4\,\mathrm{mgon}$ and $\omega = -3\,\mathrm{mgon}$ of Table 7.2 remained unchanged.

7.7 CONCLUSIONS

In this chapter, the calibration of an IATS was discussed. The proposed procedure for a thorough and automated calibration takes about one hour and can be done without additional equipment. By using up-to-date calibration parameters, it was demonstrated that the image-based angle measurements towards a target vary by ±0.2 mgon dependent on the position of the target on the image sensor. It was further demonstrated that the precision of the image-based angle measurements can be stated with less than 0.1 mgon in which this value is invariant w.r.t. the distance towards the target.

Most calibration parameters showed a good temporal stability. For example, by using 8-months-old calibration parameters, the image-based theodolite angles towards a target vary by ±0.3 mgon dependent on the position of the target on the image sensor. For calibration parameters with large temporal variations, a procedure for a fast in-field calibration was proposed.

For polar measurements, in which the image-based angle measurements and the EDM sensor must refer to the same point, the rotations φ and ω between the collimation axes of image and EDM sensor must be known. These values can also be calibrated automatically and it was shown that they are temporally stable. However, for the evaluated instrument the size and the shape of the laser spot vary with the distance (Leica 2015a, p. 67). It is subject to further investigations to check whether the centroid of the measurement spot also varies with the distance and, if necessary, distance-dependent values for φ and ω need to be used. Furthermore, the relation between the image-based and the EDM collimation axis of the evaluated IATS is modeled by two angles (φ and ω) only. For other IATSs, it might be necessary to also include an offset between the two collimation axes. Alternatively, the values for φ and ω could also be determined from the measurement data itself by comparing prominent features in the scan and the image data. This allows an on-the-fly calibration for the correct distance.

8

Summary and outlook

Today's state-of-the-art IATSs utilize the image data of their cameras primarily for visualization purposes and the number of currently implemented applications for image-based measurements is limited. In this thesis, different applications of IATSs were presented and experimentally evaluated. For the experimental measurements, only commercially available state-of-the-art IATSs, i.e., no specialized prototypes, were used.

At three different bridges, it was experimentally verified that an IATS is a powerful sensor for static and dynamic deformation monitoring. The accuracy of the image-based measurements with the evaluated IATSs is comparable or even better than the accuracy of conventional RTS measurements to retroreflective prisms. The main advantage of the IATS measurements over conventional RTS measurements is that no prisms are required on the monitored structure. Instead, prominent features of the structure itself are used as targets. These natural targets are measured automatically and accurately in the image data of the IATS's telescope camera. Accordingly, the installation of expensive retroreflective prisms, which is a cumbersome procedure that requires special machinery for some structures, is not necessary when using an IATS for monitoring purposes. Furthermore, the sampling rate of the video data, i.e., the frame rate of the camera, is typically higher and more constant than the sampling rate of the automated angle measurements of a RTS towards a prism. Image-based measurements are therefore beneficial in dynamic deformation monitoring because oscillations with higher frequencies can be resolved.

The image-based measurements of a state-of-the-art IATS were used for an experimental estimation of the vertical refraction angle which biases the vertical angle measurements of RTSs and IATSs. It was pointed out that knowledge of the refraction angle's variation over time is sufficient for a correction of the relative measurements in monitoring applications and that the absolute value of the refraction angle is not required for this purpose. The estimation of the refraction angle's variation is based on the standard deviation of its fluctuations which can be obtained from pure IATS measurements, i.e., without using any additional measurement equipment. However, the conducted experiment only provided satisfactory estimates for the refraction angle's variation for selected hours of day and further investigations on this issue are required.

From experimental measurements in a small-scale geodetic network, the accuracy of a two-face angle measurement with a state-of-the-art IATS was evaluated with better than 0.1 mgon (1σ) in horizontal and vertical direction. Under controlled environmental conditions, such as for a small-scale geodetic network indoors, it was shown that an IATS is able to measure 3D coordinates of selected points with an *accuracy* (confidence ellipsoids and external reliabilities) of a few 0.01 mm. The prerequisites for achieving highest accuracies involve a sufficient acclimatization and warm-up time of the IATS, a thorough calibration of the telescope camera, and a correction of different target specific errors.

By using the wide-angle camera of a state-of-the-art IATS, a methodology for improving the tracking of a prism was presented. Compared to the fine aiming module of a conventional RTS which is used to automatically track the prism, the AOV of the wide-angle camera of the evaluated IATS is about 10-times larger. Hence, the image data of the wide-angle camera can be used to reposition the telescope in cases in which the fine aiming module has lost the prism but the target is still inside the AOV of the wide-angle camera. The proposed method is based on visual object tracking in the image data of the IATS's wide-angle camera. After an initial selection of the object, the visual object tracking is done fully automatically. The results of the visual object tracking can also be used to verify whether the correct prism or a distracting prism is tracked by the fine aiming module.

The mapping relation between image coordinates and theodolite angles was worked out. This is an important prerequisite for evaluating the mentioned applications of image-based measurements with an IATS. Hereby, the image coordinates of a target, which result from different image processing algorithms, are related to their corresponding theodolite angles which can be used for further computations. Along with the necessary mapping parameters, simplifications for the telescope camera, whose center approximately corresponds to the center of the IATS, were worked out.

The mapping parameters for a correct relation between image coordinates and theodolite angles must be calibrated. The efficient and automated calibration of these mapping parameters was described in which the proposed calibration procedure does not require additional measurement equipment. Furthermore, the temporal stability of the calibration parameters was evaluated in which many parameters were found to be temporally stable. Accordingly, a regular calibration is only required for a few parameters. The regular calibration can be done before every measurement task because it is an automated and fast procedure which requires only a few minutes of additional time.

As already mentioned, the presented applications of IATSs were evaluated with state-of-the-art instruments. However, the processing of the image data and the steering of the IATSs were done on an external computer in which the image data (still images or video stream) was transmitted to the computer via a wired connection. Concerning the required computer hardware for executing the used image processing algorithms, the computers integrated in today's IATSs are regarded to be sufficient. However, the firmware versions of the evaluated IATSs are not designed to access the video stream from an onboard application, i.e., an application running on the IATS's internal computer, in real time. For many practical measurement applications, the usage of an external computer (including support and power supply) for steering the IATS is impractical because of the additional equipment that must be carried and installed at the measurement site. Therefore, the next milestone in the evolution of state-of-the-art IATSs is regarded to be the porting of existing applications to the onboard software of recent instruments with special emphasis on the computational efficiency of the used image processing algorithms.

Especially for image-based angle measurements with the telescope camera of an IATS, the precision of the image-based aiming, i.e., the computation of the image coordinates on sub-pixel level, excels the precision of the other sensors involved in the angle measurement (angular encoders and tilt compensator). However, the robustness of the image processing algorithms is another important issue. Concerning robustness, the image-based measurements typically perform very well for repeated measurements such as high-precision measurements to targets with a clearly defined geometry or for monitoring applications in which the same target is observed in different epochs. These applications also require measurements with a high accuracy. On the contrary, the image-based measurements with the IATS's wide-angle camera for improving the tracking of a prism do not require a high accuracy. However, concerning the robustness of the results, the visual object tracking is probably the most challenging application presented in this thesis.

Accordingly, special attention should be paid to the robustness of the algorithms when developing new image-based measurement applications – the accuracy is in the central focus of every geodesist anyhow. Hereby, it can help to reduce the image processing to a very specific task which is in contradiction to the usual approach of creating universally applicable measurement strategies. Furthermore, the total station capabilities of the IATS, e.g. the distance measurement, should be fully exploited to simplify the image processing tasks as much as possible.

References

Ahn S. J., Warnecke H.-J., and Kotowski R. (1999). "Systematic Geometric Image Measurement Errors of Circular Object Targets: Mathematical Formulation and Correction." *Photogramm. Rec.* 16(93): 485–502.

Alten K., Ralbovsky M., Vorwagner A., Toplitzer H., and Wittmann S. (2017). "Evaluation of Different Monitoring Techniques During Damage Infliction on Structures." *Procedia Eng.* 199: 1840–1845.

Althen (2015). *Servo-Inklinometer AIT230.* Datenblatt, Version 3.01. Althen GmbH Meß- und Sensortechnik, Kelkheim, Germany, 2 p.

Andreas E. L. (1990). *Selected papers on turbulence in a refractive medium*, SPIE Optical Engineering Press, Bellingham, WA.

Böckem B. (2001). "Development of a Dispersometer for the Implementation into Geodetic High-Accuracy Direction Measurement Systems." PhD thesis, No. 14252, Swiss Federal Institute of Technology Zurich, Zurich, Switzerland.

Bradski G. R. (1998). "Computer Vision Face Tracking For Use in a Perceptual User Interface." *Intel Technology J.* Q2: 1–15.

Bretscher R., Schlüter M., and Schmenger F. (2017). “Innovative Strategien des Long-Range-Scannings mit bildgebenden Tachymetern.” *gis.Science* 30(2): 40–47.

Brocks K. (1950). “Die Lichtstrahlkrümmung in Bodennähe.” *Deutsche Hydrographische Zeitschrift* 3(3-4): 241–248.

Brunner F. K. (1979). “Vertical refraction angle derived from the variance of the angle-of-arrival fluctuations”. In: Tengström E. and Teleki G. (eds.) *Refractional Influences in Astrometry and Geodesy.* IAU, International Astronomical Union Symposia 89: pp. 227–238.

Brunner F. K. (1984). *Geodetic refraction: effects of electromagnetic wave propagation through the atmosphere*, Springer, Berlin, Germany.

Brunner F. K. (2007). “On the methodology of Engineering Geodesy.” *J. Appl. Geodesy* 1(2): 57–62.

Brunner F. K. (2014). “Diskussion der Modellierung der Vertikalrefraktion mit dimensionslosen atmosphärischen Parametern.” *Allg. Verm.-Nachrichten* 121(6): 226–230.

Brunner F. K. (2015). *Refraktion und turbulente Fluktuationen des Einfallswinkels.* Unpublished report to the Alexander von Humboldt Foundation. Institute of Engineering Geodesy and Measurement Systems, Graz University of Technology, Graz, Austria, 32 p.

Brunner F. K. and Grillmayer E. (2002). “On the Temperature Dependence of Gyroscopic Measurements Using the GYROMAT 2000.” *Proc., FIG XXII Int. Congr.* Washington, D.C., pp. 1–13.

Brunner F. K. and Kukuvec A. (2011). “Utility of Geodetic Refraction.” *Proc., 5th Int. Conf. on Engineering Surveying.* Brijuni, Croatia, pp. 19–28.

Bürki B., Guillaume S., Sorber P., and Oesch H.-P. (2010). “DAEDALUS: A Versatile Usable Digital Clip-on Measuring System for Total Stations.” *Proc., Int. Conf. on Indoor Positioning and Indoor Navigation (IPIN).* Zurich, Switzerland, pp. 1–10.

Calonder M., Lepetit V., Strecha C., and Fua P. (2010). “BRIEF: Binary Robust Independent Elementary Features.” *Proc., 11th European Conf. on Computer Vision.* Heraklion, Greece, pp. 778–792.

Casott N. and Deußen D. (2000). “Vom "Bildflimmern" zur refraktionskorrigierten Vertikalwinkelmessung.” *Allg. Verm.-Nachrichten* 107(8-9): 286–292.

Charalampous E., Psimoulis P., Guillaume S., Spiridonakos M., Klis R., Bürki B., Rothacher M., Chatzi E., Luchsinger R., and Feltrin G. (2015). "Measuring sub-mm structural displacements using QDaedalus: a digital clip-on measuring system developed for total stations." *Appl. Geomatics* 7(2): 91–101.

Cheng Y. (1995). "Mean shift, mode seeking, and clustering." *IEEE Trans. Pattern Anal. Mach. Intell.* 17(8): 790–799.

Davies E. R. (2012). *Computer and Machine Vision.* 4th ed., Academic Press, Boston, MA.

Deumlich F. and Staiger R. (2002). *Instrumentenkunde der Vermessungstechnik.* 9th ed., Wichmann, Heidelberg, Germany.

DIN 18710-4:2010-09, Ingenieurvermessung - Teil 4: Überwachung.

Dold J. (1996). "Influence of large targets on the results of photogrammetric bundle adjustment." *Int. Arch. Photogramm. Remote Sens.* XXXI-B5: 119–123.

Dold J., Moser D., and Zumbrunn R. (2012). "Tracking method and measuring system comprising a laser tracker." US 8,279,430 B2. Leica Geosystems AG, Heerbrugg, Switzerland.

Ehrhart M., Kalenjuk S., and Lienhart W. (2017). "Monitoring of bridge vibrations with image-assisted total stations." *Proc., 4th Conf. on Smart Monitoring, Assessment and Rehabilitation of Civil Structures (SMAR).* Zurich, Switzerland, pp. 1–8.

Ehrhart M. and Lienhart W. (2015a). "Development and evaluation of a long range image-based monitoring system for civil engineering structures." *Proc., SPIE 9437, Structural Health Monitoring and Inspection of Advanced Materials, Aerospace, and Civil Infrastructure.* San Diego, CA, 94370K.

Ehrhart M. and Lienhart W. (2015b). "Image-based dynamic deformation monitoring of civil engineering structures from long ranges." *Proc., SPIE 9405, Image Processing: Machine Vision Applications VIII.* San Francisco, CA, 94050J.

Ehrhart M. and Lienhart W. (2015c). "Monitoring of Civil Engineering Structures using a State-of-the-art Image Assisted Total Station." *J. Appl. Geodesy* 9(3): 174–182.

Ehrhart M. and Lienhart W. (2017a). "Accurate Measurements with Image-Assisted Total Stations and Their Prerequisites." *J. Surv. Eng.* 143(2): 04016024.

Ehrhart M. and Lienhart W. (2017b). “Object tracking with robotic total stations: Current technologies and improvements based on image data.” *J. Appl. Geodesy* 11(3): 131–142.

Eschelbach C. (2009). “Refraktionskorrekturbestimmung durch Modellierung des Impuls- und Wärmeflusses in der Rauhigkeitsschicht.” PhD thesis, DGK C-638, Universität Karlsruhe (TH), Karlsruhe, Germany.

Fabiankowitsch J. (1990). “Automatische Richtungsmessung mit digitalen Differenzbildern.” PhD thesis, Technische Universität Wien, Vienna, Austria.

Fischer T. and Fischer W. (1999). “Manufacturing of High Precision Leveling Rods”. In: Lilje M. (ed.) *Geodesy and Surveying in the Future: The Importance of Heights.* FIG, Gävle, Sweden: pp. 223–228.

Fitzgibbon A. W., Pilu M., and Fisher R. B. (1996). “Direct least squares fitting of ellipses.” *Proc., 13th Int. Conf. on Pattern Recognition.* Vienna, Austria, pp. 253–257.

Flach P. (2000). “Analysis of refraction influences in geodesy using image processing and turbulence models.” PhD thesis, No. 13844, Swiss Federal Institute of Technology Zurich, Zurich, Switzerland.

Flach P. and Naterop D. (1999). “Neue Analysetechniken für Deformationsmessungen in permanenten Robotertachymeter-Netzen.” *Allg. Verm.-Nachrichten* 106(8-9): 284–291.

Fukunaga K. and Hostetler L. D. (1975). “The Estimation of the Gradient of a Density Function, with Applications in Pattern Recognition.” *IEEE Trans. Inf. Theory* 21(1): 32–40.

Geotronics (1991). *Geodimeter System 4000.* Technische Beschreibung. Geotronics AB, Danderyd, Sweden, 6 p.

GIM International (2007). *Topcon’s GPT-9000Ai Combines Imaging and Scanning.* GIM International News 04/05/2007. https://www.gim-international.eu.

Gong D., Huang Y. D., and Ball S. L. (1999). “A laser scanning videotheodolite for 3D visualisation and metrology.” *Proc., ISPRS Workshop on Vision-Based Techniques for Visualisation and Animation.* Hikodate, Japan, pp. 1–5.

Gonzalez R. C. and Woods R. E. (2002). *Digital Image Processing.* 2nd ed., Prentice Hall, Upper Saddle River, NJ.

Gottwald R. (1987). “Kern E2-SE - Ein neues Instrument nicht nur für die Industrievermessung?” *Allg. Verm.-Nachrichten* 94(4): 147–154.

Grillmayer E. (2003). “Untersuchung systematischer Fehlereinflüsse bei Messungen mit dem Kreisel DMT Gyromat 2000.” PhD thesis, Graz University of Technology, Shaker Verlag, Aachen, Germany.

Grimm D. E. (2014). “Methodenfreiheit mit der Leica Nova MS50.” *Allg. Verm.-Nachrichten* 121(8-9): 326–331.

Grimm D. E. and Hornung U. (2015). “Leica ATRplus - Leistungssteigerung der automatischen Messung und Verfolgung von Prismen.” *Allg. Verm.-Nachrichten* 122(8-9): 269–276.

Grimm D., Kleemaier G., and Zogg H.-M. (2015). *ATRplus.* White Paper. Leica Geosystems AG, Heerbrugg, Switzerland, 12 p.

Grübl F. and Schütz W. (1994). “Vortriebsvermessung, Steuerung und Überwachung maschineller Tunnelvortriebe”. In: Deutsche Gesellschaft für Erd- und Grundbau e.V. (ed.) *Taschenbuch für den Tunnelbau 1994 (18. Jahrgang).* Glückauf Verlag, Essen, Germany: pp. 157–210.

Guillaume S., Bürki B., Griffet S., and Mainaud Durand H. (2012). “QDaedalus: Augmentation of Total Stations by CCD Sensor for Automated Contactless High-Precision Metrology.” *Proc., FIG Working Week, Commission 6.* Rome, Italy, pp. 1–15.

Guillaume S., Clerc J., Leyder C., Ray J., and Kistler M. (2016a). “Contribution of the Image-Assisted Theodolite System QDaedalus to Geodetic Static and Dynamic Deformation Monitoring.” *Proc., 3rd Joint Int. Symp. on Deformation Monitoring (JISDM).* Vienna, Austria, pp. 1–9.

Guillaume S., Geiger A., and Scaramuzza M. (2016b). “Automated High Precision Optical Tracking of Aircrafts and non-cooperative Flying Objects.” *Proc., 29th Int. Technical Meeting of The Satellite Division of the Institute of Navigation (ION GNSS+).* Portland, OR, pp. 2315–2317.

Hartley R. and Zisserman A. (2004). *Multiple View Geometry in Computer Vision.* 2nd ed., Cambridge University Press, Cambridge, U.K.

Hauth S. and Schlüter M. (2010). “Digitalkameratachymeter - Einsatzmöglichkeiten für modulare und integrierte Systeme”. In: Kohlhofer G. and Franzen M. (eds.) *100 Jahre ISPRS - 100 Jahre internationale Zusammenarbeit: 3-Ländertagung der DGPF, SGPF,* *OVG in Wien.* DGPF, Publikationen der Deutschen Gesellschaft für Photogrammetrie, Fernerkundung und Geoinformation (DGPF) e.V. 19: pp. 477–484.

Hauth S., Schlüter M., and Thiery F. (2012). “Modular Imaging Total Stations - Sensor Fusion for high precision alignment.” *Proc., 3rd Int. Conf. on Machine Control and Guidance.* Stuttgart, Germany, pp. 202–210.

Hauth S., Schlüter M., and Thiery F. (2013). “Schneller und ausdauernder als das menschliche Auge: Modulare Okularkameras am Motortachymeter.” *Allg. Verm.-Nachrichten* 120(6): 210–216.

HBM (2000). *Acceleration Transducer B12.* Mounting Instructions, Version 17.2.2000. HBM Mess- und Systemtechnik GmbH, Darmstadt, Germany, 24 p.

Hennes M. (2003). “Systemeigenschaften von Robottachymetern im Nahbereich - Untersuchungen am Beispiel von Leica-Instrumenten.” *Flächenmanagement und Bodenordnung* 6: 300–310.

Hennes M., Dönicke R., and Christ H.-P. (1999). “Zur Bestimmung der temperaturgradienteninduzierten Richtungsverschwenkung beim Tunnelvortrieb.” *Vermessung, Photogrammetrie, Kulturtechnik* 97(8): 418–426.

Hertzman M., Westermark M., and Svanholm S. (2011). “Geodetic instrument and related method.” US 7,908,752 B2. Trimble AB, Danderyd, Sweden.

Hirt C., Guillaume S., Wisbar A., Bürki B., and Sternberg H. (2010). “Monitoring of the refraction coefficient in the lower atmosphere using a controlled setup of simultaneous reciprocal vertical angle measurements.” *J. Geophys. Res.* 115(D21): 1–14.

Hoben M. (2013). “Versuche zur Refraktionsbestimmung - ein Vergleich zwischen IATS, Szintillometer und Temperaturgradiententurm.” Master thesis (unpublished), Technische Universität München, Munich, Germany.

Huang Y. D. (1992). “3-D Measuring Systems Based on Theodolite-CCD Cameras.” *Proc., XVII ISPRS Congr., Commission V.* Washington, D.C., pp. 541–544.

Huang Y. D. and Harley I. (1989). “Calibration of Close-Range Photogrammetric Stations Using a Free Network Bundle Adjustment.” *Proc., Optical 3-D Measurement Techniques.* Vienna, Austria, pp. 49–56.

Ingensand H. (1992). “2000 Jahre Theodolit: von Heron bis Heinrich Wild - Ein Beitrag zur Entwicklungsgeschichte des Theodoliten.” *Vermessung, Photogrammetrie, Kulturtechnik* 90(3): 128–131.

Ingensand H. and Böckem B. (1997). “Automatic Location and Pointing Techniques in Local Positioning Systems.” *Proc., Optical 3-D Measurement Techniques IV*. Vienna, Austria, pp. 329–338.

Joyce K., Koehler M., and Vogel M. (2012). *Trimble VISION*. White Paper. Trimble Navigation Limited, Sunnyvale, CA, 18 p.

Juretzko M. (2005). “Reflektorlose Video-Tachymetrie - ein integrales Verfahren zur Erfassung geometrischer und visueller Informationen.” PhD thesis, DGK C-588, Ruhr Universität Bochum, Bochum, Germany.

Kabashi I. (2004). “Gleichzeitig-gegenseitige Zenitwinkelmessung über größere Entfernungen mit automatischen Zielsystemen.” PhD thesis, Geowissenschaftliche Mitteilungen 67, Technische Universität Wien, Vienna, Austria.

Kahmen H. and Reiterer A. (2004). “High-precision object monitoring with image assisted theodolites - state of the art.” *Proc., 8th Int. Workshop on Accelerator Alignment (IWAA)*. Geneva, Switzerland, pp. 1–11.

Kahmen H. and Seixas A. de (1999). “Object recognition with video-theodolites and without targeting the object.” *Proc., 6th Int. Workshop on Accelerator Alignment (IWAA)*. Grenoble, France, pp. 1–12.

Kalal Z., Mikolajczyk K., and Matas J. (2012). “Tracking-Learning-Detection.” *IEEE Trans. Pattern Anal. Mach. Intell.* 34(7): 1409–1422.

Kalenjuk S. and Lienhart W. (2017). “Automated Surface Documentation of Large Water Dams Using Image and Scan Data of Modern Total Stations.” *Proc., FIG Working Week, Commission 6*. Helsinki, Finland, pp. 1–15.

Katowski O. (1989). “Deformationsmessung an Bauwerken mit dem automatischen Theodolitmess-System ATMS.” *Proc., Optical 3-D Measurement Techniques*. Vienna, Austria, pp. 393–403.

Kludas T. (2012). “Surveying apparatus for tracking and surveying an object.” US 8,149,388 B2. Trimble Jena GmbH, Jena, Germany.

Kludas T. and Vogel M. (2010). “Surveying method and surveying instrument.” US 7,830,501 B2. Trimble Jena GmbH, Jena, Germany.

Kludas T., Vogel M., Grasser C., and Svanholm S. (2013). “Optical instrument and method for obtaining distance and image information.” US 8,368,875 B2. Trimble Jena GmbH, Jena, Germany.

Knoblach S. (2011). “Entwicklung, Kalibrierung und Erprobung eines kameraunterstützten Hängetachymeters.” PhD thesis, DGK C-655, Technische Universität Dresden, Dresden, Germany.

Kopacik A., Stanek V., Fabiankowitsch J., and Plach H. (1993). “Geodätische Meßverfahren bei der Belastungsprobe der "Donaubrücke der Jugend" in Bratislava (Preßburg).” *Österreichische Zeitschrift für Vermessungswesen und Photogrammetrie* 81(1): 8–16.

Kowalczyk K. and Rapinski J. (2014). “Investigating the Error Sources in Reflectorless EDM.” *J. Surv. Eng.* 140(4): 06014002.

Kraus K. (2007). *Photogrammetry: Geometry from Images and Laser Scans*. 2nd ed., de Gruyter, Berlin, Germany.

Krig S. (2014). *Computer Vision Metrics: Survey, Taxonomy, and Analysis*, Apress, New York, NY.

Kuhlmann H., Schwieger V., Wieser A., and Niemeier W. (2014). “Engineering Geodesy - Definition and Core Competencies.” *J. Appl. Geodesy* 8(4): 327–334.

Lachat E., Landes T., and Grussenmeyer P. (2017). “Investigation of a Combined Surveying and Scanning Device: The Trimble SX10 Scanning Total Station.” *Sensors* 17(4): 730.

Lackner S. and Lienhart W. (2016). “Impact of Prism Type and Prism Orientation on the Accuracy of Automated Total Station Measurements.” *Proc., 3rd Joint Int. Symp. on Deformation Monitoring (JISDM).* Vienna, Austria, pp. 1–8.

Leica (2010a). *Leica Absolute Tracker AT401.* White Paper. Leica Geosystems AG, Metrology Products, Unterentfelden, Switzerland, 16 p.

Leica (2010b). *Leica GeoMoS.* Online Help, Version 5.1. Leica Geosystems AG, Heerbrugg, Switzerland, 712 p.

Leica (2010c). *Leica TS11/TS15.* User Manual, Verision 1.0. Leica Geosystems AG, Heerbrugg, Switzerland, 216 p.

Leica (2013a). *Leica MS50/TS50/TM50.* User Manual, Version 1.1.1. Leica Geosystems AG, Heerbrugg, Switzerland, 84 p.

Leica (2013b). *Leica Nova MS50.* White Paper. Leica Geosystems AG, Heerbrugg, Switzerland, 12 p.

Leica (2014). *Leica Nova Series.* Technical Reference Manual, Version 2.1. Leica Geosystems AG, Heerbrugg, Switzerland, 1196 p.

Leica (2015a). *Leica MS60/TS60.* User Manual, Version 1.0. Leica Geosystems AG, Heerbrugg, Switzerland, 90 p.

Leica (2015b). *Leica Nova MS50.* GeoCOM Reference Manual, Version 5.50. Leica Geosystems AG, Heerbrugg, Switzerland, 289 p.

Leitz H. (1969). "Zwei elektronische Tachymeter von Zeiss." *Allg. Verm.-Nachrichten* 76(2): 73–79.

Lenzmann L. and Lenzmann E. (2004). "Strenge Auswertung des nichtlinearen Gauß-Helmert-Modells." *Allg. Verm.-Nachrichten* 111(2): 68–73.

Lienhart W. (2017). "Geotechnical monitoring using total stations and laser scanners: critical aspects and solutions." *J. Civil Struct. Health Monit.* 7(3): 315–324.

Lienhart W. and Ehrhart M. (2015). "State of the Art of Geodetic Bridge Monitoring". In: Chang F. K. and Kopsaftopoulos F. (eds.) *Structural Health Monitoring 2015: System Reliability for Verification and Implementation, Volume 1.* DEStech Publications, Lancaster, PA: pp. 449–457.

Lienhart W., Ehrhart M., and Grick M. (2017). "High frequent total station measurements for the monitoring of bridge vibrations." *J. Appl. Geodesy* 11(1): 1–8.

Lösler M. and Nitschke M. (2010). "Bestimmung der Parameter einer Regressionsellipse in allgemeiner Raumlage." *Allg. Verm.-Nachrichten* 117(3): 113–117.

Luhmann T. (2014). "Eccentricity in images of circular and spherical targets and its impact on spatial intersection." *Photogramm. Rec.* 29(148): 417–433.

Luhmann T., Robson S., Kyle S., and Boehm J. (2014). *Close-Range Photogrammetry and 3D Imaging.* 2nd ed., de Gruyter, Berlin, Germany.

Mein N., Svanholm S., Graesser C., and Vogel M. (2016). "Stereo photogrammetry from a single station using a surveying instrument with an eccentric camera." US 9,322,652 B2. Trimble AB, Danderyd, Sweden.

Metzler B. (2014). "Method for verifying a surveying instrument's external orientation." US 8,798,319 B2. Leica Geosystems AG, Heerbrugg, Switzerland.

Mischke A. (2000). “Entwicklung eines Videotheodolit-Meßsystems zur automatischen Richtungsmessung von nicht signalisierten Objektpunkten.” PhD thesis, Geowissenschaftliche Mitteilungen 54, Technische Universität Wien, Vienna, Austria.

Möser M., Hoffmeister H., Müller G., Staiger R., Schlemmer H., and Wanninger L. (2012). *Handbuch Ingenieurgeodäsie: Grundlagen.* 4th ed., Wichmann, Berlin, Germany.

Niemeier W. (2008). *Ausgleichungsrechnung.* 2nd ed., de Gruyter, Berlin, Germany.

Nikon-Trimble (2016). *Nikon Nivo-i Image Measurement Solution.* Datasheet. Nikon-Trimble Co., Ltd., Tokyo, Japan, 2 p. (in Japanese).

Ohtomo F. and Kumagai K. (2016). “Surveying instrument and three-dimensional camera.” US 2016/0238385 A1. Kabushiki Kaisha Topcon, Tokyo, Japan.

Ohtomo F., Otani H., Kaneko J., Anai T., and Nagashima T. (2010). “Multi-point measuring method and surveying device.” US 7,726,033 B2. Kabushiki Kaisha Topcon, Tokyo, Japan.

Omidalizarandi M. and Neumann I. (2015). “Comparison of target- and mutual informaton based calibration of terrestrial laser scanner and digital camera for deformation monitoring.” *Int. Arch. Photogramm. Remote Sens. Spatial Inf. Sci.* XL-1/W5: 559–564.

Otani H. and Kumagai K. (2012). “Surveying device and automatic tracking method.” US 8,294,769 B2. Kabushiki Kaisha Topcon, Tokyo, Japan.

Pettersson B., Siercks K., Voit E., Hinderling J., Zebhauser B., and Schneider K. (2015). “Surveying apparatus having a range camera.” US 2015/0085110 A1. Hexagon Technology Center GmbH, Heerbrugg, Switzerland.

Pettersson B., Siercks K., Voit E., Hinderling J., Zebhauser B., and Schneider K. (2016). “Position and orientation determination in 6-DOF.” US 9,443,308 B2. Hexagon Technology Center GmbH, Heerbrugg, Switzerland.

Pollock D. S. G. (1999). *A Handbook of Time-Series Analysis, Signal Processing and Dynamics*, Academic Press, San Diego, CA.

Psimoulis P. A. and Stiros S. C. (2007). “Measurement of deflections and of oscillation frequencies of engineering structures using Robotic Theodolites (RTS).” *Eng. Struct.* 29(12): 3312–3324.

Reiterer A. (2012). “Modeling Atmospheric Refraction Influences by Optical Turbulences Using an Image-Assisted Total Station.” *Zeitschrift für Geodäsie, Geoinformation und Landmanagement* 137(3): 156–165.

Reiterer A., Huber N. B., and Bauer A. (2010). “Image-Based Point Detection and Matching in a Geo-Monitoring System.” *Allg. Verm.-Nachrichten* 117(4): 129–139.

Roic M. (1996). “Erfassung von nicht signalisierten 3D-Strukturen mit Videotheodoliten.” PhD thesis, Geowissenschaftliche Mitteilungen 43, Technische Universität Wien, Vienna, Austria.

Rosten E. and Drummond T. (2006). “Machine Learning for High-Speed Corner Detection.” *Proc., 9th European Conf. on Computer Vision*. Graz, Austria, pp. 430–443.

Rother C., Kolmogorov V., and Blake A. (2004). “"GrabCut": Interactive Foreground Extraction Using Iterated Graph Cuts.” *ACM Trans. Graphics* 23(3): 309–314.

Rublee E., Rabaud V., Konolige K., and Bradski G. (2011). “ORB: An efficient alternative to SIFT or SURF.” *Proc., IEEE Int. Conf. on Computer Vision*. Barcelona, Spain, pp. 2564–2571.

Scherer M. (2007). “Phototachymetrie: Eine Methode zur Bauaufnahme und zur Erstellung eines virtuellen Modells.” *Allg. Verm.-Nachrichten* 114(8-9): 307–313.

Schestauer B.-J., Wagner A., Wiedemann W., and Wunderlich T. (2017). “Tachymetrisches 6DOF-Messverfahren.” *Proc., Ingenieurvermessung 2017*. Graz, Austria, pp. 213–220.

Schirmer W. (1994). “Universaltheodolit und CCD-Kamera - ein unpersönliches Meßsystem für astronomisch-geodätische Beobachtungen.” PhD thesis, DGK C-427, Technische Universität München, Munich, Germany.

Schlüter M., Hauth S., and Heß H. (2009). “Selbstkalibrierung motorisierter Digitalkameratheodolite für technische Präzisionsmessungen.” *Zeitschrift für Geodäsie, Geoinformation und Landmanagement* 134(1): 22–28.

Shi J. and Tomasi C. (1994). “Good features to track.” *Proc., IEEE Conf. on Computer Vision and Pattern Recognition*. Seattle, WA, pp. 593–600.

Snyder J. P. (1987). *Map Projections - A Working Manual.* U.S. Geological Survey Professional Paper 1395. United States Government Printing Office, Washington, D.C.

Studer M. and Ryf A. (2014). “Erkenntnisse aus dem geodätischen Langzeitmonitoring beim Bau des Gotthard-Basistunnels.” *Geomatik Schweiz* 112(6): 256–259.

Svanholm S., Grässer C., Vogel M., and Mein N. (2011). “Aiming of a geodetic instrument.” US 7,930,835 B2. Trimble AB, Danderyd, Sweden.

Svanholm S., Vogel M., and Grässer C. (2015). “Determining coordinates of a target in relation to a survey instrument having at least two cameras.” US 9,189,858 B2. Trimble AB, Danderyd, Sweden.

Szeliski R. (2010). *Computer Vision*, Springer, London, U.K.

Topcon (2007). *Topcon Imaging Station IS: TopSURV OnBoard for IS.* Reference Manual. Topcon Corporation, Tokyo, Japan, 31 p.

Topcon (2011a). *Topcon Imaging Station, IS Series: IS301/IS303/IS305.* Instruction Manual. Topcon Corporation, Tokyo, Japan, 172 p.

Topcon (2011b). *Topcon IS-3 Imaging Station.* Datasheet. Topcon Corporation, Tokyo, Japan, 4 p.

Trimble (2009). *Trimble S6 Total Station: Principles of the Tracker System.* Trimble Tech Tips. Trimble Navigation Ltd., Sunnyvale, CA, http://www.trimble.com/knowledge-center.

Trimble (2016a). *Trimble Access and Trimble SX10 Scanning Total Station Guide.* Presentation. Trimble Inc., Sunnyvale, CA, 60 p.

Trimble (2016b). *Trimble SX10 Scanning Total Station.* Datasheet. Trimble Navigation Ltd., Sunnyvale, CA, 4 p.

Tuytelaars T. and Mikolajczyk K. (2008). “Local Invariant Feature Detectors: A Survey.” *Found. Trends Comput. Graphics Vision* 3(3): 177–280.

Ullrich R. and Möser M. (2016). “Tachymetrische Identifizierung von Zielmarken durch Signalintensitätsmessungen.” *Allg. Verm.-Nachrichten* 123(10): 275–283.

Vogel M. (2006). “Vom Pixel zur Richtung: Die räumlichen Beziehungen zwischen Abbildungsstrahlen und Tachymeterrichtungen.” PhD thesis, Schriftenreihe Fachrichtung Geodäsie 20, Technischen Universität Darmstadt, Darmstadt, Germany.

Wagner A. (2016). “A new approach for geo-monitoring using modern total stations and RGB + D images.” *Measurement* 82: 64–74.

Wagner A. (2017). “New Geodetic Monitoring Approaches using Image Assisted Total Stations.” PhD thesis, Technische Universität München, Munich, Germany.

Wagner A., Huber B., Wiedemann W., and Paar G. (2014a). “Long-Range Geo-Monitoring using Image Assisted Total Stations.” *J. Appl. Geodesy* 8(3): 223–234.

Wagner A. and Wasmeier P. (2014). “Flächen- und Feature-basiertes Monitoring mit Videotachymetern”. In: Sternberg H. (ed.) *Multi-Sensor-Systeme - Bewegte Zukunftsfelder: Beiträge zum 138. DVW-Seminar am 18. und 19. September 2014 in Hamburg.* Wißner Verlag, DVW-Schriftenreihe 75: pp. 75–85.

Wagner A., Wasmeier P., Reith C., and Wunderlich T. (2013). “Bridge Monitoring by Means of Video-Tacheometer - A Case Study.” *Allg. Verm.-Nachrichten* 120(8-9): 283–292.

Wagner A., Wasmeier P., Wunderlich T., and Ingensand H. (2014b). “Vom selbstzielenden Theodolit zur Image Assisted Total Station.” *Allg. Verm.-Nachrichten* 121(5): 171–180.

Wagner A., Wiedemann W., Wasmeier P., and Wunderlich T. (2016). “Improved concepts of using natural targets for geo-monitoring.” *Proc., 3rd Joint Int. Symp. on Deformation Monitoring (JISDM).* Vienna, Austria, pp. 1–7.

Walser B. H. (2004). “Development and calibration of an image assisted total station.” PhD thesis, No. 15773, Swiss Federal Institute of Technology Zurich, Zurich, Switzerland.

Walser B., Metzler B., Aebischer B., Siercks K., and Pettersson B. (2014). “Method and system for highly precisely positioning at least one object in an end position in space.” US 8,798,794 B2. Leica Geosystems AG, Heerbrugg, Switzerland.

Wasmeier P. (2003). “The Potential of Object recognition Using a Servo-Tacheoemeter TCA2003.” *Proc., Optical 3-D Measurement Techniques VI, Volume 2.* Zurich, Switzerland, pp. 48–54.

Wasmeier P. (2009). “Grundlagen der Deformationsbestimmung mit Messdaten bildgebender Tachymeter.” PhD thesis, DGK C-638, Technische Universität München, Munich, Germany.

Webern H. von and Kahmen H. (2004). “High precision object monitoring by theodolites using gridline-methods.” *Proc., 8th Int. Workshop on Accelerator Alignment (IWAA).* Geneva, Switzerland, pp. 1–9.

Wiedemann W., Wagner A., and Wunderlich T. (2017). “Nivellieren mit bildunterstützten Totalstationen.” *Proc., Ingenieurvermessung 2017.* Graz, Austria, pp. 47–61.

Woschitz H. (2003). “System Calibration of Digital Levels: Calibration Facility, Procedures and Results.” PhD thesis, Graz University of Technology, Shaker Verlag, Aachen, Germany.

Wu Y., Lim J., and Yang M.-H. (2015). “Object Tracking Benchmark.” *IEEE Trans. Pattern Anal. Mach. Intell.* 37(9): 1834–1848.

Wunderlich T. (1985). “Die voraussetzungsfreie Bestimmung von Refraktionswinkeln.” PhD thesis, Geowissenschaftliche Mitteilungen 26, Technische Universität Wien, Vienna, Austria.

Wunderlich T. A. (2005). “Automatisches Zielen mit Tachymetern und Theodoliten”. In: Fabiankowitsch J., Eichhorn A., Haberler M., and Reiterer A. (eds.) *Festschrift anlässlich des 65. Geburtstages von Herrn o. Univ. Prof. Dr.-Ing. Heribert Kahmen.* Technische Universität Wien, Geowissenschaftliche Mitteilungen 71: pp. 29–42.

Wunderlich T., Wasmeier P., and Wagner A. (2014). “Auf dem Weg zum geodatischen Universalinstrument - wie nahe am Ziel sind IATS und MS50?” In: Riedel B. (ed.) *Terrestrisches Laserscanning 2014: Beiträge zum 139. DVW-Seminar am 11. und 12. Dezember 2014 in Fulda.* Wißner Verlag, DVW-Schriftenreihe 78: pp. 177–192.

Zach C., Pock T., and Bischof H. (2007). “A Duality Based Approach for Realtime TV-L1 Optical Flow.” *Proc., 29th DAGM Symp. on Pattern Recognition.* Heidelberg, Germany, pp. 214–223.

Zhang X., Zhu Z., Yuan Y., Li L., Sun X., Yu Q., and Ou J. (2012). “A universal and flexible theodolite-camera system for making accurate measurements over large volumes.” *Opt. Lasers Eng.* 50(11): 1611–1620.

Zhou Y., Wagner A., Wunderlich T., and Wasmeier P. (2016). “Calibration Method for IATS and Application in Multi-Target Monitoring using Coded Targets.” *Proc., 3rd Joint Int. Symp. on Deformation Monitoring (JISDM).* Vienna, Austria, pp. 1–13.

Zimmermann J., Kotzur N., Möller B., Sieber S., and Legrand V. (2013). “Geodesic measuring device comprising a thermographic camera.” US 2013/0278759 A1. Leica Geosystems AG, Heerbrugg, Switzerland.